



# Development of multi-physics and multi-scale Best Effort Modelling of pressurized water reactor under accidental situations

Alexandre Targa

## ► To cite this version:

Alexandre Targa. Development of multi-physics and multi-scale Best Effort Modelling of pressurized water reactor under accidental situations. Physics [physics]. Université Paris Saclay (COMUE), 2017. English. NNT : 2017SACLX032 . tel-01628481

**HAL Id: tel-01628481**

**<https://pastel.hal.science/tel-01628481>**

Submitted on 3 Nov 2017

**HAL** is a multi-disciplinary open access archive for the deposit and dissemination of scientific research documents, whether they are published or not. The documents may come from teaching and research institutions in France or abroad, or from public or private research centers.

L'archive ouverte pluridisciplinaire **HAL**, est destinée au dépôt et à la diffusion de documents scientifiques de niveau recherche, publiés ou non, émanant des établissements d'enseignement et de recherche français ou étrangers, des laboratoires publics ou privés.

THÈSE DE DOCTORAT  
DE  
L'UNIVERSITÉ PARIS-SACLAY  
PRÉPARÉE À  
L'ÉCOLE POLYTECHNIQUE

ÉCOLE DOCTORALE N° 573

Interfaces Approches Interdisciplinaires, Fondements, Applications et  
Innovation

Spécialité de doctorat : Énergie Nucléaire

par

**Alexandre TARGA**

Développement de modélisations multi-physiques Best Effort pour une analyse  
fine des réacteurs à eau pressurisée en conditions accidentelles.

**Thèse présentée et soutenue à l'Ecole Polytechnique,**

**le 7 Juillet 2017:**

**Composition du Jury :**

Président du Jury,	Pr. J.J. MARIGO,	Université Paris-Saclay
Rapporteur,	Pr. K. IVANOV,	North Carolina Univ.
	Pr. P. RUBIOLO,	Grenoble INP
Examineur,	Pr. C. DIOP,	CEA-SACLAY
	Dr. N. KERKAR,	EDF-SEPTEN
	Dr. K. MER-NKONGA,	CEA-CADARACHE
Directeur de thèse,	Pr. P. LE TALLEC,	Ecole Polytechnique
Encadrant de thèse,	Dr. J-C. LE PALLEC,	CEA-SACLAY
Invité,	Dr. F. DAMIAN,	CEA-SACLAY
	Dr. D. SCHNEIDER,	CEA-SACLAY



# Résumé

L'analyse de sûreté des réacteurs nucléaires nécessite la modélisation fine des phénomènes y survenant et plus spécifiquement ceux permettant d'assurer l'intégrité des barrières de confinement. Les outils de modélisation actuels favorisent une analyse fine du système réacteur par discipline dédiée, et couplée avec des modèles simplifiés. Néanmoins, le développement depuis plusieurs années d'une approche dite "Best Effort", basée sur des calculs multiphysiques et multi-échelle, est en cours de réalisation. Cette approche permettra d'accéder au suivi et à l'analyse détaillée de problèmes complexes tels que l'étude des Réacteurs nucléaires en situation standard et accidentelle. Dans cette approche, les phénomènes physiques sont simulés aussi précisément que possible (selon la connaissance actuelle) par les modèles couplés. Par exemple, des codes disciplinaires existent et permettent la modélisation précise de la neutronique, de la thermohydraulique du coeur du réacteur, ou de la thermomécanique du combustible. Une approche "Best Effort" consiste à coupler ces modèles afin de réaliser une modélisation globale et précise du système de réacteur nucléaire. Cette approche nécessite de bien définir les modèles qui sont utilisés afin de préciser exactement leurs limites, et donc de les assumer ou de les optimiser. C'est dans ce contexte de travail que s'inscrit cette thèse. Elle consiste dans le développement d'un couplage multiphysique et multi-échelle "Best Effort" afin d'obtenir une analyse précise des Réacteurs à Eau Légère en situations normale et accidentelle. Elle a consisté principalement en l'analyse des modèles et de leurs interactions et à la mise en oeuvre d'un algorithme de couplage multiphysique entre une neutronique et une thermohydraulique exprimées à l'échelle du réacteur, ainsi qu'avec une thermomécanique fine à l'échelle élémentaire du crayon combustible. En outre, un travail spécifique a été effectué afin de préparer ou d'améliorer l'accès à l'information physique locale nécessaire à la mise en oeuvre de modélisations couplées multi-échelles, à l'échelle du combustible.

---

**Mots clés:** Modélisation Multiphysique, Thermohydraulique, Thermo mécanique des Combustibles Nucléaire, Neutronique





# Abstract

The safety analysis of nuclear power plants requires a deep understanding of underlying key physical phenomena that determine the integrity of the physical containment barriers. At the present time, cutting edge models focus on a single aspect (discipline) of the physical system coupled with rough models of the other aspects needed to simulate the global system. But, safety analyses can be carried out based on Multiphysics and Multiscales modelling. This Best Effort approach would give a full and accurate (High Fidelity) comprehension of the reactor core under standard and accidental situations. In this approach, the physical phenomena are simulated as accurately as possible (according to present knowledge) by coupled models in the most efficient way. For example, codes exist that are accurate modellings of Neutronics, or modellings of thermal fluid mechanics inside the core, or modellings of thermal fluid mechanics over the whole system, or modellings of thermal mechanics of the fuel pin or over the whole device structure. A Best Effort approach would couple these models in order to realize a global and accurate modelling of the Nuclear reactor. This approach requires to define well the models that are used in order to exactly specify their limits, and hence, specify uncertainties of the coupled model results in order to assume and optimize them. It is in this context that this PhD thesis work is being undertaken. It consists in the development of a Multi-physics and multi-scale Best Effort modelling in order to obtain an accurate analysis of Pressurized Water Reactor under standard and accidental operating situations. It mainly involves the understanding of each model and their interactions, followed by the implementation of multiphysics algorithms coupling Neutronics and Thermohydraulics at reactor scale to an accurate Thermomechanics at the elementary scale of the fuel pin. In addition, a work project has been carried out in order to prepare or improve the access to the local physical informations that are needed for the implementation of multiscale coupling scheme, at the elementary scale of the fuel pin.

---

**Keywords:** Multiphysics modelling, Thermohydraulics, Fuel pin Thermomechanics, Neutronics



# Dedication

**This Thesis is dedicated to  
моей возлюбленной Дарье,  
mes parents, ma famille  
e miei Antenati.**



# Acknowledgements

First and foremost, I want to express my sincere gratitude to Pr. MARIGO who accepted to be the Jury President of PhD Thesis Defence, then I want to express my sincere gratitude to the Rapporteurs, Pr. IVANOV and Pr. RUBIOLO, as well as to the Examiners, Dr. MER-NKONGA, Pr. DIOP and Dr. KERKAR, who accepted to attend my PhD Thesis Defence, which marks the completion of these three fruitful years of PhD research.

With the same intensity, I would like to thank my PhD Director at the Ecole Polytechnique, Pr. LE TALLEC and my CEA supervisor, Dr. LE PALLEC. To them I am deeply and affectionately grateful for their guidance and patience, their strong and unflinching support and, above all, for their incredible scientific knowledge, the mathematical rigor and the Physical research analysis they steadily taught me during these three past years. None of this would have been possible without them.

I am also grateful to the Ecole Polytechnique and to the SERMA, both of whom gave me the opportunity to carry out my PhD. More specifically, I would like to thank Dir. BLANC-TRANCHANT, Director of the SERMA, and its successor, Dir. DELPECH, for their support and advices, as well as Dir. DAMIAN, Director of the "Laboratoire d'Etude, de Protection et de Conception" and the late Director Dir. AGGERY, to whom I address my deepest thoughts.

I am also very grateful to the colleagues at the SERMA, DEC, STMF and LGLS that I have had the pleasure of collaborating with during this PhD and that were particularly generous with their time.

Regarding the Neutronical part at the SERMA, I would like to thank the APOLLO3 Team for their advices, exceptional programming skills, the physical analysis that helped me handle the complexity of Neutronics and for their thoughtful and pertinent remarks and suggestions during the preparation of my numerous presentations: Anne-Marie BAUDRON, Jean-Jacques LAUTARD and Christine MAGNOT, Didier SCHNEIDER, Roland LENAIN, Jean-Michel Do, Karim AMMAR, Cyril PATRICOT and Christine POINOT.

Regarding the ThermoMechanical part at the DEC, I would like to thank Dir. MASSON, Patrick GOLBRON, Laurence NOIROT, Bruno MICHEL and Katherine MER-NKONGA for their continuous and strong both technical and academic support during the process of developing and formulating mathematically the ALCYONE part of this multiphysics coupling. In addition, I would like to thank specifically Katherine for her unflinching support to help me achieve this coupling, her scientific guidance but also for her affection and sincere support during difficult time. I am sincerely and affectionately grateful and I will always be indebted for that. None of this would have been possible without her.

Regarding the Thermohydraulical part at the STMF, I would like to thank Anouar MEKKAS and Sebastien CHEMIN who helped me handle and understand the FLICA part of this coupling.

Last but not least, regarding the SALOME part, I would like to thank Nicolas CROUZET for his unflinching faith, his exceptional programming skills and his unfading interest to help me achieve this coupling in the "MED" context of the CORPUS platform.

None of this would have been possible without them.

The administrative teams of SERMA and LMS, Michele, Jocelyne on the one hand and Alexandra and Anna on the other, as well as everyone else, were also of invaluable help to me during this time.

I also am truly grateful to all the people who have been on my side throughout these years of work. To Didier, who frequently offered me a seat in his car and most enjoyable conversations. To Roland for its strong and unflinching support. To Amelie, Arthur(s), Bertrand, Cyril, Daniele, Mathieu, Kevin, Karim and Olga, who dispensed practical and technical advices on the PhD and not only helped me avoid common traps but offered a sympathetic ear and moral support in good and bad times. I also want to thank my long-time friends, Antoine, Aude, Cedric, David, Faustine, Jacques and Victor, for those blissful moments of engaged conversations on everything but the PhD.

I am deeply grateful to my parents, my brothers Adrien and Antoine, my grand-parents and the rest of my family and my in-laws for their continuous encouragement, unwearied interest, unlimited patience and daily support.

Last but not least, I want to thank my beloved Daria SINICHKINA, who has been my fellow-traveller throughout this great adventure. Thank you so much for your love, care, corrections, and so many other things you have done for me while you were also struggling with your own Thesis. I look forward to the many happy years we will share together.

# Contents

	Page
Résumé .....	i
Abstract .....	iii
Dedication .....	v
Acknowledgements .....	vii
List of Figures .....	xv
List of Tables .....	xxi
 <b>I Introduction</b>	 <b>1</b>
 <b>II Physical context and scientific objectives</b>	 <b>7</b>
1. The Nuclear Reactor: a multi physical system .....	9
1.1 A multiphysical complex System .....	9
1.2 The multiscale system .....	12
1.3 Multiphysics coupling State-of-the-art .....	14
2. Transient scenario phenomenology of a Rod Ejection Accident .....	17
2.1 REA classical transient overview .....	17
2.2 Physical specifications .....	20
2.2.1 Neutronics representativeness .....	20
Temporal aspect . . . . .	20
Spatial aspect . . . . .	24
2.2.2 Thermomechanics representativeness .....	26
Thermomechanics initial state . . . . .	26
Mechanical transient specificities . . . . .	27
2.2.3 Thermohydraulics representativeness .....	29
Thermohydraulics initial state . . . . .	29
Thermohydraulics transient specificities . . . . .	29
2.3 REA Benchmarks identification .....	31
2.4 Academic case and transient scenario .....	34
2.4.1 Academic model .....	34
2.4.2 Academic scenario .....	35
Initial state . . . . .	35
Transient and Post accident state . . . . .	37
PWR-Academic core transient comparison . . . . .	39
2.5 Proof of Concept Coupling Framework used in this work .....	40



### III Neutronic models of the core 43

3. Neutronics equations and Numerical Models .....	45
3.1 Core Reactor Physical Description .....	45
3.2 Physical Equations .....	46
3.2.1 Symbols and definitions .....	46
3.2.2 Unknown elements of the problem .....	48
3.2.3 Variables .....	49
3.2.4 Neutron transport equation .....	49
3.2.5 Isotopic and precursor evolutions .....	50
3.2.6 Physical closure equations .....	53
3.2.7 Boundary conditions .....	58
3.3 APOLLO3 Numerical Methods - Core Calculation .....	59
3.3.1 Code Description - APOLLO3 .....	59
3.3.2 Symbols and definitions .....	59
3.3.3 Code description - Variables .....	60
3.3.4 Multigroup theory .....	61
3.3.5 Microscopic Cross Sections .....	62
3.3.6 Macroscopic cross sections .....	64
3.3.7 Discretization strategy .....	67
SPn discretization method - the static case . . . . .	68
SPn discretization method- Kinetic case . . . . .	70
Sn discretization method - Static Case . . . . .	71
3.3.8 Power computation .....	72
4. Access to the local parameters and Best Effort improvement of Neu-	
tronics models .....	73
4.1 Fast neutron flux Computation .....	73
4.2 Fine Flux Reconstruction .....	74
4.2.1 MINOS-MINARET Approach .....	75
4.2.2 Flux Reconstruction .....	77
4.2.3 Algorithm .....	80
4.2.4 Validation .....	81
4.2.5 Results .....	83
4.2.6 Conclusion .....	86
4.3 Power reconstruction at pellet level .....	87
4.3.1 Burn-up computation .....	87
4.3.2 Flux and radial Power Computation at the pellet scale .....	88
4.3.3 Prompt neutron flux computation for the clad .....	89
4.3.4 Isotopic concentrations .....	89
5. Neutronics conclusion .....	93

## IV ThermoMechanical and Thermohydraulical models 99

6. ThermoMechanical equations and Numerical Models of the fuel pin under irradiation .....	101
6.1 Physical Description .....	101
6.2 Notations and unknowns .....	102
6.3 Constitutive laws for pellet .....	105
6.3.1 Crack law .....	105
6.3.2 Creep law .....	106
6.3.3 Solid Swelling and Densification .....	107
6.3.4 Gas swelling .....	108
6.3.5 Thermal expansion .....	111
6.3.6 Fuel pellet Physical data .....	111
6.4 Constitutive laws for the fuel pin cladding .....	112
6.4.1 Viscoplastic behavior .....	112
6.4.2 Creep behavior .....	113
6.4.3 Thermal expansion .....	114
6.4.4 Fuel pellet Cladding Physical data .....	114
6.5 Boundary conditions and final mechanical problem .....	115
6.6 Thermal modelling .....	117
6.7 Discretization and code description .....	120
7. Best Effort improvement of the fuel pin ThermoMechanical models .....	121
7.1 Condensation of the Thermodynamic problem .....	121
7.2 Problem linearization and elimination of the internal variables .....	125
7.3 ALCYONE fuel pin effective temperature computation .....	126
8. Thermomechanical conclusion .....	129
9. ThermoHydraulical Physical equations and Numerical Models .....	137
9.1 Physical Description .....	137
9.2 Notations and unknowns .....	138
9.3 Physical Equations .....	142
9.3.1 Conservation laws .....	142
9.3.2 Porous Model Closure laws .....	143
9.3.3 Vapor production term .....	144
9.3.4 Stress tensor .....	145
9.3.5 Wall Friction force .....	145
9.3.6 Thermal coefficient and sources terms .....	147
9.3.7 Porous Model Boundary conditions .....	149
9.4 Discretization and Code description .....	149

10. Thermohydraulics conclusion .....	153
---------------------------------------	-----

## **V Multiphysics Best Effort coupling - Proof of Concept 159**

11. Thermohydraulics-Thermomechanics coupling - proof of concept .....	163
--	-----

11.1 Methodology .....	163
11.2 Numerical and Physical verification .....	167
11.3 Results .....	168
11.4 Conclusion .....	171

12. Neutronics - Thermohydraulics - Thermomechanics coupling Algorithms	
---	--

and methodology - Proof of Concept .....	173
12.1 Total coupling algorithms .....	173
12.2 Hydraulics simplification : Neutronics - Thermomechanics coupling Methodology .....	176
12.3 Thermal simplification : Neutronics - Thermohydraulics coupling Methodology .....	178
12.4 Neutronics - Thermomechanics - Thermohydraulics coupling Methodology .....	180

13. Neutronics - Thermohydraulics - Thermomechanics coupling results and	
--	--

analysis - Proof of Concept .....	183
13.1 Results Comparisons and Analysis .....	185
13.2 Effective Temperature Comparisons .....	210
13.3 Results Conclusion .....	212

## **VI Conclusion and Perspectives 213**

## **VII ANNEXE 221**

14. ANNEXE 0 - French Abstract .....	223
--------------------------------------	-----

15. ANNEXE I .....	227
--------------------	-----

15.1 Pressurized Water Reactor and academic simplification .....	228
15.1.1 Industrial context .....	228
15.1.2 Academic model .....	231
15.2 Nuclear reactor core material design, properties and composition ..	232

15.2.1	Core description .....	232
	Core description geometry . . . . .	232
	Power and flux property . . . . .	233
	Thermal and coolant property . . . . .	234
15.2.2	Fuel pins description and properties .....	235
15.2.3	Moderator and poison description and properties .....	236
	moderator and poison description . . . . .	236
	moderator and poison composition . . . . .	236
15.2.4	Reflector description and properties .....	237
16.	ANNEXE II .....	239
16.1	Multiphysics approach .....	240
16.1.1	Simulator approach .....	240
16.1.2	Best Estimate .....	240
16.1.3	Best Effort .....	241
16.1.4	High Fidelity .....	241
17.	ANNEXE III .....	243
17.1	Transient scenario definition .....	244
18.	ANNEXE IV .....	247
18.1	Major Hypotheses of the transport theory .....	248
19.	ANNEXE V .....	249
19.1	Physical details concerning thermal parameters of the heat transfer equation .....	250
20.	ANNEXE VI .....	253
20.1	Global average parameters coupling comparisons .....	253
20.2	Local Hot Spot parameters coupling comparisons .....	259
20.3	Effective temperature formulation comparisons .....	265
	BIBLIOGRAPHY .....	266



# List of Figures

Figure	Page
1.1 Nuclear Power Plant description . . . . .	10
1.2 Pressurized Water Reactor vessel, reactor assembly and fuel rod .	12
1.3 PWR core Scale of modelling scheme . . . . .	13
2.1 Image of a rupture of the control rod attachement (Badcock and Wilcox work on 900MW PWR) [16] . . . . .	18
2.2 Power ratio evolution ( $P(t)/P_{nom}$ ) during the transient (case REP1300-UOX) [142] . . . . .	21
2.3 Shape factor evolution $F_{xyz}(t)$ during the transient (case REP1300-UOX) [142] . . . . .	23
2.4 Burn-up heterogeneous distribution given in GWd/t (case REP1300-UOX) [142] . . . . .	24
2.5 2D Power distribution at the moment the control rod ejection is completed (case REP1300-UOX) [142] . . . . .	25
2.6 Axial penalizing Xenon distribution inside the core (case REP1300-UOX) [142] . . . . .	26
2.7 average core Fuel pin temperatures [142] . . . . .	28
2.8 Benchmark Full core average calculation Fluid temperature (upper curve) Fluid Density (bottom cureve) function of time [186] . . .	30
2.9 Benchmarks comparative table regarding the accuracy of each aspect of representativeness, and presence of each physical discipline, we are looking for in this study (perfect accuracy, average accuracy, rough accuracy) . . . . .	32
2.10 PWR small core (5x5) scheme . . . . .	34
2.11 Mini Core burn-up, assembly numbering and parameters description	36
2.12 Xenon and Power axial distribution after Xe Transient in 1/4 assembly (9) . . . . .	37
2.13 Power evolution during a REA transient . . . . .	38
2.14 APOLLO3 SA Hot spot locations and Max value of $F_{xyz}$ shape Factor evolution during the transient . . . . .	39
3.1 Precursor desintegration . . . . .	51

3.2	Uranium cross sections . . . . .	55
3.3	Density of neutron distribution as a function of the Energy . . . .	57
3.4	Space discretization (from the left to the right): A - Assembly composed by 2x2 homogeneous elements, B - Assembly composed by 17x17 homogeneous elements and C - Assembly composed by 17x17 unstructured and heterogeneous elements . . . . .	60
3.5	Multiparametred library calculation principle [188] . . . . .	65
4.1	Tab of the dynamics of the practical application of the Pin Power reconstruction modeling . . . . .	75
4.2	Summary of our Minos-Minaret coupling approach . . . . .	76
4.3	Cell heterogeneity: Fuel Pin / moderator distinction . . . . .	77
4.4	Assembly heterogeneity: Fuel Pin cell / guide tube cell distinction	78
4.5	Coarse and a fine distribution of the thermal flux . . . . .	79
4.6	MINOS-MINARET Kinetic calculation methodology . . . . .	80
4.7	Academic core case full Minaret calculation with a discretization at the scale of 4 cells/assembly, and with a refinement of a single lateral assembly at the scale of an unstructured fuel cell by mesh.	81
4.8	PPR and Minaret whole core calculations and comparison . . . .	82
4.9	PWR academic core (5x5) scheme . . . . .	83
4.10	MINOS SPn homogeneous core power maps calculation . . . . .	84
4.11	MINARET Sn Single Assembly pin power maps calculation . . .	85
4.12	MINARET Sn Single Assembly Accurate Power distribution . . .	85
4.13	Illustation of the Kinetic Post processed map of power deposit inside the fuel pin . . . . .	86
5.1	Neutronics Block diagram with exchange variables and discretization	97
6.1	1D modelling with ALCYONE [164] . . . . .	120
7.1	Space domain discretisation [116] . . . . .	123

7.2	Radial temperature distribution (in degree) inside the pellet (REA calculation example of distribution at $t=0.25$ ) . . . . .	127
8.1	ThermoMechanics Block diagram with exchange variables and discretization . . . . .	135
9.1	Initial discontinuous conditions . . . . .	150
9.2	FV9 numerical method scheme . . . . .	151
10.1	ThermoHydraulics Block diagram with exchange variables and discretization . . . . .	157
11.1	F4 - ALCYONE time coupling scheme with exchanged variables .	164
11.2	Multiphysics coupling scheme: spatial discretization and correspondency. . . . .	165
11.3	Radial Fuel Pin discretization and exchanged variables . . . . .	166
11.4	Coupling validation with Transient at constant Power . . . . .	167
11.5	Core averaged fuel pin temperature profile comparison between the fuel thermic ALCYONE standalone and F4-ALCYONE coupling using the transient scenario detailed in section ( 2.4) and Annexe( 15)	168
11.6	Observation of the thermohydraulical effet through the ALCYONE SA / FLICA4-ACLYONE comparison . . . . .	169
11.7	Tw sensivity and comparison regarding FLICA4 SA calculations with different input data of Hgap . . . . .	170
11.8	A, S and Tw relative difference (FLICA-ALCYONE coupling) . .	171
12.1	Global coupling scheme and exchanged variables . . . . .	175
12.2	APOLLO3 - ALCYONE time coupling scheme with exchange variables . . . . .	176
12.3	Multiphysics coupling scheme: spatial discretization and correspondency. . . . .	177
12.4	AP3 - FLICA4 time coupling scheme with exchange variables . . .	178
12.5	Multiphysics coupling scheme: spatial discretization and correspondency. . . . .	179
12.6	Total time coupling scheme with exchange variables . . . . .	180



12.7 Multiphysics coupling scheme: spatial discretization and correspondence. . . . .	182
13.1 Coupling models description and comparisons . . . . .	183
13.2 Global and local variables/parameters regarding our three physical disciplines . . . . .	184
13.3 Integrated core power and energy comparison . . . . .	185
13.4 Hot Spot Power comparison . . . . .	187
13.5 Shape factor $F_{xyz}$ and $F_z$ variation comparisons . . . . .	188
13.6 Total reactivity variation comparison . . . . .	188
13.7 Doppler reactivity and Core Averaged Effective fuel temperature variation comparisons . . . . .	189
13.8 Moderator reactivity and Core Averaged Moderator Density variation comparison . . . . .	189
13.9 Integrated Power time ranges definition . . . . .	190
13.10 Integrated core Power comparison $t_{12}$ . . . . .	191
13.11 Total feedbacks reactivity variation comparison $t_{12}$ . . . . .	191
13.12 Doppler reactivity and Core Averaged fuel effective temperature variation comparison $t_{12}$ . . . . .	192
13.13 Moderator reactivity and Core Averaged moderator density variation comparison $t_{12}$ . . . . .	193
13.14 Global Core Averaged - Local Host Spot Effective temperature and Moderator density variation comparison $t_{12}$ . . . . .	194
13.15 Core Averaged Fuel pin surface $T_{wall}$ comparison $t_{12}$ . . . . .	195
13.16 Hot Spot Fuel pin temperature distribution comparison . . . . .	196
13.17 Hgap Global/Local Hot Spot comparison . . . . .	197
13.18 percentage of each Hgap value regarding the core Hgap distribution at $t_3 = 0.2s$ . . . . .	198
13.19 Core averaged Fuel pellet center/surface comparison $t_{12}$ . . . . .	199

13.20	AP3-F4 Average Core / HS power with Hgap sensibility comparison around $t_{max\_power}$ . . . . .	200
13.21	Integrated Power comparison $t_{23}$ . . . . .	202
13.22	Total feedbacks reactivity comparison $t_{23}$ . . . . .	202
13.23	Doppler reactivity and Core averaged Effective temperature comparison $t_{23}$ . . . . .	203
13.24	Moderator reactivity and moderator density comparison $t_{23}$ . . . .	203
13.25	Global core averaged / Local Hot Spot effective temperature and moderator density comparison $t_{23}$ . . . . .	204
13.26	Integrated Power comparison $t_{34}$ . . . . .	205
13.27	Total feedbacks reactivity comparison $t_{34}$ . . . . .	205
13.28	Doppler reactivity and effective temperature comparison $t_{34}$ . . .	206
13.29	Moderator reactivity and Moderator density comparison $t_{3-4}$ . . .	206
13.30	Global core averaged / Local Hot Spot effective temperature and moderator density comparison $t_{3-4}$ . . . . .	207
13.31	AP3-FLICA4-ALCYONE (Rowland) and AP3-FLICA4-ALCYONE (C and SM) power pulse comparison . . . . .	210
13.32	AP3-FLICA4-ALCYONE (Rowland) and AP3-FLICA4-ALCYONE (Isotopic) power pulse comparison . . . . .	211
13.33	Best Effort Coupling perspectives diagram regarding our PhD proof of concept coupling . . . . .	216
13.34	Best Effort disciplines models perspectives diagram regarding our PhD proof of concept coupling . . . . .	217
14.1	Perspectives et améliorations du couplage Best Effort preuve de concept pour atteindre le couplage Best Effort optimum . . . . .	225
15.1	PWR 1300 MW core map . . . . .	229
15.2	PWR 1300 MW core map and assembly location . . . . .	229
15.3	Assembly within a PWR 1300MWe . . . . .	230
15.4	PWR small core (5x5) scheme . . . . .	231

17.1 Nuclear Reactor containment barriers . . . . .	245
20.1 Global core Power evolution couplings comparison . . . . .	253
20.2 Total reactivity evolution couplings comparison . . . . .	254
20.3 Doppler reactivity and core average Effective temperature evolu- tion couplings comparison . . . . .	255
20.4 Moderator reactivity and core average Moderator Density evolu- tion couplings comparison . . . . .	255
20.5 Core average fuel pellet center temperature evolution couplings comparison . . . . .	256
20.6 Core average fuel pellet surface temperature evolution couplings comparison . . . . .	256
20.7 Core average clad surface temperature evolution couplings com- parison . . . . .	257
20.8 Core average clad surface thermal flux evolution couplings com- parison . . . . .	257
20.9 Core average Hgap evolution couplings comparison . . . . .	258
20.10 Local Hot Spot Power evolution couplings comparison . . . . .	259
20.11 Fxyz and Fz shape factor evolution couplings comparison . . . . .	260
20.12 Local Hot Spot fuel pellet and cladding evolution couplings com- parison . . . . .	261
20.13 Global averaged/Local Hot Spot Effective temperature and Mod- erator density evolution couplings comparison . . . . .	262
20.14 Local Hot Spot clad surface temperature evolution couplings com- parison . . . . .	263
20.15 Local Hot Spot clad surface heat flux evolution couplings comparison	263
20.16 Local Hot Spot Hgap evolution couplings comparison . . . . .	264
20.17 AP3-FLICA4-ALCYONE (Rowland) and AP3-FLICA4-ALCYONE (C and SM) power pulse comparison . . . . .	265
20.18 AP3-FLICA4-ALCYONE (Rowland) and AP3-FLICA4-ALCYONE (Isotopic) power pulse comparison . . . . .	265

# List of Tables

Table	Page
2.1 PWR 1300MW Neutronics parameters typical order of magnitude [142] . . . . .	23
2.2 Thermohydrological core inlet parameters . . . . .	29
2.3 PWR 1300MW and Academic core Neutronics parameters typical order of magnitude [142] . . . . .	39
3.1 Neutronics notations: Neutronic quantities 1/3 . . . . .	46
3.2 Neutronics notations: Neutronic quantities 2/3 . . . . .	47
3.3 Neutronics notations: Neutronic quantities 3/3 . . . . .	48
3.4 Uranium 235 precursor (tabulated in JEFF-2) . . . . .	52
3.5 Main notation coming out the Neutronic problem formulation . .	59
5.1 Neutronics input, output and monitored parameters . . . . .	96
6.1 Notations: ThermoMechanical quantities . . . . .	102
6.2 Notations: Gaseous quantities . . . . .	103
6.3 Notations: Neutronics quantities . . . . .	103
6.4 Notations: Thermal quantities . . . . .	104
8.1 ThermoMechanics input, output and monitored parameters (where r is the space variable at core scale and x is the local space variables)	134
9.1 Notations: ThermoHydraulics quantities . . . . .	138
9.2 Notations: Phases and mixture quantities . . . . .	139
9.3 Notations: other quantities . . . . .	140
10.1 ThermoHydraulics input, output and monitored parameters (where r is the space variables at core scale and x is the local space variables)	156
13.1 Difference between AP3-FLICA4 and AP3-ALCYONE-FLICA4 calculation . . . . .	208
13.2 Difference between AP3-ALCYONE and AP3-ALCYONE-FLICA4 calculation . . . . .	209
13.3 Maximal relative difference between AP3-ALC-F4 ( $T_{eff}^{Rowland}$ ) and AP3-ALC-F4 ( $T_{eff}^{C-SM}$ ) . . . . .	210

13.4	Maximal relative difference between AP3-ALC-F4 ( $T_{eff}^{Rowland}$ ) and AP3-ALC-F4 ( $T_{eff}^{Iso}$ ) . . . . .	211
15.1	Core and Assembly description . . . . .	232
15.2	Core and Assembly description (academic core) . . . . .	232
15.3	Power and flux properties . . . . .	233
15.4	Power and flux properties (academic core) . . . . .	233
15.5	Hydraulical proprerties . . . . .	234
15.6	Hydraulical properties(academic core) . . . . .	234
15.7	Fuel pin description . . . . .	235
15.8	Thermal fuel pin properties . . . . .	235
15.9	Control rods properties . . . . .	236
15.10	Moderator and poisons properties and composition . . . . .	236
15.11	Reflector properties . . . . .	237
17.1	Features of the main rod ejection accidents [250] . . . . .	246

# Part I

## Introduction



---

The nuclear generation first came to existence more than 50 years ago. The first power reactor was activated in 1942 and it decidedly paved the way for the development of continuous research and production of many kind of Nuclear reactors.

Nevertheless, from the late 1970s until around 2002 the nuclear power industry suffered a certain decline in terms of trust which led to a decrease of construction rate. This fact has been amplified by the nuclear accident that occurred at Fukushima in 2011 and, as a consequence, the decision taken by Germany to shut down its nuclear energy production in order to focus its production on renewable energy like sun or wind power.

However, the awareness of the importance of security of supply, the world-wide increase of the electricity demand, specifically in emerging countries, and, finally, the need to limit carbon dioxide emissions have contributed to the revival of the nuclear energy option within the Energy global plan. This global plan has been acted during the COP21 in Paris.

Thus, currently, the nuclear power is one of the fundamental components of the global energy mix and in order for the international nuclear production to integrate the low carbon energy mix with success, nuclear technologies would have to handle two fundamental points that have emerged from this conclusion:

- The nuclear power plants need to be more adjustable in terms of energy production in order to be able to quickly respond to the fluctuation of the renewable energy production as well as to the fluctuation of the electricity demand,
- The nuclear power plants need to be significantly safer in terms of design and in terms of monitoring.

The main goal of these measures is to ensure that the safety goals (core sub-criticality, core cooling, confinement of radioactive material, radiation protection) are fulfilled under any circumstances during normal operations (with intermittent Energy injected into the grid), off-normal states and accidents. These measures can be grouped in Prevention, Monitoring, and Mitigation.

The safety analysis of nuclear power plants requires a deep understanding of underlying keyphysical phenomena that determine the integrity of the physical barriers preventing fission product release, e.g. fuel pellet, fuel rod cladding, pressure piping system, reactor pressure vessel, containments, etc. At the present time, cutting edge models and codes produced by scientists exist but they mainly focus on a single aspect (discipline) of the physical system coupled with rough models of the other aspects needed to simulate the system. But, safety analyses can be carried out based on Multiphysical and Multiscales modelling in order to be the more accurate as we can regard all the physical aspects of the reactor behavior. This Best Effort approach (see chapter ( 16)in Annexe part) would give a full and accurate (High Fidelity) comprehension of nuclear safety and of operating conditions.

In this approach, the physical phenomena are simulated as accurately as possible (according to present knowledge) by coupled models (industrial codes) that were used separately



---

up until now in the most efficient way. For example, codes exist that are accurate modelings of Neutronics, or modelings of thermal fluid mechanics inside the core, or modellings of thermal fluid mechanics over the whole system, or modellings of thermal mechanics of the fuel pin or over the whole device structure. A Best Effort approach would couple these models in order to realize a global and accurate modelling of the Nuclear reactor system. The Best Effort approach requires to define well the models that are used in order to exactly specify their limits, and hence, specify incertainties of the coupled model results in order to assume and optimize them.

Various research centers and research groups all over the world are enlisted in this new approach of system modeling, such as NURSIP [194] (and then NURESAFE [4]), CASL [1], MEANS [5] [263] [73], STARS [6]. The "Commissariat à l'Energie Atomique et aux Energies Alternatives" (CEA) is one of them. Nowadays, many coupled models are investigating over different systems (GEN II, III or IV) and over different aspects of these systems.

Taking, for example, the Neutronics discipline of the nuclear reactor improvement of the models and simulation leads to the establishment of 3D neutron transport modellings of the reactor core.

A first step of the multiphysic coupling has been to couple Neutronics with Thermohydraulics (the Best Estimate standard nuclear multiphysic coupling) and thus be able to study the two first safety principles, i.e., the control of the reactivity and the control of the cooling system. These coupling works have been done in many research centers or cooperative works, e.g., for instance, at the CEA itself [222] [44] [247] through NURESAFE [45], in Spain at the Polytechnical Univ. of Madrid [120] at the Politechnical Univ. of Catalunya [201] [202], in Germany at the Technische Universität München [259], at the Karlsruhe Institute of Technology [260] [261] [115], or in US at Penn State Univ. [114] [14] [70], Texas A and M Univ. [154], at the Michigan Univ. [269], at the Los ALAMOS lab. [175], mainly through CASL, MEANS and STARS projects. Next, regarding the potential threat to the fuel pin in case of standard and accidental situations of the GEN II-III Reactors, the primary contribution would be the incorporation of a fine thermomechanical model into a coupling including Neutronics and Thermohydraulics (Standard Best Estimate coupling). This way, a specific further step has been done in order to meet this ambitious goal. Many research centers in the US at the Lawrence Livermore National Lab. [73], at the North Carolina State Univ. [264], at the INL [63] [94] [154] and at the Paul Scherrer Institut [77], in Europe through NURESAFE [45] or moreover at the CEA [249] [145] [66], are working on this purpose and are source of proposals considering the coupling approach and technics, i.e., from external linkage [191] to strong external [70] [249] or internal coupling [66] and preparation work of JFNK internal coupling [66].

It is in this context that this PhD Proof of Concept thesis work is being undertaken. It consists in the "Development of a Multi-physics and multi-scale Best Effort modelling for accurate analysis of Pressurized Water Reactor under standard and accidental operating situations". It mainly involves the implementation of a multiphysics algorithms coupling

---

Neutronics and Thermohydraulics at reactor scale to an accurate Thermomechanics at the elementary scale of the assembly. In addition, a work project has been carried out in order to prepare or improve the structures to access the local physical information that would lead to the implementation of a future multiscale coupling scheme, at the elementary scale of the fuel in, i.e., the fuel cell (fuel pin surrounded by the moderator) or sub canal (coolant with fuel pin in the corners).

As it was planned, this Neutronic, Thermohydraulics and Thermomechanics multiphysics coupling yields:

- In terms of Neutronics, a better awareness of the Power evolution through precise feedback effects (Doppler, moderator), thanks to a more accurate thermal description of the Thermomechanics and Thermohydraulics aspects of the core.
- In terms of Thermohydraulics, a better awareness of the thermal exchange between the fluid and the fuel pin from the very beginning of the thermal activation.
- In terms of Thermomechanics, a better awareness of the thermomechanical evolution and thermal release through the cladding surface to the fluid, including a strong contribution at the interface between cladding and pellet (Hgap).

The road map of this paper is described below.

The first part of the present paper aims to carry out the physical context and scientific objectives of the study. After a short presentation of the multiphysical and multiscale context of this industrial complex system, we define the academic case and describe the physical scenario of the study aiming to achieve a complete and detailed comprehension of the major physical phenomenology of the scenario. Thanks to this description and explanation, we present the scientific objectives of this study according to the safety analysis and Best Effort coupling of Industrial CEA codes.

The second part is dedicated to the mathematical and numerical Neutronic models which we detail. We define their numerical formulation in order to pin point the coupling variables of our multiphysics problem as well as to define the limitations of the models and the assumptions and hypothesis we made. Finally, we present the improvement of the models we realized in order to reach our multiphysics multiscale goals.

The third part is dedicated to the description of the mathematical and numerical ThermoMechanical of the fuel pin models as well as of the Thermohydraulical models. As in the Neutronics part, we detail the mathematical models and the physical phenomena they carry out and we define briefly the numerical formulation. This allows us to pin point the ThermoMechanics and Thermohydraulics coupling variables of our multiphysics problem as well as to define the limitations of the models and the assumptions and hypothesis we made. Finally we expose the thermal approach which have been developed for the fuel pin - fluid coupling of the thermal exchange and define the fuel pin effective temperature formulations we implemented.

The last part defines the Multiphysics Best Effort Coupling approaches and results we

---

obtained. This work is a multiphysics coupling proof of concept realized in the context of a simplified but realistic Academic core case and Academic REA transient. Thus, from an academic Rod Ejection Scenario we developed, we work on the Thermomechanics-Thermohydraulics coupling and effects of the coupling on the simulation. Thereafter, we gradually increasing the multiphysics coupling, i.e., from the Hydraulics and Thermomechanics simplification up to the total Neutronics - Thermohydraulics - Thermomechanics coupling. These sections present the methodology, the results we obtain and some circum-spect physical analysis with respects to the limits on the physical representativity of our academic core and scenario.

The conclusions and perspectives of our work are presented in the final part of this document.

## Part II

# Physical context and scientific objectives



## Chapter 1

# The Nuclear Reactor: a multi physical system

In this chapter, we will introduce the physical context of the study through the definition of a nuclear reactor in terms of multiphysics and complexity. Indeed, it is necessary to well define the nuclear reactor, which is a complex system with many scales of analysis and involving many fields within the physics.

### 1.1 A multiphysical complex System

A nuclear reactor is used at nuclear power plants for electricity generation. Heat produced from nuclear fission is passed to a working fluid (primary circuit - the heated part) which runs through steam turbines that run electrical generators in order to produce electricity (secondary circuit - the electrical part). Then the remaining heat is released to the atmosphere thanks to the cooling tower (tertiary circuit).

Between these three parts of the nuclear power plant, our interest lies within the heated part which is composed of the reactor vessel (the pressure vessel containing the nuclear reactor coolant that carries the fission heat to the thermal exchanger), the reactor core shroud (the stainless steel cylinder surrounding the reactor core and which main function is to direct the cooling water flow) and the reactor core (the portion of the nuclear reactor containing the nuclear fuel components immersed in the fluid coolant and where heat generation takes place). For the purpose of this work, we will only focus on the reactor core part. This is the heart of the nuclear reaction chains that produce heat by fission inside the fuel pellet to be released to the fluid coolant.

Three prominent fields interacting in the core can be defined in order to describe the re-

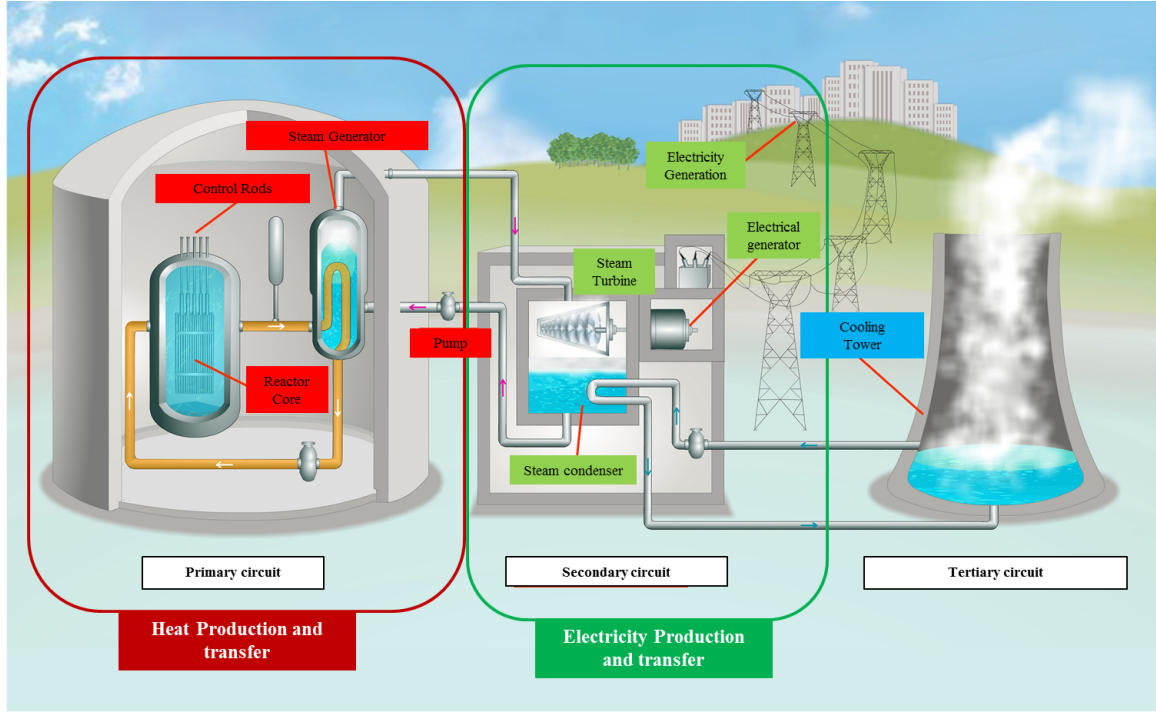


**Figure 1.1.** Nuclear Power Plant description

actor core: Neutronics, that defines the neutron transport, distribution and time evolution; the Fuel Performance, that defines the behavior of the fuel pin in terms of thermics and mechanical phenomenon; and Thermohydraulics, that defines the thermal exchanges of heat with the fluid coolant and its transport according to the evolution of the characteristics of the fluid. In a few words, these three physical fields can be defined as follows:

- Neutronics: it is the study of the motion and interaction of neutrons with materials. Free neutrons collide with the atoms of the fuel material. The shock causes the fission of the nuclei of certain atoms such as Uranium 235 ( $U^{235}$ ), that splits into two lighter nuclei (fission products), releasing kinetic energy, gamma radiation and free neutrons which can then interact with other fissile nucleus, etc. A portion of these neutrons may also be absorbed by fertile or unfertile atomic nuclei, or simply leave the core and disappear from the total neutron account. The overall behavior of the chain reaction is related to the effective multiplication factor  $k_{eff}$ . Indeed, it determines its evolution according to the neutrons production (Prod.) and consumption (Cons.):  $N$  fissions create  $Nk_{eff}$  fissions, themselves producing  $(Nk_{eff})^2$  fissions. Several evolution cases exist, depending on the value of  $K_{eff}$ :
  - $k_{eff} < 1$ , the reaction is subcritical and tends to shut down the reactor (Cons.  $>$  Prod.).
  - $k_{eff} > 1$ , the reaction is supercritical and there is a risk that the reactor undergoes a "runaway reaction" (Cons.  $<$  Prod.).

- a steady reaction is defined by  $k_{eff} = 1$  : in this case the reaction is maintained at a constant level (Cons. = Prod.).

Hence, Neutronics models are fundamental to understand and to determine the transport and distribution of the neutrons inside the core in order to estimate and control the nuclear reaction.

- Fuel performance: in Gen-II light water reactor, the fuel pin is a ceramic pellet material initially composed of Uranium Oxyde ( $UO_2$ ) circled by a Zirconium metal clad. The pellet is the location of the fissile atomic nucleus such as Uranium-235 which could absorb neutrons, decay by fission and release heat into the pellet. Moreover, the fuel pin will undergo mechanical and thermal reactions such as thermal expansion of the pellet [141] [125] [147] [227] [83] [199]. The neutrons are interacting at the scale of the nucleus, thus the slightest change of the fissile nuclei repartition inside the pellet by thermal expansion may lead to a very different neutrons distribution, to a very different nuclei fissions distribution and thus to changes in heat production and release. Other aspects of the fuel pellet, such as containment of radioactive materials inside the clad, could also be discussed from the fuel performance and safety analysis point of view [112] [111] [33] [13] [49].
- Thermohydraulics: in addition to fluid transport, the fluid coolant is also used to thermalize the neutrons (they scatter on hydrogen nuclei of water and they reach a lower energy suitable for the neutron to be absorbed by fissile nuclei) and to moderate the nuclear reaction by adding neutron poisons into the water (they absorb neutrons without fission in order to limit the neutron amount inside the core). Consequently, in addition to the coolant property of the fluid, the thermal characteristics of the fluid as well as of the fuel pin are essential data to feed the neutronic studies and control the heat production/coolability of the core.



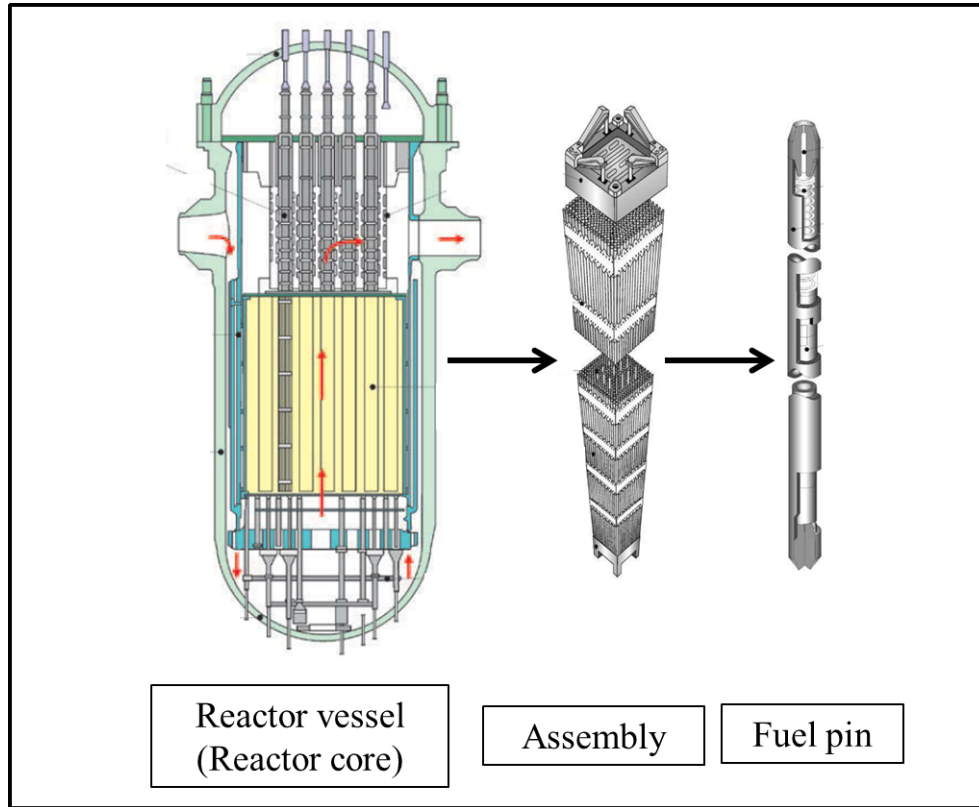


**Figure 1.2.** Pressurized Water Reactor vessel, reactor assembly and fuel rod

## 1.2 The multiscale system

The reactor core can also be described following different scales of analysis. Many parameters could be studied following several scales of description, figure ( 1.3) and in the chapter ( 15) in Annexe part, such as, for instance, the Power. The neutronic power is the energy function of time generated by the reactor core and which can be describe globally (integrated power  $P^{integrated}(t)$ ), locally (local power  $P(x,t)$ ) or regarding the medium of production or deposition (fuel pin, coolant water and so on).

- the core scale itself can provide a global prediction. This way, we mainly highlight the variation of amplitude of parameters of interest. However, this approach assumes a close to constant distribution of the studied parameters and considers the core as a homogeneous system.
- the assembly scale gives use a more accurate description of the core. Assemblies are considered as homogeneous medium but thanks to this description we can distinguish between assemblies and obtain a spatial distribution of our studied parameters such as the core heterogeneity of the power distribution in case of incidental or accidental

situations .

- the fuel cell scale: from the homogeneous assembly scale, we can refine our description up to a 17x17 fuel cell grid that is the ultimate homogeneous refinement regarding the fuel pin. Indeed, an assembly is composed of a 17x17 grid of fuel pin surrounded by water. At the fuel cell, we consider a cell composed by a single fuel pin surrounded by water. This way, we have an accurate distribution of parameters inside the assembly (assembly heterogeneity) but we do not distinguish between coolant and fuel pin, and have no insight on the fuel pin itself.
- the fuel pin scale: at this scale we distinguish the coolant from the fuel pin, and we obtain a precise distribution of parameters inside the assembly and inside the fuel pin with distinction between the clad and the pellet. Consequently, we are able to define precisely the whole behavior of the core as well as its very local evolution. This scale has obviously a very high computing cost of simulation but may lead to a thorough safety analysis.

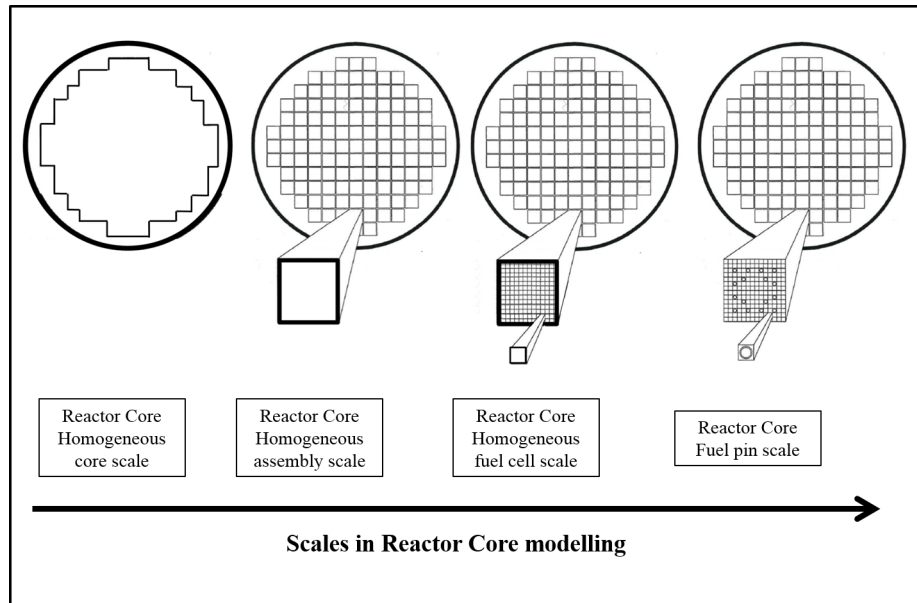


**Figure 1.3.** PWR core Scale of modelling scheme

A full fuel pin scale discretization of the core would be the Best Effort to model the core but not the most efficient approach (chapter ( 16) in Annexe part). The most efficient approach depends on the parameters we study according to the heterogeneity of their distributions and variations of their amplitude. Consequently, an homogeneous point

method would be sufficient enough if the distribution is static and/or almost planar. Conversely, a full fuel pin scale discretization would be necessary if the whole core distribution of the studied parameters is very heterogeneous with a huge variation of amplitude. A mix between an homogeneous scale and a fuel pin scale would be efficient if the studied parameters distribution is heterogeneous with a highly localized variation.

In conclusion, in order to define the scale of discretization for a Best Effort approach we need to take care of the different aspects quoted:

- Phenomenum comprehension,
- Amplitude and distribution of parameters,
- Computing cost according to the improvement of the accuracy of the calculation.

These aspects will be taken into account and confronted to the the transient phenomenology part of this document, and in more details in the following papers [141] [125] [147] [227] [83] [199], in order to scientifically defined and justify our academic case, our modelling and simulations.

### 1.3 Multiphysics coupling State-of-the-art

[112] [111] [33] [13] [49] [181]

As it was said in the previous section, during the last decade various research centers and research groups all over the world have been enlisted in this new approach of system modelling, such as NURESIM european project (NURESAFE [4] and NURISP multi-physics platform [194]), CASL [1], NEAMS [5] [263] [73], STARS [6]. The "Commissariat à l'Energie Atomique et aux Energies Alternatives" (CEA) through the CORPUS platform is one of them. Our present work is a contribution to the Multiphysics CORPUS effort as the first Neutronics - Thermohydraulics - Thermomechanics CEA coupling.

Regarding Reactivity injection Accident and taking arbitrarily, the Neutronics discipline as the key stone of the Nuclear core simulation, the first step of nuclear modelling improvement was to evolve from kinetic point models to 3D neutron transport modellings.

Then, a first step on multiphysics coupling was to couple Neutronics with a fine fuel pin Thermics in order to accurately simulate the thermal behavior of the pin and thus the neutronic thermal feedback behavior (Doppler Feedback) [134] [239].

Then, a second step was to couple Neutronics with fuel pin thermics and Thermohydraulics in order to simulate the precise thermal behavior of the pin, of the fluid and thus of the whole neutronic thermal feedback behavior (Doppler and moderator Feedbacks) [222].

Today, the third step of multiphysics coupling consists in coupling Neutronics, Thermohydraulics and a fine Thermomechanics in order to obtain thorough simulation results of the core reactor and more precisely, in case of REA, of the fuel pin and its cladding (the first containment barrier) [200].

Speaking of multiphysics, in this section we will briefly detail one intergovernmental agency

NEA-OECD (benchmarking), two of the leading ones international projects, i.e., NURESAFE [4] and CASL [1] (research, benchmarking and multiphysics platform development) and the CEA-EDF multiphysics platform SALOME [7] (used in stand alone but also used in NURESAFE for research, benchmarking and multiphysics platform development):

- NEA-OECD [178] is an intergovernmental agency that facilitates cooperation among countries with advanced nuclear technology infrastructures to seek excellence in, for instance, nuclear safety, technology, and science. One of the goals of the NEA in this area is to assist member countries in ensuring high standards of safety in the use of nuclear energy. For this purpose, NEA is working on the development of advanced multiphysics modelling project which are leading to Benchmark identification and definition, such as EGUAM [185] [187] (uncertainties and physics) and EGM-PEBV (validation and physics), in order to be proposed to international modelling community.
- CASL is an ambitious US project lead by Oak Ridge NL and where major US nuclear actors are involved: 3 National Laboratories (Idaho National Laboratory (INL), Los Alamos National Laboratory (LANL), and Sandia National Laboratories (SNL)), 4 Academic partners (the North Carolina State University (NCSU), the University of Michigan (UM), and the Massachusetts Institute of Technology (MIT), The Electric Power Research Institute (EPRI). Industrial companies such as Westinghouse Electric Company (WEC) and operators such as The Tennessee Valley Authority (TVA) are also worth mentioning. It is the first DOE Energy Innovation Hub which focuses on a single topic, with the objective of rapidly bridging the gaps between basic research, engineering development and commercialization. The CASL's VERA [238] multi-physics platform is currently coupling physics such as neutron transport, thermohydraulics, fuel performance, and coolant chemistry. For instance, research and benchmark works have been carried out such as [114], [269], [175].
- NURESAFE [4]) is mainly a European project involving major European nuclear actors, namely 4 major European nuclear industrial companies (AREVA, TRACTEBEL, EDF, FORTUM), 9 major European nuclear Research and Development Organisms (CEA, HZDR, KIT, PSI, VTT, KTH, KFKI, JSI, UJV, ENEA, NCBJ), 2 major European Technical Support Organisations (IRSN, GRS), 4 European Universities (LUT, KTH, UPisa, UCL) and two US Universities (PSU, TAMU). The NURESIME platform project pursues transient simulation studies using coupled System Thermohydraulics, CFD, subchannel Thermalhydraulics, Neutronics and fuel Thermomechanics [238]. In this framework, some multiphysics coupling have been completed such as the ATHLET-DYN3D coupling, the ATHLET-CTF-DYN3D coupling or the SCANAIR-FLICA4 coupling which are respectively dedicated to System-Neutronics coupling, System -Thermohydraulics - Neutronics coupling and Thermohydraulics - Thermomechanics coupling [238]. For instance, research and benchmark works have been carried out such as [42] [222], [44], [259] .

- SALOME [7] is an open-source software that provides a generic platform for Pre- and Post-Processing for numerical simulation. It is based on an open and flexible architecture made of reusable components. The SALOME [7] application named CORPUS [233] is dedicated to Best Effort multiphysics modeling of PWR in normal and accidental situations, mainly by using CEA codes. CORPUS research works have been carried out on coupling such as on Neutronics-Thermohydraulics, Neutronics-Thermomechanics or Core Thermohydraulics -System Thermohydraulics [44] [247], [249], [145], [191].

## Chapter 2

# Transient scenario phenomenology of a Rod Ejection Accident

The goal of this work is to realize a Best Effort modelling of the core in case of an accidental situation which violates some of the safety functions of the core and may endanger its safety barriers (chapter ( 17) in Annexe part and [147]).

For this purpose, we pinpoint a specific scenario involving our three disciplines, i.e., Neutronics, Thermohydraulics and Thermomechanics. This kind of scenario is one of the paramount concerns of the nuclear safety because of the treath on the first containment barrier, i.e., the fuel pin integrity, and requires an accurate Thermomechanics modelling. We focus our study on a Reactivity Injection Accident (RIA) initiated by a control rod ejection and called Rod Ejection Accident (REA).

In this chapter, we describe the Phenomenology and physical aspects of this transient accident. More precisely, we will focus on the risk of mechanical damaging or failure of the clad, i.e., the first barrier ([141] [125] [147]), following the neutronic pulse induced by the REA transient. In addition to a strong thermal coupling, there are two major neutronics effects we do need to define: feedback reactivity reactions which are stabilizing or destabilizing response of the matter to a disturbance in the neutron balance of the core; the heterogeneous distribution of the power which might lead to a spatial dissymetrical deposit of power on the fuel pin which itself might carry the fuel pin to dangerous conditions (fuel pin rupture or fuel melting).

### 2.1 REA classical transient overview

[142] [147] [250]

We assume that before the transient the power inside the core is constant and the neutron population balance is stable ( $K_{eff} = 1$ ). When the rod is ejected the balance is

broken ([125] [147]).

In a Rod ejection accident (REA), there is a mechanical failure of the housing of a control rod drive mechanism (figure 2.1) so that the internal pressure in the core ( $P_{int} = 155$  bar) forces the mechanism out ( $P_{ext} = 1$  bar) and the attached control rod assembly is ejected vertically from the reactor. This difference in pressure pulls the control rod out with an acceleration of about 22 g ( $22 \times 9.81 \text{ m.s}^{-2}$ ) and leading to a very short time of ejection (about 0.1 s). In addition, this accident may lead to a loss of primary coolant [69] through the failed control rod drive. This aspect is not considered here: we assume that the loss of primary coolant is negligible or nonexistent during the duration of the transient.

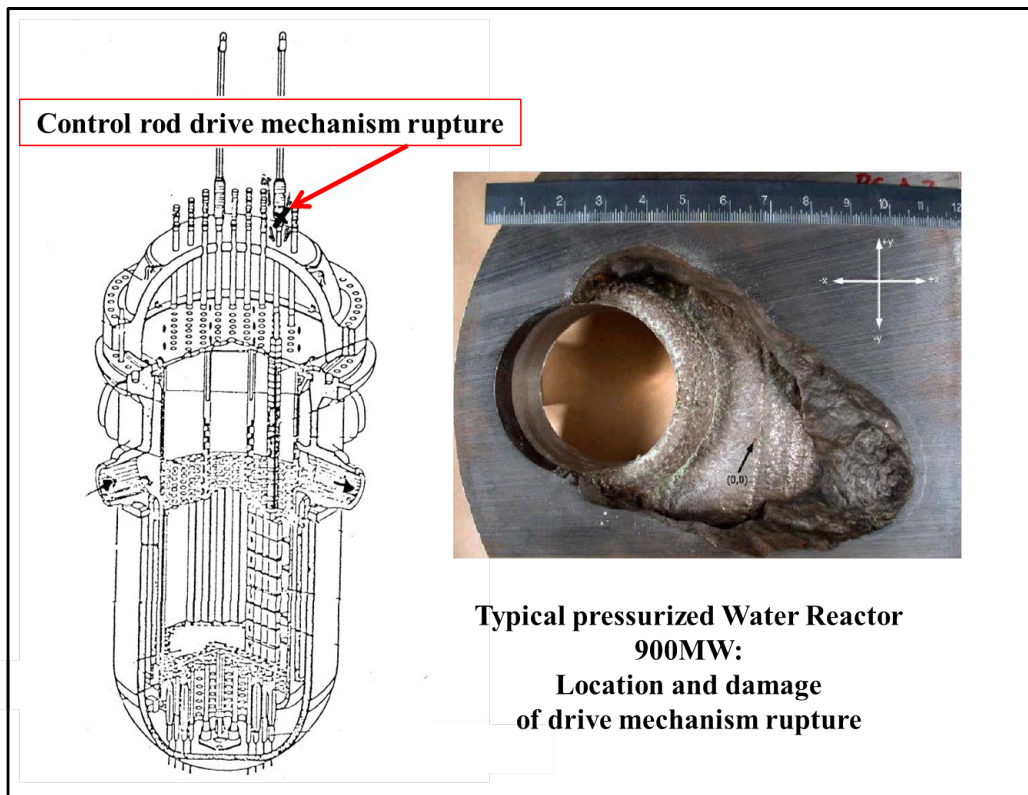


**Figure 2.1.** Image of a rupture of the control rod attachment (Badcock and Wilcox work on 900MW PWR) [16]

The complete withdrawal of a control rod induces a high, quick and localized incursion of reactivity into the core. The map of power is strongly deformed nearby the assembly where the control rod has been ejected. The intensity of the REA transient depends on its reactivity insertion  $\rho_o$  (the insertion state of the rod and the composition of the neutron-absorbing material) and the delayed neutron fraction  $\beta$  of the core (map of Burn-up and reloading map). Following these two parameters, we are able to distinguish two types of transients, i.e., the supercritical transient cases where the reactivity  $\rho_o$  is inferior to the delayed neutron fraction  $\beta$  and the supercritical prompt transient case where the reactiv-

ity  $\rho_o$  is superior to the delayed neutron fraction  $\beta$ . The last one is clearly more violent than others due to the predominancy of prompt neutrons in the neutronic reaction. It is characterized by the production of a huge peak of power proportionally to the importance of the difference  $(\rho_o - \beta)$ .

In case of a supercritical prompt transient, the celerity of reactivity insertion and neutronic feedbacks of the reaction separate the REA scenario in three distinct phases [141] [39].

The first phase of the accident corresponds to a local fast and strong power incursion due to the ejection of the control rod. During this phase of a few milliseconds, in case of low power initial value, the increase of power does not induce any significant increase of temperature inside the pellet or the coolant.

The second phase of the accident is due to the prompt neutron action and is characterised by a strong mechanical interaction between the pellet and its clad as a consequence of the quasi-adiabatic warming and the high pressure of the fission gas which lead to the sharp increase of the volume of the oxide. In case of brittle failure of the clad, during this phase, the release and spread of small pieces of fuel to the primary coolant may induce a drastic vaporisation of the water around the fuel pin and potentially a vapor explosion, which in turn might damage the neighbouring fuel pins.

The reaction shuts down by itself as a result of the fuel warming and this is called the Doppler feedback effect. Indeed, the Doppler feedback effect comes out as a dependence of the neutronic absorption to the fuel temperature. More precisely, it means the increase of sterile absorption according to the increase of the fuel temperature.

The third phase of the accident is controlled by the thermal evolution of the system and it extends over few seconds in time up to the end of the transient (according to the kinetic and intensity of the transient). This phase leads to a sharp increase of the clad temperature and a high inner pressure in the fuel pin that may induce a boiling crisis of the water around the fuel pin and the ductile failure of the clad. In this phase, in addition to the Doppler, the major feedback effect is the moderator effect which consists in the modification of the neutronic slowing down. Indeed, the moderator density decreases and induces the sharpening of the neutron spectrum. Hence, less fission occur and it is equivalent to a negative insertion of reactivity into the core.

At last, in a classical reactor, if the detected flux (that has been measured during the two previous steps [69]) exceeds a given setpoint, an automatic reactor trip (AAR) will be initiated causing insertion of the remaining control rods into the core in order to damp the neutron flux. This aspect will not be taken into account in our study.

This scenario can be described by splitting the physics into two parts. On the one hand, the Neutronics part is defined by its initial state (Bun-up, Xe inventory, Power  $P_0$ , and so



on) and its transient behavior (integrated and local power, shape factor, reactivity and cross section variation): both are needed to determine the most penalizing scenario in terms of power production. On the other hand, the ThermoMechanics and the Thermohydraulics, at their initial state (mainly, the Mechanical state of the fuel pellet and clad) will strongly impact the transient evolution in terms of Thermics (fuel temperature  $T_{pin}$  and  $T_{wall}$ , thermal flux  $\Phi_{wall}$  and so on) but also in terms of Mechanics (Gap size) and Hydraulics (moderator density, RFTC). Then, as detailed in [147] the REA transient may lead to different risks of failure (fragile or ductile). These risks will not be treated during this study but they are detailed in [147]. They underline the importance and requirement of a well and precise understanding and monitoring of the physics during the transient.

## 2.2 Physical specifications

The goal of this work is to realize a multiphysics modelling by coupling accurate Neutronics, Thermohydraulics and Thermomechanics physical models. For this purpose and in order to simplify the realization of the coupling scheme as well as the results analysis we decide to realize our study on a small core reactor model. These two points imply the need of an accurate representativeness of our case regarding a classical PWR (design specificities and symmetry) and considering a typical transient accident governed by prompt neutron (supercritical prompt transient). More precisely, our core and transient case need to be representative in terms of phenomenology and need to be the most constraining scenario considering the risk of endangering the first safety barrier (**safety analysis context even if this aspect will not be covered by this study**).

### 2.2.1 Neutronics representativeness

The REA transient is first and foremost a Neutronics transient. The paramount concern of the neutronics representativeness of this scenario is the power evolution and distribution during the transient. We must consider the two following aspects:

- Temporal aspect: typical temporal dynamics (typical shape of the curves and order of magnitude) we can observe considering the core power  $P_{neutro}(t)$  and the 3D shape factor  $F_{xyz}(t)$ .
- Spatial aspect: typical spatial distribution we can highlight through the Hot Spot localization.

### Temporal aspect

[142]

In a typical situation, we will have a transient as described in Fig ( 2.2), which was obtained using a neutronics REA simulation at the CEA [142].

- Core Power  $P_{neutro_{Integrated}}(t)$  :

The Power evolution in the core can be described following five steps [39].

During a REA, we can describe the power transient dynamic following 5 typical zones as, for instance, in the figure ( 2.2):

- Zone 1: Rod ejection at hot zero power.
- Zone 2: Dramatic increase of the Power (exponential evolution) without any significant increase of the temperature due to the low power initial value (no reactivity feedbacks).
- Zone 3: Quasi-adiabatic heat, the energy is confined inside the pellet. The  $P_{core}$  increases very violently and very locally. During the same time, the Doppler feedback effect (Doppler reactivity  $\rho_{doppler}$ ) quickly increases and compensates the reactivity from the rod ejection  $\rho_{rod}$ . At this time, the reactivity does not increase any more (max of the power increase) and finally decreases as fast as it grows.
- Zone 4: The thermal transfer in the fuel pin leads to the heating of the moderator and induces a moderator feedback effect (moderator reactivity  $\rho_{moderator}$ ).
- Zone 5: The reactivity of the core reaches the delayed neutron fraction and brings the core to a new equilibrium state. In fact, an operating reactor does not have the time to reach this state because of the emergency shutdown devices that damp the neutron flux. In our case, we won't use any emergency shutdown devices.

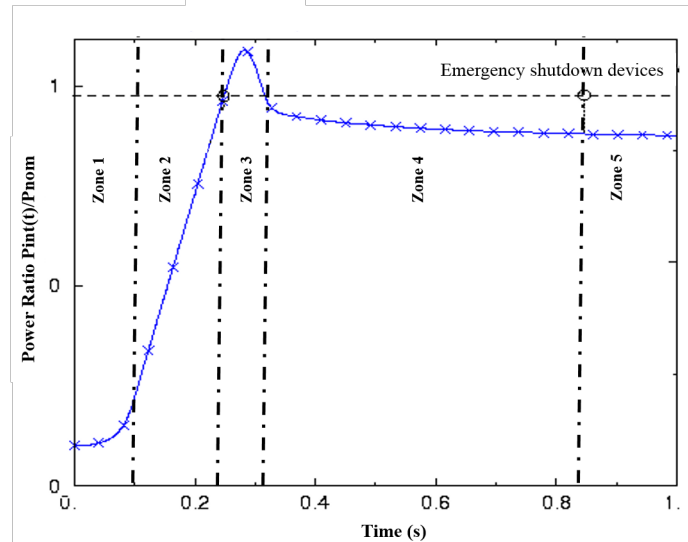


**Figure 2.2.** Power ratio evolution ( $P(t)/P_{nom}$ ) during the transient (case REP1300-UOX) [142]

This dynamic is also observed locally through the power distribution  $P(x,t)$  and more specifically in the Hot spot area. In addition to this dynamic, the width of the peak, associated to the power amplitude of the scenario, are fundamental in order to define our transient.  $P_{max}$  is function of the core initial state, i.e., the control rod reactivity and of the delayed neutron fraction. These features of the scenario carry the amount of power deposition inside the core and directly influence its behavior in terms of safety. The specific energy deposition in the fuel during the pulse is given by the integral of the power over the duration of the transient. Consequently, a high amplitude of the power pulse would be dangerous, but the width of the pulse (total energy deposition) would also bring a very significant component of threat for the fuel pin.

- Shape Factor  $F_{xyz}(t)$  : The 3D shape factor  $F_{xyz}$  corresponds to the value of the max deformation of the power distribution compared to the average value of the power inside the core [142].

$$F_{xyz} = \frac{\max_{x,y,z} |P_{pin}(x, y, z)|}{\langle P(x, y, z) \rangle} \quad (2.1)$$

More precisely, it informs on the amplitude and the variation of the power due to neutronic impacts of the transient (control rod reactivity insertion  $\rho_{rod}$  and doppler  $\rho_{Doppler}$  or moderator  $\rho_{moderator}$  feedback reactions) [39].

For instance, the following figure ( 2.3) shows a typical REA transient and  $F_{xyz}$  shape factor variation during the transient [142]. We can observe the same 5 typical Zones we observed in the previous section regarding the Power:

Both are dependent of the rod reactivity weight and core state, i.e., delayed neutron fraction and thus of the Burn-up distribution. Indeed, the Burn-up map distribution of the core evolves during the reactor operation [195]. This way, the concentration of isotopes and fission products proportionally changes from the start, i.e., Begin Of Life (BOL) or Begin Of Cycle (BOC), to the end of a fuel cycle process of the reactor operation, i.e., End Of Cycle (EOC). More precisely, the management of the reactor operation (historical effect and number of cycles) and the fuel assembly repartition at the start induce a specific distribution of the isotopes and their concentration. The isotope concentration inside the core is one of the factors that may lead the transient to the most penalizing scenario. Indeed, the fuel consumption during the fuel cycle reactor operation induces a significative reduction of the delayed neutron fraction. For instance, in a general case, we assume values from 700 pcm at BOC to 500 pcm at EOC and, and in a pessimistic case due to the reactor historical effect, we assume values from 520 pcm at BOC to 440 pcm at EOC [142]. The lesser is the number of delayed neutrons, the more the transient will be prompt critical (governed by prompt neutrons) and thus it will be fast and strong.

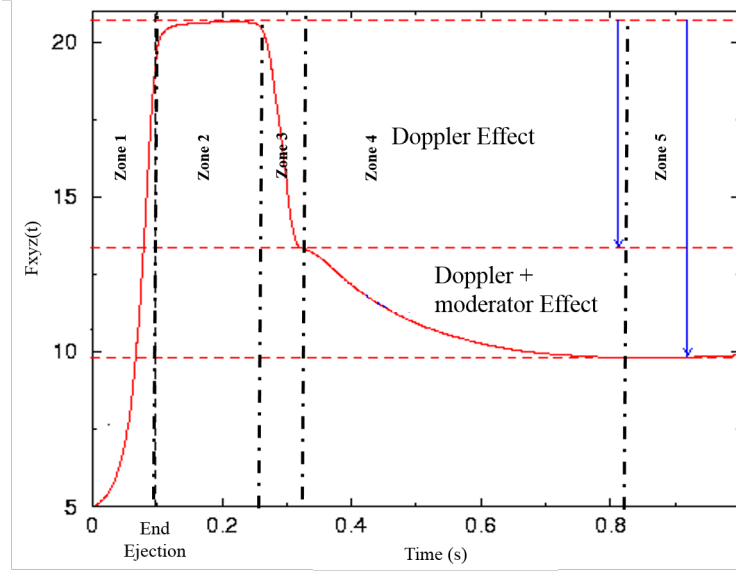


**Figure 2.3.** Shape factor evolution  $F_{xyz}(t)$  during the transient (case REP1300-UOX) [142]

Neutronics parameter	value
Delayed neutron fraction	450 pcm
Control rod reactivity weight	700 pcm $\simeq 1.5$ \$
Burn-up heterogeneity	from 10 to 45 GWd/t
Rod Ejection duration	100 ms
REA duration to asymptotic power	600 ms
Width of the power pulse	40 ms
Max integrated power	10 Pnom
Max value of the 3D shape factor $F_{xyz}$	20
Max local power	200Pnom

**Table 2.1.** PWR 1300MW Neutronics parameters typical order of magnitude [142]

Then, the tab ( 2.1) gives the standard 1300MWe PWR Neutronic Parameters regarding the stage of the fuel cycle [39].

	H	G	F	E	D	C
1	13	13	13	10		
2	30	43	30	16	13	38
3	44	16	43	30	40	13
4	28	44	30	33	30	
5	43	16	43	28		
6	28	44	30			
7	32	28				
8	50					

(GWd/t)

**Figure 2.4.** Burn-up heterogeneous distribution given in GWd/t (case REP1300-UOX) [142]

## Spatial aspect

[142]

The considerations are also taken from:

- Hot spot radial localization:

PWR reactor core is made of different types of assembly in terms of isotope inventory and number of fuel cycles (Burn up). These aspects strongly impact the neutronic reactivity (as described in the previous section) but also the local behavior of each assembly. In addition, the control rods are dispatched symmetrically (1/8 symmetry) in the core from the center to the peripheral zone of the core (chapter ( 15)in Annexe part). This disposition is explained by the fact that the core area impacted by each control rod is approximatively restricted to a square of 9 assemblies including the control rod assembly. The ejection may concern any of the control rods of the core but, considering the impact area of each control rod, the more the location of the ejected control rod is peripheral and close to the reflector, the more heterogeneous the power distribution is during the transient [141]. Moreover, It has been observed that the hot spot location generally does not appear in the assembly where the control rod had been ejected but within its nearest lateral neighbor [141].

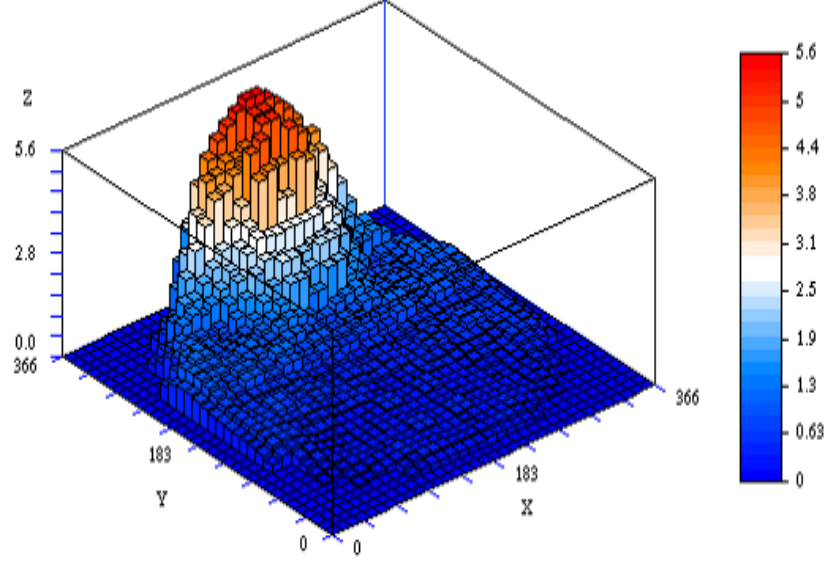


**Figure 2.5.** 2D Power distribution at the moment the control rod ejection is completed (case REP1300-UOX) [142]

- Hot spot axial localization:

During the steady situation at  $P_{nom}$  (standard operation of the reactor), the axial flux shape has a quasi symmetrical and centered distribution, in case control rods are extracted, and, in case control rods are inserted, it has a peak in the lower part of the core. After we shutdown the reactor, we observe the increase of the Xe concentration up to its maximum value, approximately at 6.7h) and then the asymptotical decrease of the Xe concentration [141] [125].

According to the safety analysis and regarding the most restrictive scenario, the rod ejection accident should happen when that the Xenon concentration has reached its maximum value. An order of magnitude of the core poisoning of a REP is given by [214]: at steady state we have about 3000 pcm for the  $Xe^{135}$ . As a consequence of the shutdown of the reactor, the concentration of the Xe and Sa increase to a maximal peak of about 5000 pcm for the  $Xe^{135}$  [214].

Consequently, due to the peaked distribution of the flux in the lower part of the core (according to the control rod insertion) the increase of Xe has a axial distribution also peaked in the lower part of the core. Thus, if for instance the reactor is accidentally restarted during this Xe transient, the axial distribution of the Xe will lead to pull up the flux distribution to the top of the core when we extract the control rods.

Thus the inserted control-rods gain a new neutronic weight as important as the Xe transient had been complete. Figure ( 2.6) shows the classical PWR Xenon axial core distribution after a Xe transient.

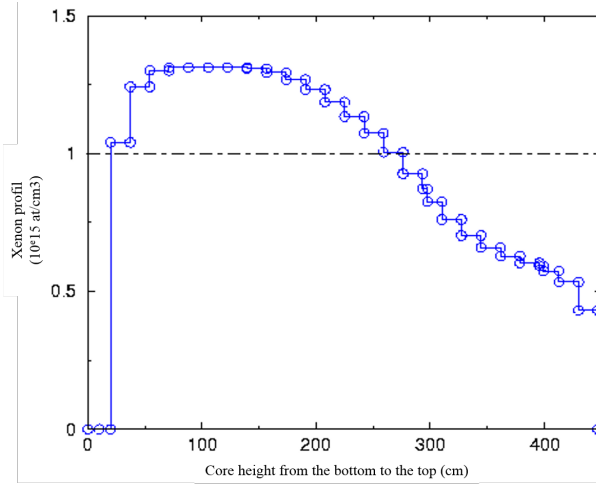


**Figure 2.6.** Axial penalizing Xenon distribution inside the core (case REP1300-UOX) [142]

## 2.2.2 Thermomechanics representativeness

### Thermomechanics initial state

In the nuclear core reactor, the fuel is located in the fuel pin. The fuel pin is a metal cladding (Zircaloy IV) filled with fuel pellets of UO<sub>2</sub>.

On the one hand, the fuel pellet is a ceramic material made of Uranium dioxide. This uranium dioxide is a semiconducting solid which has a very low thermal conductivity compared with that of zirconium metal used for the clad but conversely a higher melting point. The fuel pellet material has a very specific physical and mechanical evolution during the reactor operation from the beginning of his life to the end of each cycle. This is due to its isotopic evolution and to the fission gas production from the neutronic reactions. This Fission gas, as well as the aging of the fuel pin (mechanical avolution and Burn-up) would be sources of pellet and cladding loading under Thermal transient conditions and would modify the thermal conductivity [195].

On the other hand, the fuel pin cladding made of Zircaloy IV is the first containment safety barrier. This barrier is a fundamental safety facility in the core that requires to focus on its evolution during a very mechanical constraining scenario such as REA. The physical state of the fuel pin cladding, i.e., initial Pellet-Clad interaction, loading conditions, temperature and pressure, depend on the present state of the reactor [141] [125]

[147].

During the reactor operation, the micro-structure of the alloy changes, i.e., the irradiation creates many dislocation loops (Franck and Read mechanism [80]) and, moreover, we observe the creation of an external Zircon and hydride layer. In addition, the Zircaloy IV has an anisotropic elastoviscoplastic mechanical behavior which can be reduced by irradiation hardening [147]. These hardenings and hydrides layer induce a weakening of the clad [272] [207] [56] [47] and could jeopardize the first barrier integrity during transient such as REA.

Beside the pellet and the clad, another part of the fuel pin is essential for an accurate Fuel pin modelling. Indeed, from the start, the manufacturing gap between the pellet and the clad changes [195] [36]. The gap closure and re-opening significantly influence the thermal conductivity of the fuel pin and consequently the fuel pin behavior during the transient. Indeed, the gap thickness and composition certainly influence the gap thermal exchange coefficient  $H_{gap}$ , which varies from its manufacturing to the shutdown of the reactor. Fission gas products modify the transfer but the main component is the thickness of the gap that gives value of the  $H_{gap}$  from  $2000 \text{ W/m}^2\text{K}^{-1}$  to  $50000 \text{ W/m}^2\text{K}^{-1}$  respectively from a full open gap to a closed one. Obviously we can easily imagine the consequence of a wrong  $H_{gap}$  in modelling of the thermal fuel pin behavior or DNB as well as the PCMI and the clad failure.

In conclusion, it is very important to take into account the initial pellet - clad gap state in terms of thermal conductivity of the fuel pin [152] [132] as well as of its mechanical behavior and evolution during the transient.

## Mechanical transient specificities

The Thermo-mechanical state during the transient is obviously dependant of its initial state but also of the Power deposition from the fission  $P_{fuel}$  and the Hydraulic state of the coolant in which the fuel pin transfers a part of its energy. In the very first moment of the transient, we assume that the thermal activation occurs in the context of an adiabatic warming. Indeed, the heat diffusion time, from the center of the fuel pellet, is about few seconds due to the evolution of the thermal conductivity with the increase of the Temperature. This stage of the scenario is called Quasi Adiabatic heating. Then, the fuel pin temperature passes from a planar distribution to a radial distribution  $T(r,t)$  with the hottest temperature at the center  $T_{pinCenter}$  and the lowest temperature at the clad surface  $T_{wall}$  in contact with the fluid. Then, as it is detailed in [147] the REA transient may lead to different risks of failure (fragile or ductile).

First of all, after the Thermal activation of the fuel pellet due to the power sharply injected inside the core, we observe the warming and the Pellet Cladding Mechanical Interaction (PCMI) due to mainly the thermal dilation of the fuel pellet. The Pellet Cladding Mechanical Interaction (PCMI) process is the common process of evolution of the fuel pin. However, the REA can accentuate this process and may lead to the rupture



(brittle failure) of the clad. The REA mechanical evolution have a very significant influence on the Pellet-Cladding Mechanical Interaction process and the underlying problem about safety function of the clad as the first containment barrier.

Secondly, after the thermal activation, let us assume that the fuel pin has resisted and conservated its integrity during the PCMI process. A second potential rupture storyline of the REA transient is available. The temperature of the clad increases and the pellet transfers a significant amount of heat to the fluid. If we reach the saturation temperature of the fluid we would induce a Departure from Nucleate Boiling (DNB) [147] of the water all around the fuel pin. This DNB can lead to a drying up of the external side of the fuel pin [82] [83] [86]. The dryout phenomenon leads to an extremal change of the thermal transfer coefficient between the clad surface and the fluid due to the vaporization of the liquid medium by a gaseous medium which has a far lower thermal conductivity. Consequently, the fuel pin won't be able to transfer the heat outside the pellet and thus the fuel temperature is going to increase leading to the expansion of the fuel pellet, the fission gas as well as the clad deformation under those mechanical stresses. Then, if the DNB crisis was not sufficiently strong to damage the cladding part, during this stressful dryout phase we might observe a ductile failure of the clad.

Finally, another way of rupture exist during the rewetting phase [147] that succeeds to the boiling crisis and dryout phase. Indeed, the quenching that the clad undergo shall lead to the brittle failure (the greater the oxidation , the easier the failure). In addition, during the cooling phase, the hydrides of the clad, which have been redissolved during the thermal transient, reprecipitate under strain. Those radial hydrides, which have their normal vector parallel to the loading direction, weaken the material [56] [47].

Typical results of the core average fuel pin temperature are given in the following curves [142]:

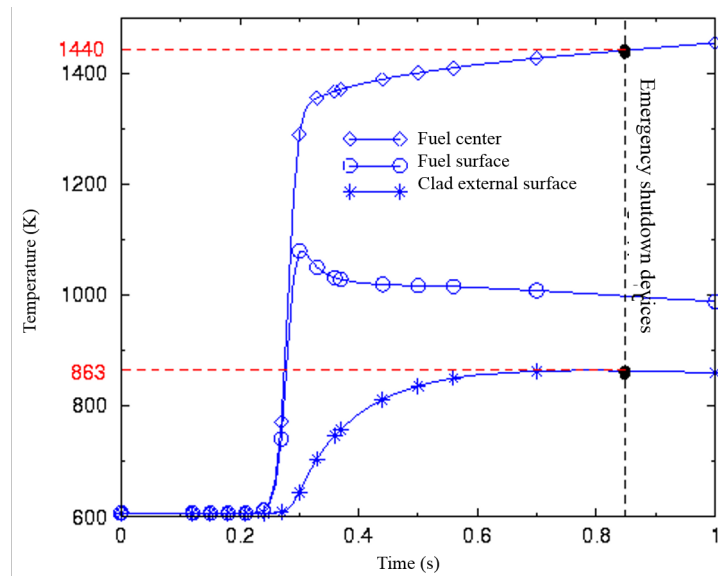


**Figure 2.7.** average core Fuel pin temperatures [142]

### 2.2.3 Thermohydraulics representativeness

#### Thermohydraulics initial state

On the hydraulic side, the coolant is mainly made of water and Boric acid uniformly distributed in the volume of the core (Boron is a neutron poison at the common concentration of about 1300ppm). The coolant remains at single phase during standard operation due to the pressurization of the reactor. In standard operation the reactor is using 4 pumps but in case of a shutdown reactor scenario, the reactor is heated by parallel hydraulic loops which induce the closure of 2 of the 4 primary loops (pumps).

Thermohydraulics initial parameters		
Fluid temperature	290	°C
mass flow	4240.72	m3/h
inner enthalpy	1322.8	kJ/kg
outer pressure	155	Bar

**Table 2.2.** Thermohydrolic core inlet parameters

#### Thermohydraulics transient specificities

During the transient, the fluid state is function of the power deposition  $P_{fluid}$  from the fission and of the thermal transfer through the cladding  $\Phi_{wall}$ . It will change the fluid thermal properties (mainly, the fluid temperature  $T_{fluid}$ , the fluid density  $D_{fluid}$  and the pressure) and the boron diffusion inside the core. The Fluid temperature and density are representative of the thermohydraulics major changes during the transient, and typical plots of these parameters (also called moderator temperature  $T_{moderator}$  and density  $D_{moderator}$ ) are given in the following curves ( 2.8) [186].

The fluid starts from single phase but diphasic phase may be reached during strong thermal transients. The phase transition is usually expressed through Critical Flux Ratio (RFTC defined in section ( 9.3.6)).

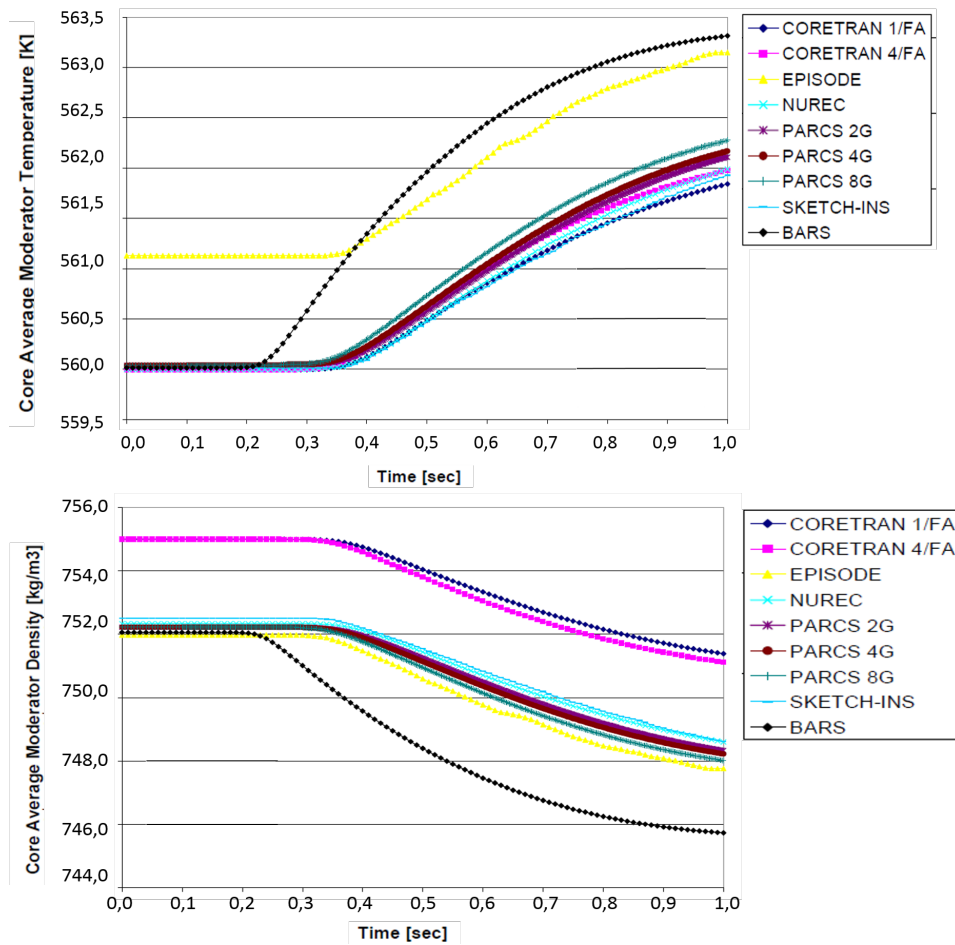


**Figure 2.8.** Benchmark Full core average calculation Fluid temperature (upper curve) Fluid Density (bottom curve) function of time [186]

## 2.3 REA Benchmarks identification

To develop and assess our methodology for treating such coupled accidental situations, we need first to define a simple but representative situation to model. A certain number of international Benchmarks propose reference calculations concerning Reactivity Injection Accident and more precisely Rod Ejection Accident. This type of calculation involves the use of accurate thermomechanics modelling (the goal of our study) coupled with an accurate Neutronics and Thermohydraulics. Nevertheless, nowadays, none of the existing benchmarks propose this type of accuracy within their modelling to be compared with. This way, we only focus on the physical representativeness of the Benchmark we list, below, in order to find out one of them matching with our goals, i.e., small core (at this stage of the study), order of magnitude of physical parameters, temporal and spatial representativeness. Figure ( 2.9) compares the listed benchmarks regarding our physical representativeness goals.

- Benchmark 1 (B1) : Case II-2B , UAM, NEA/NSC/DOC(2016), Benchmark for uncertainty analysis in modelling (UAM) for design, operation and safety analysis of LWRs, vol II (Phase II), april 2016 [187].
- Benchmark 2 (B2) : High-fidelity multi-physics system TORT-TD/CTF/FRAPTRAN for light water reactor analysis [153] from NEA Benchmark [129].
- Benchmark 3 (B3) : Enhancement to the Nodal Drift method for REA in PWR Mini-Core with lumped Thermal model [206] ,and , Advanced multi-physics simulation for reactor safety in the framework of the NURESAFE project [42] from NURISP Benchmarks [126].
- Benchmark 4 (B4) : NEA/NSC/DOC(2006)20, DOWNAR, Dec 2006, PWR MOX/UO2 core transient [64].
- Benchmark 5 (B5) : Case II-5B , UAM, NEA/NSC/DOC(2016), Benchmark for uncertainty analysis in modelling (UAM) for design, operation and safety analysis of LWRs, vol II (Phase II), april 2016 [187].
- Benchmark 6 (B6) : Case B1 (Lateral Control Rod HZP), SIEMENS, NEA/CRP/3D LWR Core, Transient Benchmark, OCDE octobre 1991-janvier 1992 [182]; and NEA/NSC/DOC(93)25, Results of LWR Core Transient octobre 1993 [183].

CHAPTER 2. TRANSIENT SCENARIO PHENOMENOLOGY OF A ROD  
EJECTION ACCIDENT

Benchmarks	Physical representativeness			Temporal aspect		Spatial aspect	Conclusion
	N	TH	TM	Dynamics	Order of magnitude		
Small Core design							
Benchmark1 (B1)		No TH	No TM	Triangulare pulse		Not representative	Multiphysics lack of accuracy Temporal and Spatial lack of representativeness
Benchmark2 (B2)				Not the most penalizing scenario	Not the most penalizing scenario	Too small core design	Temporal and Spatial lack of representativeness
Benchmark3 (B3)				Too fast dynamic	Very high Pmax	Central Peak	Temporal and Spatial lack of Representativeness
Full Core design (unwanted core design but study perspectives )							
Benchmark4 (B4)						Axial peak in the central part	Spatial lack of representativeness
Benchmark5 (B5)						Axial peak in the central part	Spatial lack of representativeness
Benchmark6 (B6)						Latteral peak but full core (1/8)	Spatial lack of representativeness
(N = Neutronics, TM = ThermoMechanics and TH = Thermohydraulics)							

**Figure 2.9.** Benchmarks comparative table regarding the accuracy of each aspect of representativeness, and presence of each physical discipline, we are looking for in this study (perfect accuracy, average accuracy, rough accuracy)

In conclusion, beyond the lack of multiphysics modelling considering accurate Neutronics, Thermohydraulics and Thermomechanics, none of the existing Benchmarks perfectly respect the temporal and spatial aspects of the transient we would like to face in for our study.

For instance, considering only the small core Benchmarks, Benchmark 3 does not ensure the temporal and spatial aspects we are looking for.

On the one hand, regarding the temporal aspect, the neutronic power is too fast (power peak before the end of the rod ejection). The reactivity and power pulse reach the adiabatic stage of the transient (zone 3 in section 2.2.1) but, then, dramatically decrease in less than 100ms. This Neutronic dynamic leading mainly to the adiabatic phase turns the Thermohydraulics-Thermomechanics coupling non-discriminatory (minor) for the transient modelling and analysis (thermal rough model would be sufficient). On the other hand, with respect to the given informations in Benchmark 3 [206] and its legacy from [236] and [126], we can easily assume a spatial representativeness of the power distribution (hot spot location) far from the spatial distribution of typical PWR we presented in section (2.2.1) and which we are looking for.

In this context, we decide to build a specific academic transient scenario for which we can control the physical representativeness (temporal and spatial). This transient scenario will be soon proposed after this study as a specific Benchmark (NEA-UAM) to be compared with future multiphysics Neutronics-ThermoMechanics-Thermohydraulics couplings at the CEA and in international research center. The previous listed Benchmarks show the methodology to follow in order to perform a scientific study and calculation, as well as some of these Benchmarks have directly inspired our work regarding the core design and the initial parameters.

## 2.4 Academic case and transient scenario

### 2.4.1 Academic model

Regarding the previous Physical explanation in section ( 2.2.1 , 2.2.2 and 2.2.3) and the inadequation in finding dedicated Benchmark to our study ( 2.3), we decide to build a specific academic transient core and scenario matching with our goals and with which we accurately handle and control the physical and the modelling parameters.

This academic reactor is a 5x5 assemblies geometry reactor made of 9 internal fuel assemblies and of an external ring of 16 reflectors assemblies (figure ( 2.10)). In addition, the core spatial discretization has been define in order to be consistent with the discretization used for the cross sections computation (this aspect and approximation could be later easily improved). It has a Power of 110 MW, and is 468,72 cm in height. The central assembly has a central control rod (Grey rod [141]).

Thanks to this reactor core modelization, the coupling scheme analysis and the simulation shall be significantly simplified in terms of computation time and data analysis. The small core has been designed in order to preserve the 1/8 core symmetry that exists in standard 1300MW core (chapter ( 15) in Annexe part) and the side-effect induced by the presence of reflector assemblies around the fuel assemblies.

This geometry preserves the physical, neutronic, thermohydraulic and mechanical specificities as well as the behaviors of the PWR 1300 MWe in case of nominal (core at critical state:  $k_{eff} = 1$ ) and accidental situations (supercritical  $K_{eff} > 1$  with feedback reactions).

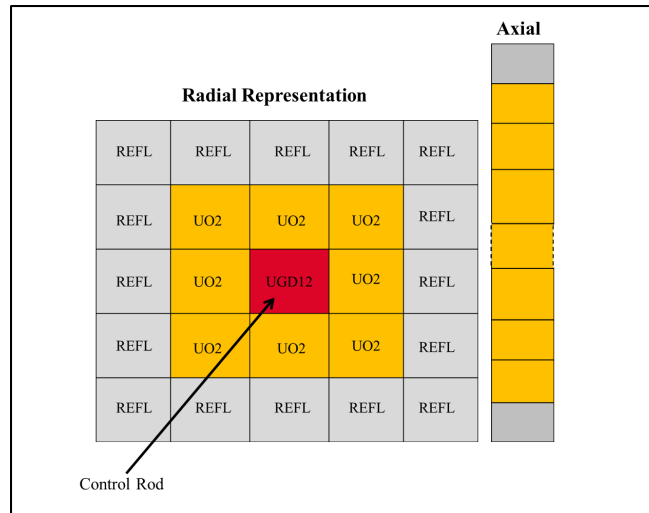


**Figure 2.10.** PWR small core (5x5) scheme

The Physical data are summarized in tables in the section ( 15.2) of the (chapter ( 15) in Annexe part).

### 2.4.2 Academic scenario

In the following sections, we are going to detail the academic scenario we realized in order to obtain a realistic PWR REA transient regarding our academic core geometry. In order to simulate this realistic scenario we work with the neutronic code APOLLO3 coupled with an adiabatic simplified thermal solver. This first dimensioning calculation is going to give us a first approximation of a REA transient scenario which is going to be improved by increasing the accuracy of our physical models during our multiphysics Best Effort study.

#### Initial state

As it had been defined in sections ( 2.1 and 2.2), the REA transient can be described following two fundamental aspects, i.e., time and space. According to this information, we have developed our academic scenario in order to reach these two aspects by working on physical specificities of the initial state of the core:

- In order to meet the time aspect of the scenario (more precisely the dynamic and strength aspect of the transient) we are working through:
  - the celerity of the ejection,
  - the initial state of the reactor core (Hot Zero Power),
  - the control rod reactivity (composition and insertion linked to the space aspect) and the delayed neutron fraction.
- In order to meet the spatial aspect of the scenario ( more precisely the axial and radial location of the hot spot during the transient) we are working through:
  - the Burn up map
  - the Xenon concentration and distribution

On the one hand, the initial state is characterized by a Hot Zero Power (P0 transient): hot shutdown reactor, power close to zero ( $P0 = 110.10E-9$  MW), with operating fluid temperature and pressure of the coolant, fuel pin heated by the coolant and control rods inserted inside the core. The control rods are defined as grey control rods inserted at the level of 82.06 cm from the top of the active part of the core (82.06/426.72 cm) with a reactivity weight of 893pcm (related to the Xe and Burnup distribution). The delayed neutron fraction is defined at 569 pcm with 6 precursor families. Moreover, the transient is defined with a control rod ejection of 0.1s.

On the other hand, regarding the spatial aspect of the scenario, the burn-up radial map had been chosen (figure ( 2.11)) in order to get a realistic and prompt transient in the lateral assemblies nearby the central one.



## CHAPTER 2. TRANSIENT SCENARIO PHENOMENOLOGY OF A ROD EJECTION ACCIDENT

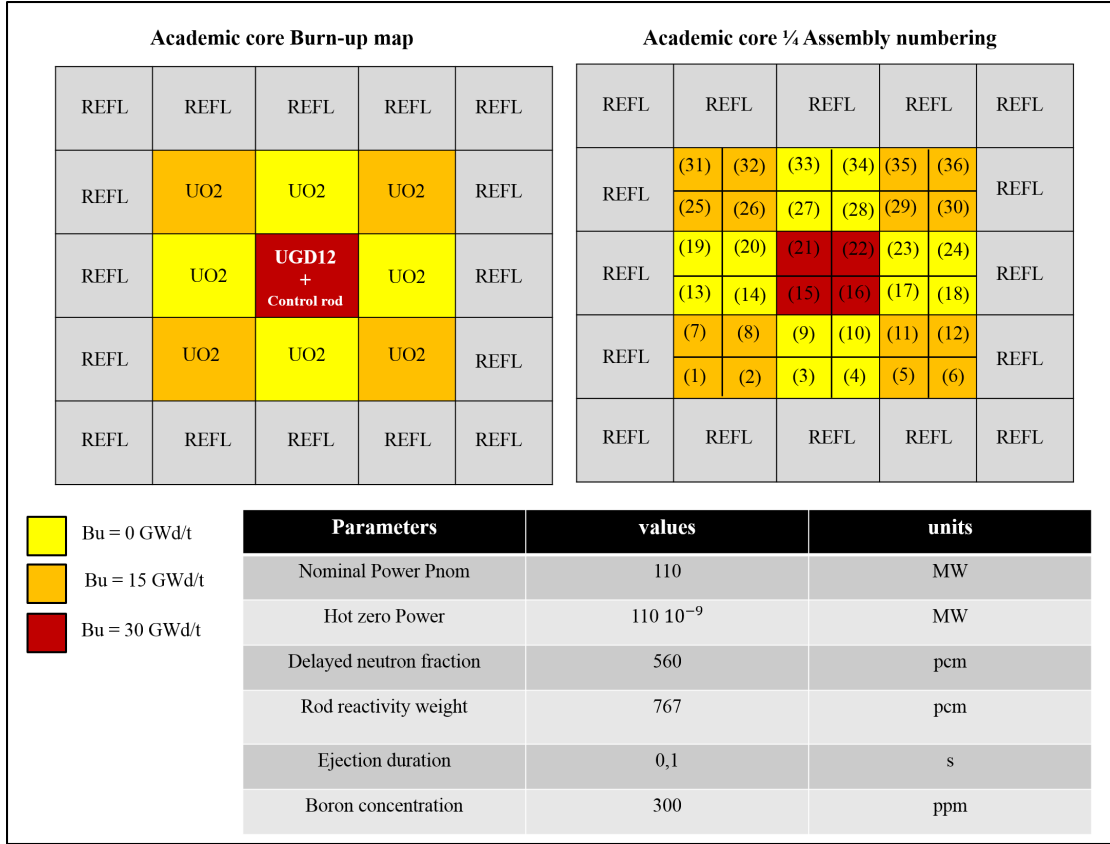


**Figure 2.11.** Mini Core burn-up, assembly numbering and parameters description

Figure ( 2.11) summarizes the burn-up map, the 1/4 assembly numbering we are going to use during this study and the parameters that characterize our P0 transient.

Moreover, we consider that the transient appears at the very moment the Xenon transient is at its maximum, i.e., the Xenon core distribution poisoning induces the moving up of the Power distribution into the upper part of the core as it is shown in figure ( 2.12). This state of the core is obtained about 8 hours after shutdown ( $P_0 = 110.10E-9$  MW, we assume no residual power inside the core) of an operating core at nominal power of about 110MW with inserted control rod.

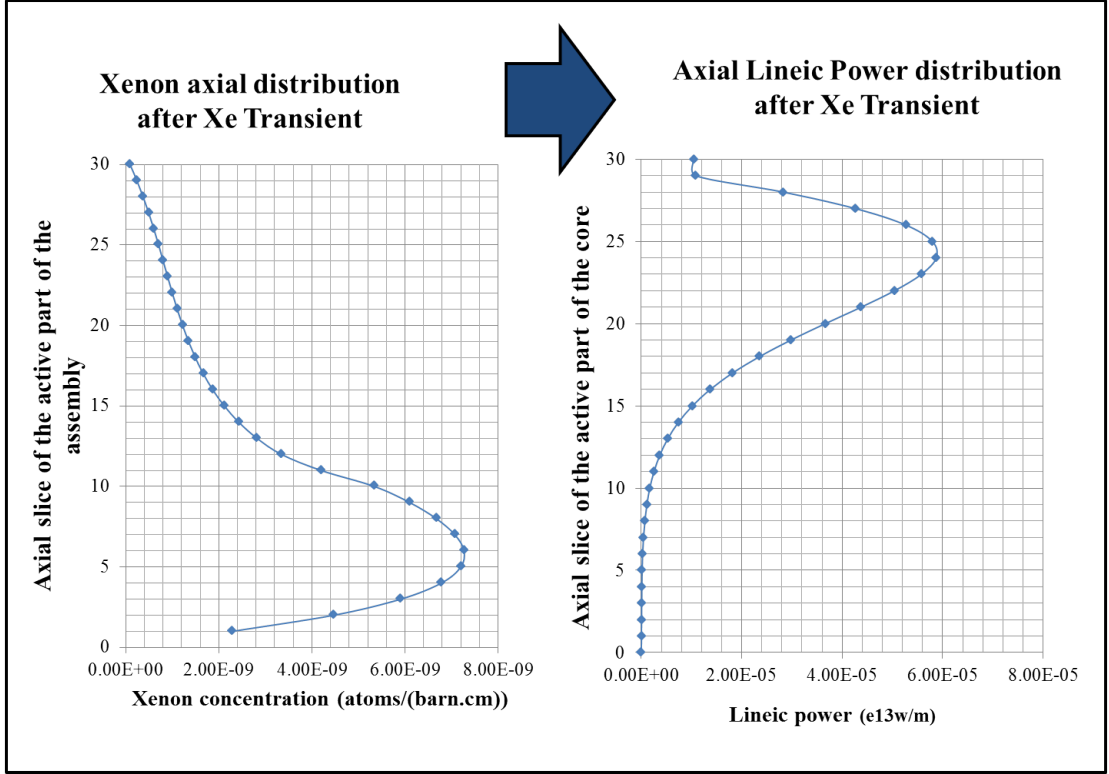


**Figure 2.12.** Xenon and Power axial distribution after Xe Transient in 1/4 assembly (9)

## Transient and Post accident state

In this scenario the reactor goes prompt critical with a control rod reactivity weight of 893 pcm and a delayed neutron fraction of 569 pcm. It produces a rapid power spike of about several milliseconds, from a quasi zero Power to a relative Power of about ten  $P_{nom}$ , in average, and of about a hundred of  $P_{nom}$  (local hot spot) at the location of the fuel pin/assembly most loaded in terms of thermal and mechanical reactions. Also, in order to simplify our coupling and study, we designed this scenario in order to get close but to prevent any risk of Departure of Nucleate Boiling, Dry-Out, Fission Gas Release or rewetting [147].

The pulse calculation is obtained thanks to the APOLLO3 kinetic solver MINOS (SPn) (detailed in part III) with specular boundary condition and a time discretization of  $\Delta t = 0.001s$ . For a computing time purpose and regarding Power pulse evolution, we assume we reach the new steady state through the asymptote of the power pulse duration of 0.4s.

The transient goes prompt critical and produces a rapid power spike lasting for about several milliseconds (a narrow pulse about 20-30 ms in width), from a quasi-zero Power to a maximal integrated Power of  $P_{integrated} = 70P_{nom} = 7021MW$  (figure 2.13). The

## CHAPTER 2. TRANSIENT SCENARIO PHENOMENOLOGY OF A ROD EJECTION ACCIDENT

integrated power here corresponds to the maximal value of the total core power developed in the academic core under consideration. The Power evolution in the core well describe the typical five steps (figure 2.13) described previously in section (2.2.1) as well as the hot spot  $F_{xyz}(t)$  evolution inside the core well describe the 5 typical zones.

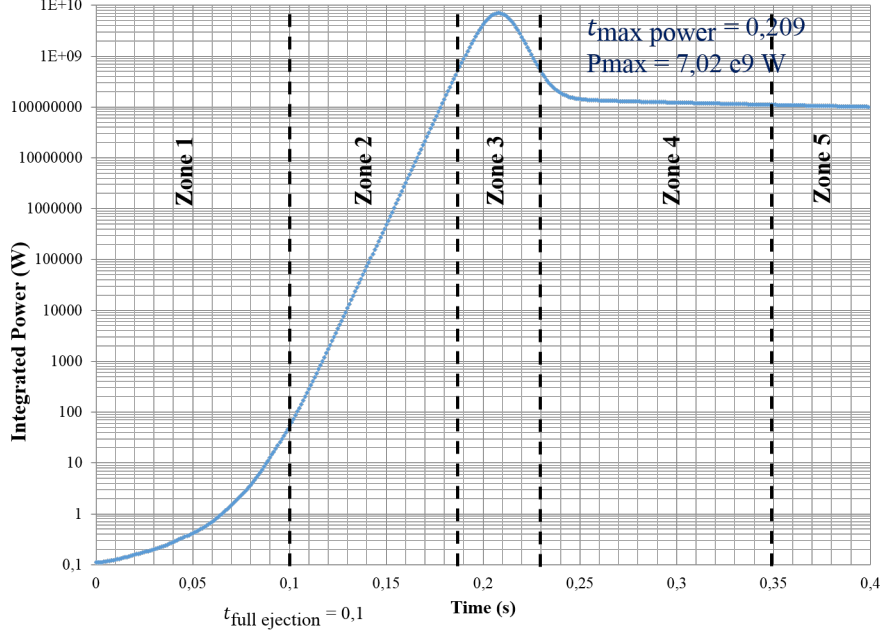


**Figure 2.13.** Power evolution during a REA transient .

The critical REA scenarios would be completed for peaks of about 20-30 ms wide, and a heterogeneous Burn-up map considering Burnup from 0 to 30GWd/t [159]. And as it is shown in figure (2.14) due to the 1/8 symmetry of our academic core, the hot spot locations are in the axial slice 27 of 1/4 assembly (9), (10), (14), (17), (20), (23), (27), (28) according to figure (2.11). Then, in the same figure we observe the  $F_{xyz}$  max Power shape factors evolution and the Hot spot cell designation.

In order to simplify our coupling and analysis, we decide to control our power pulse maximal value (mainly through the neutronic weight of the control rod) in order to avoid a critical boiling of the water with drying of the clad. Moreover, we also decide to use in the Thermomechanical part assemblies at Burn-up = 0GWd/t which will be used, in futur, to determine the impact of the mechanical state thanks to the comparison with heterogeneous Burn-up distribution calculations.

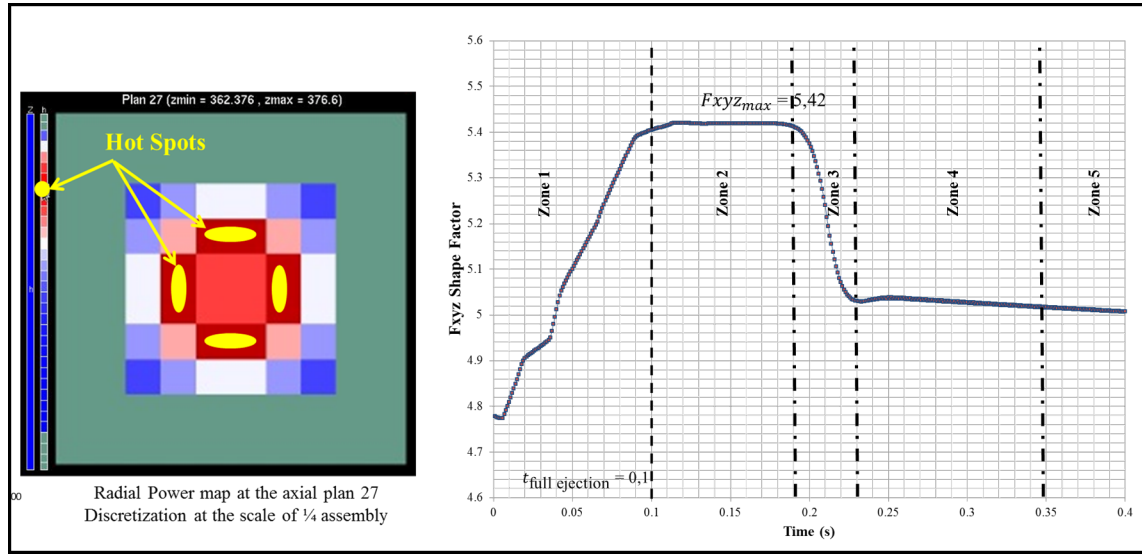


**Figure 2.14.** APOLLO3 SA Hot spot locations and Max value of Fxyz shape Factor evolution during the transient

## PWR-Academic core transient comparison

Neutronics parameter	PWR typical transient	Academic core transient
Delayed neutron fraction	450 pcm	560 pcm
Control rod reactivity weight	700 pcm $\simeq 1.5 \$$	767 pcm = 1.4 \$
Burn-up heterogeneity	heterogeneity	heterogeneity
Rod Ejection duration	100 ms	100 ms
Width of the power pulse	40 ms	50 ms
Max integrated power	10Pnom	60Pnom
Max value of the 3D shape factor Fxyz	20	5
Max local power	200Pnom	300Pnom

**Table 2.3.** PWR 1300MW and Academic core Neutronics parameters typical order of magnitude [142]

## 2.5 Proof of Concept Coupling Framework used in this work

We start this PhD work from the current standard REA Best Estimate multiphysics modelling which consists in coupling an accurate Neutronics with accurate Thermohydraulics altogether and where the thermomechanical part is reduced to the thermal equation. Our long term goal is to reach a Best Effort modelling that would allow us to evaluate and assess the Best Estimate approximation, and to most accurately model the physical phenomena in the futur.

For this purpose, in the limited time of a PhD, we decide to realize a Proof of Concept in order to show through this first modelling our availability to couple accurate physical models and definitely pave the way for future Best Effort studies.

In this framework, one of the goals of this work is to properly and efficiently couple an accurate Thermomechanics model with an accurate Neutronics and Thermohydraulics simulation. Another one is to use this multiphysics coupling within a representative simulation. At first we assume some approximations we would be able to easily correct step by step in order to perfectly reach all the Best Effort modelling goals in the future. Through this simulation, we are also looking to observe a similar evolution of the core behavior that we could obtain using a standard Best Estimate Neutronics-Thermohydraulics modelling. Finally, the last one is to get access to the local parameters at the pellet-cladding scale and sub canal scale. In this study, except from the fuel pin, we will work at the scale of the assembly. Nevertheless, a specific effort has been done in order to prepare or improve the structures to access the local physical information that would lead to the implementation of a future multiscale coupling scheme in the future.

Different fields have been described according to the mathematical and coupling requirements. We can distinguish between:

A. Fuel pin (pellet/cladding with empty zones and interstices) and weighting fuel pin  
In this field there is a coupling between 4 local models

- 1) multimaterial 3D Neutronics "model" (clad/ pellet/ gap/ bubbles) → in order to rebuild the neutron flux with  $E > 1\text{MeV}$  (this aspect will not be considered during our REA proof of concept study but it is paramount in order to well represent the fuel pin irradiation REA initial state that may strongly impact the fuel pin representativeness during the transient)
- 2) multimaterial mechanics model (clad/pellet/gap/bubbles),
- 3) fission Gas model (FG) Evolution (gap/ bubbles),
- 4) multimaterial 3D thermics (clad/ pellet-bubbles/ gap),

Comments: we are working only on a few representative fuel pins. For example, 1 average fuel pin for all pins ( 17x17) of the assembly. Nevertheless, modelling could

---

## 2.5. PROOF OF CONCEPT COUPLING FRAMEWORK USED IN THIS WORK

---

be done with 1 fuel pin for 1 sub canal/fuel cell. Due to the symmetry assumption, the 3D model will be reduced to a simplified (r,Z) model, i.e.,  $\Delta z = 14.2$  cm ( 30 fragments linked by the mechanical and thermal boundaries conditions) and  $\Delta r = 0.01$  cm  $\rightarrow$  30 annular cells / per pin section).

### B. Thermohydraulics

We use a Bifluidic-monopressure model with gas diffusion equation and drift flux equation in order to modelize differences between liquid and gas velocities. We assume that the vapor is saturated in presence of liquid. We use a 3D modelling with the ability of using a block structured adaptive refinement (AMR). Typical grids will be either  $\Delta z = 14.2$  cm and  $\Delta r = 10$  cm  $\rightarrow$  4 cells / assembly).

### C. Core Neutronics with internal heterogeneous refinement

We resolve the transport equation (in order to obtain the neutron flux according to their Energy level and direction). This equation might be coupled to the BATEMAN equation (thanks to this equation we can retrieve the evolution of the atomic density of each nucleus) but, in our case, we used the Macroscopic multiparametered library that already represents the isotopic evolution of the core according to the time/Burn-up evolution. Equations are homogenized at the scale of the assembly. Nevertheless, a specific work had been done in order to access local flux and power by a post treatment at the scale of the fuel cell (MINOS), refined and homogenized, at the scale of the fuel pellet (MINARET). We use a grid at the scale of the whole core:  $\Delta z = 14.2$  cm and  $\Delta r = 10$  cm  $\rightarrow$  4 cells / assembly) and a grid at the scale of the assembly: ( $\Delta z = 14.2$  cm and  $\Delta r = 2$  cm  $\rightarrow$  1 cell / fuel pin).

For the purpose of this work we are going to use industrial codes namely :

- APOLLO3 @code [234] which is a common project of CEA, AREVA and EdF for the development of a new generation code system for the core physics analysis. In our case, we are using MINOS and MINARET solvers [20] [168] [232], which are unsteady 3D deterministic transport equation solvers.
- FLICA4 [258] which is a 3D two-phase flow code modelled by a set of 4 homogeneous porous medium equations .
- ALCYONE [191] which is devoted to the nonlinear thermomechanical, fission gas and physico-chemical analysis of the fuel pin.

Each code has an internal simplified model of other disciplines. We then speak of internal coupling disciplines, compared to the external coupling code/code characteristics of the "Best Effort" approach. The existence of simplified models responds to the interest of efficiency of modelling in order to avoid parametrized models. These three codes are coupled within the SALOME [7] application named CORPUS [233] , dedicated to Best Effort multiphysics modeling of PWR in normal and accidental situations.



## Part III

### Neutronic models of the core





## Chapter 3

# Neutronics equations and Numerical Models

While working on this multiphysics problems we are required to accurately construct the different models upon which the multiphysic coupling will be based. These models are established in order to describe the different fields of the Nuclear Reactor Physics: Thermohydraulics, Fuel pin Thermomechanics and Neutronics. In this chapter, the Neutronics models are mathematically and numerically formulated. This allows us to pin point the coupling variables of our multiphysics problem as well as to define the limitations of the models and the assumptions and hypothesis we made.

### 3.1 Core Reactor Physical Description

[214] [39]

Inside the Nuclear core reactor, the neutron propagation is coupled with the transmutation of the isotope of the medium in which the neutrons are propagating. They are governed by:

- The integro-differential Boltzmann equation of neutrons transport;
- The generalized BATEMAN equation of isotopic evolution, for steady situations, or precursors evolution equation for fast and accidental situations.

The studies are done in order to have access to the physical data of the reactor power, flux of particules, isotopic concentrations, etc. This means that we need to solve the previous equations that steer the neutron and isotopic evolution of the different parts of the core as functions of time and space.

## 3.2 Physical Equations

### 3.2.1 Symbols and definitions

We first introduce the main notation of the physical problem.

Neutronic quantities 1/3		
$k_{eff}$	multiplying effective parameter k	$\emptyset$
$k$	Boltzmann constant	$m^2.kg.s^{-2}.K^{-1}$
$T_i$	temperature of the medium i	K
t	time	s
n	neutron population volumic density	$n.cm^{-3}$
$\Theta$	neutron life time in the medium ( $2.5 \cdot 10^{-5}$ s in a PWR)	s
$N_k(\mathbf{r}, t)$	number of each nucleus k in a volume V	$Nuclei.cm^{-3}$
$\lambda_k$ or $\lambda_i$	half life time per each nucleus k or precursor family i (given by a parametrized library). We can specify the desintegration from a nucleus m to a nucleus k by $\lambda_{k \leftarrow m}$	$s^{-1}$
$M_i$	mass of the nucleus i	kg
$C_i = c_i^{(k)}$	number of precursors in family i of an isotope k. A precursor is an isotope k which is an unstable nucleus that decays and produces a delayed neutron. A delayed neutron is a neutron emitted after a nuclear fission event, by one of the fission products, or, actually, by a fission product daughter after a beta decay. This event occurs any time from a few milliseconds to a few minutes after the fission event (in comparison neutrons born within $10^{-14}$ second of the fission are termed "prompt neutron"). Beyond few minutes we assume that the system reaches its steady state, hence the kinetic evolution of precursor is neglected.	$Nuclei.cm^{-3}$
$\beta_i = \beta_i^k$	ratio of the quantity of delayed neutrons over the total number of neutrons emitted. This ratio is defined for each precursor family i	$\emptyset$
$\nu_{t,k}(E)\beta_i^k$	quantity of delayed neutrons emitted from the precursor i by induced fission at the Energy E and the nucleus k.	n
$\mathbf{r}$	position vector	
$\Omega$	unit vector (solid angle) in direction of motion, $\Omega = \frac{\mathbf{v}(E)}{\ \mathbf{v}(E)\ }$ , where $\mathbf{v}$ ( $cm.s^{-1}$ ) is the neutron velocity vector and v its neutron modulus velocity	$\emptyset$
E	neutron kinetic Energy	W
$\mathbf{v}$	the neutron velocity vector and v its neutron modulus velocity	$cm.s^{-1}$

**Table 3.1.** Neutronics notations: Neutronic quantities 1/3

Neutronic quantities 2/3		
$n(\mathbf{r}, E, \mathbf{\Omega}, t)$	amount of neutron in a differential volume $dr$ about $r$ , associated with particles of differential energy $dE$ about $E$ moving in a differential solid angle in $d\mathbf{\Omega}$ about $\mathbf{\Omega}$ , at time $t$ .	$n.cm^{-3}$
$\Psi(\mathbf{r}, E, \mathbf{\Omega}, t)$	angular neutron flux associated with particles of differential energy $dE$ about $E$ moving in a differential solid angle in $d\mathbf{\Omega}$ about $\mathbf{\Omega}$ , at time $t$ . $\Psi(\mathbf{r}, E, \mathbf{\Omega}, t) = v \cdot n(\mathbf{r}, E, \mathbf{\Omega}, t)$ and $\langle E \rangle = (1/2mv^2)/E_{ref}$	$n.cm^{-2}.s^{-1}$ .
$\Phi(\mathbf{r}, E, t)$	Total neutron flux (scalar flux), in a differential volume $dr$ about $r$ , associated with particles of differential energy $dE$ about $E$ , at time $t$ . The integrated flux is the total distance travelled in one second by all the particles in the one $cm^3$ volume. $\Phi(\mathbf{r}, E, t) = \int_{4\pi} \Psi(\mathbf{r}, E, \mathbf{\Omega}, t) d\mathbf{\Omega}$	$n.cm^2.s^{-1}$
$\Phi^p$	flux of high energy neutron ( $E > 1MeV$ )	$n.cm^2.s^{-1}$
$P_v^{local}$	local volumic Power and $P_{lineic}^{local} = P_v^{local} \times PelletSection$ (in $W.cm^3.s^{-1}$ )	$W.cm^3.s^{-1}$
$\nu_{t,k}(E)$	average number of neutrons produced per fission from a nucleus $k$ and an incident energy $E$	$n$
$\nu_{p,k}(E)$	total average number ofneutrons produced per induced fission from a nucleus $k$ and an incident energy $E$	$n$
$\nu_{p,fs,k}$	average number of prompt neutrons produced per spontaneous fission from a nucleus $k$	$n$
$\chi_{p,k}(E, T)$	Probability density function for neutron of exit energy $E$ from all neutrons produced by fission (Energy spectrum of prompt neutrons ) of an isotope $k$	$\emptyset$
$\chi_{d,i}(E)$	Probability density function for neutron of exit energy $E$ from all neutrons produced by delayed neutron precursor $i$ (Energy spectrum of delayed neutrons)	$\emptyset$
$\chi_{p,fs,k}(E)$	Probability density function for neutron of exit energy $E$ from all neutrons produced by spontaneous fission (Energy spectrum of prompt neutrons ) of an isotope $k$	$\emptyset$

**Table 3.2.** Neutronics notations: Neutronic quantities 2/3

Neutronic quantities 3/3		
$\sigma_{q,k}(E, \mathbf{\Omega})$	microscopic cross section, which includes all possible interactions q with nucleus k: absorption (a), scattering (s), fission (f) and total (t), of an isotope k. We may specify the cross section according to the energy E leading to the production of a nucleus k from a nucleus m by $\sigma_{q,k \leftarrow m}(E)$ or the scattering interaction of a neutron at energy E' and incident direction $\mathbf{\Omega}'$ which takes the energy E and direction $\mathbf{\Omega}$ .	$cm^2$
$\Sigma_{q,k}(N_k(\mathbf{r}, t), T_k, E, \mathbf{\Omega})$	macroscopic total cross section, which includes all possible interactions q with nucleus k: absorption (a), scattering (s), fission (f) and total (t). $\Sigma_{q,k}(N_k(\mathbf{r}, t), T_k, E, \mathbf{\Omega})$ is given by the formula: $\Sigma_{q,k}(N_k(\mathbf{r}, t), T_k, E, \mathbf{\Omega}) = N_k(\mathbf{r}, t) \cdot \sigma_{q,k}(E, T_k, \mathbf{\Omega})$ where $T_k, N_k$ are respectively the temperature and the density of the nuclei k for the cross section an q reaction and E the neutron energy. The variable $T_k$ will only be taken into account and specified for the reaction of absorption (q = a). Indeed, the variation of temperature effect may drastically increase or decrease the sterile capture of a neutron by Doppler feedback effect (mainly by $U^{238}$ ). (given by a parametrized library)	$Nuclei.cm^{-1}$
$S_{ext}(\mathbf{r}, E, \mathbf{\Omega}, t)$	Source term (external neutron source)	$n.cm^3.s^{-1}$

**Table 3.3.** Neutronics notations: Neutronic quantities 3/3

Above  $E_{ref}$  is a reference energy used for adimensioning the neutron flux. More over, in the multigroup theory, detailed below, the energy dependance corresponds to an adimensional index.

### 3.2.2 Unknown elements of the problem

The three main unknowns are:

- The neutron flux :  $\Psi(\mathbf{r}, E, \mathbf{\Omega}, t)$ ,
- The isotropic concentration by isotope k:  $N_k(\mathbf{r}, t)$ ,
- The density of precursor by precursor family i:  $c_i(\mathbf{r}, t)$ .

### 3.2.3 Variables

The variables of the problem equations are:

- 3 space variables ( $\mathbf{r}$ ),
- 3 celerity variables ( $E$  the energy and  $\mathbf{\Omega}$  the direction of the propagation),
- time  $t$ .

### 3.2.4 Neutron transport equation

The neutron transport equation [39] expresses the neutron balances inside an elementary volume  $D = d\mathbf{r}dEd\mathbf{\Omega}$ , considering an elementary time step  $dt$  defined around  $t$ . Hence we take into consideration 3 space variables ( $x, y, z$ ) or  $\mathbf{r}$ , 3 celerity variables ( $E, \mathbf{\Omega}$ ) and the time  $t$ . From the Energy  $E$  and the propagation direction  $\mathbf{\Omega}$  we can define the neutron velocity by  $\mathbf{v} = v(E)\mathbf{\Omega}$ . But we will rarely use this variable in our formulations. Major hypotheses of the transport equation are given in the chapter (18) in Annexe part. Finally, the neutron transport equation writes:

$$\begin{aligned}
 \frac{1}{v} \frac{\partial \Psi(\mathbf{r}, E, \mathbf{\Omega}, t)}{\partial t} = & -\mathbf{\Omega} \cdot \nabla \Psi(\mathbf{r}, E, \mathbf{\Omega}, t) \\
 & - \sum_k (N_k(\mathbf{r}, t) \sigma_k(E) \Psi(\mathbf{r}, E, \mathbf{\Omega}, t)) \\
 & + \sum_k \left( N_k(\mathbf{r}, t) \int_0^\infty dE' \int_{4\pi} d\mathbf{\Omega}' \sigma_{s,k}(E' \rightarrow E, \mathbf{\Omega}' \rightarrow \mathbf{\Omega}) \Psi(\mathbf{r}, E', \mathbf{\Omega}', t) \right) \\
 & + \frac{1}{4\pi} \sum_k \left( N_k(\mathbf{r}, t) \int_0^\infty dE' \nu_{p,k}(E') \sigma_{f,k}(E') \chi_{p,k}(E' \rightarrow E) \Phi(\mathbf{r}, E', t) \right) \\
 & + \frac{1}{4\pi} \sum_k (\nu_{p,fs,k} \lambda_{fs,k} N_k(\mathbf{r}, t) \chi_{p,fs,k}(E)) \\
 & + \frac{1}{4\pi} \sum_i (\lambda_{d,i} c_i(\mathbf{r}, t) \chi_{d,i}(E)) \\
 & + S_{ext}(\mathbf{r}, E, \mathbf{\Omega}, t).
 \end{aligned} \tag{3.1}$$

The transport equation terms are defined as follows:

- the term on the left represents the neutron evolution rate in the system at a given position in the phase space;
- the first term on the right describes the transport of neutrons into or out of the phase space volume of interest ( $\nabla \Psi = \sum_{i=1}^{dim} \frac{\delta \Psi_i}{\delta x_i}$ );

- the second term on the right accounts for all neutrons that disappear from that phase space by scattering or absorption reactions;
- the third term on the right accounts for all neutrons that collide in an other phase space and appear to that phase space through scattering;
- the fourth and the fifth terms on the right represent the production of prompt neutrons due to induced fission, the fourth term, or spontaneous fission, the fifth term (the prompt neutron emission takes from  $10^{-18}$ s to  $10^{-14}$ s.);
- the sixth term on the right represents the production of neutrons in this phase space due to delayed neutron precursors (i.e. unstable nuclei which undergo neutron decay (from  $10^{-2}$ s to 1 min));
- the last term on the right represents a generic source term of neutrons.  $S_{ext}$  is  $\neq 0$  when  $t = 0$  but  $= 0$  in other cases.

The possible dependence of certain terms with respect to the temperature is intentionally omitted for clarity and will be specified later.

### 3.2.5 Isotopic and precursor evolutions

The neutron transport equation is coupled to the isotopic evolution equation, the Bateman equation, which model the isotopic evolution inside the core. However, we usually solve these equation separately according to the fact we assume that, between two functioning states split-up by a specific time step, we can neglect the isotopic evolution. According to the celerity of the event, two ways of calculation can be used:

- The first equation is the Kinetic Precursor Evolution equation (used in case of quick neutronic reaction, usually for transient situations (it means  $t < 1$  day)) [39]. This equation consists in distinguishing the delayed neutron emission over the total amount of neutrons that are participating in the nuclear reaction. Indeed, a fission event produces some fission products and the prompt neutrons necessary to maintain the reaction. However, some specific fission products may release energy by producing delayed neutrons. Such nucleus are called precursors. The delayed neutrons have a crucial function on the evolution of the reactivity and moreover on its control according to their generation time that is much more important than the generation time of prompt neutrons: delayed neutron generation time is from  $10^{-2}$ s to 1 min compared to the prompt neutron generation which is at least  $10^{-14}$ s. The delayed neutron source is defined using the precursor concentration. These precursors are specific nuclei  $k$  that have the property to decay by the  $(\beta^-, n)$  way of desintegration. A nucleus family precursor  $c_i^{(k)}$  is identified by a family group of constants  $(\lambda_i, \beta_i)$  that are the different times of life  $\lambda_i$  and the ratio of delayed neutron  $\beta_i$  that appear from their fission.

Theoretically, we have almost 200 precursor families with their respective  $\lambda_i$  and  $\beta_i$  but we generally take into account only 6 to 8 families. The reason of this choice is due to the fact that the characteristic time of desintegration of these 6-8 families is contained in the following range of time:  $[50\mu s; 50s]$ . This characteristic time is long enough to be distinct from the prompt desintegration and sufficiently quick to be taken into account in the kinetic equation and not directly in the BATEMAN equation; that assessment explains our choice to consider only 6-8 families from 200.

$$\begin{aligned} \frac{dc_i^{(k)}(\mathbf{r}, t)}{dt} = & -\lambda_i^{(k)} c_i^{(k)}(\mathbf{r}, t) \\ & + N_k(\mathbf{r}, t) \beta_i^{(k)} \int_0^\infty (dE' \nu_{t,k}(E') \sigma_{f,k}(E') \Phi(\mathbf{r}, E', t)) \end{aligned} \quad (3.2)$$

We have 1 equation (3.2) per each  $c_i$  of the equation (3.1). The term on the left represents the time rate of precursor concentration evolution in the system. The first term on the right describes the natural desintegration of a precursor  $c_i^{(k)}$  according to its life time  $\lambda_i$  and the second term on the right accounts for all precursors that appear from nuclear fission reaction. One example is the scheme of desintegration of the  $Br^{87}$  precursor presented in figure (3.1).

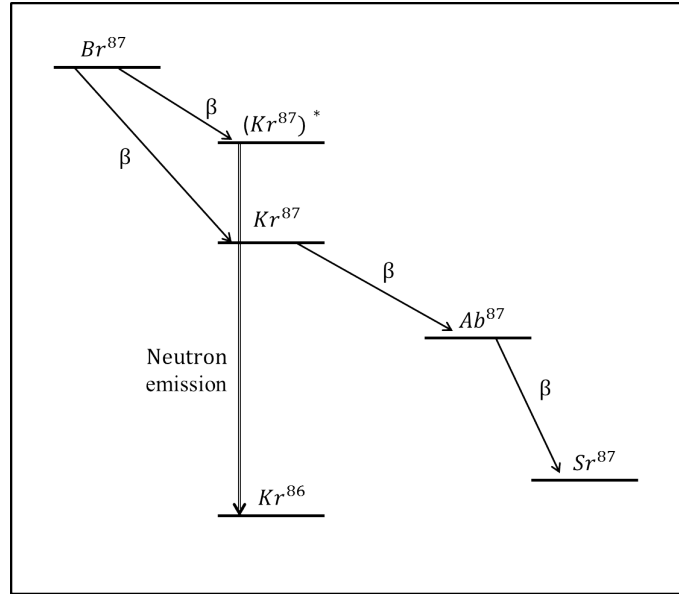


**Figure 3.1.** Precursor desintegration

This figure (3.1) show two different natural ways of desintegration that the  $Br^{87}$  precursor might follow. On one path we only produce beta desintegration up to the creation of the  $Sr^{87}$ . On the other path, after a beta desintegration that creates the  $Kr^{87}$ , which decays to  $Kr^{86}$  plus 1 neutron. An other example of delayed neutron is



the neutron production from Uranium 235 precursor (tabulated in JEFF-2) is defined below:

Group of precursors (i)	life time $\lambda_i$ (s)	$\frac{\beta_i}{\beta}$	$E_i$ (MeV)
1	54.51	0.0038	0.25
2	21.84	0.213	0.46
3	6.00	0.188	0.405
4	2.23	0.407	0.450
5	0.496	0.128	
6	0.179	0.026	
		$\beta = 0.0068$	

**Table 3.4.** Uranium 235 precursor (tabulated in JEFF-2)

This tab ( 3.4) describes 6 couples  $(\lambda_i, \beta_i)$  of the Uranium 235 precursor family with their respective Energy released from their fission.

- The second equation is the Generalized BATEMAN equation (Nuclide Depletion equation that is used in case of a long time step operation (it means  $t > 1$  day), knowing that at this characteristical time step the isotopic evolution is considered quasistatic) [205] [18] .

The Bateman equation is a mathematical model describing abundances and activities in a decay chain as a function of time, based on the decay rates and initial abundances. In this equation the precursors of the previous equation are assumed to be in equilibrium and defined as their nucleus type  $N_k$ .

$$\begin{aligned}
 \frac{dN_k(\mathbf{r}, t)}{dt} = & \sum_{m \neq k} \left( \sum_q \int_0^\infty (\sigma_{q, k \leftarrow m}(E) \Phi(\mathbf{r}, E, t) dE) \right) N_m(\mathbf{r}, t) \\
 & + \sum_{m \neq k} (\lambda_{k \leftarrow m} N_m(\mathbf{r}, t)) \\
 & - \lambda_k N_k(\mathbf{r}, t) \\
 & - \left( \sum_q \int_0^\infty \sigma_{q, k}(E) \Phi(\mathbf{r}, E, t) dE \right) N_k(\mathbf{r}, t)
 \end{aligned} \tag{3.3}$$

The first term of the second part of this equation corresponds to the production of nucleus k by nuclear reactions, where  $\sigma_{q, k \leftarrow m}$  is microscopic nucleus Cross section at the Energy E leading to the production of a nucleus k from a nucleus m and the nuclear reaction q. The second term corresponds to the production by nuclear desintegrations where  $\lambda_{k \leftarrow m}$  is the desintegration rate of a nucleus m to the nucleus

k. The third term corresponds to the desintegration of nucleus k and the last term corresponds to the decrease of nucleus k by nuclear reactions.

### 3.2.6 Physical closure equations

[214] [35]

In these part, critical functions are the cross sections  $\Sigma_{q,k}$ , the maxwell spectrum of the delayed and prompt neutron, and the number of neutron produced by fission  $\nu_{t,k}$ .

- **Cross sections** [35] [55] [39]

Interactions between neutrons and nucleus of the medium are defined by functions  $\sigma_k(E)$  called microscopic cross sections of the nucleus k. The cross section  $\sigma_{f,k}(E)$  takes care about the fission interaction,  $\sigma_{a,k}$  takes care of the absorption interaction and the  $\sigma_{s,k}(E' \rightarrow E, \Omega' \rightarrow \Omega)$  takes care of the scattering interaction of a neutron at the kinetic energy  $E'$  and the incident direction  $\Omega'$  which takes the energy  $E$  and the direction  $\Omega$  by inelastic collision at the point  $\mathbf{r}$ . These functions are assumed to be given [23], positive and bounded.

The macroscopic cross section  $\Sigma_{q,k}$  is a function of the quantity of a specific isotope  $N_k(\mathbf{r}, t)$ , which is time and space dependent (the quantities of each specific isotope  $N_k(\mathbf{r}, t)$  is obtained according to the BATEMAN equation and also according to the thermohydraulical computation with for example the density of the moderator  $D_m$ , the boron concentration  $C_b$ , or, the control rod concentration and composition, according to the control rod management), and the microscopic cross section  $\sigma_{q,k}$  defined as a physical description of a single isotope. The cross section function is expressed above corresponding to its reaction q.

$$\Sigma_{q,k} = N_k(\mathbf{r}, t) \sigma_{q,k} .$$

We can distinguish the macro and micro cross sections in two groups of nuclear reaction, i.e., we have the absorption and fission cross sections that are only dependant of the Energy of the incident neutron and we have the scattering cross sections that are related to their change of energy from  $E$  to  $E'$  as well as for their angular directive vector from  $\Omega'$  to  $\Omega$ . Hence we have two expressions of the macroscopic cross sections:

- absorption (q=a) and fission (q=f) cross section:

$$\Sigma_{q,k}(E) = N_k(\mathbf{r}, t) \sigma_{q,k}(E) .$$

– scattering ( $q=s$ ) cross section:

$$\Sigma_{s,k}(E' \rightarrow E, \boldsymbol{\Omega}' \rightarrow \boldsymbol{\Omega}) = N_k(\mathbf{r}, t) \sigma_{q,k}(E' \rightarrow E, \boldsymbol{\Omega}' \rightarrow \boldsymbol{\Omega}) .$$

Several types of formalism can be used in order to calculate the cross section. For example, the Briet-Wigner expression or the Riech-Moore expression. The Briet-Wigner expression of the total scattering cross sections ( $\sigma_s$ ) is given below (3.4):

$$\sigma_{s,k}(E) = \frac{\pi}{k^2} g_j \frac{\Gamma_s^2}{(E - E_o)^2 + \frac{\Gamma^2}{4}} + \frac{4\pi R}{k} g_j \frac{\Gamma_s(E - E_o)}{(E - E_o)^2 + \frac{\Gamma^2}{4}} + 4\pi R^2 . \quad (3.4)$$

This equation computes all the scattering reactions that may occur for the nucleus. Below we detail the symbols and variables used:

- $R$  - is the nucleus core diameter
- $k = \frac{2\pi}{\lambda}$  where  $\lambda$  is the de Broglie wavelength in relation to relative motion.
- $\Gamma_q$  - corresponding to the absorption ( $q = \gamma$ ), scattering ( $q = s$ ) and totale linewidths ( $\Gamma = \Gamma_s + \Gamma_\gamma$ ), obtained by experiments.
- $E$  - relative Energy of the system.
- $E_o$  - value of  $E$  at the resonance peak.
- $g_j$  - spin statistical factor ( $g_j = \frac{2J+1}{2(2I+1)}$ ) where  $J$  and  $I$  are respectively the spin of the composed nucleus and of the target nucleus.

This expression of the total scattering cross sections corresponds to the integral of all the differential scattering cross sections  $\sigma_{s,k}(E \rightarrow E')$ , thus:

$$\sigma_{s,k}(E) = \int_0^\infty dE' \sigma_{s,k}(E \rightarrow E').$$

The differential scattering cross sections are fundamental in Nuclear reactor analysis since they determine accurately the manner in which neutrons move about in a reactor core, as well as the rate at which they leak out of the reator. These scattering cross sections can be recalculated by multiplying the total scattering cross section by a shape factor according to each scattering energy  $E'$ . The shape factors are obtained through experiments or simply calculated as it is detailed in the paper [65]:

$$\sigma_{s,k}(E \rightarrow E') = \sigma_{s,k}(E) P(E \rightarrow E') \quad (3.5)$$

where  $P(E \rightarrow E') dE$  is the experimental probability that a neutron scattering with initial energy  $E$  will emerge with a new energy  $E'$  in the interval  $E'$  to  $E'+dE'$ .

In addition, after an elastic or inelastic collision beetwen a neutron and a nuclei we have an angular distribution of the scaterred neutrons. This distribution is given

by experimental data and cross sections are computed using a Legendre Polynomial method in order to lead to the common cross section expression [39]:

$$\sigma_{s,k}(E' \rightarrow E, \Omega' \rightarrow \Omega) = \sigma_{s,k}(E' \rightarrow E, \mu)$$

by replacing  $\Omega' \rightarrow \Omega = \mu$ , and so:

$$\sigma_{s,k}(E' \rightarrow E, \mu) = \sum_{n=0}^{\infty} (2n+1) \sigma_{sn,k}(E' \rightarrow E) P_n(\mu).$$

Futhermore, the cross section models are based on nuclear reaction models that are not sufficiently precise yet. Consequently, cross sections obtained using mathematical calculations are modified according to data from experimental measurements (figure 3.2).

Finally, the absorption ( $q=\gamma$ ) and fission ( $q=f$ ) cross sections are given by the following formula (3.6):

$$\sigma_{q,k}(E) = \frac{\pi}{k^2} g_j \frac{\Gamma_s \Gamma_q}{\Gamma_s (E - E_o)^2 + \frac{\Gamma^2}{4}}. \quad (3.6)$$

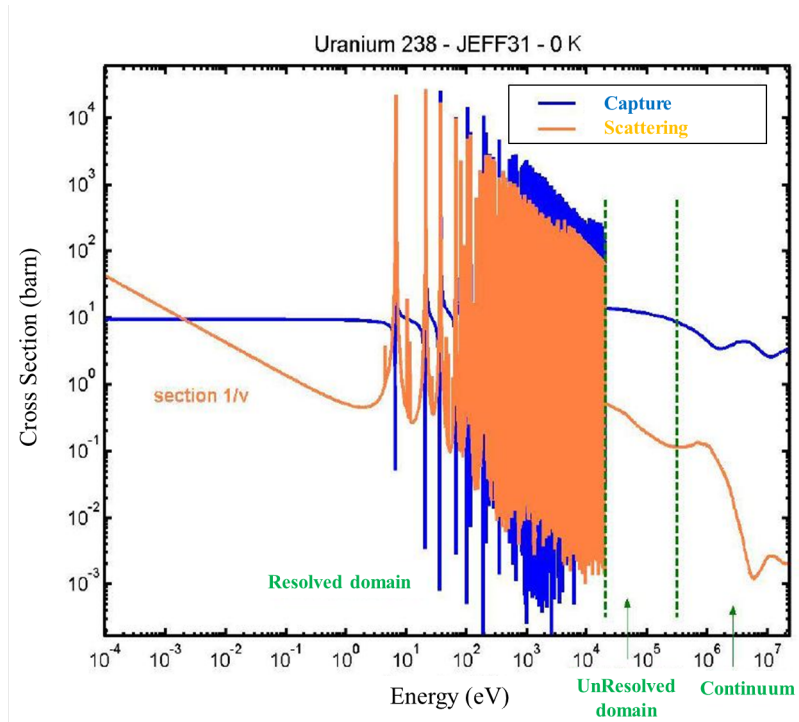


**Figure 3.2.** Uranium cross sections

- **Doppler effect** [103] [174] [39]

Thanks to the above different formalisms, we are able to obtain the analytic expression of the cross section at 0 K temperature. In order to take into account the thermal motion, we assume that the nucleus has a free gas spectrum inside an isotropic medium at  $T$ , the absolute temperature. This spectrum is described by the following Maxwell-Boltzmann celerity formula:

$$P(\mathbf{V}, T)d\mathbf{V} = \left(\frac{\alpha}{\pi}\right)^{3/2} \exp(-\alpha V^2)d\mathbf{V} \quad (3.7)$$

where  $\alpha = M/(2kT)$ ,  $k$  is the boltzmann constant,  $M$  the mass of the nucleus and  $\mathbf{V}$  the celerity vector of the nucleus with its modulus  $V$ . The cross section at temperature  $T$ ,  $\sigma(\mathbf{v}, T)$ , is defined as the cross section that conserves, for an unmoving nucleus, the reaction rate obtained with the experimental data cross section. The reaction rate is proportional to the celerity multiplied by the cross section, hence:

$$\mathbf{v}\sigma(\mathbf{v}, T) = \int |\mathbf{v} - \mathbf{V}| \sigma(|\mathbf{v} - \mathbf{V}|) P(\mathbf{V}, T) d\mathbf{V} \quad (3.8)$$

where  $\mathbf{v}$  is the incident neutron celerity. By integrating this expression and by expressing velocity from energy  $v = \sqrt{\frac{2E}{m_n}}$  we obtain [174]:

$$\sigma(E, T) = \int_0^\infty \sigma(E') S(E, E', T) dE' \quad (3.9)$$

with

$$S(E, E', T) = \left[ \frac{1}{\Delta(E)\sqrt{\pi}} \sqrt{\frac{E'}{E}} \cdot e^{(-\frac{A}{kT}(\sqrt{E}-\sqrt{E'})^2)} \cdot e^{(-\alpha V^2)} - \frac{1}{\Delta(E)\sqrt{\pi}} \sqrt{\frac{E'}{E}} \cdot e^{(-\frac{A}{kT}(\sqrt{E}+\sqrt{E'})^2)} \cdot e^{(-\alpha V^2)} \right] \quad (3.10)$$

where  $\Delta(E) = 2 \sqrt{\frac{EkT}{A}}$  is the doppler length,  $E' = \frac{A+1}{A} E_{MC}$  is the energy in the laboratory frame of reference with  $A=M/m_n$  the mass rate between the atom mass and the mass of the neutron that collides with the atom and  $E_{MC}$  is the energy in the mass center system. Above  $S(E, E', T)$  represents the doppler nucleus. The main contribution of  $S(E, E', T)$  comes from the energy  $E'$  around the resonance peak.

The Doppler broadening induces the modification of the shape of the cross section curve:

- it decrease the amplitude of the peak but in return it increases its width,
- the area under the curve is independant of the Temperature.

Hence, when the Temperature increases the Doppler length increase and the neutron capture too. That leads to a negative feedback effect called Doppler effect.

• **Maxwell spectrum** [149]

The density function of delayed and prompt neutron (figure 3.3), is a function of temperature as given by a Maxwell Boltzmann distribution with  $T$  the temperature of the neutron. According to the assembly and core geometry of PWRs, the moderator is the medium where the neutron is thermalized and defines the temperature of the neutron. This way, we are using the notation  $T_m$  for the temperature of the neutron in order to highlight the dependance of the temperature of the neutron to the temperature of the moderator.

$$\chi_{k'}(E_{k'}) dE = \frac{2\sqrt{E_{k'}/kT_m}}{\sqrt{\pi}} \exp\left(-\frac{E_{k'}}{kT_m}\right) \frac{dE}{kT_m} \quad (3.11)$$

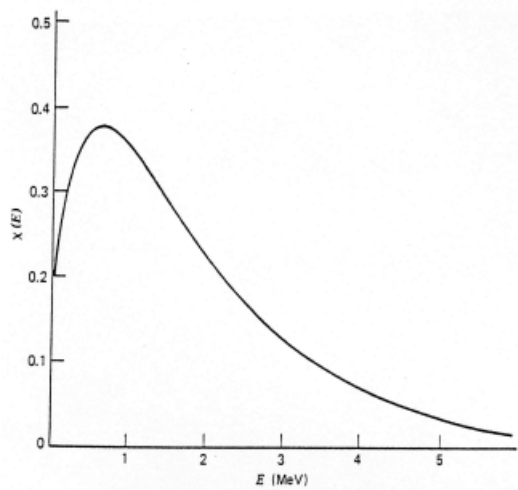


**Figure 3.3.** Density of neutron distribution as a function of the Energy

- **Average number of neutrons produced per fission** [22]

The number of neutrons produced per U5 fission varies linearly according to the energy of the incident neutron.

$$\nu(E) = \begin{cases} 2.432 + 0.066E & \text{if } E < 1 \text{ Mev} \\ 2.349 + 0.15E & \text{if } E > 1 \text{ Mev} \end{cases}$$

### 3.2.7 Boundary conditions

[214] [35]

Neutronics calculation can be completed at different scales. We define an input geometry (at the scale of the assembly or the scale of the whole core) and we need to solve the boltzmann equation. This calculation requires boundaries conditions that we can formulate following different way. Let us assume a domain  $V \in \mathbb{R}^3$  and its local boundary  $dV$ . For each  $\mathbf{r}_e \in dV$  we consider  $\mathbf{n}_{ext}$  the output vector perpendicular to  $dV$ . The calculation of the neutronic equation requires an input boundary flux  $\Psi(\mathbf{r}_e, E, \boldsymbol{\Omega})$ . Several possibly are given below in order to specify this input boundary flux:

- Specular albedo condition  $\beta$

Considering  $\boldsymbol{\Omega}$  the direction of an outgoing particule. The general input condition can be:

$$\Psi(\mathbf{r}_e, E, \boldsymbol{\Omega}) = \beta \Psi(\mathbf{r}_e, E, \boldsymbol{\Omega}')$$

with:

- $\beta = 0$ , for the Void condition (useful for core computation). In other words,  $\Psi(\mathbf{r}_e, E, \boldsymbol{\Omega}) = 0$  over  $\Gamma = \{(\mathbf{x}, \mathbf{v}) \in \delta\chi \times V \mid \mathbf{v} \cdot \mathbf{n}(\mathbf{x}) < 0\}$ , where  $\chi$  is the planar section of the core and  $V$  the velocity space.

We assume here that no neutron are injected into the domain.

- $\beta = 1$ , for the Mirror condition. (useful for a grid with symmetrical aspect  $\rightarrow$  fuel pin grid / assembly grid).  

$$\Psi(\mathbf{r}_e, E, \boldsymbol{\Omega}) = \Psi(\mathbf{r}_e, E, \boldsymbol{\Omega}')$$

We assume here that all the outgoing neutrons are reflected into the domain with the symmetric direction  $\boldsymbol{\Omega}'$ .

- $\beta \neq 1$  and  $\beta \neq 0$ , for the diffusion condition.  

$$\Psi(\mathbf{r}_e, E, \boldsymbol{\Omega}) = \Psi(\mathbf{r}_e, E, \boldsymbol{\Omega}'')$$

We assume here that all the outgoing neutrons are reflected into the domain with a random angle  $\Omega''$ .

- Periodical Condition

In the case of a periodical grid (fuel pin grid or assembly grid) we can assume that the flux is also periodical. Hence we can write:

$$\Psi(\mathbf{r}_e, E, \Omega) = \Psi(\mathbf{r}_e + \delta\mathbf{r}, E, \Omega)$$

### 3.3 APOLLO3 Numerical Methods - Core Calculation

#### 3.3.1 Code Description - APOLLO3

APOLLO3 ® is a common project of CEA, AREVA and EDF for the development of new generation code system for nuclear core physics analysis providing improved accuracy, flexible software architecture and high computation performances and taking into account both R&D and industrial application requirements.

#### 3.3.2 Symbols and definitions

We first introduce the main notation coming out the problem formulation in tab ( 3.5).

Neutronic APOLLO3 symbols		
$T_{eff}$	effective temperature (average temperature of the fuel pin medium)	K
$T_{mod}$	fluid moderator temperature	K
$D_{mod}$	fluid moderator density	$kg.m^{-3}$
$C_{Boron}$	boron concentration	ppm
$S_b$	control rod state of insertion	$\emptyset$
$Bu$	burn-up	$GW.d.t^{-1}$

**Table 3.5.** Main notation coming out the Neutronic problem formulation



### 3.3.3 Code description - Variables

The Input distributed variables (function of  $r$  and  $t$ ) are:

- $T_{eff}$ , the effective temperature,
- $T_{moderator}$ , the fluid moderator temperature,
- $D_{moderator}$ , the moderator density,
- $C_b$ . the Boron concentration (assumed constant in our study),

The Output variables (functions of  $r$  and  $t$ ) are:

- $P_V^{local}$ , the local volumic power,
- $\Phi^p$ . the fast neutron flux,

Three types of grids will be used (figure 3.4):

- spatial discretization A : 1 element per 1/4 assembly at farfield (MINOS),
- spatial discretization B : 1 element per fuel cell on nearfield (MINOS),
- spatial discretization C : 1 unstructured element per fuel cell with 1 medium for the fuel pin and 1 medium for the fluid (MINARET).

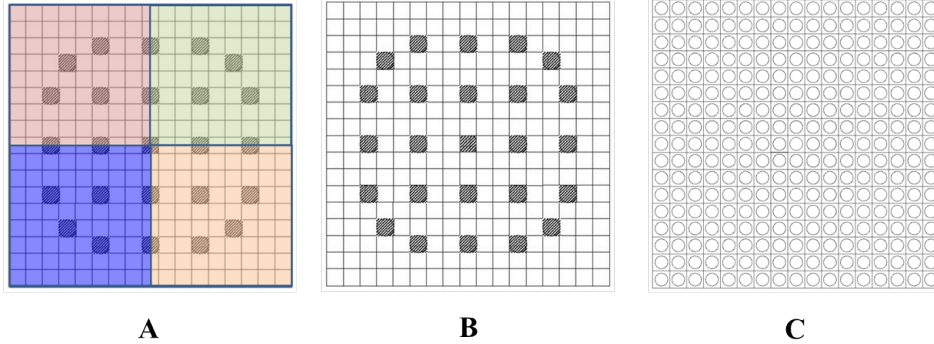


**Figure 3.4.** Space discretization (from the left to the right): A - Assembly composed by 2x2 homogeneous elements, B - Assembly composed by 17x17 homogeneous elements and C - Assembly composed by 17x17 unstructured and heterogeneous elements

### 3.3.4 Multigroup theory

Naturally, some approximations and a calculation scheme are required in order to simplify our problem. So it had been decided to split the deterministic calculation of the nuclear reaction into two different steps. The first step is dedicated to a very precise calculation of representative assemblies isolated and computed with reflection boundary conditions. These calculations provide the physical quantities of the different representative assemblies, namely isotropic distributions and cross sections, required to compute the whole core with real boundary conditions. Thus, for the first step calculation we are using the code APOLLO2 in order to produce the multi-parametred library (MPO). This 3D calculation consists of a detailed calculation of an elementary unit of the nuclear core (assembly) in which most of the heterogeneous aspect of the unit are taken into account. This calculation authorizes the reduction of a number of data by an homogeneization of the detailed data at the scale of the whole assembly or by homogeneization at the scale of all the representative portions of the assembly. This spatial homogeneization is followed by a condensation in energy. The number of energy groups is strongly reduced. The second step is dedicated to the core 2D or 3D calculation, using the quantities calculated during the previous step. In this work, we are using the neutron solvers MINOS and MINARET (and their coupling solver) in order to solve the transport equation. Both steps use the same multigroups theory detailed below. In order to solve the neutron transport equation as well as to compute the cross section in term of neutron energy, we split the neutron energy continuum into a number  $G$  of groups of neutron energy over the interval of variation  $[E_1; E_G]$ . Each group is defined as a range composed by the neutron energy included between two neutron energy boundaries  $E_g$  and  $E_{g+1}$  and  $g \in G$ . Hence, the neutronic transport is replaced by a set of equations according to each group  $g$  of neutron energy [57]. This way, the flux can be rewritten:

$$\Psi^g(\mathbf{r}, \mathbf{\Omega}, t) = \int_{E_g}^{E_{g+1}} dE \Psi^g(\mathbf{r}, \mathbf{\Omega}, E, t) \quad (3.12)$$

and the neutron transport equation (3.1) reduces to :

$$\begin{aligned} \frac{1}{v^g} \frac{\partial \Psi^g(\mathbf{r}, \mathbf{\Omega}, t)}{\partial t} = & -\mathbf{\Omega} \cdot \nabla \Psi^g(\mathbf{r}, \mathbf{\Omega}, t) - \sum_k (N_k(\mathbf{r}, t) \sigma_k^g) \Psi^g(\mathbf{r}, \mathbf{\Omega}, t) \\ & + \sum_{g'} \sum_k \left( N_k(\mathbf{r}, t) \int_{4\pi} d\mathbf{\Omega}' \sigma_{s,k}^{g' \rightarrow g}(\mathbf{\Omega}' \rightarrow \mathbf{\Omega}) \Psi^{g'}(\mathbf{r}, \mathbf{\Omega}', t) \right) \\ & + \frac{1}{4\pi} \sum_{g'} \sum_k \left( N_k(\mathbf{r}, t) \nu_{p,k}^{g'} \sigma_{f,k}^{g'} \chi_{p,k}^{g' \rightarrow g} \Phi^{g'}(\mathbf{r}, t) \right) \\ & + \frac{1}{4\pi} \sum_k \left( \nu_{p,fs,k} \lambda_{fs,k} N_k(\mathbf{r}, t) \chi_{p,fs,k}^g \right) + \frac{1}{4\pi} \sum_i \left( \lambda_{d,i} c_i(\mathbf{r}, t) \chi_{d,i}^g \right) + S_{ext}^g(\mathbf{r}, \mathbf{\Omega}, t) \end{aligned} \quad (3.13)$$

which we write in a more compact form as:

$$\begin{aligned} \frac{1}{V^g} \frac{\partial \Psi^g(\mathbf{r}, \boldsymbol{\Omega}, t)}{\partial t} = & -\boldsymbol{\nabla} \cdot (\boldsymbol{\Omega} \Psi^g(\mathbf{r}, \boldsymbol{\Omega}, t)) - \Sigma_t^g(\mathbf{r}, t) \Psi^g(\mathbf{r}, \boldsymbol{\Omega}, t) \\ & + \sum_{g'=1}^G \left( \int_S d\boldsymbol{\Omega}' \Sigma_s^{g' \rightarrow g}(\mathbf{r}, \boldsymbol{\Omega}' \rightarrow \boldsymbol{\Omega}, t) \Psi^{g'}(\mathbf{r}, \boldsymbol{\Omega}', t) \right) + S^g(\mathbf{r}, \boldsymbol{\Omega}, t) . \end{aligned} \quad (3.14)$$

In addition, cross section (section 3.3.5) and the other data depending on the energy  $E$  are also replaced by average cross section over considered group  $g$ . These cross sections are called "multigroup cross sections". The computation of these cross sections is a fundamental point of the reactor calculation and they are detailed in the following section (3.3.5).

### 3.3.5 Microscopic Cross Sections

[35] [174] [128] [39]

Nuclear data characterize fundamental nuclear interactions, in our case, interactions between neutrons and nuclei that compose our system. These nuclear data are mostly cross section but also rates (reproduction rate, probability to get fragments, etc.) and radioactive decay data.

In order to be useful to the codes (transport and isotopic evolution codes), the nuclear data needs to undergo processing according to physical, numerical and also computer science requirements. This is the purpose of the American code NJOY or the french CAL-ENDF. After that, we are using the shelf-shielding processing in order to generate the whole constant parameters (multigroup library) used by the deterministic solver of the transport equation APOLLO2. At last we count on the production of a library cross sections that would be homogeneized in space and condensed in terms of energy (less energy groups).

All the basic nuclear data are defined with an international norm ENDF (Evaluated Nuclear Data Format) [104]. They are calculated thanks to experimental measures and evaluations. This data corresponds to the interaction between a neutron and a nuclei at the energy  $E$  of the incident particle and the temperature  $T$  of the target element. All the data  $D$  are defined by a set of values  $(x_i, D(x_i))$ , where  $x_i$  is the variable that the Data depends on and  $D(x_i)$  its values. Hence, each element (MAT) is associated to general informations (MF=1), resonance parameters (MF=2), values of ponctual cross sections (detailed for each kind of reaction at  $T=0^\circ \text{C}$ ) (MF=3), angular distributions (MF=4), energy (MF=5) and angular distribution and energy combined together (MF=6) of all the emitted particles as well as thermalization parameters (MF=7). These data are given for almost 400 nucleus with an energy domain from  $10^{-5} \text{eV}$  to  $20 \text{MeV}$ .

In a second phase, we take into account the thermal motion, we assume that the nucleus

has a free gas spectrum inside an isotropic medium at the absolute temperature  $T$  as it had been described in the <doppler section of the part( 3.2.6). We conserve the reaction rate whilst we modify the cross section according to the temperature of the system and so we take into account the doppler broadening yielding the cross sections  $\sigma_{q,k}(E, T)$ .

We then process the cross sections while conserving the reaction rate within the Multigroup method. The domain of energy is split in intervals called groups and the data are defined by an average value  $D^g$  on this interval of energy. For every isotope  $k$ , for every reaction  $x$  (where  $x = a$  or  $f$ ) and for any energy group  $g$  of the energy grid, a multigroup cross section is given by:

$$\sigma_{x,\rho}^g(\mathbf{r}) = \frac{\int_g \sigma_{x,\rho}^g(E') \Phi(\mathbf{r}, E') dE'}{\Phi^g(\mathbf{r})} \quad (3.15)$$

where  $\mathbf{r}$  corresponds to the space variable and  $\Phi^g(\mathbf{r})$  is the multigroup flux. According to this method, the cross sections previously dependant exclusively on the energy become space dependant due to the ponderation flux. That induce a spatial influence of the cross section and hence the influence of the core geometry on the cross sections (we generally over estimate the absorption rate which leads to a wrong estimation of the reaction rate). That is why the cross section requires a self-shielding region processing [150].

The major difficulties of this method are:

- the flux  $\Phi(\mathbf{r}, E')$  is unknown (we calculate this flux using the BONDARENKO method) [28];
- the multigroup flux is the solution of the equation where these coefficient will be plugged in.

For tractability reasons, we would like to process the cross sections before hand. Hence, we replace the flux by a function  $w(r, E)$ , that is representative of the neutron spectrum inside the core, so we obtain:

$$\sigma_{x,\rho}^g \approx \frac{\int_g \sigma_{x,\rho}^g(E') w(r, E') dE'}{w(\mathbf{r})} . \quad (3.16)$$

This approximation can be accepted in case of unresonant nucleus or in case the cross section is being used far from the resonance domain, otherwise this approximation is unacceptable. That is why we usually process the cross section with a large number of groups or using a table of probabilities.

In the same way, we are able to calculate the scattering cross section:

$$\sigma_{x,\rho}^{g \rightarrow g'}(\mathbf{r}) = \frac{\int_g F_{g \rightarrow g'} \sigma_{x,\rho}^g(E') \Phi(\mathbf{r}, E') dE'}{\int_{g'} \Phi(\mathbf{r}, E') dE'} \quad (3.17)$$

where  $F_{g \rightarrow g'}$  is called a "feed function", which describes the probability and features of the different types of collision that may occur.

Hence we finally obtain the multigroup microscopic cross sections:

$$\sigma_{x,\rho}^g(r, T) \text{ and } \sigma_{s,\rho}^{g \rightarrow g'}(r, T), \text{ where } x = a \text{ or } f.$$

After an elastic or inelastic collision between a neutron and a nuclei we have an angular distribution of the scattered neutron. This distribution is given by the experimental data and an associated interpolation law (as it has been defined in the ENDF).

The scattering cross section is projected over the Legendre Polynomials which form an orthogonal  $L^2([-1 : 1])$  Hilbert basis. So we have:

$$\sigma^{scattering}(\mathbf{r}, \boldsymbol{\Omega}' \cdot \boldsymbol{\Omega}) = \sum_{l=0}^{\infty} (2l+1) \sigma_l^{scattering}(\mathbf{r}) P_l(\boldsymbol{\Omega}' \cdot \boldsymbol{\Omega}) \quad (3.18)$$

Where,

$$\sigma_l^{scattering}(\mathbf{r}) = 2\pi \int_{-1}^1 \sigma^{scattering}(\mathbf{r}, \mu) P_l(\mu) d\mu \quad (3.19)$$

Hence we obtain the scattering cross section:  $\sigma_{s,\rho}^{g \rightarrow g'}(r, T, \Omega \rightarrow \Omega)$ .

### 3.3.6 Macroscopic cross sections

[188] [151] They are precomputed in a multiparameter library named SAPHYB by solving equations (3.1) and (3.3) in specific scenarii. The generation of the multiparameter library by APOLLO2 is realized for 300 to 400 nucleus, with the temperature ranging from 300 to 2000 kelvins, angular discretization about 100-1000 directions and energy splitting about 300-12000 groups at the very least. The calculations are done in nominal conditions and performed under various conditions (temperatures, fuel compositions, control rod configurations, etc.), where each calculation provides a set of homogenized quantities that are stored in the library [276]. The conditions come from experimental data and arbitrarily define a specific scenario for this specific reactor operation and geometry (core geometry and fuel cycle process, that define the time step of the calculation, and disposition inside the core, etc., as in figure 3.5). Scenario are built according to industrial measurements during the reactor core operation. Other calculations are carried out for a few values changes around the initial conditions values (temperatures, Boron concentration and the control rod configuration) that lead to a NxN table of macroscopic cross section values  $\Sigma_{g,k}$ . This table contains all the possible combinations of the value of a cross section for a set of parameters: temperatures, fuel concentrations, boron concentration,

control rod configuration. The standard number of isotopes is about 127 fission products and 30 fissile nuclei in the isotopic evolution chains but this can be changed from the start).

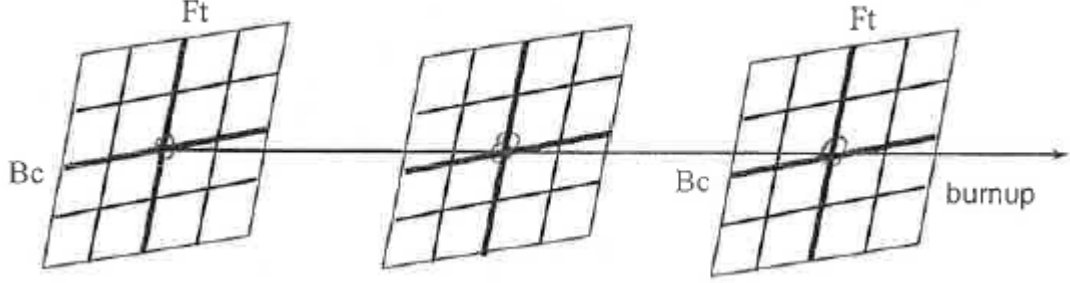


**Figure 3.5.** Multiparametred library calculation principle [188]

From this detailed calculation, the homogenization is done through a user defined output geometry, which may consist of several homogenization zones and, generally, a collapsed multigroup energy mesh.

The cross sections from the detailed neutron transport calculation are spatially homogenized (at the scale of the fuel cell or the assembly) and condensed in terms of energy on a macrogroups energy grid. This phase is realised thanks to a flux-volume ponderation [151]:

$$\Sigma_{x,I}^G = \frac{\sum_{i \in I, g \in G} \Sigma_{x,i}^g(E') \Phi_i^g V_i}{V_I \Phi_I^G} \quad (3.20)$$

with

$$\Phi_I^G = \frac{\sum_{i \in I, g \in G} \Phi_i^g V_i}{V_I} \quad (3.21)$$

and

$$V_I = \sum_{i \in I} V_i \quad (3.22)$$

here  $x = a$  or  $f$ , denotes the reaction type,  $I$  is the spatial macro domain which contains the sub-domains  $i$  and volumes  $V_i$  (mesh), and  $G$  is the macro group of the energy condensation which contains the energy groups  $g$  from the detailed energy grid.

This kind of ponderation conserves the reaction rate from the reference calculation because:

$$\Sigma_{x,I}^G(E') \Phi_I^G V_I = \sum_{i \in I, g \in G} \Sigma_{x,i}^g(E') \Phi_i^g V_i \quad (3.23)$$

Finally, the isotopic cross sections can be restricted to the users defined list of isotopes

which is a subset of the isotopes involved in the calculation. The specified nuclei are calculated separately but the others are calculated as a representative moderator nucleus. So, in this case, one fictive or residual isotope may exist and represents the rest of the composition (the unspecified nuclei  $x$  of the medium). This operation can also be used in order to create a very representative nucleus of all the nucleus of the core in a specific medium  $m$  and in the energy interval  $g$ .

$$\Sigma_m^g = \sum_{x \in m} N_{xm} \sigma_x^g \quad (3.24)$$

and

$$\Sigma_m^{g \rightarrow g'} = \sum_{x \in m} N_{xm} \sigma_x^{g \rightarrow g'} . \quad (3.25)$$

From a numerical point of view, the macroscopic cross section  $\Sigma_{q,k}$  is an input parameter defined within a multiparametred library, SAPHYB, which is parametrized thanks to specific physical variables directly used in the numerical algorithm [275]:  $Bu$ ,  $T_{eff}$ ,  $T_{mod}$ ,  $D_{mod}$ ,  $C_{boron}$  and  $S_b$ . In other words, we have:

$$\Sigma_{q,k}^g (Bu, T_{eff}, T_{mod}, D_{mod}, C_{boron}, S_b) \quad (3.26)$$

and

$$\Sigma_{q,k}^{g \rightarrow g'} (Bu, T_{eff}, T_{mod}, D_{mod}, C_{boron}, S_b) \quad (3.27)$$

We can use both the macroscopic cross sections (3.14) or the microscopic cross sections (3.13) for the core calculation, with their own strengths and weaknesses. The macroscopic cross sections are well defined (large energy groups which have been condensed conserving the reaction rate which links the isotopes between them) and contain all the quantities required for the flux calculation. Nevertheless, these cross sections are made for a standard scenario in nominal condition. A more precise calculation should use cross section that should be recalculated after each flux calculation in order to take into account exactly the core state and the unknown evolution of the parameters. Otherwise we can use only the microscopic cross sections and recalculate the  $N_i$  with the Bateman equation. It would mean for the equation to be solved through a rough flux with very few energy groups (2-30 groups) compared to the 300-12000 groups of the APOLLO2 calculation. Thus, that is why we mostly use the macroscopic cross sections from the SAPHIB library.

In addition, the effective temperature  $T_{eff}$  represents the temperature of the fuel pin. Its precision is relative to the precision of the model ( section 7.3).

Delayed Neutron parameters can be calculated with the code APOLLO2. It can pick

up the value from the ENDF and GENDF files or calculate the values of the parameters ( the life time  $\lambda$  , the neutron fraction  $\beta$  and the time neutron of generation  $\Lambda$ ) thanks to the BEFF modulus. This values should be add to the Saphib in order to be used by the core solver in case of transient scenario.

### 3.3.7 Discretization strategy

A few different models are available within APOLLO3 and well described in [101]. The first discretization consists of splitting the Energy continuum on significant intervals of energy according to the multigroup theory. The second approximation consists of discretization in terms of neutron position or angle. The angular integration is a delicate issue which leads to several solutions depending on the approximation used in the numerical method. There are three basic choices we detail in the following sections:

- Spherical harmonics method (Pn): this method results from the real spherical harmonic development of the angular flux distribution.
- Simplified spherical harmonics method (SPn): this method is used as an alternative to the diffusion theory in order to solve the Boltzmann equation in the core. The SPN solution gives a substantial improvement with respect to the diffusion solution and takes into account a large part of the transport effects.
- Discrete ordinates method (Sn): this method results from the angular discretization of the differential form of the transport equation.

Some other different models are also available within APOLLO3: the Diffusion method, the collision probability method (Pij), the Interface Current method (IC) or the method of characteristics. These solvers are well-detailed in the paper [101]

During this study, we are going to describe a post-treated multi solver/multiscale approach using the SPn (MINOS) and the Sn (MINARET) methods. Considering the physical specification of our transient scenario and our proof of concept context, we legitimately decide to work on SPn and Sn solver (avoiding diffusion approximations but paving the way for more accurate simulations).



### SPn discretization method - the static case

Regarding the MINOS [20] solver, we focus, among others methods, on the SPN equations for Cartesian geometries.

The boltzmann transport equation (3.1), under its multigroup form, writes:

$$\begin{aligned} \frac{1}{V^g} \frac{\partial \Psi^g(\mathbf{r}, \mathbf{\Omega}, t)}{\partial t} = & -\nabla \cdot (\mathbf{\Omega} \Psi^g(\mathbf{r}, \mathbf{\Omega}, t)) - \Sigma_t^g(\mathbf{r}, t) \Psi^g(\mathbf{r}, \mathbf{\Omega}, t) \\ & + \sum_{g'=1}^G \left( \int_S d\mathbf{\Omega}' \Sigma_s^{g' \rightarrow g}(\mathbf{r}, \mathbf{\Omega}' \rightarrow \mathbf{\Omega}, t) \Psi^{g'}(\mathbf{r}, \mathbf{\Omega}', t) \right) + S^g(\mathbf{r}, \mathbf{\Omega}, t) \end{aligned} \quad (3.28)$$

In particular, the neutron steady-state of a nuclear system can be modeled by the multi-group time independent Boltzmann transport. For each energy group  $g=1, \dots, G$ , we have:

$$\nabla \cdot (\mathbf{\Omega} \Psi^g(\mathbf{r}, \mathbf{\Omega})) + \Sigma_t^g(\mathbf{r}) \Psi^g(\mathbf{r}, \mathbf{\Omega}) = \sum_{g'=1}^G \left( \int_S d\mathbf{\Omega}' \Sigma_s^{g' \rightarrow g}(\mathbf{r}, \mathbf{\Omega}' \rightarrow \mathbf{\Omega}) \Psi^{g'}(\mathbf{r}, \mathbf{\Omega}') \right) + S^g(\mathbf{r}, \mathbf{\Omega}) \quad (3.29)$$

where  $\Psi^g(\mathbf{r}, \mathbf{\Omega})$  is the angular flux according to its energy interval  $g$ . The vector  $\mathbf{r}$  represents the spatial variable of the domain  $R$  ( $\mathbf{r} \in R \subset \mathbf{R}^3$ ). The unit vector  $\mathbf{\Omega}$  represents the traveling direction of a neutron. The direction  $\mathbf{\Omega}$  is expressed in terms of  $(\theta, \varphi)$  in spherical coordinates, with  $\theta$  the colatitude and  $\varphi$  the azimuthal angle. We define  $\mu = \cos(\theta)$ ,  $S$  represents the unit sphere and  $\int_s(\dots)d\mathbf{\Omega}$  defines the normalized integral  $\int_s d\mathbf{\Omega} = 1$  while  $\Sigma_t$  and  $\Sigma_s$  are the macroscopic isotropic total and anisotropic scattering cross-sections. Finally  $S^g(\mathbf{r}, \mathbf{\Omega})$  is a source term which includes the fission source and an external source  $S^{ext}$ .

$$\frac{1}{k_{eff}} S^g(\mathbf{r}, \mathbf{\Omega}) = \frac{1}{k_{eff}} \cdot \chi^g(\mathbf{r}) \cdot \sum_{g'=1}^G \left( \nu \Sigma_f^{g'}(\mathbf{r}) \left( \int_S d\mathbf{\Omega}' \Psi^{g'}(\mathbf{r}, \mathbf{\Omega}') \right) + S_g^{ext}(\mathbf{r}, \mathbf{\Omega}) \right) \quad (3.30)$$

where  $k_{eff}$  is the effective multiplication factor,  $\chi$  designs the fission spectrum,  $\nu$  is the number of neutrons emitted per fission,  $\Sigma$  is the macroscopic fission cross-section.

When the external source  $S_g^{ext}(\mathbf{r}, \mathbf{\Omega})$  in Eq. (3.30) is null, the problem Eq. (3.29) is an eigenvalue problem and  $k_{eff}$  corresponds to the dominant eigenvalue. This problem is solved to help to gauge the criticality of the system.

The static equations can be rewritten:

$$\nabla(\cdot\Omega\Psi^g(\mathbf{r},\Omega,t)) + \Sigma_t^g(\mathbf{r},t)\Psi^g(\mathbf{r},\Omega,t) = \sum_{g'=1}^G \left( \int_S d\Omega' \Sigma_s^{g' \rightarrow g}(\mathbf{r},\Omega' \rightarrow \Omega,t) \Psi^{g'}(\mathbf{r},\Omega',t) \right) + S^g(\mathbf{r},\Omega,t) \quad (3.31)$$

or in a more compact form,

$$F\Psi = K_{eff}M\Psi \quad (3.32)$$

Where

$$F = \chi^g(\mathbf{r}) \cdot \sum_{g'=1}^G \left( \nu \Sigma_f^{g'}(\mathbf{r}) \left( \int_S d\Omega' \Psi^{g'}(\mathbf{r},\Omega') \right) \right)$$

and

$$M = \left( \nabla(\cdot\Omega\Psi^g(\mathbf{r},\Omega,t)) + \Sigma_t^g(\mathbf{r},t)\Psi^g(\mathbf{r},\Omega,t) - \sum_{g'=1}^G \left( \int_S d\Omega' \Sigma_s^{g' \rightarrow g}(\mathbf{r},\Omega' \rightarrow \Omega,t) \Psi^{g'}(\mathbf{r},\Omega',t) \right) \right).$$

More Details about the Static SPn method are given in the following paper [20].

### SPn discretization method- Kinetic case

[41] [232]

The neutron dynamics of a nuclear system (in absence of any external source) can be modeled by the multigroup time-dependent Boltzmann transport equation (3.1) associated with the time - dependent precursor equations (3.2). Written with the multigroup theory equation Eq (3.1) writes:

$$\begin{aligned} \frac{1}{V^g} \frac{\partial \Phi^g(\mathbf{r}, \boldsymbol{\Omega}, t)}{\partial t} = & -\boldsymbol{\nabla} \cdot (\boldsymbol{\Omega} \Phi^g(\mathbf{r}, \boldsymbol{\Omega}, t)) - \Sigma_t^g(\mathbf{r}, t) \Phi^g(\mathbf{r}, \boldsymbol{\Omega}, t) \\ & + \sum_{g'=1}^G \left( \int_S d\boldsymbol{\Omega}' \Sigma_s^{g' \rightarrow g}(\mathbf{r}, \boldsymbol{\Omega}' \rightarrow \boldsymbol{\Omega}, t) \Phi^{g'}(\mathbf{r}, \boldsymbol{\Omega}', t) \right) + S^g(\mathbf{r}, \boldsymbol{\Omega}, t) \end{aligned} \quad (3.33)$$

where the source term  $S^g$  is given by:

$$S^g(\mathbf{r}, t) = \chi_p^g(\mathbf{r}) \sum_{g'=1}^G (1 - \beta^{g'}) \nu \Sigma_f^{g'}(\mathbf{r}, t) \left( \int_S d\boldsymbol{\Omega}' \Phi^{g'}(\mathbf{r}, \boldsymbol{\Omega}, t') + \sum_{i=1}^L (\lambda_i c_i(\mathbf{r}, t) \chi_i^g(\mathbf{r})) \right). \quad (3.34)$$

Above  $\chi_p^g$  designs the energy spectrum of prompt neutron of energy group g and  $\chi_p$  designs the energy spectrum of precursor group i neutron of energy group g,  $\beta_i^g$  is the delayed neutron fraction in energy group g of precursor group i. This equation is discretized as in the previous section but the Kinetic equation with the precursor group  $i=1, \dots, L$  becomes.

$$\begin{aligned} \frac{\partial c_i^{(k)}(\mathbf{r}, t)}{\partial t} = & -\lambda_i^{(k)} c_i^{(k)}(\mathbf{r}, t) \\ & + \sum_{g'} \beta_i^{g'} \nu^{g'} \Sigma_f^{g'} \int_{4\pi} d\boldsymbol{\Omega} \Phi^{g'}(\mathbf{r}, \boldsymbol{\Omega}, t) \end{aligned} \quad (3.35)$$

A special attention is given to the time approximation used to solve these kinetic equations. In this work, we solve the simplified PN transport kinetics equations using a difference  $\theta$ -scheme on the angular flux equations and an integral  $\theta$ -scheme on the precursors equations (exact integration of the precursor equations with a linear expansion of the cross sections and polynomial representation of the flux). More Details about the Kinetic SPn method are given in the following papers [41] [232].

### Sn discretization method - Static Case

MINARET [169] is a deterministic 2D/3D transport solver developed in the frame of APOLLO3 code [168] [176] [169] [95] for nuclear core calculations to solve the steady state and kinetic neutron transport equation (3.1). The code follows the multi-group formalism to discretize the energy variable. Several solver can be used in order to approximate the angular variable, i.e., the  $P_N$ , the  $SP_N$  or the  $S_N$  solver [168]. In this we will focus on the  $S_N$  solver that we are going to use in the context of this work.

The  $S_N$  solver uses discrete ordinate method to deal with the angular variable and a Discontinuous Galerkin Finite Element Method (DGFEM) to solve the neutron transport equation spatially. The mesh is unstructured in 2D and semi-unstructured in 3D (cylindrical). Curved triangles [169] can be used in order to fit the geometry of the rod exactly but this option will not be discussed in this paper. In addition, the transport solver can be accelerated with a DSA method which corresponds to the acceleration by diffusion.

For a static problem, the  $S_N$  method consists in the resolution of the Transport equation (3.1) written for each energy group  $g = 1, \dots, G$ , in terms of space and angular variables  $\mathbf{r}$  and  $\Omega$  suppressing time variations.

$$\nabla \cdot (\Omega \Psi^g(\mathbf{r}, \Omega)) + \Sigma_t^g(\mathbf{r}) \Psi^g(\mathbf{r}, \Omega) = \sum_{g'=1}^G \left( \int_S d\Omega' \Sigma_s^{g' \rightarrow g}(\mathbf{r}, \Omega' \rightarrow \Omega) \Psi^{g'}(\mathbf{r}, \Omega') \right) + S^g(\mathbf{r}, \Omega) \quad (3.36)$$

where  $\Psi^g(\mathbf{r}, \Omega)$  is the angular flux according to its energy interval  $g$ . The vector  $\mathbf{r}$  represents the spatial variable ( $\mathbf{r} \in R \in \mathbf{R}^3$ ). The unit vector  $\Omega$  represents the travelling direction of a neutron. The direction  $\Omega$  is expressed in terms of  $(\theta, \varphi)$  in spherical coordinates, with  $\theta$  the colatitude and  $\varphi$  the azimuthal angle. We define  $\mu = \cos(\theta)$ ;  $S$  represents the unit sphere and  $\int_s(\dots)d\Omega$  defines the normalized integral  $\int_s d\Omega = 1$ .  $\Sigma_t$  and  $\Sigma_s$  are the macroscopic isotropic total and anisotropic scattering cross-sections. Finally,  $S^g(\mathbf{r}, \Omega)$  is a source term which includes the fission source and an external source  $S^{ext}$ .

$$S^g(\mathbf{r}, \Omega) = \frac{1}{k_{eff}} \cdot \chi^g(\mathbf{r}) \cdot \sum_{g'=1}^G \left( \nu \Sigma_f^{g'}(\mathbf{r}) \left( \int_S d\Omega' \Psi^{g'}(\mathbf{r}, \Omega') \right) + S_g^{ext}(\mathbf{r}, \Omega) \right) \quad (3.37)$$

where  $k_{eff}$  is the effective multiplication factor,  $\chi$  designs the fission spectrum,  $\nu$  is the number of neutrons emitted per fission,  $\Sigma$  is the macroscopic fission cross-section. When the external source in Eq. (3.37) is null, the problem (3.36) is an eigen value problem and  $k_{eff}$  corresponds to the dominant eigen value. More Details about the static Sn method are given in the following papers [168] [176] [169] [95].

### 3.3.8 Power computation

From the neutronic flux calculation, we can compute the Power deposition for an elementary cell. The neutronic power computation [144] corresponds to the reaction rate  $(\Sigma(x, E)\Phi(x, E))$  multiplied by the energy distribution  $\chi(E)$  and the value of Energy released by fission  $\nu$ .

$$P_{cell}^{integrated} = \int_{x \in cell} \int_E \nu \chi(E) \Sigma(x, E) \Phi_{comb}(x, E) dx dE, \quad (3.38)$$

or in a multigroups formulation:

$$P_{cell}^{integrated} = \int_{x \in cell} \sum_g \nu \chi^g \Sigma^g(x) \Phi_{comb}^g(x) dx,$$

Thus the volumic and lineic power is given by the formula:

$$P^{volumic} = \frac{P^{integrated}}{cell\_Volume} \quad (3.39)$$

$$P^{lineic} = \frac{P^{integrated}}{cell\_height} \quad (3.40)$$

In standard neutronic calculation we compute the power at a discretization scales which does not distinguish between the fluid and fuel pin. With out power reconstruction, we split this power between a fluid and a pin component using an experimental coefficient  $\gamma$ , yielding:

$$P_{fluid}^{integrated} = \gamma P^{integrated} \quad (3.41)$$

$$P_{fuel\_pin}^{integrated} = (1 - \gamma) P^{integrated} \quad (3.42)$$

In chapter ( 4.2) we will propose on improved strategy based on a local reconstruction.

## Chapter 4

# Access to the local parameters and Best Effort improvement of Neutronics models

In this chapter we detail existing approaches and discuss the improvements realized or needed to be realized in order to access the local parameters relative to Neutronics. Consequently, we will present both improvements, i.e., the fast neutron flux computation and fine flux computation, leading to an enhancement of the neutronic model and aimed to be used in multiphysics-multiscale coupling.

### 4.1 Fast neutron flux Computation

The neutron flux is consistently relative to the state of the reactor core and thus of the core reactivity. The control of the reactivity is one of the fundamental safety principles the reactor needs to respect. In the same time, the neutron flux gives us information on the Power production and obviously on the energy deposition inside the pellet and the fluid. This aspect of the neutron flux is taken into account in the Thermomechanical and Thermohydraulical model as source terms of equations. One should therefore split the power locally deposited (eq. (3.38)) into a part deposited in the fluid and a part deposited in the pin. Moreover, the neutron flux can be divided in three parts, i.e., the thermal neutron flux part with an energy under 0.6 eV that yields fission through interaction between thermalized neutrons and Uranium nuclei, the epithermic part and the fast neutron flux part that corresponds to neutrons with an energy beyond 1MeV. This fast neutron flux influences the mechanical part where neutrons with this high energy interact with the

clad and induce neutronic creeping (section 6.3) over a long period (paramout in the REA for the representativeness of initial state of the fuel pin). A classical way of computing the Fast neutron flux is to define the energetical grid by accounting for the Energy cut at the energy of 1 MeV from which defined the fast neutron flux. This approach is simple to realize for a fine energy grid of about 8 to 30 groups of energy at minimum and is obvious when dealing with for more than hundreds of energy groups. Nevertheless, in case of standard 2 groups of energy separated at a thermalized neutron energy of 0.6 eV, adding a third group corresponding to the fast neutron energy cut is inaccurate.

## 4.2 Fine Flux Reconstruction

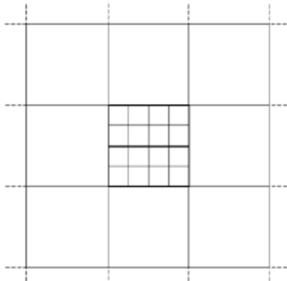
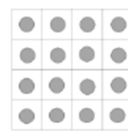
During a classic reactor operation, we observe flux variation at the scale of the fuel cell while the global distribution of the core is almost flat. Indeed, a fundamental mesh in the assembly is the fuel cell made of the fuel pin or guide tube surrounded by fluid. These two media do not interact equally with neutrons and thus the power deposition is clearly not the same. Futhermore, we can easily distinguish fuel cell containing fuel pin against fuel cell containing only guide tube filled with water. This heterogeneous distribution of the flux inside the assembly will be exacerbated in case of a transient where the rod ejection is located and thus could induce a heterogeneous neutron pulse at the scale of the assembly. This deformation of the core flux distribution also will be observed at the scale of the fuel cell. Knowing the fact that REA is characterized by a strong interaction between the different areas of reactor physics (Neutronics, thermal fuel mechanics and thermal hydraulics) which might jeopardize the fuel pin, an accurate representation of neutron flux distribution is of interest.

In this part, we focus only on the discipline of Neutronics and more precisely on the reconstruction using coarse flux distribution over the whole core in order to obtain an accurate and realistic localization and deposit of power inside some interesting subdomains of the core and an information on fast neutron flux.

The objective of this study is to access the local power deposit inside the fuel and the coolant (gamma fraction) using a two solver power reconstruction. The pin power reconstruction method consists in computing simultaneously an unsteady 3D deterministic homogenized simplified transport equation solver over the whole core and a 3D deterministic heterogeneous transport solver over a single chosen assembly (typically the highest load assembly in terms of power).

Several approaches and dynamics of the practical application of the modeling are possible. They are described in the following tab. The 3 levels of modeling developments of the tab 4.1 are defined according to their physical parameters, to boundary conditions, to the time evolution of the solver as well as to the type of coupling used between solvers. Each increasing step improves the coupling (colored words in bold letters highlight inputs of new steps). The second approach (level 2) has been lately developped at the CEA and would

need to be confronted in the future to our case in static conditions and then implemented in a kinetic scenario. It would be a perfect coupling of coarse and fine calculations. In this approach, the calculation on the single fine assembly uses the right value of the flux. Herein, we have developed the simpler version of level 1 (coarse kinetic calculation of core post- treated by a static assembly calculation) with the solver MINOS (SPn) and MINARET (Sn), see in figure ( 4.1).

	Modeling	SPn	Sn	Coupling Scheme	Local parameters
<b>Level 1</b>	Mesh grid (scales)			<b>Post processing</b>	<b>Power deposit inside the fuel (<math>P_{comb}</math>) and power deposit inside the fluid (<math>P_{fluid}</math>)</b>
	Cross sections condensation	<b>Assembly</b>	<b>Fluid / Fuel pin</b>		
	Domains (Boundary Conditions)	<b>Whole core (zero flux)</b>	<b>Specific assembly (mirror)</b>		
	Time evolution	<b>Kinetic calculation</b>	<b>Static calculation</b>		
<b>Level 2</b>	Mesh grid	Level 1	Level 1	Sn BC inherited from SPn No coupling from Sn to SPn	$P_{comb} + P_{fluid}$
	Cross sections	Assembly + Fuel cell	step 1		
	Domains (Boundary Conditions)	Whole core (zero flux)	Specific assembly (SPn Flux)		
	Time evolution	Kinetic calculation	Static calculation		
<b>Level 3</b>	Mesh grid	Level 1	Level 1	Sn BC inherited from SPn Cross section SPn evaluated from SPn results	$P_{comb} + P_{fluid}$
	Cross sections	Level 2	Level 1		
	Domains (Boundary Conditions)	Whole core (zero flux)	Specific assembly (SPn Flux)		
	Time evolution	Kinetic calculation	<b>Kinetic calculation</b>		

**Figure 4.1.** Tab of the dynamics of the practical application of the Pin Power reconstruction modeling

### 4.2.1 MINOS-MINARET Approach

Let us consider a domain  $\Gamma$  of  $\mathbb{R}^3$  and some subdomains  $\gamma_s \in \Gamma$ , with  $s=1, 2, \dots, n$ . Over this entire domain  $\Gamma$ , we are calculating the flux  $\Phi_{\Gamma}^{G_i}(R)$  with an energetic discretization according to the neutron macro energetic groups  $G_i$ . For a specific subdomain  $\gamma_s$  (typically



## CHAPTER 4. ACCESS TO THE LOCAL PARAMETERS AND BEST EFFORT IMPROVEMENT OF NEUTRONICS MODELS

an assembly), we are looking to rebuild the flux  $\Phi_{\gamma_{s,core}}^{g_{ij}}(R, r)$ ,  $r \in R$ , where  $g_{ij}$  are neutron micro energetic group subdivisions of the macro energetic groups  $G_i$  and  $r$  a spatial discretization of the variable  $R$  of this subdomain.

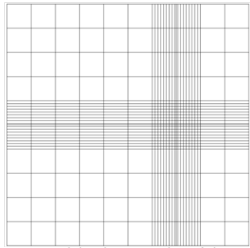
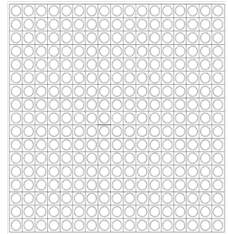
The two calculations are realized in parallel and separately from each other. On the first hand, the macro-groups flux  $\Phi_{\Gamma}^{G_i}(R)$  calculation is done by solving the equations of section ( 3.3) with a zero flux boundary condition on the external surface  $\partial\Gamma_{ext}$  of the domain  $\Gamma$

$$\Phi_{\partial\Gamma_{ext}}^{G_i}(R) = 0. \quad (4.1)$$

On the other hand, on the external surface  $\partial\gamma_{ext}$  of the subdomain  $\gamma_s$ , the flux  $\Psi_{\gamma_{s,\infty}}^{g_{ij}}(R, r)$  calculation is done with a reflection boundary condition, i.e. all the flux parts that leave the assembly are re-entered into the assembly at the same point at which they leave

$$\Psi_{\gamma_{s,\infty}}^{g_{ij}}(r, \Omega) = \Psi_{\gamma_{s,\infty}}^{g_{ij}}(r, -\Omega), \forall r \in \partial\gamma_{ext}. \quad (4.2)$$

We describe the calculation strategy in the following figure ( 4.2) according to the domain, equations, solver and boundary conditions of this approach. At this point, there is no coupling (see figure 4.5).

	MINOS solver of APOLLO3®	MINARET solver of APOLLO3®
Calculation grid (2D)	 <p>Hybrid Whole Core</p> <p>Discretization: ¼ assembly by mesh with a refinement of 1 fuel cell by mesh</p>	 <p>Single Assembly</p> <p>Discretization: 1 Unstructured fuel cell by mesh</p>
Equations	<p>Transport equation :</p> $\frac{\partial \Phi_{\Gamma}^{G_i}(x, \Omega, t)}{\partial t} = D^{G_i}(x, \Omega, t) + Dis^{G_i}(x, \Omega, t) + Sc^{G_i}(x, \Omega, t) + S^{G_i}(x, \Omega, t)$ <p>And Kinetic equation : <math>\frac{\partial c_i(x, t)}{\partial t} = -\lambda_i c_i(x, t) + Pr(x, t)</math></p>	<p>Transport equation in static condition → eigenvalue problem</p> <p>And precursors are in equilibrium</p>
Solver	<b>MINOS SPn</b> neutronic <b>equation</b> with <b>kinetic condition</b> (~10 Energy groups)	<b>MINARET Sn</b> neutronic <b>equation</b> with <b>static condition</b> (~30 Energy groups)
Boundary condition	<p><b>Zero flux boundary condition</b></p> $\Phi_{\partial\Gamma_{ext}}^{G_i}(x) = 0$	<p><b>Reflexion boundary condition</b></p> $\Psi_{\delta\gamma_{ext}}^{g_{ij}}(r, \Omega) = \Psi_{\delta\gamma_{ext}}^{g_{ij}}(r, -\Omega)$

**Figure 4.2.** Summary of our Minos-Minaret coupling approach

### 4.2.2 Flux Reconstruction

From the two flux expressed above (in their scalar form  $\Phi_{\Gamma}^{G_i}(\mathbf{R})$  and  $\Psi_{\gamma_{s,\infty}}^{g_{ij}}(\mathbf{r})$ , at a time step  $t_i$  of the transient, we are aiming to obtain the flux  $\Phi_{\gamma_{s,\infty}}^{g_{ij}}(\mathbf{R}, \mathbf{r})$ , reconstructed by combining the most detailed space and energy representation of the pin cells spectra, i.e. the fine-group flux  $\Psi_{\gamma_{s,\infty}}^{g_{ij}}(\mathbf{r})$ , with the macrogroup flux  $\Phi_{\Gamma}^{G_i}(\mathbf{R})$ . The correction is done following the classical approach [10], weighting the macrogroup flux:

$$\Phi_{\gamma_{s,\infty}}^{g_{ij}}(\mathbf{R}, \mathbf{r}) = \Phi_{\Gamma}^{G_i}(\mathbf{R}) \cdot H_{\gamma_{s,\infty}}^{g_{ij}}(\mathbf{R}, \mathbf{r}) \quad (4.3)$$

with the fine-group shape factor:

$$H_{\gamma_{s,\infty}}^{g_{ij}}(\mathbf{R}, \mathbf{r}) = \frac{\Psi_{\gamma_{s,\infty}}^{g_{ij}}(\mathbf{R}, \mathbf{r})}{\sum_{g_{ij} \in G_i} (\int_{r \in R} \Psi_{\gamma_{s,\infty}}^{g_{ij}}(\mathbf{R}, \mathbf{r}) dr)} \cdot \frac{\int_{r \in R} \Psi_{\gamma_{s,\infty}}^{g_{ij}}(\mathbf{R}, \mathbf{r}) dr}{\int_{r \in R} (\Psi_{\gamma_{s,\infty}}^{g_{ij}}(\mathbf{R}, \mathbf{r})) dr} >_{\gamma_{s,\infty}} N_S \quad (4.4)$$

Above  $\int_R dr$  corresponds to a spatial integration over the cell R. The shape factor can be split in two separate contributions:

$$H_{\gamma_{s,\infty}}^{g_{ij}}(\mathbf{R}, \mathbf{r}) = H_{cell}(\mathbf{R}, \mathbf{r}) \cdot H_{domain}(\mathbf{R}, \mathbf{r}). \quad (4.5)$$

Hence, we have the first contribution  $H_{cell}$  which corresponds of the Ratio of each medium of the fuel cell with respect to the whole fuel cell:

$$H_{cell}(\mathbf{R}, \mathbf{r}) = \frac{\Psi_{\gamma_{s,\infty}}^{g_{ij}}(\mathbf{R}, \mathbf{r})}{\sum_{g_{ij} \in G_i} (\int_{r \in R} \Psi_{\gamma_{s,\infty}}^{g_{ij}}(\mathbf{R}, \mathbf{r}) dr)},$$

which allows in figure ( 4.3) to distinguish between the moderator (in blue) and the central Fuel pin or Guide Tube (in red) :

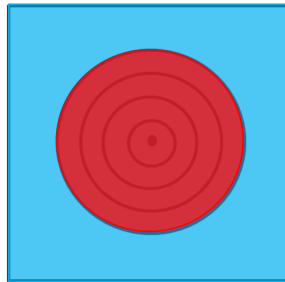


**Figure 4.3.** Cell heterogeneity: Fuel Pin / moderator distinction

The second contribution  $H_{domain}$  corresponds of the ratio of a specific fuel cell with respect to the whole domain (by axial plan),

$$H_{domain}(\mathbf{R}, \mathbf{r}) = \frac{\int_{r \in R} \Psi_{\gamma_{s,\infty}}^{g_{ij}}(\mathbf{R}, \mathbf{r}) dr}{\langle \int_{r \in R} (\Psi_{\gamma_{s,\infty}}^{g_{ij}}(\mathbf{R}, \mathbf{r})) dr \rangle_{\gamma_{s,\infty}} N_S}$$

which allows in figure ( 4.4) to distinguish between a fuel cell with a central fuel pin (in red) and a fuel cell with a central Guide Tube (in blue). Here  $\langle \cdot \rangle_{\gamma_{s,\infty}}$  is the average of cell values among all cells of the assembly  $\gamma_{s,\infty}$  and  $N_s$  the number of cells in  $\gamma_{s,\infty}$ .

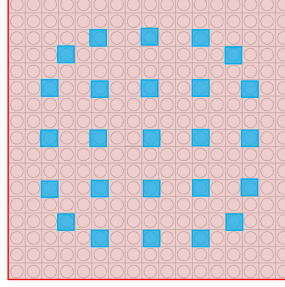


**Figure 4.4.** Assembly heterogeneity: Fuel Pin cell / guide tube cell distinction

In addition, we observe that we have by construction,

$$\sum_{g_{ij} \in G_i} \left( \int_{r \in \gamma_s} H_{\gamma_{s,\infty}}^{g_{ij}}(\mathbf{R}, \mathbf{r}) dr \right) = 1$$

and thus, the reconstructed flux preserves the correct value of the integral of the flux over the subdomain  $\gamma_s$ :

$$\sum_{g_{ij} \in G_i} \left( \int_{r \in \gamma_s} \Phi_{\gamma_{s,core}}^{g_{ij}}(\mathbf{R}, \mathbf{r}) dr \right) = \Phi_{\Gamma}^{G_i}(\mathbf{R})$$

We obtain by post treatment of the coarse flux by the shape factor (eq. ( (4.4))) this kind of post-treated curve:

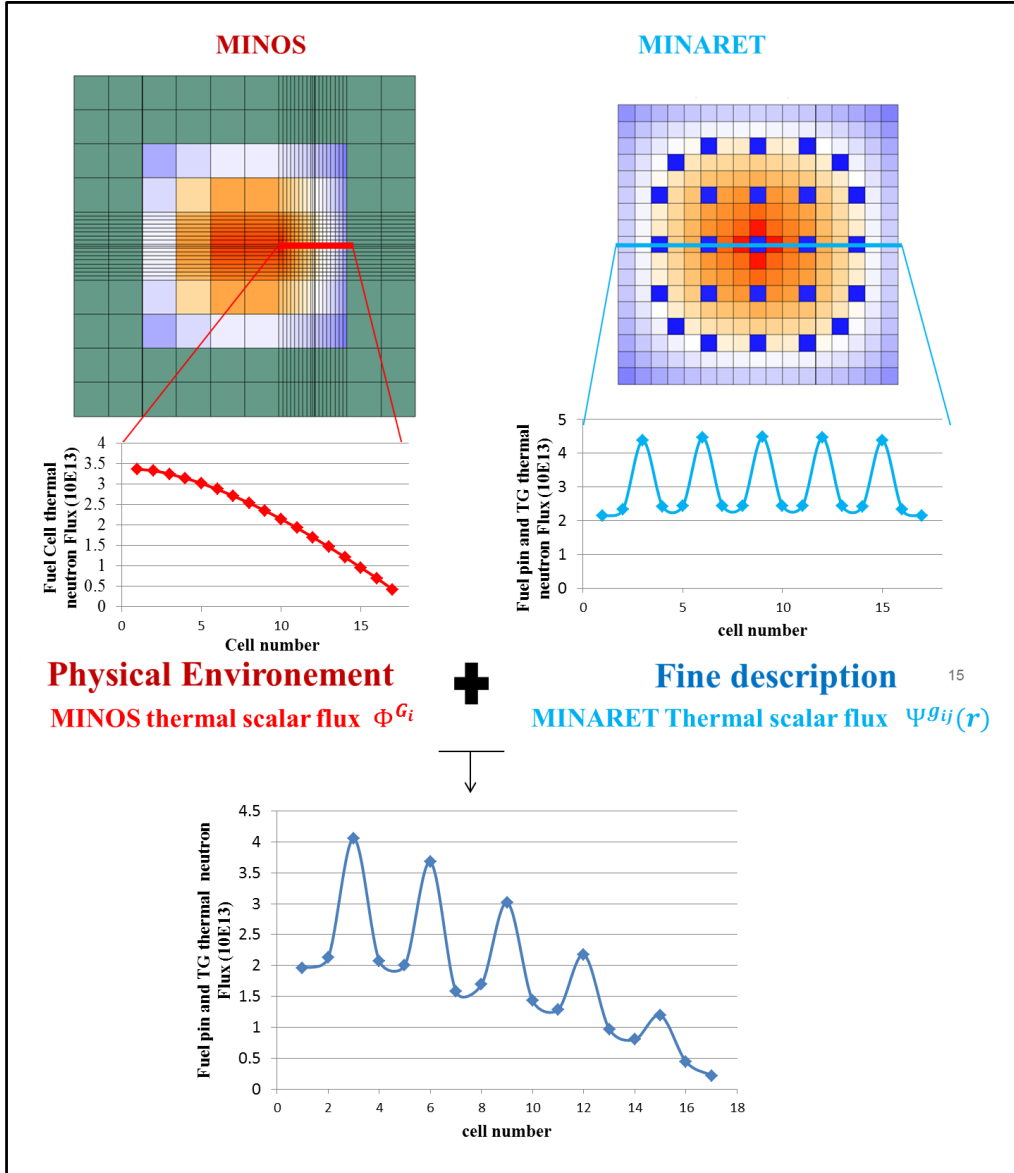


**Figure 4.5.** Coarse and a fine distribution of the thermal flux

In this post treatment, we are using a 8 (MINOS) and a 30 (MINARET) groups energetic grid. Hence, according to the cut-off values of the energetic grid we are able to isolate the flux which is higher than  $E = 1\text{MeV}$  (used for fuel pin REA initial state).

$$\phi^{E>1\text{MeV}} = \sum_{g_{ij}>1\text{MeV}} \phi^{g_{ij}} \quad (4.6)$$

### 4.2.3 Algorithm

At each step of the transient calculation, the method describe above is used to rebuild the Pin Power. The algorithm is detailed below:

- Phase 0 : First time step: Simultaneous initialization of both calculations. Both solvers are set respecting the same initial conditions (Burn up map, temperatures, density, isotopic concentration, etc.);
- Phase 1 : MINARET neutronic static calculation for the current parameter,
- Phase 2 : MINOS neutronic transient calculation at time  $t_i$ .
- Phase 3 : Post-treatment of the MINOS flux: it consists in multiplying it by the shape factor ( (4.4)) that is derived from the fine MINARET flux to get  $\Phi_{\gamma s, core}^{gij}(\mathbf{R}, \mathbf{r})$  ;
- Phase 4 : Calculation of the power inside the fuel and the fluid:  

$$P_{medium}^{integrated} = \int_{x \in medium} \int_E \nu \chi(E) \Sigma(x, E) \Phi_{comb}(x, E) dx dE;$$
- Phase 4 : Modification of thermo-mechanic and thermo-hydraulic parameters in MINOS and updating of the Cross Sections according to the control rod ejection evolution, thermo-mechanic and thermo-hydraulic parameters;
- Phase 6 : New time step: return to phase 2.

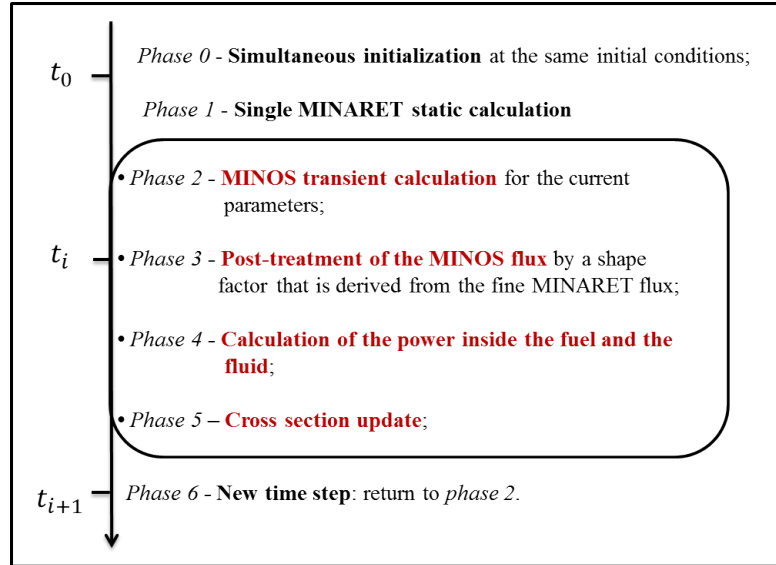


**Figure 4.6.** MINOS-MINARET Kinetic calculation methodology

#### 4.2.4 Validation

An exact validation of our work could be achieved using the level 2 of figure ( 4.1). Nevertheless, while waiting for its final implementation, we have performed a Minaret (Sn and n=4) 32 energy groups static calculation over our academic core case with a discretization at the scale of 4 meshes/assembly, and with a refinement of a single lateral assembly at the scale of the fuel pin, i.e., 1 unstructured fuel cell by mesh (figure ( 4.7)). This way, the Minaret calculation over the fine assembly is incorporated within our total academic core. Thus the result of the calculation inside the refined assembly should yield the "exact" neutronic solution that we shall be able to compare to our reconstructed approach.

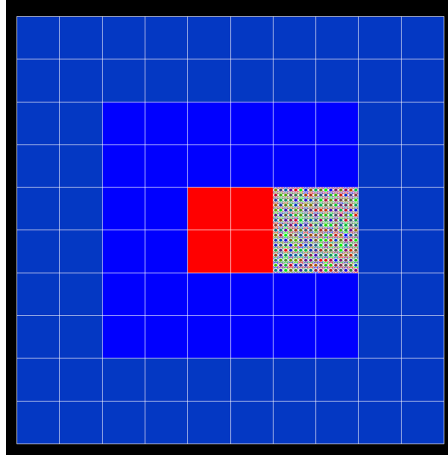


**Figure 4.7.** Academic core case full Minaret calculation with a discretization at the scale of 4 cells/assembly, and with a refinement of a single lateral assembly at the scale of an unstructured fuel cell by mesh.

For the purpose of this comparison, we performed the calculations in 2D. We obtain the following Fuel Pin Power results we summarize in figure ( 4.8). We observe that the two graph lines have a similar profile as it is shown in the tab ( 4.8). Nevertheless, we observe a difference of 117 kW between the sums of the Fuel Pin Power inside the whole assembly (Total Assembly fuel pin power of 1018kW for the MINOS-MINARET and of 901kW for the MINARET validation). This difference in power seems to come from the nearby assemblies calculations (difference in grid size and in group discretization) and could also be related to the difference between the solvers we use for the calculations (Minos(SPn) 8 energy groups for the PPR calculation and Minaret (Sn) 32 energy groups for the validation) inside the assembly of interest. In addition, we observe a variation of the local power distribution as it is shown in the error map and, more precisely, the slight shift of the hot spot fuel pin location. It induces a maximal local power difference of 0.96kW (relative difference of +19%) at the MINOS-MINARET Hot spot location and a power difference of -0.2kW (relative difference of -20%) in the cell nearby the reflector.

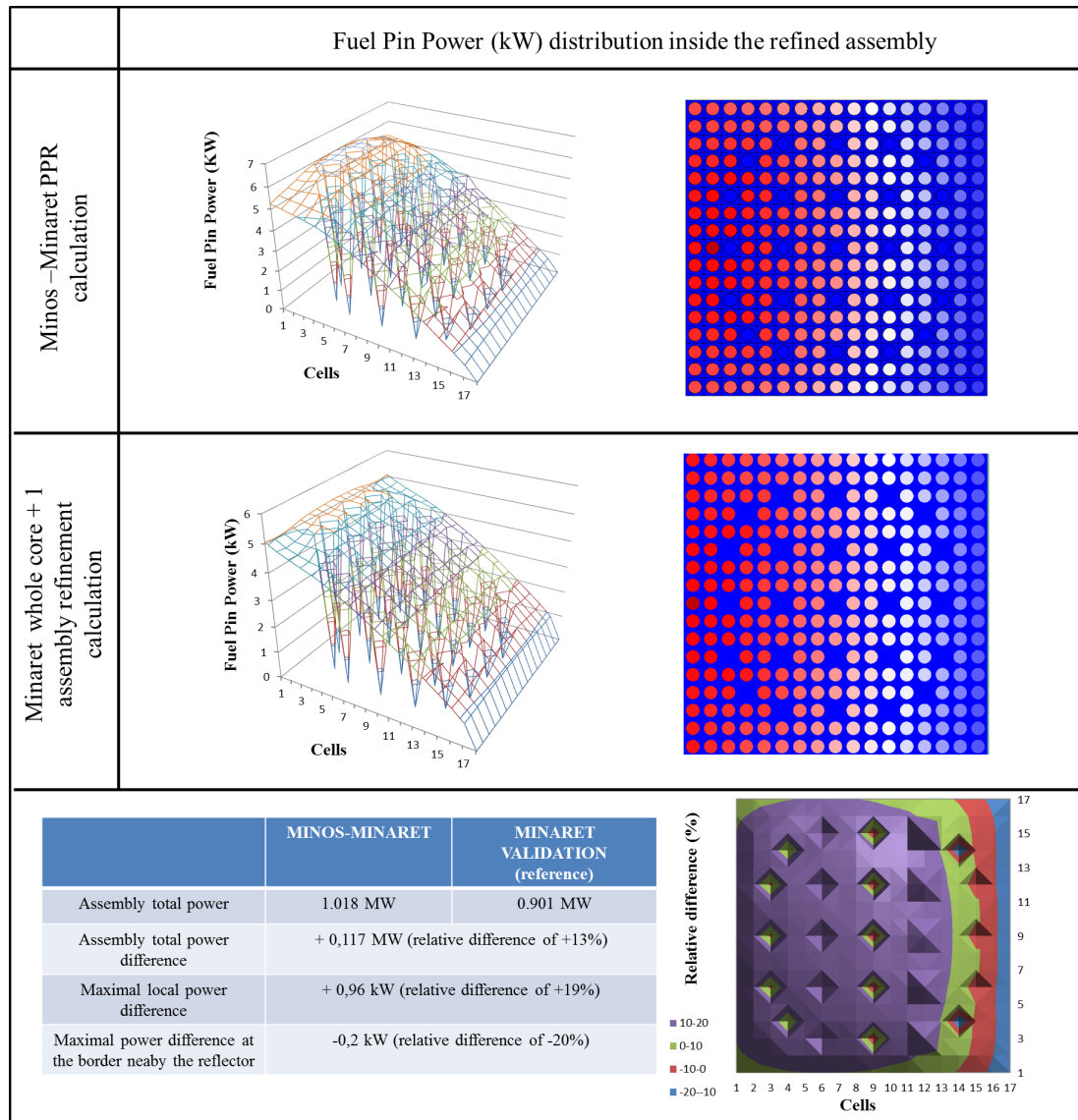


**Figure 4.8.** PPR and Minaret whole core calculations and comparison

In conclusion, through the comparison with a Minaret reference calculation, we validate our post treatment approach physically as an interesting simplified method in order to access local power deposit inside the fuel and the coolant. This method still lacks of accuracy at this stage to be used in a proper multiscale coupling. With respect to the hot spot difference, improvements would be required on the fuel assembly and reflector cross sections computation (by reducing uncertainties between 8 and 32 groups homogenization) as well as on the refinement of assemblies nearby the reconstructed one (for instance by using a gradient in the refinement) in order to move forward in the physical representativity of our simulation. Finally, it would also be necessary to compare our approach to a multisolver coupling calculation (level 2 of the tab ( 4.1)) in order to definitely validate the

our results and to determine the best method to be used in the framework of a multiphysics-multiscale Best Effort coupling within a realistic computing time.

### 4.2.5 Results

In order to simplify the implementation of the coupling scheme we are working on a small core reactor. This reactor is a 5x5 geometry reactor made of 9 internal fuel assemblies and an external ring of 16 reflectors ( section 4.9). It has a power of 177.2MW, and is 468.72 cm in height. This geometry preserves the physical, neutronic and mechanical specificities as well as the behaviors of the PWR 1300MWe in case of nominal and accidental situations. The central assembly contains the control rod. Hence, the neutronic static calculation would be done over an isolated assembly corresponding to the lateral assembly nearby the central one. According to studies on REA [141], this assembly corresponds to the highest load assembly in terms of power. Indeed, the hot spot does not appear in the assembly where the control rod had been ejected but within its nearest lateral neighbor [141]. However, the static calculation could easily be realized on every other assembly of the core.

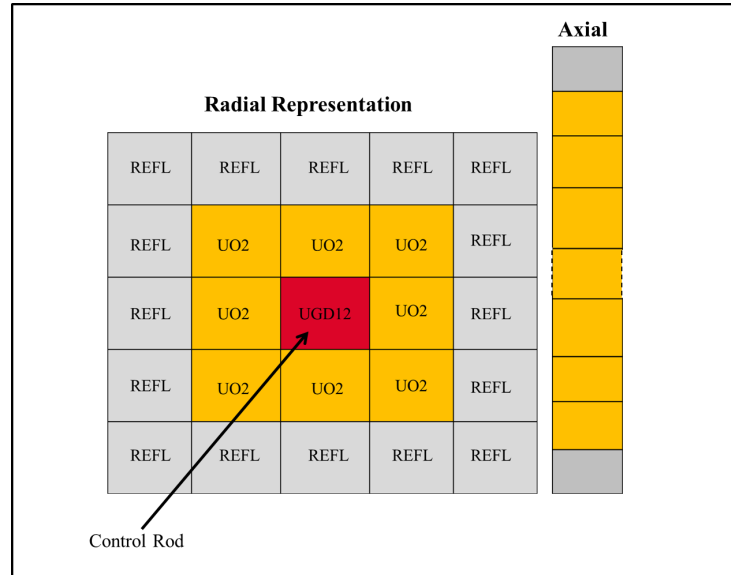


**Figure 4.9.** PWR academic core (5x5) scheme

We assume that before the transient the power inside the core is constant and the neutron population balance is stable. When the rod is ejected the balance is broken. In this study we focus on hot zero power which would lead the reactor to go prompt critical, producing a rapid power spike of about several milliseconds, increasing from quasi-zero to about ten times the nominal power. In addition, the core is set at the start of the fuel cycle process (Burn-up = 0 MWj/d) for all its assemblies. The control rod system is only contained by the central assembly. For these reasons we arbitrarily draw the neutronic



parameter of the rod as well as of the whole core from the previous study [142] [34] [141]. The refinement of the grid is done in this specific assembly at the scale of the fuel cell and at the scale of the fuel pin for the single Sn assembly. The Rod ejection accident (REA) is based on assuming that the attached control rod assembly is ejected vertically from the reactor. During the ejection period, only the neutronic discipline is affected. We decide to limit our study to this brief moment. This choice gives us the right to focus on the neutronic Pin Power Reconstruction without any feedback effect. In conclusion, we neglect the thermal, mechanical and hydraulic aspects of the rest of the scenario, which are going to be used and analyzed during the next coupling study. This way, the macroscopic cross section  $\sigma_{NuclearReaction}^{EnergyGroup}$  would only evolve according to the control rod axial changes inside the core.

We first observe one of the power maps from the phase 1 MINOS Kinetic calculation, at a representative time step  $t_i$ , as it is expressed in Pin Power Reconstruction methodology of the previous section. For purposes of the present paper, the power reconstruction was only performed in 2D. The shape of the power map is applied over the solver grid (hybrid due to the junction between the single nodes of the refined assembly and the external surface boundary). The result ( figure 4.10) does not distinguish the fuel pin from the fluid.

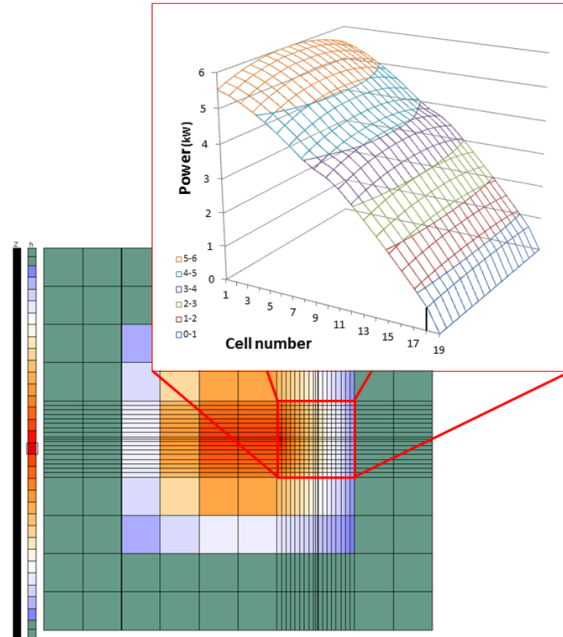


**Figure 4.10.** MINOS SPn homogeneous core power maps calculation

Next, we obtain an accurate distribution of the power inside the single assembly calculated with the Sn solver (figure 4.11). This way, we properly distinguish the guide tube from the fuel pin. Unfortunately, this single assembly power distribution (symmetrical) does not take into account the environmental aspects of the flux distribution that is dealt with in the whole core calculation.

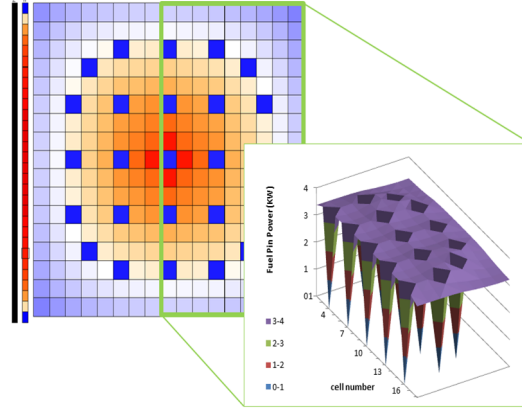


**Figure 4.11.** MINARET Sn Single Assembly pin power maps calculation

Through the Pin Power Reconstruction methodology that we have defined in the previous section, we then obtain two distinct and accurate power maps over the assembly of interest. These two power maps are presented in figure ( 4.12).

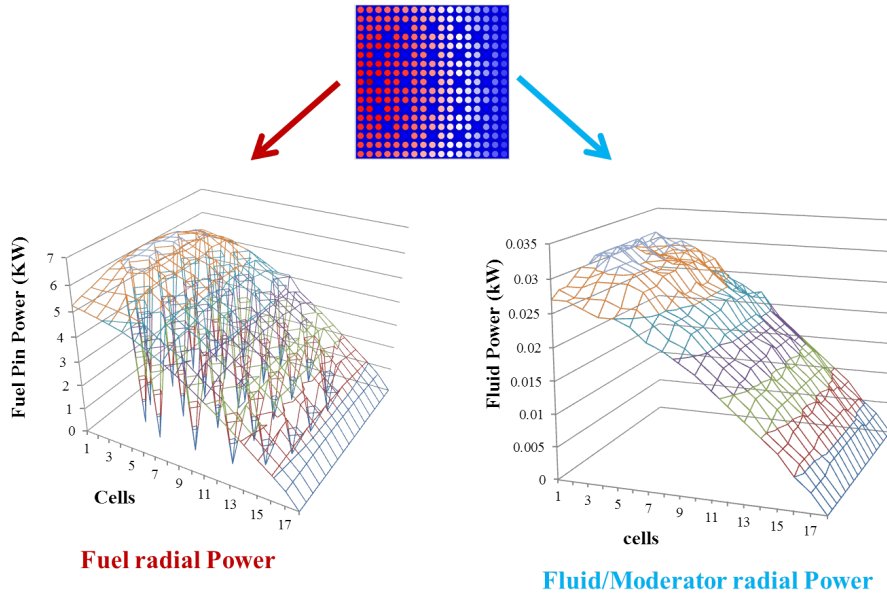


**Figure 4.12.** MINARET Sn Single Assembly Accurate Power distribution

In the first one, we observe the precise post processed map of the power deposit inside the fuel. In the second one, we observe the post processed map of the power deposit inside the fluid. This was not accessible in the original MINOS calculation. The fluid is composed mainly of water ( $H_2O$ ) and also of a tiny but significant portion of Boron. The Hydrogen has a moderating effect on the neutron celerity. Indeed, the scattering cross sections are huge and induce a significant amount of inelastic collision with the neutron.

We effectively find this physical effect in addition to the gamma fraction in the map of the power deposit inside the fluid due to the cross sections production that takes into account these phenomena. These distributions of the fluid and fuel pin power fraction shall take all their significance during the multiphysics coupling.

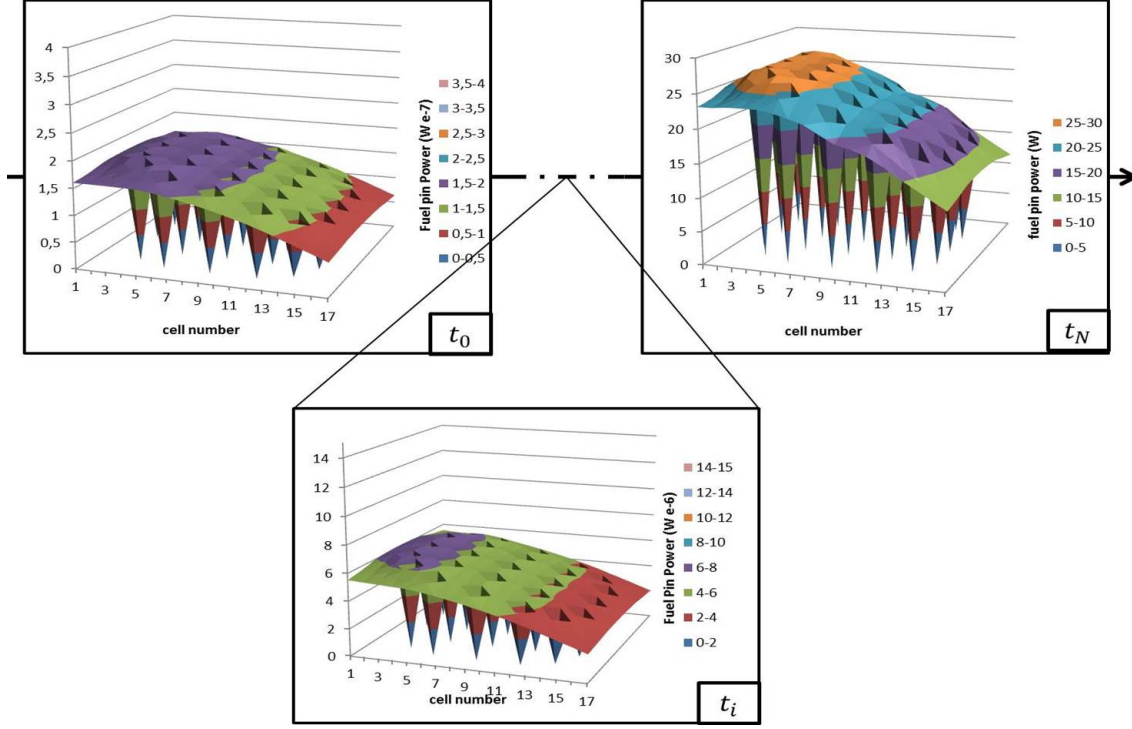


**Figure 4.13.** Illustration of the Kinetic Post processed map of power deposit inside the fuel pin

## 4.2.6 Conclusion

The Pin power reconstruction method that we develop allows us to precisely distinguish the contribution of the power deposit inside the fuel pin and inside the fluid. This computation is obtained by a post proceeding of a whole core deterministic homogeneous calculation (which takes care of the environmental aspects of the flux distribution) by a single assembly deterministic heterogeneous calculation (that handles the precise flux distribution at the scale of the fuel pin).

This choice of the Pin Power Reconstruction post treatment approach has simplified the implementation and provides flexibility in achieving a variety of reconstructions in terms of localization of the assembly of interest and in terms of geometry. This method should be easily adapted to a case of a PWR 1300MWe or inserted into a multiphysics-multiscale modeling. Moreover, the discretization inside the fuel pin or inside the fluid should be im-

proved in order to take care of the Rim effects. The improvement of our simulation would also be done by adding a Gamma transport method into our coupling, for instance, by coupling our Pin power reconstruction method to a Gamma transport solver. Indeed, gamma power only comes from interactions that occur at the exact location the power is deposited (which minimize the gamma deposition). Hence, the Gamma transport would be necessary in order to get a more precise distribution of the power deposition inside the fluid and more specifically about the gamma power produces inside the fuel pellet and finally deposited into the fluid.

### 4.3 Power reconstruction at pellet level

The neutronics reactor core resolution should be done by the APOLLO3 code. This way, the space discretization should be realized at the scale of the fuel pin (with annular cells inside the fuel pellet) in order to accurately describe the local behavior of the fuel pin. Without power reconstruction approaches (such as in section ( 4.2) and considering the time computing limitation of this type of accurate simulation, another strategy have been used in our coupling.

The power reconstruction at the pellet level is done through ALCYONE code [197] by a local resolution of neutronic equations and post treatments (during transient or reactor operation) as detailed below.

#### 4.3.1 Burn-up computation

In this construction, the burn-up variation will be given by an engineering law detailed in [197] [155]:

$$\Delta\tau = \frac{\frac{P_{lineic}}{S_{fuel}} (1 - P_{g\gamma}) \Delta t}{\rho \cdot f_{ML} \cdot 86400 \cdot 10^{-3}} \quad (4.7)$$

Where  $P_{lineic}$  is the lineic power given by APOLLO3 (section 3.3.8),  $S_{fuel}$  the fuel surface section,  $P_{g\gamma}$  is the corrective factor from the Gamma Power deposit in the clad,  $f_{ML}$  is fraction coefficient of mass of metal in the fuel and  $\Delta t$  the time step. In theory,  $P_{lineic}$  would be obtained in section ( 4.2) by:

$$P_{lineic} = \frac{\left( \int_{r \in Pellet} \sum_{g_{ij}} \nu \chi^{g_{ij}} \Sigma^{g_{ij}}(r) \Phi^{g_{ij}}(R, r) \right)}{h_{fuel}} dr, \quad (4.8)$$

where  $R$  is a fuel cell and  $r$  the local position inside the cell of  $R$  ( $r \in R$ ),  $\Sigma^{g_{ij}}(r) \Phi^{g_{ij}}(R, r)$  is the reaction rate multiplied by the energy distribution  $\chi^{g_{ij}}$ , the value of Energy released by fission  $\nu$  and  $h_{fuel}$  the axial height of the fuel slice. In practice, we have used

in ALCYONE on unprocessed Power and flux distribution obtained from:

$$P_{lineic} = \frac{\left( (1 - \gamma) \sum_{g_{ij}} \nu \chi^{g_{ij}} \Sigma^{g_{ij}}(r) \Phi^{g_{ij}}(R) \right)}{h_{fuel}} \quad (4.9)$$

and  $(1 - \gamma)$  the core power fraction deposited in the fuel pin (see Eq. (3.41)).

### 4.3.2 Flux and radial Power Computation at the pellet scale

The power density distribution through the pellet is computed with a simplified approach coming from the METEOR first-generation fuel performance code. This approach is based on the one-dimensional (1-D) axisymmetric assumption first proposed by [197], [155], in the RADAR model. The average, 1 group of energy, neutron flux is given by (4.10):

$$\Phi = \frac{\Delta\tau}{\Delta t} \frac{2.1310^{-4}}{1.08(\sigma_{pf,235} N_{U^{235}} E_{pf,235} + \sigma_{pf,239} N_{Pu^{239}} E_{pf,239} + \sigma_{pf,241} N_{Pu^{241}} E_{pf,241})} \quad (4.10)$$

where  $\Phi$  is the average neutron flux ( $n.cm^{-2}.s^{-1}$ ),  $\Delta\tau$  is the burn-up variation (MWd/tM) during the time step  $\Delta t$  given equation (4.7), and  $\sigma_{pf,k}$ ,  $N_{pf,k}$ ,  $E_{pf,k}$  are respectively the microscopic cross-sections, the isotope concentration and fission energy, of a specific isotope k.

Then, the radial Power distribution is given by:

$$P^{vol}(r) = \Phi.R(r) \quad (4.11)$$

where

$$R(r) = I_0(\alpha r) [(\sigma_{f235} N_{U^{235}}(r) E_{235} + \sigma_{f239} N_{Pu^{239}}(r) E_{239} + \sigma_{f241} N_{Pu^{241}}(r) E_{241})] \quad (4.12)$$

Above  $I_0$  is a Bessel function,  $\alpha$  is the inverse of the neutron diffusion free mean path which is expressed by :

$$\alpha = \left( \frac{3}{\lambda_{tr} \lambda_{abs}} \right)^{0.5}$$

and where  $\lambda_{tr}$  and  $\lambda_{abs}$  are respectively the transport and the absorption free mean path:

$$\begin{aligned} \lambda_{tr}^{-1} &= n_{mol} [\sigma_s(Heavy_{Nuclei}) + 2\sigma_s(oxygen)] \\ \lambda_{abs}^{-1} &= n_{mol} (\sum_i \sigma_{a,i} U^i + \sum_i \sigma_{a,i} Pu^i) \end{aligned}$$

with  $n_{mol}$  the number of heavy nuclei by  $cm^3$ .

### 4.3.3 Prompt neutron flux computation for the clad

The fast neutron computation is given by:

$$\phi^p = \gamma \cdot \Phi \quad (4.13)$$

where

$$\gamma = 9.09 - 3.368 \cdot 10^{-3} \tau + 1.25 \cdot 10^{-6} \tau^2 - 1.326 \cdot 10^{-10} \tau^3 \quad (4.14)$$

$\tau$  is the burn-up and  $\Phi$  the average flux computed in (4.10).

### 4.3.4 Isotopic concentrations

The fissile atom concentration such as  $N_{U^{235}}$ ,  $N_{Pu^{239}}$  and  $N_{Pu^{241}}$  are derived from the PRODHEL model [138], which also computes the nonfissile atom concentration and will replace in the PLEIADES platform the extended version of the RADAR model previously used in METEOR.

The PRODHEL model [138] is a simplified neutron module able to be integrated into a fuel performance code. It is presently implemented in ALCYONE. PRODHEL calculates the evolution over time of the inventory in heavy nuclei, fission products and helium in the pellet (mean values and radial profiles). For this, the code takes into account:

- nuclear reactions occurring in the presence of a neutron flux in the fuel, such as the fission and neutron capture reactions, (n, 2n) and (n,  $\gamma$ ) reactions,
- decay reactions,
- ternary fissions occurring in the calculation of helium production.

The input data of the code are:

- a library containing all the information necessary to calculate the nuclear reactions in the pellet (list of decay reactions associated with each type of nucleus, cross sections values),
- data concerning the main fuel characteristics: initial values of heavy nuclide concentrations, fuel density,
- data on the rod irradiation: linear power function of time, periods of irradiation and inter-cycles, duration of the cooling period.

The evolution of the isotopic concentrations over time is obtained from the synthetic equation (nowadays this equation is used only to calculate the 23 heavy nuclei in order to compute the radial Power  $P(r)$  but the Fission Product term is not linked to the gas swelling aspect yet):

$$\frac{dN(r, t)}{dt} = [X]N(r, t), \quad (4.15)$$

which is a rewriting of the Bateman equation (3.3) of section (3.2.5). Above:

- $N = N(r, t)$  is the vector of concentrations at time  $t$  and radial position  $r$  in the pellet,
- $[X]$  is a reaction matrix including four contributions, written according to the following formulae:

$$[X] = [X]_{\lambda} + [X]_{\sigma} + [X]_{epi} \quad (4.16)$$

Where:

- The matrix  $[X]_{\lambda}$  treats the radiation decay processes acting on the nuclei ( $\alpha$ ,  $\beta^+$ ,  $\beta^-$  or  $\gamma$ ):

$$[X]_{\lambda}(i, j) = -\lambda_i \cdot \delta(i, j) + \lambda_j \cdot \sum_k (R_{j,k} \cdot \epsilon(i, j, k)). \quad (4.17)$$

where  $i$  is the indice of the nucleus at the end of the reaction,  $j$  is the indice of the nucleus at the beginning of the reaction,  $\lambda_i$  and  $\lambda_j$  are the decay constants and  $\delta(i, j)$  is the kronecker symbol. The symbols  $R_{j,k}$  are call the "links connections" by process  $k$  beetwen nuclei from the beginning to the end. It defines the decay fraction of the nucleus  $j$  by a decay process  $k$ . The symbol  $\epsilon(i, j, k)$  is the function that determines if the decay process  $k$  for a nucleus  $i$  is possible. In this case  $\epsilon(i, j, k) = 1$ , otherwise  $\epsilon(i, j, k) = 0$ .

- The matrix of neutron reactions  $[X]_{\sigma}$  includes the values of the cross sections:

$$[X]_{\sigma}(i, j) = \Phi \cdot F(r) \cdot [E]_{\sigma} \quad (4.18)$$

where  $\Phi$  is a 1 group neutron flux which is taken as constant over the fuel pellet slice and is obtained from the equation (4.10). The function  $F(r)$  is a shape function, which considers the diminution of the number of fissions as we enter deeper into the pellet. This corrective factor is applied to each cross section reaction. This shape factor is defined according to the thermal neutron flux distribution  $\Phi_{thermal}(r)$  [197] calculated with ALCYONE as a solution of a second order linear differential equation:  $\Delta \Phi_{thermal}(r) - \alpha^2 \Phi_{thermal}(r) = 0$  with Robin boundary condition, where we have  $\Phi_{thermal}(R_{pellet}) = 1$  at  $r = R_{pellet}$  the radius of the pellet and we have  $\nabla \Phi_{thermal}(0) = 0$  at  $r = 0$ .  $A$  is a corrective factor and  $\alpha$  is defined as follows:

### 4.3. POWER RECONSTRUCTION AT PELLET LEVEL

$$\alpha^2 = A.3[\sum_{iso}(\sigma_{capture}^{iso} + \sigma_{fission}^{iso})N_{iso}].[\sum_{iso}\sigma_{scattering}^{iso}N_{iso} + \sigma_{scattering}^O N_O]$$

After the calculation, the function  $\Phi_{thermal}(r)$  is normalized to 1. This way,  $F(r)$ , which is equal to the renormalized  $\Phi_{thermal}(r)$ , is also equal to 1 by integration over  $r$  of the pellet. The matrix  $[E]_\sigma$  is defined as follow:

$$[E]_\sigma(i, j) = -\sum_k \sigma_k^i \cdot \delta(i, j) + \sum_k \sigma_k^j \cdot reac_k(i, j) \quad (4.19)$$

where  $\sigma_k^i$  is the cross section of the nucleus  $i$  and the reaction  $k$ . The cross sections are computed in the same way as done for APOLLO3 (Eq. (3.3.5)). The computation is done with 172 groups of Energy, in nominal situation. The library is parametrized with the Burn-up  $\tau$ . The symbol  $reac_k(i, j)$  is a function which is equal to 1 if the nuclei  $i$  and  $j$  are linked by the decay process  $k$ , otherwise  $reac_k(i, j) = 0$ .

- The treatment of the epithermal captures is dealt with a special term  $[X]_{epi}$  to estimate the reaction rate and the associated radial profile, picked at the edge of the pellet.

$$[X]_{epi} = \Phi g(r)[E]_{epi}$$

It involves:

- \* the plane neutron flux in the pellet:  $\Phi$ , defined above,
- \* the  $g(r)$  function whose goal is to correct the one-group approach in order to calculate the radial distribution of  $^{239}\text{Pu}$  due to neutron captures in the resonances of  $^{238}\text{U}$ . The treatment originally introduced by Palmer [197] is used, with new values of parameters, fitted on the available experimental data:

$$g(r) = 1 + Ae^{[-B\sqrt{R_{MAX}-r}]} \quad (4.20)$$

where  $A$  and  $B$  are experimental coefficient, and  $R_{MAX}$  is the radius of the fuel pellet.

- \* the matrix  $[E]_{epi}$  has only for nonzero elements:

$$[E]_{epi}(U^{239}, U^{238}) = -[E]_{epi}(U^{238}, U^{238}) = \sigma_{epi}^{U^{238}}$$

and

$$[E]_{epi}(Pu^{240}, Pu^{240}) = -[E]_{epi}(U^{240}, U^{241}) = \sigma_{epi}^{Pu^{240}}$$

where  $\sigma_{epi}^{U^{238}}$  and  $\sigma_{epi}^{Pu^{240}}$  are the epithermal capture cross sections of  $^{238}\text{U}$  and  $^{240}\text{Pu}$ .





## Chapter 5

# Neutronics conclusion

Finally, in this chapter, we summarized all the previous models and improvement point and we rewrote them in order to prepare the coupling part of this study.

### Neutronics Models (initial static state and kinetic transient state):

In this part, we have mathematically defined the Neutronics static and kinetic models we are going to use in our coupling. The core reactor physical description can be carried out using:

- Kinetic equations:
  - The transport equation (Eq. (5.1)), which defines the neutron flux variation function of time, space, angle and neutron energy, and thus the power production. The neutron flux is defined using a Zero Flux boundary condition around the core domain.

$$\begin{aligned}
 \frac{1}{v} \frac{\partial \Psi(\mathbf{r}, E, \boldsymbol{\Omega}, t)}{\partial t} = & -\boldsymbol{\Omega} \cdot \boldsymbol{\nabla} \Psi(\mathbf{r}, E, \boldsymbol{\Omega}, t) - \sum_k (N_k(\mathbf{r}, t) \sigma_k(E) \Psi(\mathbf{r}, E, \boldsymbol{\Omega}, t)) \\
 & + \sum_k \left( N_k(\mathbf{r}, t) \int_0^\infty dE' \int_{4\pi} d\boldsymbol{\Omega}' \sigma_{s,k}(E' \rightarrow E, \boldsymbol{\Omega}' \rightarrow \boldsymbol{\Omega}) \Psi(\mathbf{r}, E', \boldsymbol{\Omega}', t) \right) \\
 & + \frac{1}{4\pi} \sum_k \left( N_k(\mathbf{r}, t) \int_0^\infty dE' \nu_{p,k}(E') \sigma_{f,k}(E') \chi_{p,k}(E' \rightarrow E) \Phi(\mathbf{r}, E', t) \right) \\
 & + \frac{1}{4\pi} \sum_k (\nu_{p,fs,k} \lambda_{fs,k} N_k(\mathbf{r}, t) \chi_{p,fs,k}(E)) + \frac{1}{4\pi} \sum_i (\lambda_{d,i} c_i(\mathbf{r}, t) \chi_{d,i}(E)) + S_{ext}(\mathbf{r}, E, \boldsymbol{\Omega}, t)
 \end{aligned} \tag{5.1}$$

- The precursors evolution equation (Eq. (5.2)) with which the transport equation is coupled in cases of transients and which defines the delayed neutron

emission over the total amount of neutrons (delayed + prompt neutrons) that are participating in the nuclear reaction function of time and space.

$$\begin{aligned} \frac{dc_i^{(k)}(\mathbf{r}, t)}{dt} = & -\lambda_i^{(k)} c_i^{(k)}(\mathbf{r}, t) \\ & + N_k(\mathbf{r}, t) \beta_i^{(k)} \int_0^\infty (dE' \nu_{t,k}(E') \sigma_{f,k}(E') \phi(\mathbf{r}, E', t)) \end{aligned} \quad (5.2)$$

- Static equation:

- The Bateman equation (Eq. (3.3)), is governed by long time operations (time step superior to 1 day). It means that this equation does not directly impact the transient calculation. But it defines the isotopic evolution of the core  $N_k(r, t_0)$ , function of the isotope k, time and space. This equation is needed in order to define the isotopic inventory at the state of the core preaccident that impacts the transient calculation. This equation is also used in order to process the multiparameter cross sections library we are using during our transient calculation regarding each reaction q.

$$\begin{aligned} N_k(r, t) \sigma_{q,k}(E \rightarrow E') &= N_k(r, t_0) \sigma_{q,k}(E \rightarrow E') \\ &= \Sigma_{q,k}(Bu(r), T_{eff}(r, t), D_{mod}(r, t), E \rightarrow E') \end{aligned} \quad (5.3)$$

These cross sections are precalculated and parametrized as function of the Burn-up as well as of the fuel temperature and the fluid density (in our case, the fluid temperature is implicitly defined regarding a constant pressure hypothesis inside the core and do not appear as one of the parameter of the cross sections), which change during the transient regarding the hydraulical, thermal and mechanical state of the core. The Burn-up is defined at constant value during the transient (initial state) regarding each assembly of the core.

**Neutronics numerical specificities:**

Moreover, these equations are computed within a multigroup formulation (Eq. (3.12)) which corresponds to the splitting of the continuum neutron energy term into a discrete and restricted number of neutron energy groups (2 groups in our coupling case). The calculation is obtained using the SPn Kinetic solver of MINOS (APOLLO3 code) over a 3D extruded Finite Elements discretization. This replaces the pointwise cross section

$$\Sigma_{q,k}(Bu(r), T_{eff}(r, t), D_{mod}(r, t), E \rightarrow E')$$

by the multigroup aggregate

$$\Sigma_{q,k}^{g \rightarrow g'}(Bu(r), T_{eff}(r, t), D_{mod}(r, t))$$

with Bu(r) a given function of position, and  $T_{eff}(r, t)$  or  $D_{mod}(r, t)$  space and time varying functions at the scale of the transient accident.

---

**Phenomenological and physical aspects of the transient:**

- Transient aspects:

Considering an accidental situation of a control rod ejection in the central assembly within our academic reactor core context, the neutronics equation (Eq. (5.1)) provide a representative spatially heterogeneous Power/Flux map distribution at each point  $r$  ( $P_{neutro}(r,t)$ ) as given in equation (3.38). This power is used as a source term in the Thermohydraulical ( $P_{fluid}(r,t) = \gamma P_{neutro}(r,t)$ ) and in the Thermo-Mechanical ( $P_{fuel}(r,t) = (1-\gamma) P_{neutro}(r,t)$ ) models, with  $\gamma$  the proportion of power deposited into the fluid. This induces a variation of the hydraulical, thermal and mechanical physical parameter distributions inside the core. In return, these physical variations of  $T_{eff}$  and  $D_{mod}$  at each point  $x$  and time  $t$  modify the multiparameter cross sections locally at each point  $r$  (considering a constant  $Bu$  for each assembly):

$$\Sigma_{q,k}^{g \rightarrow g'}(Bu(r), T_{eff}(r, t), D_{mod}(r, t))$$

These cross sections are used in the Transport and Precursor equations and change the Flux and the precursor proportion. The local variation of the Power will be observed using the 3D  $F_{xyz}(t)$  ( $F_{xyz} = \frac{\max_{x,y,z} |P_{pin}(x,y,z)|}{\langle P(x,y,z) \rangle}$ ), shape factor curves which, at time  $t$ , gives the ratio of the maximal power (maximal with respect to the position  $r$ ) compared to the average core power.

- Static processing:

In order to monitor the neutronic behavior of the core during the transient it can be expected to deal with core integrated neutronic parameters such as the effective multiplication factor  $K_{eff}$  through static parallel processing. The  $K_{eff}$  corresponds to the solution of the eigenvalue problem form  $F \Psi = K_{eff} M \Psi$ , of equation (Eq. (3.32)) in static case at the core scale. If we change the cross sections value or the core state, i.e., the hydraulical, thermal and mechanical physical parameter used in the multiparameter Cross Sections library, then we observe variations of the core behavior through the  $K_{eff}$ . Hence,  $K_{eff}$  gives a scalar measurement of the impact of physical parameter variations. Then, we observe the impact of the physical parameters on the reactivity (or its variation) using the Doppler reactivity  $\rho_{Doppler}(T_{eff}, t)$  for the fuel thermal variation (we only change the Fuel parameter and let the moderator parameters constant):

$$\Delta \rho_{Doppler}(T_{eff}, t) \simeq \frac{1}{k_{eff}(T_{eff}(t_0), D_{mod}(t))} - \frac{1}{(keff(T_{eff}(t), D_{mod}(t)))} \quad (5.4)$$

or, respectively, on the moderator reactivity  $\rho_{moderator}(D_{mod}, t)$  for the hydraulical variations (respectively, we only change the moderator parameters):

$$\Delta \rho_{Doppler}(T_{eff}, t) \simeq \frac{1}{k_{eff}(T_{eff}(t), D_{mod}(t_0))} - \frac{1}{(keff(T_{eff}(t), D_{mod}(t)))} \quad (5.5)$$

**Neutronics coupling aspects:**

The following bloc diagram summarizes the previous sections and conclusion, indicating the equations, the core discretization (at the scale of 1/4 assembly), Neutronics parameters we observe and coupling variables we use in a Best Effort coupling approach, i.e., Neutronics variables in green, Hydrodynamics variables in blue and Thermomechanics variables in red.

The coupling variables consist in:

- Input variables (distributed in space):
  - Fuel temperature  $T_{eff}(r, t)$  (eq. (3.26)),
  - Moderator density  $D_{mod}(r, t)$  (eq. (3.26)) ,
- And output variables (distributed in space):
  - Power production ( $P_{neutro_{integrated}}$  and  $P_{neutro}(r, t)$ ):
  - Fuel power  $P_{fuel}(r, t)$  (eq. (3.41)),
  - Fluid power  $P_{fluid}(r, t)$  (eq. (3.42)).

The impact of coupling will be observed on the following neutronics parameters:

- Reactivities:  $\rho_{Global}(T_{eff}, D_{mod}, t)$ ,  $\rho_{Doppler}(T_{eff}, t)$  or  $\rho_{Moderator}(D_{mod}, t)$
- Power Shape Factors  $F_{xyz}(r)$ .

Parameters Name	Parameters Symbols	Coupling Type	Type
Fuel temperature	$T_{eff}(r, t)$	input	Distributed in space
Moderator density	$D_{mod}(r, t)$	input	Distributed in space
Power productions	Integrated Power - $P_{neutro_{integrated}}$ Local Power - $P_{neutro}(r, t)$ Fuel power - $P_{fuel}(r, t)$ Fluid power - $P_{fluid}(r, t)$	Neutronics observation Neutronics observation output output	Global Distributed in space Distributed in space Distributed in space
Reactivity	$\rho_{Global}(T_{eff}, D_{mod}, t)$ $\rho_{Doppler}(T_{eff}, t)$ $\rho_{Moderator}(D_{mod}, t)$	Neutronics observation	Global
Power Shape Factors	$F_{xyz}(r)$	Neutronics observation	Global

**Table 5.1.** Neutronics input, output and monitored parameters

These output, input and state variables are summarized in the following block diagram.

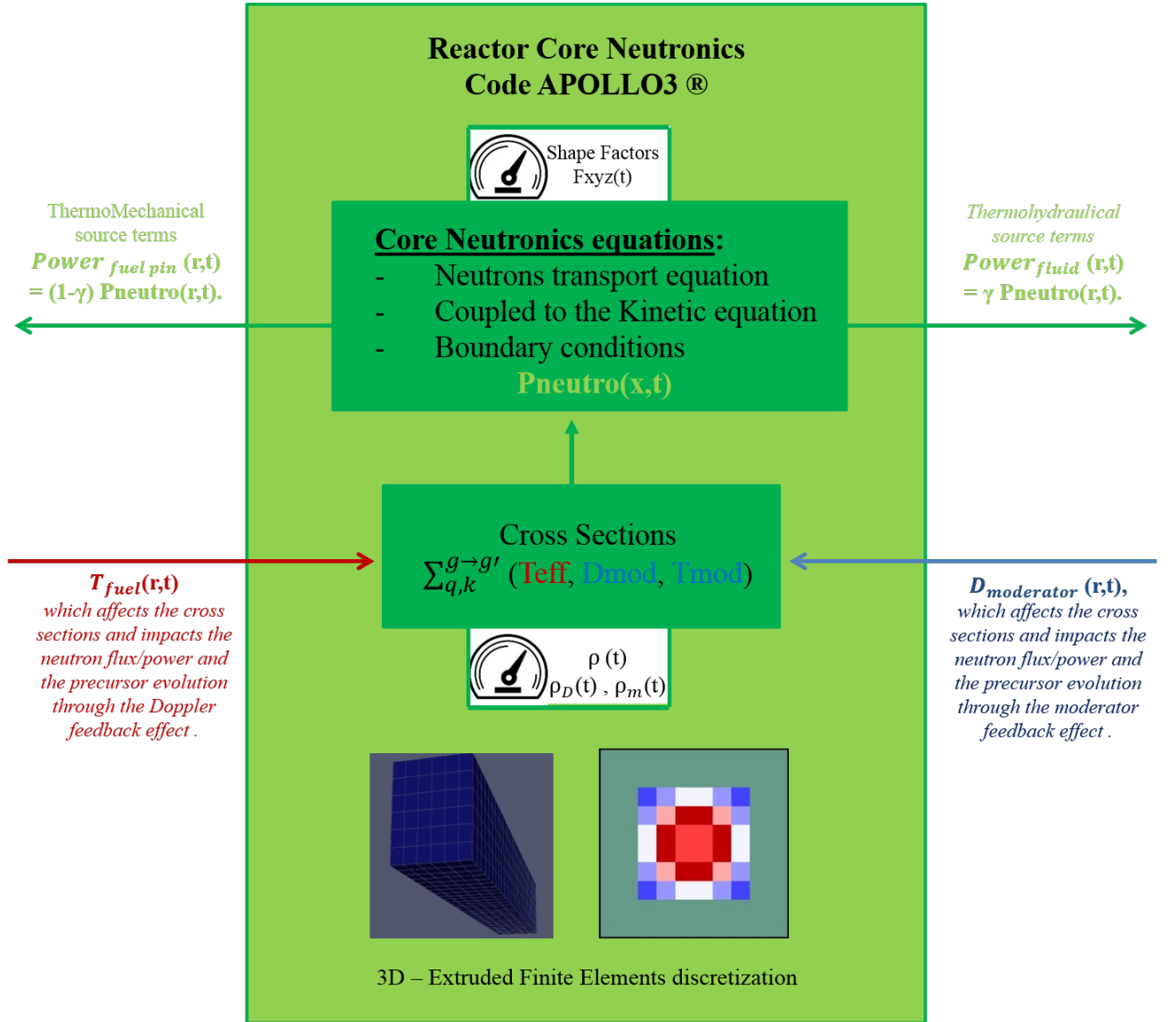


**Figure 5.1.** Neutronics Block diagram with exchange variables and discretization

### Neutronics models Limitations and perspectives of improvement

- Key points taken up and improvements carried out by this study:
  - Considering cross sections using an equivalent fuel pellet temperature  $T_{eff}$  (due to a homogeneous fuel pellet in the Neutronics calculations) and compared to the accurate discretization of the ThermoMechanical code (which produces a fuel pellet temperature distribution  $T(r)$ ), it is compulsory to post treat the accurate temperature  $T(r)$  given by the fuel pin thermal model in order to respect the physical behavior of the core regarding the Doppler feedback reaction. A fundamental key point of our modelling is the proper calculation of  $T_{eff}$  regarding this physical aspect. Here we developed and used the improved strategy (Santamarina and Isotopic formulations) detailed in section ( 7.3). The ultimate perspective would be to use the fuel pellet temperature distribution  $T(r)$  directly inside our neutronics calculations (fine fuel grid).
  - Regarding the Power source term produced by the Neutronic calculation, limitations appear from the evaluation of the  $\gamma$  coefficient. Indeed, it is usually assumed constant in time and space and it prevents any analysis of the impact of the core heterogeneity on these Power distributions. Thus, in order to improve the accuracy of the  $P_{fluid}(x,t)$  and  $P_{fuel}(x,t)$  terms, we developed a Fine Flux Reconstruction detailed in section ( 4.2) and which allowed us to distinguish between power produced to be deposited in the fluid and in the fuel. This method still lacks accuracy at this stage to be used in a proper multiscale coupling and would need to be coupled with a Gamma transport solver. Nevertheless, this first step showed a substantial asset in the perspective of a future multiphysics and multiscale Best Effort coupling considering all the disciplines at the same level of physical description of the core.
- Present Neutronics challenges in perspective of a Best Effort multiphysics calculation:
  - Regarding the Cross sections calculation, limitations appear from their spatial computation. Indeed, the multiparameter cross sections library is pre-calculated using a single assembly with reflection boundary condition. These cross sections do not take care of the environmental aspects such as of the core/reflector flux transition that should require a re-evaluation of the cross sections [140]. These aspects would be a source of uncertainty and discrepancy in an accurate Best Effort calculation.
  - Moreover, in our transient calculation, considering two different neutron sources separately, i.e., the prompt and delayed neutrons, limitations appear from the multigroup computation of the Cross Sections. Indeed, in order to move from a continuum Energy to a discrete formulation (multigroup formulation) we are using a weightedneutron flux and spectrum only based on prompt neutron. Thus, this operation neglects the delayed neutron flux and spectrum contribution which would be source of discrepancy [66].

## Part IV

# ThermoMechanical and Thermohydraulical models





## Chapter 6

# ThermoMechanical equations and Numerical Models of the fuel pin under irradiation

While working on this multiphysics problems we are required to accurately construct the different models upon which the multiphysic coupling will be based. In this chapter, the Thermomechanical fuel performance models are mathematically and numerically formulated. This allows us to pin point the ThermoMechanics coupling variables of our multiphysics problem as well as to define the limitations of the models and the assumptions and hypothesis we made.

### 6.1 Physical Description

In the nuclear core reactor, the fuel is located in the fuel pin [17] [209]. The fuel pin is a metal cladding (Zircaloy IV) filled with fuel pellet of  $\text{UO}_2$ . The fuel pin is the elementary level component of the fuel core. The Thermomechanical aspect is traditionally compute by using constant input values or solid thermal equation. In this chapter, we present models that allow accurate description of the fuel pin and its dynamics (including the mechanical initial state that strongly impacts the mechanical transient evolution). This thermomachanical model is a significant physical asset in order to accurately reflect the fuel pin thermodynamics. Moreover, it involves strong interactions with other disciplines such as in our case Neutronics and Thermohydraulics.

## 6.2 Notations and unknowns

We first introduce the main notation of the problem [165].

ThermoMechanical quantities		
$\sigma_{comb}$	total pellet stress	$N.m^2$
$E_{comb}$	pellet Young modulus	$N.m^2$
$\epsilon_{T_{comb}}$	total strain	$\emptyset$
$\epsilon_{crack}$	crack strain	$\emptyset$
$\epsilon_{creep}$	creep strain	$\emptyset$
$\epsilon_{SS\_D}$	Solid swelling strain	$\emptyset$
$\epsilon_{GS}$	gaseous swelling strain	$\emptyset$
$\epsilon_{Thermal_{FuelPellet}}$	thermal strain in pellet	$\emptyset$
$\sigma_{clad}$	total clad stress	$N.m^2$
$E_{clad}$	clad Young modulus	$N.m^2$
$\epsilon_{T_{clad}}$	total clad strain	$\emptyset$
$\epsilon_p$	plastic clad strain	$\emptyset$
$\epsilon_\nu$	viscous strain in clad	$\emptyset$
$\epsilon_{Thermal_{Clad}}$	thermal strain in clad	$\emptyset$
$J_1(\sigma)$	First invariant of the deviatoric stress tensor	$N.m^2$
$J_2(\sigma)$	second invariant of the deviatoric stress tensor	$N.m^2$
$J_3(\sigma)$	Third invariant of the deviatoric stress tensor	$N.m^2$
$\sigma^{eq}$	von Mises equivalent stress	$N.m^2$
$\mathbf{X}$	internal stress associated with kinematics hardening	$N.m^2$
$p$	porosity	$\emptyset$
$D_G$	fuel grain size	m
$R_o$	yield stress	$N.m^2$
$H$	hardening modulus	
$\nu_t$	slip rate	
$F_t$	tangential force	N
$F_n$	normal force	N
$\mu$	friction coefficient	$\emptyset$
$\rho$	density	$kg.m^{-3}$
$\Omega$	domain used to describe the fuel element geometry	$\emptyset$
$\Omega_\Phi$	frontier with force boundary conditions $\Phi_{BC}$	$\emptyset$
$\Omega_u$	frontier with displacement boundary condition $\mathbf{u}_{BC}$	$\emptyset$
$\alpha$	thermal expansion coefficient	$k^{-1}$

**Table 6.1.** Notations: ThermoMechanical quantities

## 6.2. NOTATIONS AND UNKNOWNNS

Gaseous and chemistry quantities		
$G_{bia}$	the gas concentration per unit volume of fuel located in intragranular bubbles	$mol.m^{-3}$
$C_{bia}$	the number of intragranular bubbles per unit volume of fuel	$\emptyset$
$r_{bia}$	the radius of intragranular bubbles	$m$
$G_{res}$	the gas concentration per unit volume of fuel located in UO2 atomic network	$mol.m^{-3}$
$G_{bie}$	the gas concentration per unit volum of fuel located in intergranular bubbles	$mol.m^{-3}$
$C_{bie}^s$	the number of intergranular bubbles per intergranular unit surface	$m^{-2}$
$r_{bie}$	the radius of intergranular bubbles	$m$
$G_{por}$	the gas concentration per unit volume of fuel located in manufacturing porosity	$mol.m^{-3}$
$G_{rel}$	the gas concentration per unit volume of fuel released in the rod plenum	$mol.m^{-3}$
$\Phi_{FG}$	Fission product production	$\mu mole/mm^3$

**Table 6.2.** Notations: Gaseous quantities

Neutronics and chemistry quantities		
$\Phi(r)$	scalar neutron flux	$n.cm^{-2}.s$
$\Phi^p(r)$	fast neutron flux ( $E > 1MeV$ )	$n.cm^{-2}.s$
$P_{lin}$	lineic neutron power	$W.cm^{-1}$
$P_{vol}$	volumic average neutron power	$W.cm^{-3}$
$P_{vol}(r)$	volumic neutron power	$W.cm^{-3}$
$\sigma_{pf}$	mean value of the one-group fission cross section of each fissile atom (subscript pf)	$cm^2$
$C_{pf}E_{pf}$	concentration of each fissile atom multiplied by its corresponding fission energy	$N.MW.cm^{-3}$
$BU$	Burn-up and $\Delta\tau$ its time step variation	$MWd.t^{-1}$
$\frac{dF}{dt}$	reaction rate $\frac{dF}{dt} = N_k \sigma_k^q \Phi$	$fission.m^{-3}.s^{-1}$

**Table 6.3.** Notations: Neutronics quantities

CHAPTER 6. THERMOMECHANICAL EQUATIONS AND NUMERICAL MODELS OF THE FUEL PIN UNDER IRRADIATION

---

Thermal quantities		
$h$	wall heat transfer coefficient	$W.m^{-2}.K^{-1}$
$T_{wall}$	wall temperature	K
$T_{\infty}$	fluid temperature computed in the thermohydraulic model	K
$T_{Gas_{local}}$	local gas temperature	K
$\Phi_{wall}$	Wall thermal flux	$W.m^{-2}$

**Table 6.4.** Notations: Thermal quantities

The unknown elements (functions of r and t and parametrized by z) of the problem are:

- Temperature of the Fission gas:  $T_{gas}$ ,
- Concentration of the Fission gas:  $D_{gas}$ ,
- Internal pressure of the Fission gas:  $P_{gas}$ ,
- Fuel Pellet Mechanical unknowns: stress  $\sigma_{comb}$ , and irreversible strains  $\epsilon_{crack}$ ,  $\epsilon_{creep}$ ,  $\epsilon_{SS\_D}$ ,  $\epsilon_{GS}$  and  $\epsilon_{Thermal_{FuelPellet}}$
- Clad Mechanical unknowns: stress  $\sigma_{clad}$ , and irreversible strains  $\epsilon_p$ ,  $\epsilon_{\nu}$  and  $\epsilon_{Thermal_{clad}}$
- Thermal transfer coefficient: h

The input surface variables will be:

- Fuel pellet surface temperature :  $T_{wall}$ ,
- Pressure, at this level we neglect the difference between the local pressure and the reference pressure, thus p is not a coupling variable.

Input volumic variables:

- Fuel Power:  $P_{lin}$  as predicted in ( (4.8)) and ( (4.9)) in order to build all the Neutronics parameters of the mechanical problem,
- Fast neutron Flux:  $\Phi^p$  or Fuel power in order to rebuild  $\Phi^p$ .

Output surface variables:

- Thermal coupling coefficient  $A_p$ :  $A_p = \frac{\partial \Phi_{wall}}{\partial T}$ ,
- Thermal coupling coefficient  $S_p$ :  $S_p = \Phi_{wall} - \frac{\partial \Phi_{wall}}{\partial T_{wall}} \cdot T_{wall}$ ,

Typical computational grids are made of:

- 28 radial nodes per fuel pin.
- 30 axial meshes per fuel pin.

The mechanical state of the fuel element is computed by solving the static equilibrium equation ( (6.1)) integrated according to a weak formulation with the finite element method:

$$\nabla \cdot \boldsymbol{\sigma} = 0. \quad (6.1)$$

The thermal equation (conservation of energy) writes:

$$\rho c_p \frac{dT}{dt} - \nabla \cdot \lambda \nabla T - P_{volumic}(r) = 0. \quad (6.2)$$

In addition to this equilibrium principle, the nonlinear behavior of the fuel element is taken into account through several constitutive equations describing the thermomechanical behavior of the pellet, cladding, and pellet-cladding interface, as discussed below.

### 6.3 Constitutive laws for pellet

The pellet constitutive law introduces a linear relation between stress and reversible strain of the form (for more details see [17]):

$$\frac{d\boldsymbol{\sigma}_{comb}}{dt} = \mathbf{E}_{comb} : \left[ \frac{d\boldsymbol{\epsilon}_{T_{comb}}}{dt} - \frac{d\boldsymbol{\epsilon}_{crack}}{dt} - \frac{d\boldsymbol{\epsilon}_{creep}}{dt} - \frac{d\boldsymbol{\epsilon}_{SS\_D}}{dt} - \frac{d\boldsymbol{\epsilon}_{GS}}{dt} - \frac{d\boldsymbol{\epsilon}_{Thermal_{FuelPellet}}}{dt} \right] \quad (6.3)$$

where the variables are defined in section ( 6.2).

#### 6.3.1 Crack law

In order to take into account the anisotropy resulting from cracking, the cracking evolution is defined by three independent yields conditions:

$$\mathbf{f}_{crack} \cdot \mathbf{e}_i = (\mathbf{n}_i : [\boldsymbol{\sigma} - \mathbf{R}(\boldsymbol{\epsilon}^{crack})]) \leq 0 \quad (6.4)$$

with  $i = 1, 2$  or  $3$  and  $\mathbf{n}_i = (\mathbf{e}_i \otimes \mathbf{e}_i)$ . In equation (6.4),  $\boldsymbol{\epsilon}^{crack}$  is the inelastic strain tensor associated to cracking.  $\mathbf{R}$  is the "tensile strength tensor", defined by:

$$R_{ij} = \langle \sigma_i^R - E_i^{crack} \cdot \epsilon_{ii}^{crack} \rangle \cdot \delta_{ij} \quad (6.5)$$

With  $\sigma_i^R$  and  $E_i^{crack}$ , respectively the yield tensile strength of the material and the softening modulus in direction  $i$ .  $\langle X \rangle$  is a function equal to  $x$  if  $x > 0$  and  $0$  if  $x < 0$ . In

equation (6.4) and (6.5), the subscript  $i$  ( $i=1,2,3$ ) refers to the orientation of a unit vector  $\mathbf{e}_i$  normal to the fracture plane. In general, yield criteria as given by (6.4) are defined in the principal coordinate system of the stress tensor at crack initiation. The aim of this study being to describe a crack pattern that can be adequately defined in a cylindrical coordinate system, it is assumed in the calculation that the principal coordinate system ( $\mathbf{e}_i$ ) of the stress tensor can be replaced by the cylindrical coordinate system ( $\mathbf{e}_r, \mathbf{e}_\theta, \mathbf{e}_z$ ) centred on the fragment axis. The crack deformation tensor is defined as follows:

$$\boldsymbol{\epsilon}_{crack} = \epsilon_{crack_{ii}} \mathbf{n}_i \quad (6.6)$$

Each deformation is calculated from the differential system  $d\mathbf{f} = 0$  (coherency law) when the threshold is reached. This equation writes (when  $\mathbf{f}_{crack} \cdot \mathbf{e}_i = 0$ ) :

$$d\mathbf{f}_{crack} \cdot \mathbf{e}_i = \frac{\partial \mathbf{f}_{crack} \cdot \mathbf{e}_i}{\partial \boldsymbol{\sigma}} : d\boldsymbol{\sigma} + \frac{\partial \mathbf{f}_{crack} \cdot \mathbf{e}_i}{\partial \mathbf{R}} : d\mathbf{R} = \mathbf{n}_i : \left[ d\boldsymbol{\sigma} - \frac{\partial \mathbf{R}}{\partial \boldsymbol{\epsilon}_{crack}} : d\boldsymbol{\epsilon}_{crack} \right] = 0 \quad (6.7)$$

which writes:

$$\mathbf{n}_i : \frac{d\boldsymbol{\epsilon}_{crack}}{dt} = \frac{\mathbf{n}_i : \frac{d\boldsymbol{\sigma}}{dt}}{\mathbf{n}_i : \frac{\partial \mathbf{R}}{\partial \boldsymbol{\epsilon}_{crack}} \mathbf{n}_i}. \quad (6.8)$$

Above the 4<sup>th</sup> order tensor  $\frac{\partial \mathbf{R}}{\partial \boldsymbol{\epsilon}_{crack}}$  corresponds to the tangential cracking modulus.

Reactors start-up and shutdown stages during nominal or transient conditions lead to a cyclic thermal loading of the fuel pellet [163]. Thus, crack closure should be taken into account in the model. Nevertheless, these aspect are not used in this work.

Constitutive equations of the fuel cracking model and its validation are more detailed in [163].

### 6.3.2 Creep law

[163] [155]

The total creep strain rate is computed thanks to an incompressible visco plastic formulation. Introducing  $\mathbf{S}$  the deviatoric part of the stress tensor ( $\mathbf{S} := \boldsymbol{\sigma} - \frac{1}{3}Tr[\boldsymbol{\sigma}]\mathbf{I}$ ) and  $\sigma_{eq}$  the Von-Mises equivalent stress, we write:

$$\frac{d\boldsymbol{\epsilon}_{creep}}{dt} = \frac{3}{2} \cdot \frac{d\epsilon_{creep}^{eq}}{dt} \cdot \frac{\mathbf{S}}{\sigma_{eq}} \quad (6.9)$$

$$\frac{d\epsilon_{creep}^{eq}}{dt} = \left(1 + 2.44 \cdot 10^{-19} \frac{dF}{dt}\right) \max\left[\frac{d\epsilon_{st1}}{dt}, \frac{d\epsilon_{st2}}{dt}\right] + \frac{d\epsilon_{irrad}}{dt}. \quad (6.10)$$

Above  $\epsilon_{st1}$  is the stationary creep at low temperature and stress,  $\epsilon_{st2}$  is the stationary creep at high temperature and stress, and  $\epsilon_{irrad}$  is the creep due to irradiation [91]. These terms are given by:

$$\frac{d\epsilon_{st1}}{dt} = \frac{A_1}{D_G^2} \sigma_{eq}^{B_1} e^{\frac{-Q_1}{RT}} \quad (6.11)$$

$$\frac{d\epsilon_{st2}}{dt} = \frac{A_2}{D_G^2} \sigma_{eq}^{B_2} e^{\frac{-Q_2}{RT}} \quad (6.12)$$

$$\frac{d\epsilon_{irrad}}{dt} = A_3 \sigma_{eq}^{B_3} \frac{dF}{dt} e^{\frac{-Q_3}{RT}} \quad (6.13)$$

where  $A_1$ ,  $B_1$ ,  $A_2$ ,  $B_2$ ,  $A_3$  and  $B_3$  are experimental constant values,  $D_G$  the fuel grain size,  $Q_1$ ,  $Q_2$  and  $Q_3$  are activation energy (J/mol),  $R$  the universal gas constant (J/mol/K) and  $\frac{dF}{dt}$  is the fission density rate.

### 6.3.3 Solid Swelling and Densification

The volume variation adds solid swelling (SS) and densification (D):

$$\frac{d\epsilon_{SS+D}}{dt} = \frac{d\epsilon_{SS}}{dt} + \frac{d\epsilon_D}{dt}. \quad (6.14)$$

The densification process is function of the porosity variation as the result of the annihilation of small pores caused by the fission energy activation and thus dependent to the Burn-up  $\tau$  through an industrial law  $f(\tau)$ .

$$\frac{d\epsilon_D}{dt} = \frac{1}{3} \frac{df(\tau)}{dt} \mathbf{I}. \quad (6.15)$$

The densification is assumed to be isotropic and significant when defining the initial mechanical state of the fuel pin. Nevertheless, during a ramp of power or transient situation, the densification is not taken into account in the transient simulation [155]. Solid swelling is linked to solid fission products that tend to modify the crystallographic dimensions of uranium dioxide (some details are given in the following reference [156]) and it is given by:

$$\frac{d\epsilon_{SS}}{dt} = \frac{1}{3} \left( A \rho \frac{d\tau}{dt} \right) \mathbf{I} \quad (6.16)$$

The solid swelling is significant for defining the initial mechanical state of the fuel pin



but, regarding an experimental constant value  $A$  [155], the time duration of our transient and thus the Burn-up variation of the pin, this term will be considered as negligible in a transient simulation.

### 6.3.4 Gas swelling

The volume variation due to the gas swelling (GS) is computed through the differential equation system for gaseous swelling  $f_{GS}(\sigma_{comb})$  detailed below:

$$\frac{d\epsilon_{GS}}{dt} = f_{GS}(\sigma_{comb}) \quad (6.17)$$

The constitutive equations presented in this paper are simplified in order to illustrate the main phenomena taken into account in the simulation of gaseous fission product behavior. A complete description of the constitutive equations used in the MARGARET advanced model of the PLEIADES platform can be found in Ref. [193]. Equation (6.17) is a short writing for the following coupled system of differential equations:

- Balance equation for fission gas product transfer

$$\frac{dG_{bia}}{dt} = f_1(C_{bia}, r_{bia}, G_{res}) + f_2(C_{bia}, r_{bia}, G_{res}) - \frac{G_{bia}}{\tau} \quad (6.18)$$

$$\frac{dG_{res}}{dt} = -f_1(C_{bia}, r_{bia}, G_{res}) - f_2(C_{bia}, r_{bia}, G_{res}) + \Phi_{FG} \quad (6.19)$$

$$\frac{dG_{bie}}{dt} = -\frac{dG_{bia}}{dt} - \frac{dG_{res}}{dt} + \Phi_{FG} - f_{th}(C_{bie}^s, r_{bie})D_{por}kT \left( \frac{G_{bie}}{C_{bie}^s \frac{S_g}{V_g} \frac{4}{3}\pi\alpha\theta r_{bie}^3} - \frac{G_{por}}{f_{por}} \right) \quad (6.20)$$

$$\frac{dG_{por}}{dt} = f_{th}(C_{bie}^s, r_{bie})D_{por}kT \left( \frac{G_{bie}}{C_{bie}^s \frac{S_g}{V_g} \frac{4}{3}\pi\alpha\theta r_{bie}^3} - \frac{G_{por}}{f_{por}} \right) - \frac{dG_{rel}}{dt} \quad (6.21)$$

$$\frac{dG_{rel}}{dt} = f_{th}(C_{bie}^s, r_{bie})D_{rel}P_H \left( \frac{G_{por}}{f_{por}} - p_{int} \right) \quad (6.22)$$

- Gas state equations

$$\left( p_{hia} + \frac{2\gamma}{r_{bia}} \right) \frac{4}{3}r_{bia}^3 = \frac{G_{bia}}{C_{bia}}kT \quad (6.23)$$

$$\left( p_{hie} + \frac{2\gamma\sin(\theta)}{r_{bie}} \right) \frac{4}{3}\pi\alpha\theta r_{bie}^3 = \frac{G_{bie}}{C_{bie}^s \frac{S_g}{V_g}}kT \quad (6.24)$$

- Constitutive equation for pressurized cavities' behavior in solid medium

$$\frac{dC_{bia}}{dt} = f_3(C_{bia}, r_{bia}) - \frac{C_{bia}}{\tau} \quad (6.25)$$

$$\frac{dr_{bia}}{dt} = \frac{D_u \Omega}{kT r_{bia}} (p_{hia} - p_H) \quad (6.26)$$

$$\frac{dr_{bie}}{dt} = \frac{D_{gb} \Omega}{kT r_{bie}} (p_{hie} - p_H) \quad (6.27)$$

The equations ( (6.18) - (6.27)) compose the balance equations for fission gas product transfer where  $G_{bia}$  is the gas concentration per unit volume of fuel located in intragranular bubbles,  $C_{bia}$  is the number of intragranular bubbles per unit volume of fuel,  $r_{bia}$  is the radius of intragranular bubbles,  $G_{res}$  is the gas concentration per unit volume of fuel located in UO2 atomic network,  $G_{bie}$  is the gas concentration per unit volume of fuel located in intergranular bubbles,  $C_{bie}^s$  is the number of intergranular bubbles per intergranular unit surface,  $r_{bie}$  is the radius of intergranular bubbles,  $G_{por}$  is the gas concentration per unit volume of fuel located in manufacturing porosity and  $G_{rel}$  is the gas concentration per unit volume of fuel released in the rod plenum.

Equations (6.18) to (6.24) are used to compute the evolution of the fission gas rate through a conservation principle between the amount of gas  $G_{res}$  available in the UO2 atomic network and the amount  $G_{rel}$  released in the rod plenum. Functions  $f_1$  and  $f_2$  (in Eqs (6.18) and (6.19)) compute the amount of gas going from the UO2 atomic network to intragranular bubbles, respectively, through two different mechanisms: gas diffusion in UO2 and gas captured by moving intragranular bubbles. The variable  $\tau$  in Eqs (6.18) and (6.25), equals to the mean time needed for intragranular bubbles to move at grain boundary, is used to compute the gas flow rate due to intragranular bubbles transport in Eq. (6.18), and to compute the bubbles concentration rate leaving the grain in Eq. (6.25). Fission gas production  $\Phi_{FG}$  (from Eq. (6.30)) during the transient stage is added as a source in Eqs. (6.19) and (6.20), which are, respectively, used for the balance of gas in the UO2 atomic network and in intergranular bubbles. A Heaviside function  $f_{th}$  is used in Eqs. ( (6.20) - (6.22) to avoid gas release to porosity and plenum when the surface concentration  $C_{bie}^s$  (assumed constant in our case and equal to the number of precipitation sites regarding a data tab function of the temperature and the pressure of the fuel pin) and the radius of intergranular bubbles  $r_{bie}$  are lower than threshold values.  $f_{por}$  is the porosity volumic fraction and  $p_{int}$  the internal pressure of the fuel pin. The gas flow rates between intergranular bubbles, manufacturing porosity, and rod plenum, are computed through a diffusion principle with two parameters called  $D_{por}$  and  $D_{rel}$ , respectively, for the porosity and the plenum.

Gas state Eqs. (6.23) and (6.24) are derived from the ideal gas law, and the gas tension surface effect  $\gamma$  is not neglected due to the small values of bubble radius. In Eq. (6.24),

two shape factors,  $\theta$  and  $\alpha$ , are introduced to account for the lenticular geometry of intergranular bubbles. Function  $f_3$  in Eq. (6.25) compute the decrease in the intragranular bubble concentration rate due to coalescence, which is seen as a consequence of a nonuniform displacement of intragranular bubbles.

The coupling effect with mechanical hydrostatic pressure  $p_H$  in Eq. (6.28) is taken into account through Eqs. (6.26) and (6.27), where the main strain mechanism of the bubble is assumed to be a vacancy flux due to self UO2 diffusion ratio  $D_u$  in Eq. (6.26) and surface grain boundary diffusion ratio  $D_{gb}$  in Eq. (6.27),  $p_{hia}$  and  $p_{hie}$  are respectively normal stress at the interface between gas and solid for intragranular and intergranular bubbles and where  $\Omega$  is the atomic volum of atoms.

$$p_H = -\frac{1}{3}tr[\sigma_{comb}]. \quad (6.28)$$

For each time step of the thermomechanical resolution, this differential equation system is solved in order to compute the gaseous swelling rate as the sum of intragranular swelling and intergranular swelling:

$$\epsilon_{GS} = C_{bia} \frac{4}{3} \pi \alpha r_{bia}^3 + C_{bie} \frac{4}{3} \pi \alpha r_{bie}^3 \quad (6.29)$$

where the concentration of intergranular bubbles per unit volume is derived from the concentration per unit surface  $C_{bie}^s$  multiplied by the ratio between the total surface grain boundary  $S_g$  and the total grain volume  $V_g$ :  $C_{bie} = C_{bie}^s \frac{S_g}{V_g}$ .

In this model, the Gas Fission Product  $\Phi_{FG}$  is taken into account by using a generation term distinct from the PF generation term of the PRODHIL model (i.e. (section 4.3)). This empirical PF generation model comes from a METEOR heritage [203] and provides an "average" gas fission product concentration, e. g. we do not distinguish gases between them but we observe an average behavior of the gases mixture. Its expression is defined below:

$$\Phi_{FG} = \int_{\Delta t} (0.578 \times 10^{-4} - 0.043 \times 10^{-4} \phi^p) P_{volumic}(r) dt \quad (6.30)$$

where  $\Phi_{FG}$  is the term of FP production ( $\mu mole/mm^3$ ),  $\phi^p$  is the neutron flux for  $E > 1MeV$ ,  $P_{Volumic}(r)$  is the local volumic power and  $\Delta t$  is the evolution time step. Because the constitutive gaseous swelling equations  $f_{GS}(\sigma_{comb})$  cannot be easily introduced into Eq. (6.3), an external iteration process is needed between the mechanical problem, Eqs. (6.1) and (6.3), and the gaseous swelling problem, Eq. (6.17). This iteration process is based on the fixed point method where the coupling variables are the effective stress in the bulk material and the gaseous swelling strain variation  $d\epsilon_{GS}$  during time step  $\Delta t$ .

### 6.3.5 Thermal expansion

It is given by the following orthotropic law:

$$\frac{d\epsilon_{Thermal\_FuelPellet}}{dt} = \alpha \frac{dT}{dt} \quad (6.31)$$

with a different dilatation coefficient in each direction:

$$\alpha = \begin{pmatrix} \alpha_{rr} & 0 & 0 \\ 0 & \alpha_{\theta\theta} & 0 \\ 0 & 0 & \alpha_{zz} \end{pmatrix}. \quad (6.32)$$

### 6.3.6 Fuel pellet Physical data

They are governed by semi-empirical laws which have been experimentally validated.

- Pellet Young modulus [251]

$$E \begin{cases} = (1 - 2.5P)(2.2693 \times 10^2 + 1.5399 \times 10^{-2}T - 9.597 \times 10^{-6}T^2) & \text{if } T \leq 2610 \text{ and } P \leq 0.30 \\ = \frac{1-P}{1+6P}(2.2693 \times 10^2 + 1.5399 \times 10^{-2}T - 9.597 \times 10^{-6}T^2) & \text{if } T \leq 2610 \text{ and } P > 0.30 \\ = (1 - 2.5P)(-1.33445 \times 10^3 + 1.18106T - 2.38803 \times 10^{-4}T^2) & \text{if } T > 2610 \text{ and } P \leq 0.30 \\ = \frac{1-P}{1+6P}(-1.33445 \times 10^3 + 1.18106T - 2.38803 \times 10^{-4}T^2) & \text{if } T > 2610 \text{ and } P > 0.30 \end{cases} \quad (6.33)$$

- UO2 density [251]

$$\rho = 10950 \cdot (1 - P_o) \cdot (1 + \zeta_{vol}) \quad (6.34)$$

where  $P_o$  is the initial porosity and  $\zeta_{vol}$  the volumic deformation.

- Porosity [251] The porosity  $P$  is relative to a mechanical densification model [155] (this model is not activated in case of ramp of power). The empirical equation of the porosity is defined below [155]:

$$P = \frac{P_o - GS}{1 - G} \quad (6.35)$$

where  $P_o$  is the initial porosity and the swelling due to the Fission Products:

$GS = 6.42384 \cdot 10^{-5} \rho \Delta\tau$ , where  $\rho$  is the volumic mass and  $\Delta\tau$  is the Bu.

- Shear modulus [251]

$$G \left\{ \begin{array}{ll} = (1 - 2.25P)(85.83 - 5.157 \times 10^{-3}T - 3.747 \times 10^{-6}T^2) & \text{if } T \leq 2610 \\ & \text{and } P \leq 0.30 \\ = \frac{1-P}{1+3.85P}(85.83 - 5.157 \times 10^{-3}T - 3.747 \times 10^{-6}T^2) & \text{if } T \leq 2610 \\ & \text{and } P > 0.30 \\ = (1 - 2.25P)(-5.7625 \times 10^2 + 5.02189 \times 10^{-1}T - 1.00939 \times 10^{-4}T^2) & \text{if } T > 2610 \\ & \text{and } P \leq 0.30 \\ = \frac{1-P}{1+3.85P}(-5.7625 \times 10^2 + 5.02189 \times 10^{-1}T - 1.00939 \times 10^{-4}T^2) & \text{if } T > 2610 \\ & \text{and } P > 0.30 \end{array} \right. \quad (6.36)$$

- Poisson coefficient [251]  $\nu = \frac{E}{2G} - 1$
- Elastical limit [251]  $\sigma_{el} = 210 MPa$

## 6.4 Constitutive laws for the fuel pin cladding

The clad constitutive law is defined as follows [165] [17]:

$$\frac{d\boldsymbol{\sigma}_{clad}}{dt} = \mathbf{E}_{clad} : \left[ \frac{d\boldsymbol{\epsilon}_{T_{clad}}}{dt} - \frac{d\boldsymbol{\epsilon}_p}{dt} - \frac{d\boldsymbol{\epsilon}_\nu}{dt} - \frac{d\boldsymbol{\epsilon}_{ThermalClad}}{dt} \right] \quad (6.37)$$

### 6.4.1 Viscoplastic behavior

The plastic orthotropy of the material is describe by hill's quadratic yiel criterion [147] [163] [155]:

$$\sigma_{eq}^{Hill}(\boldsymbol{\sigma}_{clad}, T, \phi^p) = \sqrt{\boldsymbol{\sigma}_{clad} : \mathbf{H}(T, \phi^p) : \boldsymbol{\sigma}_{clad}} \quad (6.38)$$

where  $\sigma_{eq}^{Hill}$  is the equivalent stress,  $\boldsymbol{\sigma}_{clad}$  is the stress tensor and  $\mathbf{H}$  is a temperature and irradiation dependent symmetric fourth rank tensor. The viscoplastic strain rate tensor  $\frac{d\boldsymbol{\epsilon}_p}{dt}$ , obeys the normality rule and is given by:

$$\frac{d\boldsymbol{\epsilon}_p}{dt} = \frac{dp}{dt} \frac{\partial \sigma_{eq}^{Hill}}{\partial \boldsymbol{\sigma}_{clad}} \quad (6.39)$$

where the equivalent viscoplastic strain rate  $\frac{dp}{dt}$  is given by:

$$\frac{dp}{dt} = \frac{dp_0}{dt} \left( \frac{\sigma_{eq}^{Hill}(\sigma_{clad}, T, \phi^p)}{\eta((p, T, \phi^p, \xi))} \right)^{1/m} \quad (6.40)$$

Above  $m$  is the strain rate sensitivity exponent which in certain case may vary as function of temperature and prompt neutron flux,  $\frac{dp_0}{dt}$  is the reference strain rate fixed to  $1s^{-1}$ ,  $\phi^p$  is the fission flux (Energy  $E \geq 1\text{MeV}$ ),  $\xi = \frac{z}{l}$  is the normalized axial position with  $l$  the total height of the clad tube and  $z$  the axial position from the bottom of assembly, and  $\eta$  is a non linear viscosity coefficient related to the strength ( $\xi$  dependent) coefficient and the strain hardening coefficient. More detailed are given in ref [147].

### 6.4.2 Creep behavior

The nonlinear behavior of the cladding under irradiation is taken into account in the creep model of ALCYONE following the formulation [52]:

$$\frac{d\epsilon_\nu}{dt} = \frac{3}{2} \cdot d\epsilon_\nu^{eq} \cdot \frac{\mathbf{S}}{\sigma_{eq}} \quad (6.41)$$

where  $\mathbf{S}$  is the deviatoric part of the stress tensor,  $\sigma_{eq}$  is the Von Mises equivalent stress and  $\epsilon_\nu^{eq}$  given by:

$$\begin{aligned} \frac{d\epsilon_\nu^{eq}}{dt} = & A \cdot (\sigma_{eq})^{n_p} \cdot e^{-Q_p/RT} \cdot e^{-Bt} \\ & + C \cdot (\sigma_{eq})^{n_s} \cdot e^{-Q_s/RT} \Phi^p \end{aligned} \quad (6.42)$$

In the equation (6.42)  $\frac{d\epsilon_\nu}{dt}$  is the creep strain rate,  $t$  the time,  $T$  the temperature and  $\Phi^p$  the fast neutron flux, ( $A, n_p, Q_p, B, C, n_s, Q_s$ ) are materials parameters and  $R$  is the universal gas constant. The creep rate enhancement due to the effect of the fast neutron flux  $\Phi^p$  ( $E > 1\text{MeV}$ ) on the material is taken into account in the second term of (6.42), which models creep by irradiation. The thermal creep of the material is introduced in the first term of (6.42). To account for the material behavior in the whole loading range, we use two different sets of material parameters for creep at a low stress level (base irradiation) and creep at a high stress level. The anisotropic behavior of the cladding, which is particularly important for some alloys, can also be taken into account by using Hill's equivalent stress [243] instead of the Von Mises equivalent stress in (6.42).

### 6.4.3 Thermal expansion

It is given by the following orthotropic law:

$$\frac{d\epsilon_{Thermal\_FuelClad}}{dt} = \boldsymbol{\alpha} \frac{dT}{dt} \quad (6.43)$$

where,

$$\boldsymbol{\alpha} = \begin{pmatrix} \alpha_{rr} & 0 & 0 \\ 0 & \alpha_{\theta\theta} & 0 \\ 0 & 0 & \alpha_{zz} \end{pmatrix} \quad (6.44)$$

### 6.4.4 Fuel pellet Cladding Physical data

- Clad Young modulus [251]

$$\mathbf{E} \begin{cases} = 1.088 \times 10^5 - 54.75T - 9.597 \times 10^{-6}T^2 & \text{if } T \leq 1090 \\ = 1.01221 \times 10^5 - 47.7969T & \text{if } 1090 < T \leq 1250 \\ = 0.921 \times 10^5 - 40.5T & \text{if } T > 1250 \end{cases} \quad (6.45)$$

- Poisson coefficient [251]  
 $\nu = 0.34$

- Elastical limit [251]  
 $\sigma_{el} = 295 MPa$

## 6.5 Boundary conditions and final mechanical problem

The mechanical boundary conditions are:

- Hydraulic loading over the external surface of the clad:  
 $\boldsymbol{\sigma} \cdot \mathbf{n} = -p_{fluid} \cdot \mathbf{n},$
- No penetration of the fluid through the wall:  
 $\mathbf{u}_{solid} \cdot \mathbf{n} = \mathbf{u}_{fluid} \cdot \mathbf{n},$   
(This law is used in the thermohydraulic model),
- Clad-Pellet unilateral contact: The mechanical 1D contact between the clad and the pellet corresponds to an unilateral relation. In case of a multi-D description, the mechanical contact between the clad and the pellet is done by the CAST3M operator **CAST3M IMPO**, which is also used in order to compute the contact between pellet fragments. This operator takes into account the non penetration and friction condition of the problem.

$$U_N = \xi_r^c(r_c) + h_{gap} - \xi_r^f(r_f) \geq 0. \quad (6.46)$$

Above  $U_N$  is the present gap opening. When it reaches 0 (closing) a positive normal stress vector  $N$  is generated (force per unit surface)

$$N \geq 0, U_N \cdot N = 0, \quad (6.47)$$

together with a coulomb friction stress vector  $T$

$$U_T > 0, -T = \mu \xi \text{ or } U_T = 0, -T < \mu \xi \quad (6.48)$$

where  $\mu$  is the friction coefficient,  $\xi = \frac{U_T}{|U_T|}$  is the displacement direction.

Its value is equal to  $\mu = 0.47$ . Friction is of primary importance with respect to stress-or-strain concentration in the cladding [219], [31] and regarding fuel cracking. [242], [271] Measures of the friction coefficient between nonirradiated fuel materials and Zircaloy materials are usually within 0.4 to 0.7 and are almost independent of the contact pressure, temperature, and oxide thickness. Irradiation can enhance friction and even lead to chemical bonding between the pellet and the cladding [271] at high burnup. Nevertheless, friction phenomena will not be taken into account in this study where the only unknown will be the radial displacement.



- invariant axis displacement:  $\xi_r^f(0) = 0$ ,
- Along the z direction, we will assume the axisymmetric generalized plane strain assumption assuming that  $\sigma_{zz}$  is independent of z inside the cladding and the pellet (each slice is processed independently but coupled to the other slices through pressure and weight of above slices) which controls the axial stress  $\sigma_{zz}(z)$ . From the static equilibrium Eq. (6.1) integrated according to a weak formulation with the finite element method, considering the axisymmetry assumption and the constitutive law corresponding to the pellet (6.3) and the clad (6.37) materials, the fuel pin mechanical problem takes the form.

$$u^m = \begin{pmatrix} K_{11}^m & K_{12}^m \\ K_{21}^m & K_{22}^m \end{pmatrix} \cdot \begin{pmatrix} u_r^m \\ \epsilon_{zz}^{m,0} \end{pmatrix} = \begin{pmatrix} f_r^m \\ F_z^m \end{pmatrix}, \quad (6.49)$$

where  $u_r^m$  is the unknown vector of the radial displacement of the material m,  $\epsilon_{zz}^{m,0}$  is the generalized plane strain of the material m and  $K_{11}^m, K_{12}^m, K_{21}^m$  are the different stiffness operator,  $f_r^m$  is the resulting radial external forces and  $F_z^m$  is the resulting vertical external forces (that is the vertical resultant of the gravity force applied inside the section, and of the pressure forces  $P_{ext}(z)$  and  $P_{int}(z)$  applied on the external surface of the considered section) per unit Z at section z.  $P_{int}(z)$  is evaluated through an axial linear interpolation of the value of the pressure over the whole fuel pin (initial pressure + fission gas release) and  $P_{ext}(z)$  is considered as constant and equal to the input data ( $P_{ext} = 155$  bar). Moreover, the second line of equation (6.49) expresses the vertical balance of each material section.

$$\int_{S^m} \sigma_{zz}^m dS = F_z^m, \quad (6.50)$$

where  $S_{pellet}$  and  $S_{clad}$  are respectively the pellet and clad area and  $\sigma_{zz}^m$  is a function  $\sigma_{zz}^m = f(\epsilon_{rr}^m, \epsilon_{\theta\theta}^m, \epsilon_{zz}^{m,0})$ . Knowing the  $F_z^m$  we can determine  $\epsilon_{zz}^{m,0}$  and then solve the above system in order to calculate  $u_r^m$ . In case of contact between the pellet and the clad, the equation (6.49) can be rewritten as followed:

$$\begin{pmatrix} K_{11}^m & K_{12}^m & 0 \\ K_{21}^m & K_{22}^m & 1 \\ 0 & 1 & 0 \end{pmatrix} \cdot \begin{pmatrix} u_r^m \\ \epsilon_{zz}^{m,0} \\ R_z^m \end{pmatrix} = \begin{pmatrix} f_r^m \\ F_z^m \\ \epsilon_{zz}^0 \end{pmatrix}, \quad (6.51)$$

where the third line is used in order to impose the generalized plane strain continuity ( $\epsilon_{zz}^{pellet,0} = \epsilon_{zz}^{clad,0}$ ),  $R_z^{clad}$  (respectively  $-R_z^{pellet}$ ) is the pellet/clad vertical contact force density.

## 6.6 Thermal modelling

As seen before in section ( 6.2), in both cladding and pellet the temperature distribution is computed using the energy conservation law:

$$\rho C_p \frac{dT}{dt} + \nabla \cdot \lambda \nabla T + P_{volumic}(x) = 0, \quad (6.52)$$

where  $\rho$ ,  $C_p$  and  $\lambda$  are respectively the density, thermal capacity and the thermal conductivity of the medium,  $P_V^{local}$  is the volumic input power given by eq. (4.11).

Thermal conductivity, capacity and emissivity are defined as follows:

- Fuel pin Thermal conductivity [155]. It is a function of the porosity, the temperature and the Burn-up:

$$\lambda_f = \lambda_T \lambda_P \lambda_B \quad (6.53)$$

whith  $\lambda_T$  a reference temperaure dependent conductivity , and  $\lambda_P$  and  $\lambda_B$  correctors taking into account burn-up and pressure effects. In more details, we have:

$$\begin{cases} \lambda_B = 1 & \text{if } \tau = 0 \\ \lambda_B = \lambda_B^1 \lambda_B^2 & \text{if } \tau > 0 \end{cases}$$

and

$$\begin{aligned} \lambda_B^1 &= \alpha \operatorname{atan}\left(\frac{1}{\alpha}\right) \text{ with } \alpha = \frac{A_1}{\tau^{A_2}} + A_3 \sqrt{\frac{T}{\tau}}; \\ \lambda_B^2 &= \left[ 1 + \frac{A_4 \tau}{(A_5 \tau) \left( 1 + e^{\frac{A_6 - T}{A_7}} \right)} \right] \left[ 1 - \frac{A_8 (1 - e^{-\tau})}{1 + e^{\frac{T - A_{10}}{A_{11}}}} \right]; \\ \lambda_P &= \frac{1 - P}{1 + 2P}; \\ \lambda_T &= \frac{1}{A_{12} + A_{13} T} + \frac{A_{14}}{T^2} \cdot e^{\frac{-A_{15}}{T}}; \end{aligned}$$

Above,  $A_i$  with  $i \in [1; 15]$  are experimental constant values [155], T is the temperature,  $\tau$  is the burn-up and P is the total porosity.

- Fuel pin Thermal capacity (W.s/K) [203]. It is a function of the absolute temperature:

$$C_p(T_k) = A_1 + A_2 T_k - A_3 T_k^2 + A_4 T_k^3 \quad (6.54)$$

where  $C_p(T_k)$  is the thermal capacity in  $cal.mole^{-1}.K^{-1}$  then converted thank to the isotopic inventory in  $Wh.g^{-1}.K^{-1}$  and  $A_i$  with  $i \in [1; 4]$  are experimental constant value [203].

- Fuel pin Emissivity [155]  
 $\epsilon_f = 0.87$
- Clad Thermal conductivity (W/(m.K)) [155]  
 $\lambda_{clad} = A_1 + A_2T - A_3T^2 + A_4T^3$  where  $A_i$  with  $i \in [1; 4]$  are experimental constant values [155],
- Clad Emissivity [155]  

$$\epsilon_{cl} = \begin{cases} = 0.325 + 20.1246\epsilon_{oxide} & \text{if } T \leq 1500K \text{ and } \epsilon_{oxide} \leq 3.88\mu m \\ = (0.325 + 20.1246\epsilon_{oxide})e^{\frac{1500-T}{300}} & \text{if } T > 1500K \text{ and } \epsilon_{oxide} \leq 3.88\mu m \\ = 0.3808642 - 50 \times 10^{-6}\epsilon_{oxide} & \text{if } T \leq 1500K \text{ and } \epsilon_{oxide} > 3.88\mu m \\ = (0.3808642 - 50 \times 10^{-6}\epsilon_{oxide})e^{\frac{1500-T}{300}} & \text{if } T > 1500K \text{ and } \epsilon_{oxide} > 3.88\mu m \end{cases}$$

The time and space discretization will be detailed in section ( 7.1). A special attention is given the gap conductance between fuel and cladding, where we must impose a thermal flux continuity and the constitutive equation relating this flux to the temperature jump:

$$\lambda_{clad} \frac{\partial T_{clad\_int}}{\partial n} = \lambda_f \frac{\partial T_{fuel\_ext}}{\partial n} = \Phi_{gap}, \quad (6.55)$$

$$\Phi_{gap} = h_{gap}(T_{clad\_int} - T_{fuel\_ext}). \quad (6.56)$$

The bulk heat transfert coefficient  $h$  consists of a radiation component  $h_{rad}$ , a gap component  $h_{gap}$  independent of contact pressure  $P$ , and a component  $h_{contact}$  (contact term), depending on the contact pressure:

$$h_{gap} = h_{rad} + h_{cond} + h_{contact}. \quad (6.57)$$

It is demonstrated unambiguously in the literature (e.g. [96]) that heat transfer by convection can be neglected. Therefore, this term has not been considered the equation (6.57). The contribution of the radiative component is very small during normal operations (less than 1%) because of the relatively low surface temperatures. Under accident conditions, however, this term may make a substantial contribution. For the radiation component  $h_{rad}$  we have:

$$h_{rad} = C_{f,cl} \frac{T_f^4 - T_{cl}^4}{T_f - T_{cl}} \quad (6.58)$$

with

$$C_{f,cl} = \frac{C_s}{1/\epsilon_f + 1/\epsilon_{cl} - 1} \quad (6.59)$$

where  $C_s$  is the Stefan-Boltzmann constant,  $\epsilon_i$  is the Emissivity and  $T_i$  is the temperature at the surface  $i$ . Here and in the text below, subscript  $i$  relates to the fuel (f) and cladding (cl), and subscript  $g$  relates to gas.

The gap component  $h_{gap}$  consists of the heat transfer coefficient  $h_{i,g}$  of the surface zone and the heat transfer coefficient  $h_g$  in the gap:

$$\frac{1}{h_{cond}} = \frac{1}{h_{f,g}} + \frac{1}{h_{cl,g}} + \frac{1}{h_g} \quad (6.60)$$

The previous equation (6.60) expresses the series connections of the thermal resistances in gas.

The heat transfer coefficient  $h_{i,g}$  is given by:

$$h_{i,g} = \frac{\lambda_{i,g}}{\Delta S_i} = \frac{\lambda_g \{ \beta_1 \Delta S_i (1 - \lambda_g / \lambda_i) + 1 \}}{\Delta S_i} \quad (6.61)$$

where  $\lambda$  is the Thermal conductivity,  $\Delta S_i = \beta_2 \Delta R$ ,  $\Delta R$  is the arithmetic mean roughness and  $\beta_1, \beta_2$  are model parameters [155].

The heat transfer model for the actual (real) gap must take into consideration that the gap width may be small compared to the mean free path of the gas (Knudsen condition) and that the gas molecules therefore lose their energy by direct collision with the solid. This effect is allowed by a fictitious enlargement of the real gap by the so-called "gas extrapolation length"  $l$ , where  $l$  depends on the gas conditions, the gas composition and the solid. Hence the heat transfer coefficient in the gas,  $h_g$ , can be defined as follows:

$$h_g = \frac{\lambda_g}{s + l_f + l_{cl}} \quad (6.62)$$

where  $l$  is the gas extrapolation length and  $s$  is the real gap width. See the chapter (19) in Annexe part for more details.

The equation (6.61) differs from other models. By introducing the parameter  $\beta_1$ , the surface increase by roughness is taken into account; However, if the model parameter  $\beta_1$  is set to zero, equation (6.60) can be written in the form,

$$h_{cond} = \frac{\lambda_g}{s + \beta_2 (\Delta R_f + \Delta R_{cl}) + l_f + l_{cl}} \quad (6.63)$$

which was first given by Ross and Stoute [221].

The heat transfer coefficient  $h_{contact}$  reproduces the improvement in bulk heat transfer due to contact pressure. In accordance with equation (6.57), the quantity  $h_{contact}$  can therefore be interpreted as the heat transfer coefficient in a vacuum under contact conditions. Factors influencing the heat transfer coefficient  $h_{contact}$  are discussed in [131]. The

correlation is given by,

$$h_{contact} = \beta_5 \bar{\lambda} \Delta \bar{R} \left( \frac{P}{\Delta \bar{R}^2 H} \right)^{\beta_6} \quad (6.64)$$

where  $\beta_5, \beta_6$  are model parameters,  $P$  is the contact pressure,  $H$  is equal to the  $\min[\sigma_{fuel}, \sigma_{clad}]$  in term of yield stress tensor and  $\bar{\lambda}, \Delta \bar{R}$  are respectively average values of thermal conductivity and arithmetic mean roughness.

Equation (6.64) differs also from other correlations in the open literature. It was shown that for pairs of different materials (Al-Al, steel-steel, Al-steel, UO<sub>2</sub>-Zircaloy) the parameter  $\beta_6$  was always approximately 0.7, and that equation (6.64) can be considered to apply reasonably well over several orders of magnitude of  $P$ . In any case, we must observe that because (6.64) the bulk heat transfer coefficient  $h_{gap}$  strongly depends on the contact condition. This strong and localized nonlinearity introduces a nonlinear thermomechanical coupling which will impact the results of our coupling chapter (13).

## 6.7 Discretization and code description

Alcyone is using a 3D finite element method (based on Finite Element code CASTEM [2]) but the fuel pin geometry which has a rotational symmetry allows us to use an axisymmetric model, i.e., 1D Finite Element modelling in figure (6.1). In fact, a 1.5D modelling is used. This modelling consists in coupling all the axial fuel pin slices together thanks to boundaries conditions in  $\epsilon_{zz}$  (section (6.5)).

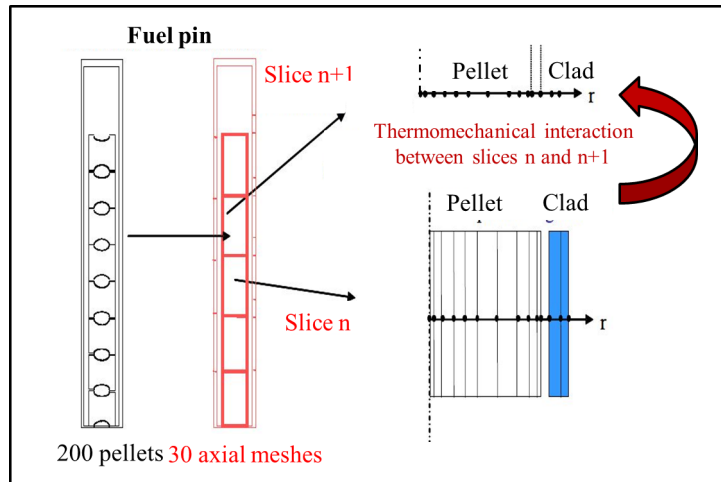


Figure 6.1. 1D modelling with ALCYONE [164]

## Chapter 7

# Best Effort improvement of the fuel pin ThermoMechanical models

In this chapter, on the one hand, we focus on the thermal transfer between the fuel pin and the fluid through an implicit linearized approach developped in the context of the multiphysics modelling of this PhD work. On the other hand, we detail different formulations of the average temperature (called effective temperature  $T_{eff}$ ) seen by the neutronic part.

### 7.1 Condensation of the Thermodynamic problem

In this part, we describe the fuel pin thermal problem in order to lay out the numerical method used to couple this equation with the fluid equations [249].

Let us recall the thermal problem formulation of section ( 6.6) and present its numerical discretization [116] .

- Energy conservation

$$\rho(T)C_p(T)\frac{\partial T(x)}{\partial t} - \nabla(\lambda(T)\nabla(T(x))) = P(x, t) \quad (7.1)$$

which can be rewritten using thermal flux variable in an axisymmetric geometry:

$$\rho(T)C_p(T)\frac{\partial T(x)}{\partial t} + \frac{\partial \Phi^c(x)}{\partial x} = P(x, t) \quad (7.2)$$

with,

$$\Phi^c(x) = -\lambda(T) \frac{\partial T(r)}{\partial r} \quad (7.3)$$

$$\frac{\partial \Phi^c(x)}{\partial x} = \frac{1}{r} \frac{\partial r \Phi^c(r)}{\partial r}. \quad (7.4)$$

Above  $T$  and  $\Phi^c$  are the temperature and the thermal flux,  $\rho(T)$  is the density,  $C_p(T)$  is the specific heat capacity,  $\lambda(T)$  is the thermal conductivity and  $P(x, t)$  the power locally deposited by external sources.

At the point  $x = r_{wall}$ , the thermal flux exchange at this boundary is equal to the thermal flux exchange with the fluid:

$$\Phi_{wall}^{FuelPin} = \Phi_{wall}^{Fluid}. \quad (7.5)$$

The constitutive law relating the clad surface (wall) heat flux to the temperature jump writes:

$$\Phi_{wall}^{Fluid} = \nu_p(T_p, T_f)(T_{wall} - T_f). \quad (7.6)$$

The equation (7.5) can be rewritten thanks to the equation (7.6):

$$\Phi_{wall}^{Fluid} = \nu_p(T_p, T_f)(T_{wall} - T_f) = -\lambda \frac{\partial T_{wall}}{\partial r} = \Phi_{wall}^{FuelPin} \quad (7.7)$$

where  $\nu_p$  is the thermal exchange coefficient (W/K/m<sup>2</sup>) and  $T_f$  is the fluid temperature.

- In addition, we have the following boundary conditions:

A.  $T(r_{wall}) = T_{wall}$ , at the clad surface;

B. symmetry hypothesis:  $\frac{\partial T(r)}{\partial r}|_{r_o} = 0$ , at the pin center.

- Numerical solution

Equation (7.2) is solved according to the following spatial discretization and time implicit scheme:

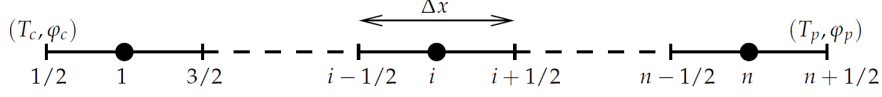


**Figure 7.1.** Space domain discretisation [116]

$$\rho C_p \frac{T_i^{n+1} - T_i^n}{\Delta t} + \frac{\Phi_{i+1/2}^{cn+1} - \Phi_{i-1/2}^{cn+1}}{\Delta r} + \frac{\Phi_{i+1/2}^{cn+1} + \Phi_{i-1/2}^{cn+1}}{2r_i} = P_i^{n+1} \quad (7.8)$$

with,

$$\Phi_{i+1/2}^{cn+1} = -\lambda \frac{T_{i+1}^{n+1} - T_i^{n+1}}{\Delta r},$$

$$\Phi_{i-1/2}^{cn+1} = -\lambda \frac{T_i^{n+1} - T_{i-1}^{n+1}}{\Delta r}.$$

This can be rewritten:

$$\left( \frac{-\lambda}{\Delta r^2} \right) \left( 1 - \frac{\Delta r}{2r_i} \right) T_{i-1}^{n+1} + \left( \frac{2\lambda}{\Delta r^2} + \frac{\rho C_p}{\Delta t} \right) T_i^{n+1} + \left( \frac{-\lambda}{\Delta r^2} \right) \left( 1 + \frac{\Delta r}{2r_i} \right) T_{i+1}^{n+1} = \left( P_i^{n+1} + \frac{\rho C_p}{\Delta t} T_i^n \right) \quad (7.9)$$

Moreover, at the external wall, because of the boundary conditions we have:

$$\left( \frac{-\lambda}{\Delta r^2} \right) T_{N-1}^{n+1} + \left( \frac{3\lambda}{\Delta r^2} + \frac{2\lambda}{r_N \Delta r} + \frac{\rho C_p}{\Delta t} \right) T_N^{n+1} = \left( P_N^{n+1} + \frac{\rho C_p}{\Delta t} T_N^n + \left( \frac{2\lambda}{\Delta x^2} + \frac{2\lambda}{r_N \Delta r} \right) T_{wall}^{n+1} \right) \quad (7.10)$$

and

$$\Phi_{wall}^{cn+1} = -\lambda \frac{T_{wall}^{n+1} - T_N^{n+1}}{\Delta r/2}. \quad (7.11)$$

Let us now use a time explicit prediction  $\lambda = \lambda(T^*)$  and  $C_p = C_p(T^*)$  to compute



capacity and conduction. This way, equation (7.9) reduces to the following tridiagonal system which can be solved using a LU matrix decomposition:

$$\begin{pmatrix} a_{1,1} & a_{1,2} & & & \\ a_{2,1} & a_{2,2} & a_{2,3} & & \\ \dots & \dots & \dots & \dots & \\ & & a_{N-1,N-2} & a_{N-1,N-1} & a_{N-1,N} \\ & & & a_{N,N-1} & a_{N,N} \end{pmatrix} \begin{pmatrix} T_1^{n+1} \\ T_2^{n+1} \\ \dots \\ T_{N-1}^{n+1} \\ T_N^{n+1} \end{pmatrix} = \begin{pmatrix} s_1 \\ s_2 \\ \dots \\ s_{N-1} \\ s_N \end{pmatrix} \quad (7.12)$$

The temperature distribution is obtained by resolution of the algebrical system (7.12). This algebrical expression can be rewritten  $T = A^{-1}S$ , with  $A = a_{ij}$ ,  $A^{-1} = a_{ij}^{-1}$ ,  $T = T_i$  and  $S = s_i$ , that is:

$$T_i = \sum_{j=1}^N a_{ij}^{-1} s_j. \quad (7.13)$$

The wall temperature  $T_{wall}^{n+1}$  only appears in the  $s_N$  term of the linear system, thus the dependancy is linear and can be expressed explicetely in the following form:

$$s_N = s_N^0 + s_N^{wall} T_{wall}^{n+1} \quad (7.14)$$

and,

$$\begin{aligned} s_N^0 &= P_N^{n+1} + \frac{\rho C_p}{\Delta t} T_N^n, \\ s_N^{wall} &= \frac{2\lambda}{\Delta r^2} + \frac{2\lambda}{r_N \Delta r}. \end{aligned}$$

Plugged into (7.14), this yields:

$$T_N^{n+1} = \left( \sum_{j=1}^{N-1} a_{Nj}^{-1} s_j + a_{NN}^{-1} s_N^0 \right) + a_{NN}^{-1} s_N^{wall} T_{wall}^{n+1}. \quad (7.15)$$

Thus, by injecting the equation (7.11) into the previous equation (7.15), we obtain the following condensed expression of the wall heat flux:

$$\Phi_{wall}^{cn+1} = \frac{-\lambda}{\Delta r/2} \left( T_{wall}^{n+1} (1 - a_{NN}^{-1} s_N^{wall}) - \left( \sum_{j=1}^{N-1} a_{Nj}^{-1} s_j + a_{NN}^{-1} s_N^0 \right) \right). \quad (7.16)$$

This heat flux expression can be rewritten as:

$$\Phi_{wall}^{cn+1} = A_N^* T_{wall}^{n+1} + S_N^* = a_N^* (T_{wall}^{n+1} - s_N^*) \quad (7.17)$$

where, all contributions of the pin temperature have been eliminated, with the following definition of the coefficients:

$$\begin{aligned} A_N^* &= \frac{-2\lambda}{\Delta r} (1 - a_{NN}^{-1} s_N^{wall}), \\ S_N^* &= \frac{-2\lambda}{\Delta r} \left( \sum_{j=1}^{N-1} a_{Nj}^{-1} s_j + a_{NN}^{-1} s_N^0 \right), \\ a_N^* &= A_N^*, \\ s_N^* &= S_N^*/A_N^*. \end{aligned}$$

These coefficients depend on the value  $T^*$  used in the capacity and conduction prediction.

## 7.2 Problem linearization and elimination of the internal variables

This expression (7.17) can be plugged into the constitutive law [116],

$$\Phi_{wall}^{Fluid} = \nu_p(T_{wall}, T_f)(T_{wall} - T_f) \quad (7.18)$$

yielding the following equation,

$$\nu_p(T_{wall}, T_f)(T_{wall} - T_f) = a_N^* (T_{wall}^{n+1} - s_N^*). \quad (7.19)$$

In the fluid problem, this constitutive law will be linearized. This linearization is done between the time steps  $n$  and  $n+1$ , yielding:

$$\Phi_{wall}^{n+1} \simeq \Phi_{wall}^n + \left( \frac{\partial \Phi_{wall}}{\partial T_{wall}} \right)^n (T_{wall}^{n+1} - T_{wall}^n) + \left( \frac{\partial \Phi_{wall}}{\partial T_f} \right)^n (T_f^{n+1} - T_f^n) \quad (7.20)$$

and reducing Eq. (7.19) to :

$$\Phi_{wall}^n + \left( \frac{\partial \Phi_{wall}}{\partial T_{wall}} \right)^n (T_{wall}^{n+1} - T_{wall}^n) + \left( \frac{\partial \Phi_{wall}}{\partial T_f} \right)^n (T_f^{n+1} - T_f^n) = a_N^* (T_{wall}^n - s_N^*) + a_N^* (T_{wall}^{n+1} - T_{wall}^n) \quad (7.21)$$

This specifies the wall temperature variation:

$$(T_{wall}^{n+1} - T_{wall}^n) = \frac{(a_N^* (T_{wall}^n - s_N^*) - \Phi_{wall}^n) - \left( \frac{\partial \Phi_{wall}}{\partial T_f} \right)^n (T_f^{n+1} - T_f^n)}{\left( \frac{\partial \Phi_{wall}}{\partial T_{wall}} \right)^n - a_N^*} \quad (7.22)$$

This equation can be injected into the equation (7.20) in order to obtain the flux only according to the temperature  $T_f^{n+1}$ :

$$\Phi_{wall}^{n+1} = \frac{\left( \frac{\partial \Phi_{wall}}{\partial T_{wall}} \right)^n a_N^* (T_{wall}^n - s_N^*) - a_N^* \Phi_{wall}^n}{\left( \frac{\partial \Phi_{wall}}{\partial T_{wall}} \right)^n - a_N^*} - \frac{a_N^* \left( \frac{\partial \Phi_{wall}}{\partial T_f} \right)^n}{\left( \frac{\partial \Phi_{wall}}{\partial T_{wall}} \right)^n - a_N^*} (T_f^{n+1} - T_f^n). \quad (7.23)$$

This equation can be injected into the thermal hydraulic problem which is aimed to provide the fluid temperature  $T_f^{n+1}$  and thanks to the equation (7.22) we then obtain the wall temperature  $T_{wall}^{n+1}$ , which is going to be used in order to calculate the other temperatures of the fuel pin, through (7.14).

### 7.3 ALCYONE fuel pin effective temperature computation

Inside the fuel pellet the temperature is radially no uniform as shown in figure (7.2) obtained from an ALCYONE-APOLLO3 calculation at  $t=0.25$ , at the Hot Spot, during a REA transient detailed in section (2.4.2).

In case of modelling with neutronics the Doppler feedback is strongly dependent on the fuel temperature. The effective temperature  $T_{eff}$  is a temperature formulation at the scale of a homogeneous fuel pellet slice trying to preserve the local distribution of the temperature inside the pellet  $T(r)$  as well as its impact on the neutron absorption through Doppler effect.

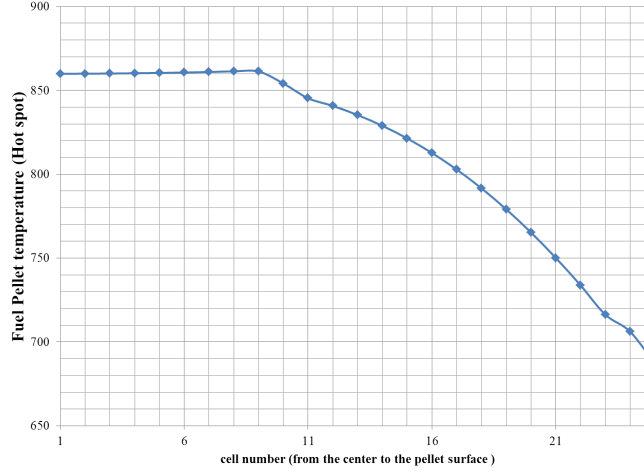


**Figure 7.2.** Radial temperature distribution (in degree) inside the pellet (REA calculation example of distribution at  $t=0.25$ )

A first choice of  $T_{eff}$  uses the Rowland equation (7.24) calculated thanks to an harmonic radial distribution of the temperature inside the pellet [223] [141]:

$$T_{eff}^{Rowland} = 5/9T_{surface\_pellet} + 4/9T_{center\_pellet} \quad (7.24)$$

In case the temperature distribution does not have a parabolic shape (in case of old assemblies with rim effect) we can use a second choice of  $T_{eff}$ , the Chanbert and Santamarina equation [40] [141]:

$$T_{eff}^{C\_SM} = \langle T(r) \rangle - \frac{1}{18}(T_{center\_pellet} - T_{surface\_pellet}) \quad (7.25)$$

where  $\langle T(r) \rangle = \frac{\int_0^{r_{fuel\_ext\_surface}} rT(r)dr}{\int_0^{r_{fuel\_ext\_surface}} r dr}$  is the mean temperature in the pellet.

A final option that we have also implemented uses the average temperature  $T(r)$  of each ring balanced by the absorption rate  $A^k(r)$  of the major absorbing element  $k$  of the fuel, in order to get a more realistic neutronic absorption inside the pellet. This new  $T_{eff}$  formulation [141] is given by:

$$T_{eff}^{Iso} = \frac{\int_{\Omega} T(r) \sum_{k=1}^K A^k(r) dr}{\int_{\Omega} \sum_{k=1}^K A^k(r) dr} \quad (7.26)$$

where  $A^k(r) = N^k(r)\sigma_a^k(r)\Phi(r)$ . Here  $N^k$  is the quantity of each isotope  $k$  ( $k$  is mainly corresponding to Pu240 and U238),  $\sigma_a^k(r)$  are the microscopic cross sections and  $\Phi(r)$  is the prompt neutron flux .

This equation is also expressed in a discretized formulation by:

$$T_{eff}^{Iso} = \frac{\sum_{i=1}^R \sum_{k=1}^K T_i A_i^k}{\sum_{i=1}^R \sum_{k=1}^K A_i^k} \quad (7.27)$$

where R is the number of rings in the fuel pin discretization.

## Chapter 8

# Thermomechanical conclusion

Finally, in this chapter, we summarized all the previous models and improvement point and we rewrote them in order to prepare the coupling part of this study.

### Mechanical models and numerical aspects:

In this part, we mathematically defined the ThermoMechanical models of ALCYONE code we are going to use in our coupling. The ThermoMechanical models are directly defined at the scale of a single fuel pin and thus guarantee the access to local parameters. The mechanical state of the fuel element is computed by solving the static equilibrium mechanical model (6.1), integrated according to a weak formulation with the finite element method. In addition to this equilibrium principle, the nonlinear behavior of the fuel element is taken into account through several constitutive equations describing the thermo-mechanical behavior of the pellet, cladding and pellet-cladding interface. The calculation is obtained by using a 1.5D modelling [164]. The fuel pin physical description can be realized using:

- Constitutive laws for the pellet Eq. (6.3):

$$\frac{d\boldsymbol{\sigma}_{comb}}{dt} = \boldsymbol{E}_{comb} : \left[ \frac{d\boldsymbol{\epsilon}_{T_{comb}}}{dt} - \frac{d\boldsymbol{\epsilon}_{crack}}{dt} - \frac{d\boldsymbol{\epsilon}_{creep}}{dt} - \frac{d\boldsymbol{\epsilon}_{SS\_D}}{dt} - \frac{d\boldsymbol{\epsilon}_{GS}}{dt} - \frac{d\boldsymbol{\epsilon}_{Thermal_{FuelPellet}}}{dt} \right] \quad (8.1)$$

- Transient aspects:
  - A Gaseous Swelling law,  $\frac{d\epsilon_{GS}(T_{pellet})}{dt}$  in Eq. (6.17), through a differential equation system mainly function of the fuel temperature; and of the fuel power and of the fast neutron flux at steady state,
  - A pellet thermal expansion law,  $\frac{d\epsilon_{Thermal_{FuelPellet}}(T_{pellet})}{dt}$  in Eq. (6.31), directly function of the fuel temperature in the pellet.
- In order to define the initial Mechanical state of the fuel, in addition to the initial value of the fuel cracking, Gaseous swelling and thermal expansion, we also lay out:
  - A pellet creep law,  $\frac{d\epsilon_{creep}(T_{pellet}, dF/dt)}{dt}$  in Eq. (6.9), which defines the stationary thermal creep and irradiation as function of the fuel temperature and of the fission rate,
  - A solid swelling and densification laws,  $\frac{d\epsilon_{SS\_D}(BU)}{dt}$  in Eq. (6.14), function of the Burn-up.

These latter laws are defined in order to determine the initial state of fuel pellets regarding their age (burn-up) and operation history before the Rod Ejection Accident transient starts. This initial state is fundamental to be the most accurate physically in order to precisely study or prevent any risk of Pellet Cladding Mechanical Interaction (PCMI). Nevertheless, due to our academic case scenario and Bu, these terms will be neglected in transient simulations. The constitutive laws for the pellet in transient situation then rewrite:

$$\frac{d\sigma_{comb}}{dt} = \mathbf{E}_{comb} : \left[ \frac{d\epsilon_{T_{comb}}}{dt} - \frac{d\epsilon_{GS}}{dt} - \frac{d\epsilon_{Thermal_{FuelPellet}}}{dt} \right] \quad (8.2)$$

Moreover, Fuel pellet Physical data are defined in section ( 6.3.6).

- Constitutive laws for the cladding (Eq. (6.37) ):

$$\frac{d\sigma_{clad}}{dt} = \mathbf{E}_{clad} : \left[ \frac{d\epsilon_{T_{clad}}}{dt} - \frac{d\epsilon_p}{dt} - \frac{d\epsilon_\nu}{dt} - \frac{d\epsilon_{Thermal_{clad}}}{dt} \right] \quad (8.3)$$

- Transient aspects:
  - A viscoplastic law,  $\frac{d\epsilon_p(T_{clad})}{dt}$  in Eq. (6.39), mainly function of the clad temperature; and of the fast neutron flux at steady state,
  - A cladding thermal expansion law,  $\frac{d\epsilon_{Thermal_{clad}}(T_{clad})}{dt}$  in Eq. (6.43), directly function of the clad temperature.
- And, regarding the initial Mechanical state, by:
  - A cladding creep law,  $\frac{d\epsilon_\nu(T_{clad}, \phi^{fast})}{dt}$  in Eq. (6.41), which defines the long term thermal creep and the creep by irradiation.

---

This last term will be neglected in the transient simulation but is fundamental in order to define the initial state of the cladding before the transient. The constitutive laws for the pellet in transient situation are thus:

$$\frac{d\boldsymbol{\sigma}_{clad}}{dt} = \mathbf{E}_{clad} : \left[ \frac{d\boldsymbol{\epsilon}_{T_{clad}}}{dt} - \frac{d\boldsymbol{\epsilon}_p}{dt} - \frac{d\boldsymbol{\epsilon}_{Thermal_{clad}}}{dt} \right] \quad (8.4)$$

Moreover, clad physical data are defined in section ( 6.4.4).

- Boundary and interface conditions detailed in section ( 6.5):
  - On the external clad surface, we have a hydraulical loading  $\sigma.e_r = -p_{hydro}.e_r$  which becomes a non-coupling conditions by assuming a constant pressure during the whole transient.
  - On the internal clad surface, we consider an axisymmetric generalized plane strain assumption in case of contact or without contact:
    - Pellet-Clad Gap  $> 0$ :  $(\sigma.e_r)_{clad} = (\sigma.e_r)_{pellet} = -p_{plenum}.e_r$
    - Pellet-Clad Gap  $= 0$ :  $(\sigma.e_r)_{clad} = (\sigma.e_r)_{pellet}$

#### Thermal model and numerical aspects:

In this part, we also mathematically defined the Thermal models of ALCYONE code which can be directly defined by a thermal equation (conservation of energy Eq. ( 6.52)) over the fuel pin (outside the gap) and function of the Power.

$$\rho C_p \frac{dT}{dt} + \nabla \cdot \lambda \nabla T + P_{volumic}(x) = 0, \quad (8.5)$$

We defined a set of thermal equations (conductivity, capacity and emissivity) regarding the pellet material, with a mechanical dependency through the fuel porosity, and the clad material, both function of the temperature.

Finally, a special attention is given to the gap conductance between the fuel and the clad,  $H_{gap}(r, t)$  in eqs. (6.55), (6.56) and (6.57):

$$\lambda_{clad} \frac{\partial T_{clad\_int}}{\partial n} = \lambda_f \frac{\partial T_{fuel\_ext}}{\partial n} = \Phi_{gap}, \quad (8.6)$$

$$\Phi_{gap} = h_{gap}(T_{clad\_int} - T_{fuel\_ext}). \quad (8.7)$$

$$h_{gap} = h_{rad} + h_{cond} + h_{contact} \quad (8.8)$$

We defined this coefficient as a sum of a radiative component  $h_{rad}$ , a conductive component independent from the contact pressure  $h_{cond}$  and one that is depending on the contact



pressure  $h_{contact}$  (in case of gap closure). The clad surface temperature  $T_{wall}$  is defined as a boundary condition, given by the Thermohydraulics, and is one of the coupling variables of the fuel pin thermal problem.

**Neutronics and Power reconstruction at the fuel pin level:**

Neutronics Bateman equation and Power reconstruction at pellet level are used in the ALCYONE code in section ( 4.3). They are used respectively in order to define the initial isotopic state inventory at the scale of a fuel pellet cell (for instance, in our study, 25 radial cells in the pellet) and in order to rebuild the Power distribution at the pellet scale.

**Phenomenological and physical aspects of the Transient:**

Considering an accidental situation of a control rod ejection in the central assembly within our academic reactor core context, the ThermoMechanical equations (6.3), (6.37) and (6.52) provide at each time step a new Thermal and Mechanical state.

More precisely, the transient induces a strong change of the fuel power deposition  $P_{fuel}(r,t)$  due to the neutronics evolution. This Fuel power induces the change of the thermal state of the fuel pin,  $T(r,t)(x)$ , where  $r$  is the core scale and  $x$  the local scale. In return, it impacts:

- The effective temperature  $T_{eff}(r,t)$  and, thus, the neutronics evolution through the Doppler feedback effect;
- The mechanical state of the fuel pin, mainly by expansion, which may close the Pellet-Clad gap,  $Gap(r,t)$ , and, thus, modify the mechanical and Thermal behavior of the fuel pin;
- The external clad surface thermal flux evolution  $\Phi_{wall}(r,t)$  which modifies the hydraulic state of the core ( $T_{fluid}(r,t)$  and  $D_{fluid}(r,t)$  respectively called in neutronics part by  $T_{mod}(r,t)$  and  $D_{mod}(r,t)$ ) respectively. Then, this Thermohydraulic variation will impact the neutronics evolution through the moderator feedback effect.

---

### ThermoMechanical coupling aspects:

From these descriptions, we observe that the coupling from the Mechanics to the Thermics is weak and mainly based on the pellet porosity (slow process) or fuel pin deformation through the average plenum pressure variation, yield stress tensor (in case of contact) and clad-pellet gap thickness variation. Nevertheless, it has a strong impact when it induces gap closure or opening. In return, the coupling from the Thermics to the Mechanics is based on the fuel pin temperature distribution by slice (pellet, clad and gap). Then, regarding the Neutronics and Thermohydraulics, we observe a strong coupling with the Thermomechanics through the rebuilt source term  $P_{fuel}(r(x),t)$  and the boundary condition  $T_{wall}(r,t)$ . The following diagram summarizes the previous sections and conclusions, indicating the equations, the core discretization (academic core description is done through ALCYONE representative fuel pin multi-instances with each Alcyone instance discretized at the fuel pin scale: 30 axial cells and 25 radial cells), ThermoMechanical parameters we observe and coupling variables we use in a Best effort coupling approach, i.e., Neutronics variables in green, Hydrodynamics variables in blue and Thermomechanics variables in red.

The coupling variables consist in:

- Input variables (distributed in space at core scale):
  - Fuel power  $P_{fuel}(r,t)$  (eq. (3.42)) used to compute the fuel power  $P_{fuel}(r,t)(x)$  (eq. (4.12)) at the pin scale  $x$ ),
  - The clad external surface temperature  $T_{wall}(r,t)$  (eq. (7.19)).
- Output variables (respectively distributed in space and surface variables):
  - The fuel temperature  $T_{fuel}(r,t)(x)$  (eq. (6.57)) used to compute the effective temperature  $T_{eff}(r,t)$  (detailed in section (7.3)),
  - The thermal flux  $\Phi_{wall}(r,t)$  (through the variable  $S_p = \Phi_{wall} - A_p T_{wall}$  and the pin homogenized conductance  $A_p = \frac{\partial \Phi_{wall}}{\partial T_{wall}}$ , in eq. (7.19).

The impact of coupling will be observed on the following ThermoMechanical parameters:

- Clad-Pellet thermal transfer coefficient  $H_{gap}(r,t)$ ,
- Clad-Pellet Gap size  $Gap(r,t)$ ,
- Clad surface thermal flux  $\Phi_{wall}(r,t)$ ,

---

CHAPTER 8. THERMOMECHANICAL CONCLUSION

---

Parameter Names	Parameters Symbols	Coupling Type	Type
Fuel Power	$P_{fuel}(r,t)(x)$	input	Distributed in space
Clad surface temperature	$T_{wall}(r, t)$	input	Distributed in space
Fuel pin temperature	$T_{fuel}(r,t)(x)$ $T_{pellet_{center}}(r_{pellet_{center}}, t)$ $T_{pellet_{surface}}(r, t) = T_1$ $\Delta T_{gap}(r, t) = T_1 - T_{clad_{in}}(r, t)$ $T_{eff}(r, t)$	Thermal observation    output	Distributed in space
Clad surface thermal flux	$\Phi_{wall}(r, t)$	output	Distributed in space
Clad-Pellet Thermal transfer coefficient	$H_{gap}(r, t)$	Thermal observation	Distributed in space
Clad-Pellet Gap size	$Gap(r, t)$	Mechanical observation	Distributed in space

**Table 8.1.** ThemoMechanics input, output and monitored parameters (where  $r$  is the space variable at core scale and  $x$  is the local space variables)

For transient, these output, input and state variables are summarized in the following block diagram.

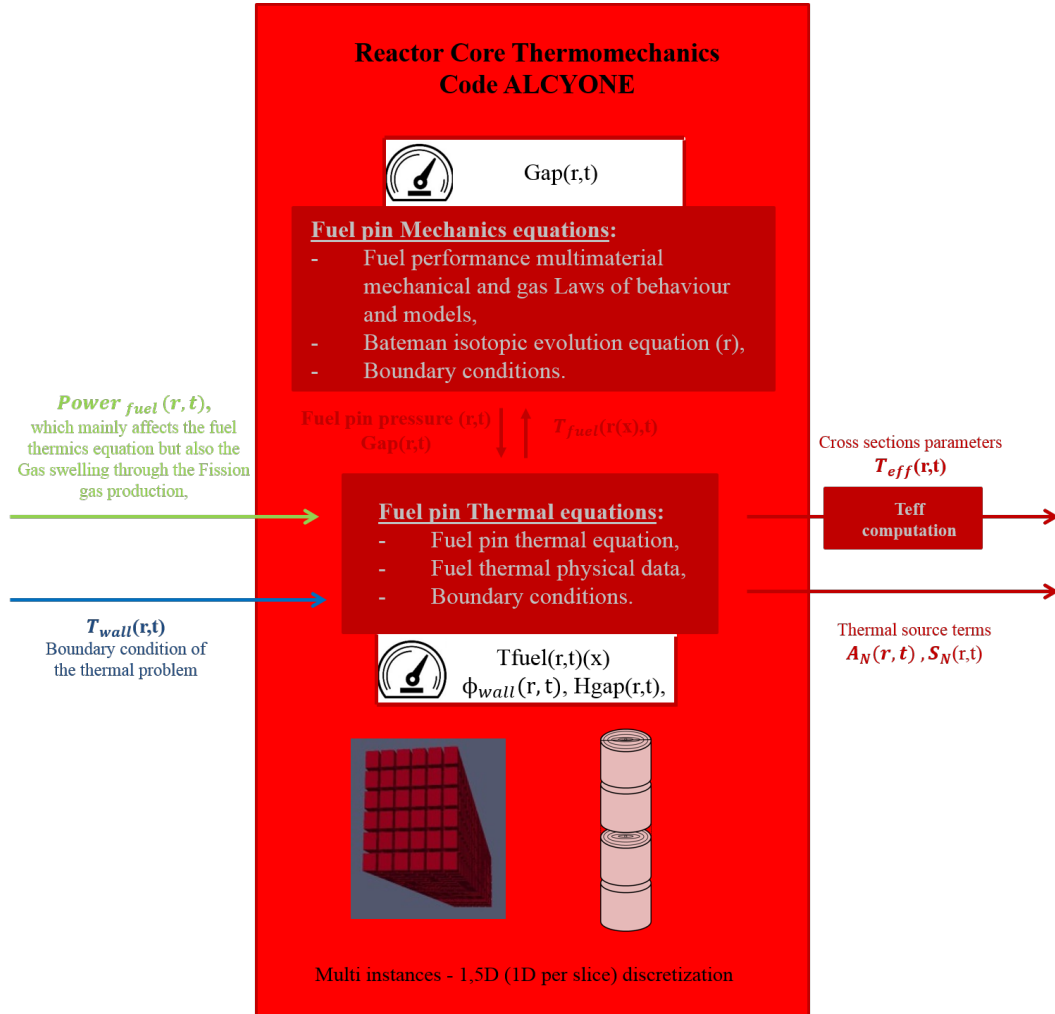


**Figure 8.1.** ThermoMechanics Block diagram with exchange variables and discretization

**Model improvements and limitations:**

- Key points taken up and improvements carried out by this study:
  - By using an accurate ThermoMechanical model at the fuel pin scale we access to the accurate local behavior of pellet, clad and pellet-clad gap.
  - We also access to the precise distribution of the Temperature inside the fuel pin  $T(r,t)(x)$  which is not directly used in our simulations yet.
  - Finally, by using an implicit linearized approach, detailed in section (8.1), we precisely access to the homogenized conductance  $Ap = \frac{\partial \Phi_{wall}}{\partial T_{wall}}$  and thus we obtain a better estimation of the global behavior of the fuel pin.
- Present ThermoMechanical challenges in perspective of a Best Effort multiphysics calculation:
  - Regarding the gap conductance which strongly controls the thermal transfer inside the fuel pin, some limitations appear from the models used in order to define the gas release law and fuel pin internal pressure (whole pin average value) by slice and function of time.
  - Regarding the solver aspects of the Thermomechanical part, limitations appear regarding the ability to realize 2D and 3D calculations over a whole fuel pin instead of a single section of a fuel pin. The axisymmetrical assumption is sufficient enough when we are working at the scale of a representative fuel pin per 1/4 assembly, but dissymmetrical effects should appear in case of couplings, directly at the scale of the fuel pin in particular next to guide tubes.

## Chapter 9

# ThermoHydraulical Physical equations and Numerical Models

While working on this multiphysics problems we are required to accurately construct the different models upon which the multiphysic coupling will be based. In this chapter, the Thermohydraulical models are mathematically and numerically formulated. This allows us to pin point the Thermohydraulics coupling variables of our multiphysics problem as well as to define the limitations of the models and the assumptions and hypothesis we made.

### 9.1 Physical Description

Computations of complex two-phase flows are required for the safety analysis of nuclear reactors [258]. These computations keep causing problems for the development of Best Effort computer codes dedicated to design and safety studies of nuclear reactors. For the modeling of two-phase flows, several sets of equations have been worked out. They range in complexity from the homogeneous equilibrium model to two-fluid models involving different pressures per phase. Here, we present the Thermohydraulics models and the numerical method for single pressure two-phase flow computations, which is based on an approximate Riemann solver.

## 9.2 Notations and unknowns

We first introduce the main notation of the problem.

Porous Model Nomenclature		
Nomenclature	k	liquid(l) or gas(g)
	w	fluid/clad interface (wall)
Thermodynamic quantities		
$C_{pk}$	specific heat	$J.kg^{-1}.K^{-1}$
$C_{pk}$	specific heat at saturation	$J.kg^{-1}.K^{-1}$
$e_k$	intern energy	$J.kg^{-1}$
$h_k = e_k + p/\rho_k$	specific enthalpy	$J.kg^{-1}$
$h_{k,sat}$	specific enthalpy at saturation	$J.kg^{-1}$
$h_{deb} = \frac{G_l h_l + G_g h_g}{G}$	outlet enthalpy (enthalpie debitante)	$J.kg^{-1}$
$G_k$	mass flow rate of the phase k ( $G_k = \rho \mathbf{u}_k A$ ) where A is the cross-sectional vector area/surface, and $G_k^Z$ means $G_k$ following the direction Z	$kg.s^{-1}$
p	Pressure	Pa
$L = h_{g,sat} - h_{l,sat}$	latent heat	$J.kg^{-1}$
$Pr_k = \frac{\mu C_p}{\lambda}$	Prandlt number	1
$Pr_{k,sat}$	Prandlt number at saturation	1
$Nu = \frac{H D_h}{\lambda}$	Nusselt number	1
$Re = \frac{\rho  \mathbf{u}  D_h}{\mu}$	Reynolds number	1
$Re_k = \frac{G_k^Z D_h^Z}{\mu_k}$	Reynolds number for the phase k following the main direction Z	1
$Fr = \frac{G^Z}{\rho_q^2 \cdot D_h^Z \cdot   \mathbf{g}  }$	Froude number following the main direction Z ( $\mathbf{g}$ : g-force)	1
$We = \frac{G^Z \cdot D_h^Z}{\rho_q \cdot \sigma}$	Weber number following the main direction Z	1
$T_k$	temperature	K
$T_{sat}$	temperature at saturation	K
$T_{w,kc}$	wall temperature consitant with the heat transfert coefficient for the phase k ( $\simeq T_k$ )	K
$\lambda_k$	thermal conduction	$W.m^{-1}.K^{-1}$
$\lambda_{k,sat}$	thermal conduction at saturation	$W.m^{-1}.K^{-1}$
$\mu_k$	dynamic viscosity	Pa.s
$\mu_{k,sat}$	dynamic viscosity at saturation	Pa.s
$\rho_k$	density	$kg.m^{-3}$
$\rho_{k,sat}$	density at saturation	$kg.m^{-3}$
$\rho_q$ where $\frac{1}{\rho_q} = \frac{1-X_q}{\rho_l} + \frac{X_q}{\rho_g}$	density	$kg.m^{-3}$
$\sigma$	surperficial tension (tension superficielle)	$N.m^{-1}$
$F_k$	isothermal friction coefficient (phase k)	1

**Table 9.1.** Notations: ThermoHydraulics quantities

Phase quantities		
$E_k = e_k +  \mathbf{u}_k ^2/2$	total Energy	$J.kg^{-1}$
$h_k = h_k +  \mathbf{u}_k ^2/2$	total Enthalpy	$J.kg^{-1}$
$K_k^t$	diffusion coefficient (turbulent diffusion)	1
$M_k^t$	viscosity coefficient (turbulent viscosity / turbulent condition)	1
$\alpha_k$	volume fraction of liquid or gas	1
$\Pi_k$	cauchy stress tensor. This tensor contains a viscous stress tensor $\check{\tau}$ and the turbulence effect modelling $-pI$ . $\Pi_k = -pI + \check{\tau}$	$kg.m^{-1}s^{-2}$
$\mathbf{u}_k$	liquid or gas velocity	$m.s^{-1}$
$\mathbf{u}_r = \mathbf{u}_g - \mathbf{u}_l$	relative celerity	$m.s^{-1}$
$X_q = \frac{G_g}{G_l + G_g}$ $= \frac{\alpha \cdot \rho_g  \mathbf{u}_v }{(1-\alpha) \cdot \rho_l  \mathbf{u}_l  + \alpha \rho_g  \mathbf{u}_g }$	vapor quality	1
$X = \frac{h - h_l}{h_g - h_l}$	vapor titration	1
$X_{deb} = \frac{h_{deb} - h_{l,sat}}{h_{g,sat} - h_{l,sat}}$	hydraulic flow titration	1
$\mathbf{G}_k$	mass flow rate $\mathbf{G}_k = \rho_k \mathbf{u}_k$	1
mixture quantities		
$c = \frac{\alpha_g \cdot \rho_g}{\rho} = \frac{\alpha \cdot \rho}{(1-\alpha) \cdot \rho_l + \alpha \rho_g}$	vapor mass fraction	1
$e = \sum_{k=g,l} (\alpha_k \cdot \rho_k e_k) / \rho$	average intern energy	$J.kg^{-1}$
$E = \sum_{k=g,l} (\alpha_k \cdot \rho_k E_k) / \rho$	average total energy	$J.kg^{-1}$
$h = \sum_{k=g,l} (\alpha_k \cdot \rho_k h_k) / \rho$	average intern enthalpy	$J.kg^{-1}$
$H = \sum_{k=g,l} (\alpha_k \cdot \rho_k H_k) / \rho$	average total Enthalpy	$J.kg^{-1}$
$\mathbf{u} = \sum_{k=g,l} (\alpha_k \cdot \rho_k \mathbf{u}_k) / \rho$	average celerity (barycentric celerity)	$m.s^{-1}$
$\rho = \sum_{k=g,l} (\alpha_k \cdot \rho_k)$	mixture density	$kg.m^{-3}$

Table 9.2. Notations: Phases and mixture quantities



CHAPTER 9. THERMOHYDRAULICAL PHYSICAL EQUATIONS AND  
NUMERICAL MODELS

other quantities		
$\mathbf{g}$	gravity	$m.s^{-2}$
$k_s$	sand rugosity equivalent to the real rugosity	m
$k_s^+$	adimensional rugosity	1
$\mathbf{U}$	vector of conservative quantity	
$Q_{tot}$	Power (heat) density source term (volumetric source term of thermal power)	$W.m^{-3}$
$\Phi_{wall}^{vol}$	Thermal flux transfer from the fuel pellet wall surface to the liquid volume ( $Q_{wall}^{vol} = (\Phi_{wall} * S_{wall})/V_{fluid}$ )	$W.m^{-3}$
$\Phi_{wall}$	Wall surface thermal flux	$W.m^{-2}$
$\Phi_{I,g}$	heat transfer beetwen liquid and vapor	$W.m^{-2}$
$\mathbf{q}$	heat flux induced by the thermal conductivity and the turbulent mixing term	$kg.m.s^{-3}$
$\Phi$	thermal flux from the wall	$W.m^{-2}$
$\tau$	wall dragging force (friction force)	$kg.m^{-2}.s^{-2}$
$\check{\tau}$	viscous stress tensor (deviatoric stress tensor), $\check{\tau} = \lambda_{lame}(\nabla \cdot \mathbf{u})\mathbf{I} + 2\mu\mathbf{d}$	$kg.m^{-1}s^{-2}$
$\mathbf{d}$	rate-of-strain tensor $\mathbf{d} = 1/2((\nabla \cdot \mathbf{u}) + (\nabla \cdot \mathbf{u})^T)$	$kg.m^{-1}s^{-2}$
$\lambda_{Lame}$	Lame's first parameter, $\lambda_{Lame} = \frac{E_{young}\nu_{poisson}}{(1+\nu_{poisson})(1-2\nu_{poisson})}$	Pa or $N.m^2$
$\mu$	Shear modulus (lame's first parameter), $\mu = \frac{E_{young}}{2(1+\nu_{poisson})}$	Pa or $N.m^2$
$E_{young}$	Young modulus (elastic modulus)	Pa or $N.m^2$
$\nu_{poisson}$	Poisson coefficient (negative ration of transverse to axial strain)	1
$S$	section area	$m^2$
$P_h$	humid perimeter ( $N\pi D$ ) which correspond to the length of N pin clad surface per subchannel	m
$P_{heat}$	heat perimeter which correspond to the length of fuel pin clad surface per subchannel (core design)	m
$D_h = 4A/P_h$	hydraulic diameter (where A is the sub channel area)	m
$D_{heat} = 4A/P_{heat}$	heat diameter (where A is the sub canal area)	m
$\Gamma$	Diffusion source term	
$\Gamma_{w,g}$	vapor generation on the wall	
$\Gamma_{I,g}$	evaporation or condensation within the bulk flow, mass transfer	
$K_{cv}$	Diffusion coefficient	
$Y_o$	two phase multiplyer corrector	
$\vartheta$	porosity	
A	Boron advection term	

Table 9.3. Notations: other quantities

The distributed unknown which are function of position and time are split in four groups:

- Gas :  $\alpha_g$  ,  $\mathbf{u}_g$  ,  $\rho_g$  ,  $E_g$  or  $H_g$ ,
- Liquid :  $\alpha_l$  ,  $\mathbf{u}_l$  ,  $\rho_l$  ,  $E_l$  or  $H_l$ ,
- Pressure  $p$ ,
- Boron concentration:  $N_{boron}$ .

The input variables which are needed for calculation of these unknown are:

- Thermal coupling coefficient  $A_p$ :  $A_p = \frac{\partial \Phi_{wall}}{\partial T}$  (see section ( 7.1)) ,
- Thermal coupling coefficient  $S_p$ :  $S_p = \Phi_{wall} - \frac{\partial \Phi_{wall}}{\partial T_{wall}} \cdot T_{wall}$  (see in section ( 7.1)) ,
- Volumic neutronic Power :  $P_\gamma$  (see section ( 3.3.8) equation (3.41)),

The output data to be used by the other models are (at each location in space and time):

- Fuel pellet surface temperature :  $T_{wall}$  ,
- Moderator density :  $D_{mod}$  ( $D_{liquid}$ ),
- Moderator temperature :  $T_{mod}$  ( $T_{liquid}$ ),
- Boron concentration :  $C_{boron}$ , in  $N_{boron}/m^3$  (assumed constant in our study).

Observe that for thermohydraulics, the coupling occurs inside the volume (volumic coupling).

### 9.3 Physical Equations

In our model, we use the Navier-Stokes equation for two fluid flows. The medium is considered as a porous medium considered as a singlehomogeneous medium with porosity  $\vartheta$  [75] [76] [256].

#### 9.3.1 Conservation laws

The conservation laws therefore write:

- Global Mass

$$\vartheta \frac{\partial \rho}{\partial t} + \nabla \cdot (\vartheta \rho \mathbf{u}) = 0 \quad (9.1)$$

- Gas Diffusion (with respect to the gas mass fraction  $c$ )

$$\vartheta \frac{\partial (\rho c)}{\partial t} + \nabla \cdot (\vartheta \rho c \mathbf{u} + \vartheta \rho c (1 - c) \mathbf{u}_r - \vartheta K_c \nabla c) = \vartheta \Gamma, \quad (9.2)$$

- Boron Diffusion and transport

$$\vartheta \frac{\partial (N_{boron})}{\partial t} + \nabla \cdot (\vartheta N_{boron} \mathbf{u}) - \nabla \cdot \left( A \nabla \left( \frac{N_{boron}}{\rho} \right) \right) = \vartheta \mathbf{S} = 0 \text{ (no boron generation)} \quad (9.3)$$

- Global Momentum

$$\begin{aligned} \vartheta \frac{\partial \sum_{k=g,l} (\alpha_k \rho_k \mathbf{u}_k)}{\partial t} + \nabla \cdot \left( \sum_{k=g,l} \vartheta \alpha_k \rho_k \mathbf{u}_k \otimes \mathbf{u}_k + \alpha_k \mathbf{\Pi}_k \right) \\ = \vartheta \rho \mathbf{g} + \vartheta \boldsymbol{\tau} \end{aligned} \quad (9.4)$$

- Global Energy

$$\begin{aligned} \vartheta \frac{\partial \sum_{k=g,l} (\alpha_k \rho_k E_k)}{\partial t} + \nabla \cdot \left( \sum_{k=g,l} (\vartheta \alpha_k \rho_k \mathbf{u}_k E_k - \alpha_k \mathbf{\Pi}_k \cdot \mathbf{u}_k) - \mathbf{q} \right) \\ = Q_{tot} + \vartheta \rho \mathbf{u}_k \cdot \mathbf{g} \end{aligned} \quad (9.5)$$

above the proportion of gas and liquid can be either monitored by their mass fraction  $c_k = \frac{\alpha_k \rho_k}{\rho}$  or by their volumic fraction  $\alpha_k = \frac{V_k}{V}$ .

### 9.3.2 Porous Model Closure laws

[11]

- Drift flux correlation

We can assume, in first approximation, that the two fluids have the same average velocity, hence:

$$\mathbf{u}_r := \mathbf{u}_g - \mathbf{u}_l = 0 \quad (9.6)$$

This equation is used to close the model and replaces a second momentum conservation equation which otherwise should have been written for the vapor phase.

- Equations of state

They are of the classical form [43] [29] [24]. :

$$\rho_g = \rho_g(p, h_g) \quad (9.7)$$

$$\rho_l = \rho_l(p, h_l) \quad (9.8)$$

$$T_g = T_g(p, h_g) \quad (9.9)$$

$$T_l = T_l(p, h_l) \quad (9.10)$$

As the gas fraction is low, the fluid temperature shall be taken equal to the liquid temperature  $T_l$ .

- Pressure condition. For small bubbles we use:

$$p_g = p_l = p. \quad (9.11)$$

- Enthalpy condition

$$h_g = h_g^{sat}(p) \quad (9.12)$$

The vapor is supposed to remain at saturation in the presence of liquid. This equation is used to close the model and shall replace a second energy conservation equation which otherwise should have been written for the vapor phase.

### 9.3.3 Vapor production term

This source term in the gas diffusion equation has two components:

$$\Gamma = \Gamma_{w,g} + \Gamma_{I,g} \quad (9.13)$$

with w - wall and I - fluid-gas interface. The vapor generation on an heating wall is defined by [211]:

$$\Gamma_{w,g} = \frac{4\chi\Phi_{wall}}{D_{heat}L(p)},$$

where  $D_{heat}$  is the heat diameter,  $L(p)$  is the specific latent heat and  $\chi$  is the heat flux fraction:  $\chi = 0$  means that all the heat flux is used to heat up the liquid (one-phase), while  $\chi = 1$  means that the liquid is fully saturated. Between these two extreme conditions, the heat flux fraction is defined from the wall temperature:

$$\chi = \frac{(T_{w,lc} - T_{sat} - \Delta T_{sat})}{(T_{w,lc} - T_l - \Delta T_{sat})} \quad (9.14)$$

where  $T_{w,lc} = T_l + \frac{\Phi_{wall}}{H_g}$  is the wall temperature consistent with the heat transfer coefficient for liquid convection, with  $H_g$  the heat transfert coefficient to the gas. The second part of the  $\Gamma$  source term models the interfacial mass transfer, i.e. condensation or flashing. It is deduced from the heat transfer  $\Phi_{I,g}$  between liquid and vapor:

$$\Gamma_{I,g} = \frac{\Phi_{I,g}}{L} \quad (9.15)$$

In FLICA4 the following three different thermohydraulical situations [11] are considered:

- simple liquid fluid at equilibrium state :  $\Phi_{I,g} = 0$ ,
- liquid fluid with thermodynamical disequilibrium:  $\Phi_{I,g} = K_{lv} \cdot \rho \cdot \left( \frac{C^{*2}}{1-C^*} \right)$ ,
- diphasic fluid  $\Phi_{I,g} = K_{lv} \cdot \rho \cdot \left( \frac{c(C^*-c)}{1-C^*} \right)$ ,

Above  $C^* = \frac{h-h_{l,sat}}{L}$  is a measure of thermal disequilibrium. The coefficient  $K_{lv}$  has two expressions which have been experimentally calibrated:

- At low velocity, if  $|\rho \mathbf{u}^Z| < G_{min}^Z$ :

$$K_{lv} = \frac{K_{vo} \cdot G_{min}^{Z2} \cdot \left( 1 - \frac{p}{p_{crit}} \right)}{\rho \cdot \mu_l \cdot \log \left( 1 + \frac{Re}{35000} \right)}$$

- At large velocity,  $|\rho \mathbf{u}^Z| > G_{min}^Z$ :

$$K_{lv} = \frac{K_{vo} \cdot |\rho \mathbf{u}^Z|^2 \cdot \left(1 - \frac{p}{p_{crit}}\right)}{\rho \cdot \mu_l \cdot \log\left(1 + \frac{Re}{35000}\right)} \cdot \left|\frac{\mathbf{u}_g^Z}{\mathbf{u}^Z}\right|$$

where  $p_{crit} = 22.1 MPa$ ,  $G_{min}^Z = 100 kg \cdot m^{-2} s^{-1}$  and  $K_{vo} = 10^{-5}$ .

### 9.3.4 Stress tensor

The turbulent models, embodied by the diffusion and mixed coefficient ( $K^t$  and  $M^t$ ), are based on the characteristic mixing length [211]. The stress tensor takes therefore the form:

$$\Pi_k^{ij} = \vartheta p \delta_{ij} - \mu_k \left(1 + \mathbf{M}_k^t\right) \cdot \left(\frac{\partial \vartheta \mathbf{u}_k^i}{\partial x_j} + \frac{\partial \vartheta \mathbf{u}_k^j}{\partial x_i}\right). \quad (9.16)$$

Here  $\mu_k \mathbf{M}_k^t$  is a turbulent viscosity for each phase k. The anisotropic formulation used for the turbulent conditions is:

$$\mathbf{M}_l^t = \mathbf{M}_0^t (Re - Re_t)^{b_M} \cdot f_M(Y_0)$$

where  $\mathbf{M}_0^t = 0.04$  is an experimental parameter taken constant in the whole domain. [245] [25] [212] [244] and  $f_M(Y_0) = (Y_0)^{C_m}$  with  $C_m$  an experimental input parameter [25].

The two phase multiplying coefficient  $Y_0$  is defined following the FLICA3 expression [25]:

$$Y_0 = 1 + (Y - 1) \left(1 + \frac{P_{heat}}{P_h} \Phi_{wall} 10^{-6}\right), \quad (9.17)$$

where Y is an input parameter from the HTFS formulation [50].

### 9.3.5 Wall Friction force

The effect of the friction induced by the pins and grids which are distributed inside the core is modelled by a volumic density force  $\boldsymbol{\tau}$ . The term  $\boldsymbol{\tau}$  is the sum of the parietal friction force ( $\tau_w$ ) and the friction force on singular obstacles ( $\tau_s$ ).

$$\boldsymbol{\tau} = \boldsymbol{\tau}_w + \boldsymbol{\tau}_s \quad (9.18)$$

- parietal friction force. It has the expression:

$$\boldsymbol{\tau}_w = -\frac{1}{2D_h}\rho\mathbf{f}\cdot\mathbf{u}\|\mathbf{u}\|, \quad (9.19)$$

where the tensor  $\mathbf{f}$  is given by a specific correlation [25].

- singular friction force. It takes the form:

$$\boldsymbol{\tau}_s = -\frac{1}{2}\rho'\mathbf{K}_s\cdot\mathbf{u}\|\mathbf{u}\|, \quad (9.20)$$

where the tensor  $\mathbf{K}_s$  is an antisymmetric tensor:

$$\mathbf{K}_s = \begin{pmatrix} K_s^Z & K_s^{ZX} & K_s^{ZY} \\ K_s^{ZX} & K_s^X & K_s^{XY} \\ K_s^{ZY} & K_s^{XY} & K_s^Y \end{pmatrix}$$

The coefficient  $K_s^{ij}$ , with  $i \neq j$ , models the rotative effect induced by the mixing grid. These coefficients are defined by the user depending on the geometry of the problem. The parameter  $\rho'$  is defined as follows:

- homogeneous friction force

$$\rho' = \rho$$

- friction force with acceleration [211]

$$\rho' = \frac{\rho^2}{\rho^*}$$

with

$$\frac{1}{\rho^*} = \alpha_l \frac{1}{\rho_l} + \alpha_g \frac{1}{\rho_g}$$

$$\alpha_{lq} = \begin{cases} \frac{(1-X_g)^2}{1-\alpha_g} & \text{if } \alpha_g \neq 0 \\ 1 & \text{else} \end{cases}$$

$$\alpha_{gq} = \begin{cases} \frac{X_q^2}{\alpha_g} & \text{if } \alpha_g \neq 0 \\ 1 & \text{else} \end{cases}$$

$$X_q = \frac{G_g^Z}{G^Z} = \frac{\alpha_g \rho_g \mathbf{u}_g^Z}{(1 - \alpha_g) \rho_l \mathbf{u}_l^Z + \alpha_g \rho_g \mathbf{u}_g^Z}.$$

### 9.3.6 Thermal coefficient and sources terms

The heat flux induced by the thermal conductivity and the turbulent mixing term is given by:

$$\mathbf{q} = K_l \nabla \vartheta h_{deb} \quad (9.21)$$

where the conduction  $K_l$  has laminar and turbulent components decomposed as follows:

$$K_l = \frac{\lambda_l}{C_{pl}} (1 + K_l^t). \quad (9.22)$$

Above  $K_l^t$  is an experimental parameted defined as follows [245] [25] [211] [244]:

- laminar flow ( $Re < 3000$ ):  $K_l^t = 0$ ,
- turbulent flow ( $Re > 3000$ ):  $K_l^t = 0.04(Re - 3000)$ .

The source term  $Q_{tot}$  represents the source energy given by the fuel to the fluid by fission or thermal transfer:

$$Q_{tot} = P_{fluid} + \Phi_{wall}^{vol} \quad (9.23)$$

where  $P_{fluid} = \frac{\gamma P^{integrated}}{V_{fluid}}$  (see section ( 3.3.8 )) is the fluid Power deposition from APOLLO3 per subchannel and  $\Phi_{wall}^{vol} = (\Phi_{wall} * S_{wall})/V_{fluid}$  is the Thermal flux transfer from the fuel pellet wall surface  $\Phi_{wall}$  (see eq. (7.18)) to the liquid volume.

The heat transfer between clad surface and the fluid (liquid k=l or gas k=g) modeled in FLICA4 covers several regimes: single-phase liquid or gas, nucleate boiling and annular dryout. The single phase is used by default in the FLICA4 code with a threshold effect related to the Thermal critical flux rate.

- single-phase

For single-phase conditions,  $T_w < T_{sat}$ , where  $T_{sat}$  is tabulated regarding the pressure, the heat transfer coefficient is defined by:



$$\Phi_{wall} = H (T_w - T_l) \quad (9.24)$$

where  $T_i$  is the liquid temperature inside FLICA4 problem,  $\Phi_{wall}$  and  $T_w$  are the coupling variable from ThermoHydraulical-ThermoMechanical coupling, and the exchange coefficient  $H$  is calculated by the following equation :

$$H = \frac{\nu_p}{D_{heat}} = Nu \lambda_w / D_{heat}$$

with parameters  $D_{heat}$  and  $\lambda_w = \lambda(p, \min[T_{sat}; \frac{T_w + T_l}{2}])$ . The thermal conductivity  $\lambda$  is tabulated in a multiparametrized library as function of pressure and temperature.

Usually, three different cases are considered in order to calculate the Nusselt number:

- For laminar conditions ( $Re < 2000$ ), the Nusselt number is constant, and specified by the user, the Dittus-Boelter give us: [51]

$$Nu = Nu_{lam} = 4.36,$$

- For turbulent conditions ( $Re > 5000$ ), the Nusselt number is a function of Reynolds and Prandtl numbers,

$$Nu_{turbulent} = 0.023 * Re^{0.8} Pr_l^{0.4},$$

- For transition between laminar and turbulent conditions, a linear interpolation based on Reynolds number is used.

- Boiling Phase: this variant is not used in our model.

- Annular dryout phase

This phase is triggered when the ratio RFTC between a critical value  $\Phi_{wall}^{critical}$  of the heat flux and the real value  $\Phi_{wall}$  is less than 2:

$$\text{dryout if } RFTC = \frac{\Phi_{wall}^{critical}}{\Phi_{wall}^{single\_phase}} < 2. \quad (9.25)$$

The critical flux is an experimental value which has been tabulated in different conditions [254].

When we reach this limit, we directly transition from a single phase to an annular dryout, and in this cas we use the film boiling classical Bishop, Sandberg and Tong [26] expression:

$$\Phi_{wall} = H_{BST} (T_w - T_{film}) \quad (9.26)$$

where  $H_k$  is expressed as follows:

$$H_{BST} = \frac{\lambda_f}{D_h} \cdot 0.0193 \cdot \left( \frac{D_{heat} G_f}{\mu_f} \right)^{0.80} \left( \frac{\mu_f C_{pf}}{\lambda_f} \right)^{1.23} \left( \frac{\rho_\nu}{\rho} \right)^{0.068} \left( \frac{\rho_\nu}{\rho} \right)^{0.068}.$$

It is function of the thermodynamic parameters, i.e.,  $\lambda_f$  is the thermal conductivity,  $\mu_f$  the dynamic viscosity,  $\rho_k$  is the density,  $C_{pf}$  is the specific heat,  $G$  is the mass flow rate. The film temperature is defined by:

$$T_{film} = 0.5 (T_w + T_{sat}).$$

Both case Eq. ( (9.24)) or Eq. ( (9.26)) enter the framework Eq. ( (7.18)) used in our coupling strategy.

### 9.3.7 Porous Model Boundary conditions

- Lateral conditions:
  - Wall impermeability:  $\mathbf{u}_{solid}\mathbf{n} = \mathbf{u}_{fluid}\mathbf{n} = \mathbf{0}$  on  $\delta\Omega_{solid}$ ,
  - Adiabatic conditions:  $\Phi_{reflector} = 0$ ,
- Hydraulic Flow conditions for upper and lower boundaries: inner hydraulic flow  $Q_z(0)$  = outer hydraulic flow  $Q_z(z_{max})$  ,

## 9.4 Discretization and Code description

As seen above, FLICA4 [11] is a Thermohydraulics-Diphasic porous code defined by 3 conservative equations, 1 vapor diffusion equation and 2 closure laws. The numerical method is finite volume Roe/FV9 scheme with an implicit time discretization. The Roe/FV9 scheme is based on an extension of Roe's approximate Riemann solver to define convective fluxes and on the second order Finite Volume scheme FV9 to estimate the diffusive fluxes. In more details, the system of equations for the two-phase flow (9.1) to (9.2) writes:

$$\frac{d\mathbf{U}}{dt} + \nabla \cdot (\mathbf{F}(\mathbf{U}) + \mathbf{G}(\mathbf{U}, \nabla \mathbf{U})) = \mathbf{S}(\mathbf{U}), \quad (9.27)$$

where  $\mathbf{U}$  is the vector of conservative variables  $U = \rho, \rho c, \rho u, \rho E$ , the fluxes  $\mathbf{F}$  and  $\mathbf{G}$  are respectively the inviscid flux(convection) and the viscous flux (diffusion), and  $\mathbf{S}$  is the source term. Finite volume method consists in integrating the equation (9.27) on each cell of the mesh which requires in the calculation of numerical flux at each interface between two adjacent cells.

$$V_c \frac{d\mathbf{U}}{dt} + \int_{\partial C} \mathbf{F}(\mathbf{U}) \cdot \mathbf{n} d\Gamma + \int_{\partial C} \mathbf{G}(\mathbf{U}, \nabla \mathbf{U}) \cdot \mathbf{n} d\Gamma = V_c \mathbf{S}(\mathbf{U}), \quad (9.28)$$

where  $V_c$  is the cell volume and  $\Gamma$  surface interface of the cell. The finite volume approximation assumes that the conservative variables are constant over each control volume  $C$ . For convective fluxes  $F(U)$ , the numerical method developed in FLICA4 is based on a Roe's approximate Riemann solver [258] at the cell interface  $\partial C_{i,j,k-i+1,j,k}$  (located at  $x$  on the interface between two adjacent cells  $C_{i,j,k}$  and  $C_{i+1,j,k}$ ) solving:

$$\frac{\partial \mathbf{U}}{\partial t} + \frac{\partial \mathbf{F}(\mathbf{U})}{\partial x} = 0, \quad (9.29)$$

with discontinuous initial conditions at  $t=0$   $U(x^{i,j}, 0) = U_{i,j}$  and  $U(x^{i+1,j}, 0) = U_{i+1,j}$  for each control volume (see figure ( 9.1)). Its linearized form writes:

$$\partial_t \mathbf{U} + \frac{\partial \mathbf{F}}{\partial \mathbf{U}} \partial_x \mathbf{U} = 0. \quad (9.30)$$

This linearized problem with the above initial condition can be exactly solved by projecting the problem on the eigenvalues of the jacobian  $\frac{\partial \mathbf{F}}{\partial \mathbf{U}}$  and the solution at  $x = 0$  is then used to build the corresponding flux  $i$  (Eq. (9.28)).

All the others specification of the Roe's approximate Riemann solver and calculation are accurately described in the dedicated report from the STMF laboratories [48] and [258].

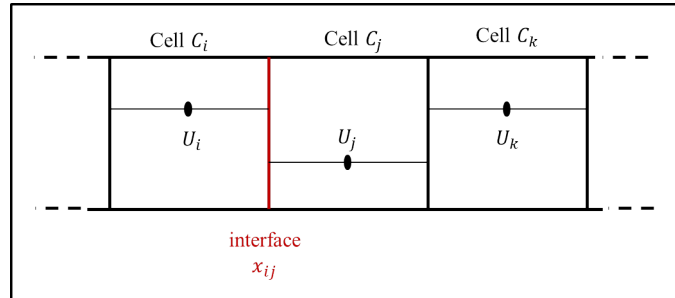


**Figure 9.1.** Initial discontinuous conditions

For the diffusion term, we need to calculate  $\mathbf{G}(\mathbf{U}, \nabla \mathbf{U})$  on the cell interface  $\partial C$ , and more precisely  $\nabla \mathbf{U}$  on  $\partial C$ . In this regard, we are using the Finite Volume nine point method FV9 [71] [27]. In order to compute the gradient  $\frac{\partial \mathbf{U}}{\partial x_d} \cdot \mathbf{n}_d$  along the normal  $\mathbf{n}_d$  to the face (with implicit summation on the coordinate  $d = i, j, k$ ), between two adjacent cells  $C_{i,j,k}$  at the left side and  $C_{i+1,j,k}$  at the right side of their interface  $\partial C_{i,i+1}$  (see figure ( 9.2)), we draw the perpendicular bisector to the interface  $\partial C_{i,i+1}$  and we take interest in the intersection between this line and the plane formed by 3 cell centers (at the left or right side). This plane contains the center  $\mathbf{C}_{i,j,k}$  of the cell  $C_{i,j,k}$  (respectively  $C_{i+1,j,k}$ ) and 2 centers from neighboring cells of  $C_{i,j,k}$  (respectively  $C_{i+1,j,k}$ ) such as the line passes through the triangle  $(\mathbf{C}_{i,j,k}, \mathbf{C}_{i,j,k}^{Neighbour-1}, \mathbf{C}_{i,j,k}^{Neighbour-2})$ . It yields the point  $M_{i,j,k}$  (respectively  $M_{i+1,j,k}$ ) of barycentric coordinates  $(\alpha_{i,j,k}, \alpha_{i,j,k}^{Neighbour-1}$  and  $\alpha_{i,j,k}^{Neighbour-2})$ . We calculate

$U(M_{i,j,k})$  (respectively  $U(M_{i+1,j,k})$ ) by linear interpolation between  $C_{i,j,k}$ ,  $C_{i,j,k}^{Neighbour-1}$  and  $C_{i,j,k}^{Neighbour-2}$ :

$U(M_{i,j,k}) = \alpha_{i,j,k} U(C_{i,j,k}) + \alpha_{i,j,k}^{Neighbour-1} U(C_{i,j,k}^{Neighbour-1}) + \alpha_{i,j,k}^{Neighbour-2} U(C_{i,j,k}^{Neighbour-2})$  (respectively  $U(M_{i+1,j,k})$ ). We then set:

$$\frac{\partial U}{\partial x_i} \cdot \mathbf{n}_i = \frac{U(M_{i,j,k}) - U(M_{i+1,j,k})}{d(M_{i,j,k}, M_{i+1,j,k})}, \quad (9.31)$$

where  $U(M_{i,j,k})$  is the prediction of  $U$  at the point  $M_{i,j,k}$  (respectively  $U(M_{i+1,j,k})$ ) and  $d(M_{i,j,k}, M_{i+1,j,k})$  is the distance between the two points  $M_{i,j,k}$  and  $M_{i+1,j,k}$ .

We have presented above the finite volume interpolation FV9 to use when the viscous flux is aligned with the gradient of  $U$ . Specific developments must be used in the construction of the normal direction when flux and gradient are not aligned.

More details about the numerical methods are given in [11], [8] and details regarding the nonconforming grid specifications are given in [27].

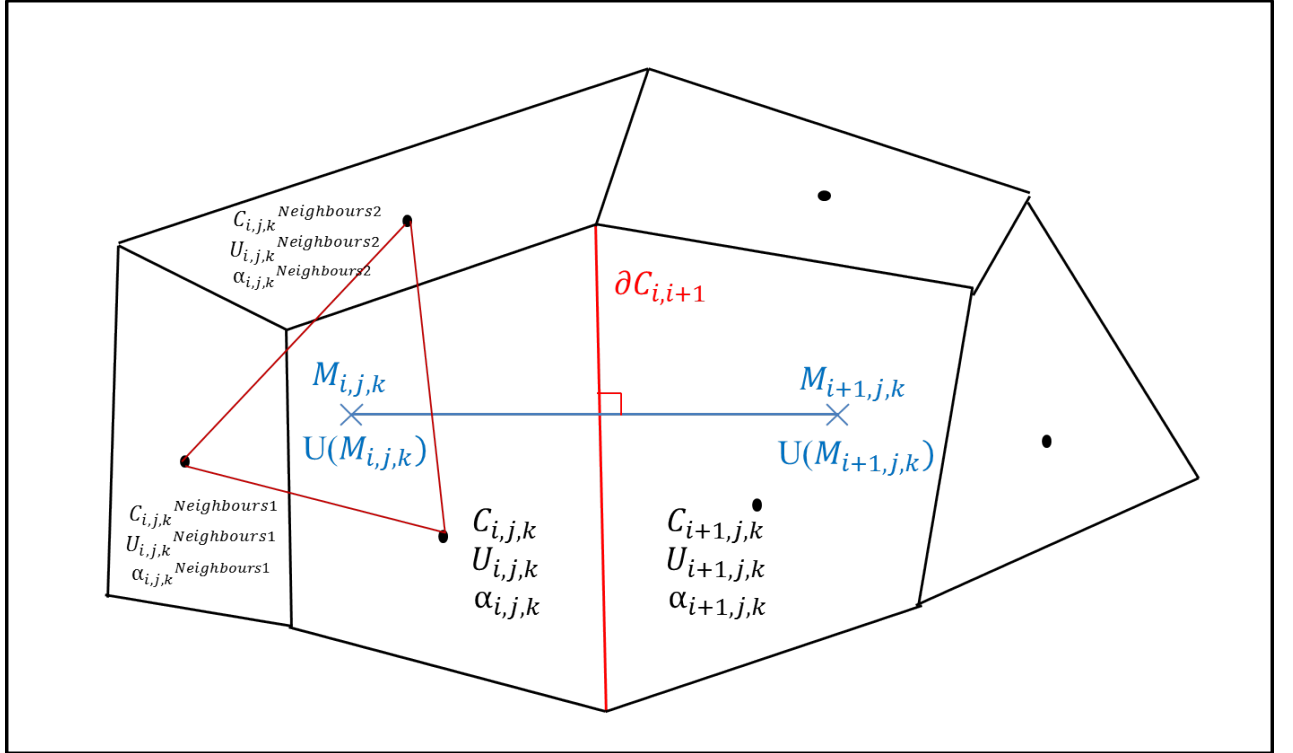


Figure 9.2. FV9 numerical method scheme



## Chapter 10

# Thermohydraulics conclusion

Finally, in this chapter, we summarized all the previous models and improvement point and we rewrote them in order to prepare the coupling part of this study.

### Mechanical models and numerical aspects:

In this part, we mathematically defined the Thermohydraulics models of the FLICA4 code we are going to use in our coupling strategy. The core reactor physical description can be realized using:

- There conservation laws for porous media:

- Conservation of mass (Eq. (9.1))

$$\vartheta \frac{\partial \rho}{\partial t} + \nabla \cdot (\vartheta \rho \mathbf{u}) = 0 \quad (10.1)$$

- Conservation of momentum (Eq. (9.4))

$$\begin{aligned} \vartheta \frac{\partial \sum_{k=g,l} (\alpha_k \rho_k \mathbf{u}_k)}{\partial t} + \nabla \cdot \left( \sum_{k=g,l} \vartheta \alpha_k \rho_k \mathbf{u}_k \otimes \mathbf{u}_k + \alpha_k \mathbf{\Pi}_k \right) \\ = \vartheta \rho \mathbf{g} + \vartheta \boldsymbol{\tau} \end{aligned} \quad (10.2)$$

- Conservation of energy (Eq. (9.5))

$$\begin{aligned} \vartheta \frac{\partial \sum_{k=g,l} (\alpha_k \rho_k E_k)}{\partial t} + \nabla \cdot \left( \sum_{k=g,l} (\vartheta \alpha_k \rho_k \mathbf{u}_k E_k - \alpha_k \mathbf{\Pi}_k \cdot \mathbf{u}_k) - \mathbf{q} \right) \\ = Q_{tot} + \vartheta \rho \mathbf{u}_k \cdot \mathbf{g} \end{aligned} \quad (10.3)$$

- One Fluid-Gas diffusion equation governing the vapor mass fraction  $c$  (Eq. (9.2)) and hence the void volume fraction  $\alpha_g$  since  $c = \frac{\alpha_g \rho_g}{\rho}$

$$\vartheta \frac{\partial (\rho c)}{\partial t} + \nabla \cdot (\vartheta \rho c \mathbf{u} + \vartheta \rho c (1 - c) \mathbf{u}_r - \vartheta K_c \nabla c) = \vartheta \Gamma, \quad (10.4)$$

- Closure laws are defined in section (9.3.2) and correspond to the drift flux correlation  $u_r$  (Eq. (9.6)), state equations regarding the density  $\rho_g$  and  $\rho_l$  (Eqs. (9.7) and (9.8)), temperatures  $T_g$  and  $T_l$  (Eqs. (9.9) and (9.10)), pressure  $p = p_g = p_l$  (Eq. (9.11)) and enthalpy  $h_g$  (Eq. (9.12)) conditions.
- The constitutive terms of the previous equations are the vapor production term  $\Gamma$  (Eq. (9.13) in section 9.3.3), the stress tensor  $\mathbf{\Pi}_k$  (Eq. (9.16) in section 9.3.4), the wall friction force  $\tau$  (Eq. (9.18) in section 9.3.5), thermal flux  $\mathbf{q}$  and heat source  $Q_{tot}$ . A specific attention is given to the thermal flux  $\mathbf{q}$  and source term  $Q_{tot} = P_\gamma + \Phi_{wall}^{vol}$  definitions (respectively Eq. (9.21) and (9.23) in section 9.3.6) according to the fluid phase and conditions.
- Boundary conditions are defined in section (9.3.7) and correspond to:
  - The adiabatic condition:  $\Phi_{reflector} = 0$ ,
  - The hydraulic flow conservation:  $Q_z(0) = Q_z(z_{max}) = 4240.72 \text{ m}^3/\text{h}$

In REA simulation, the Boron concentration (Eq. (9.3)) is supposed to stay constant during the transient.

The calculation is obtained by using the numerical Roe/FV9 finite volume method of FLICA4 code, (Eq. (9.30)) and (Eq. (9.31)) detailed in section (9.4).

### Phenomenological and physical aspects of the Transient:

The transient induces a strong change of the fluid power  $P_{fluid}(r,t)$ , directly deposited to the fluid and a strong change of the fuel power deposition inside the fuel pin, both due to the neutronics evolution. The fuel power inside the fuel pin is partly transferred to the fluid from the cladding and through a thermal flux  $\Phi_{wall}(r,t)$  which is added to the Fluid

---

power energy source term. This Fluid power and this Fuel heat induces a change of the thermal state of the fluid ( $g = \text{gas}$  and  $l = \text{liquid}$ ):

- Void coefficient :  $\alpha_{k=g,l}$ ,
- Celerity:  $u_{k=g,l}$ ,
- Density:  $\rho_{k=g,l}$ ,
- Energy:  $E_{k=g,l}$ ,
- Enthalpy:  $h_{k=g,l}$ ,
- Pressure:  $p$  .

In this evolution, there might be a major threshold effect if we exceed the thermal critical flux rate ( $\text{RFTC}(\Phi_{wall}(r,t))$  in Eq. (9.25)) and reach ebullition or Dry-out conditions.

This change of state has two effects on the coupled models:

- The fluid density  $\rho(r,t) = \alpha_g \rho_g + \alpha_l \rho_l$  (also called  $D_{mod}(r,t)$  in the neutronics part) directly impacts the neutronics evolution through the moderator feedback effect.
- The clad surface temperature  $T_{wall}(r,t)$  changes and directly impacts the fuel pin thermal state  $T_{fuel}(r,t)(x)$  in equation (6.52), where  $r$  is the core scale and  $x$  the local scale and the mechanical state of the fuel pin.

### ThermoMechanical coupling aspects:

The following bloc diagram summarizes the previous sections and conclusion, indicating the equations, the core discretization (at the scale of 1/4 assembly), Thermohydraulical parameters we observe and coupling variables we use in a Best Effort coupling approach, i.e., Neutronics variables in green, Hydrodynamics variables in blue and Thermomechanics variables in red.

The coupling variables consist in:

- Input variables (respectively distributed in space and surface variables):
  - Fluid power  $P_{fluid}(r,t)$  (eq. 3.41).
  - The thermal variables  $S_p = \Phi_{wall} - A_p T_{wall}$  and the pin homogenized conductance  $A_p = \frac{\partial \Phi_{wall}}{\partial T_{wall}}$ , in eq. (7.23) related to the thermal flux  $\Phi_{wall}(r,t)$  at the clad external surface.
- Output variables (distributed in space):
  - Moderator density  $D_{mod}(r,t)$  (eq. (9.10)) ,



- The clad external surface temperature  $T_{wall}(r, t)$  (eq. (7.22)).

Moreover, the impact of coupling will be observed on though the Thermal critical flux rate RFTC if it is activated during the transient.

Parameters Name	Parameters Symbols	Coupling Type	Type
Fluid Power	$P_{fluid}(r, t)$	input	Distributed in space
Thermal variables	$\Phi_{wall}(r, t)$ $A_p(r, t)$ $S_p(r, t)$	input	surface
Clad surface temperature	$T_{wall}(r, t)$	output	Distributed in space
Fluid Density	$D_{mod}(r, t)$	output	Distributed in space
Thermal critical flux rate	RFTC(r,t)	ThermoHydraulical observation	Distributed in space

**Table 10.1.** ThermoHydraulics input, output and monitored parameters (where  $r$  is the space variables at core scale and  $x$  is the local space variables)

These output and input variables are summarized in the following block diagram.

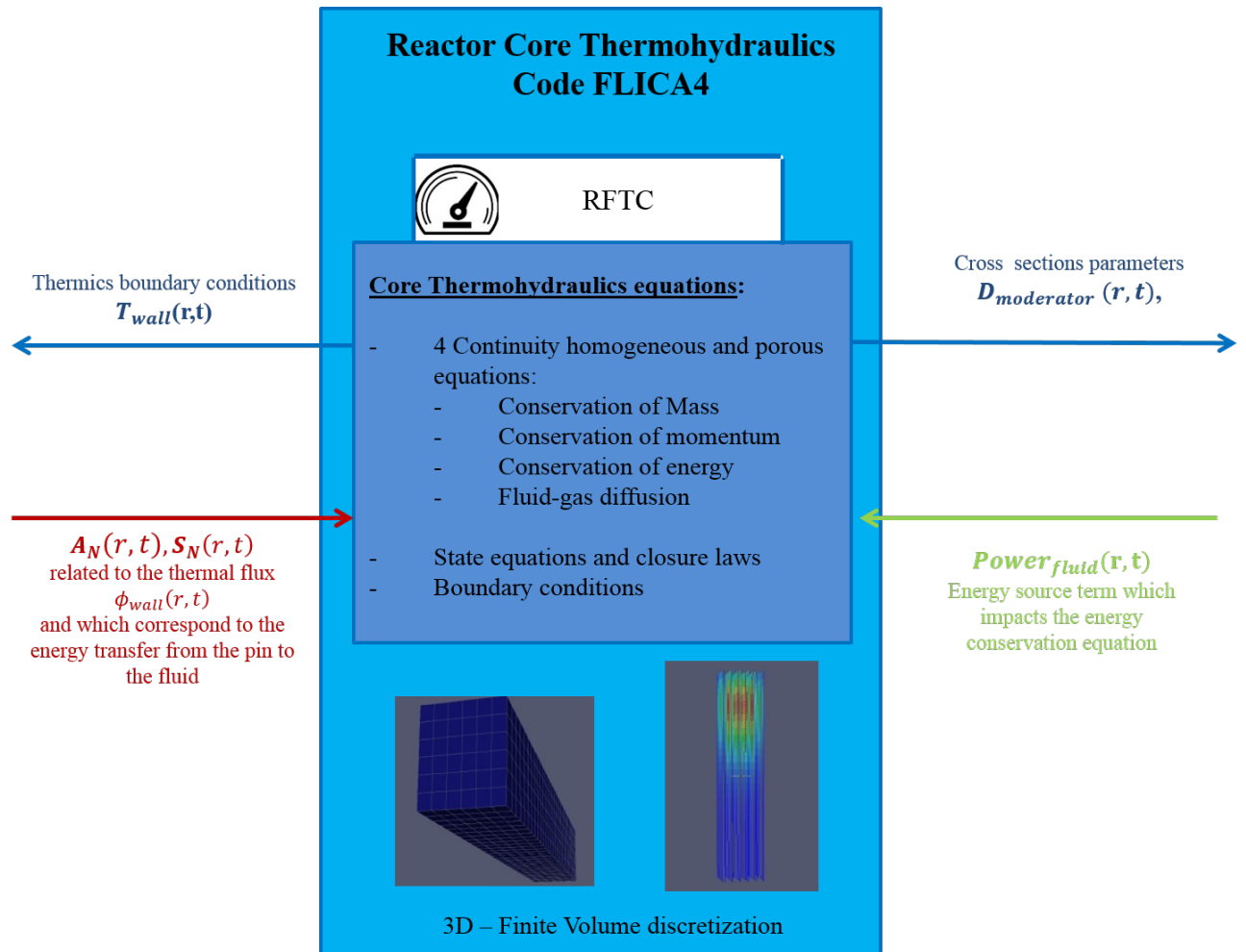


**Figure 10.1.** ThermoHydraulics Block diagram with exchange variables and discretization

**Model improvements and limitations:**

- Key points taken up and improvements carried out by this study:
  - By using an implicit linearized approach, detailed in section ( 7.1), we precisely access to the homogenized conductance  $A_p = \frac{\partial \Phi_{wall}}{\partial T_{wall}}$  and we obtain a better estimation of the global behavior of the fluid. This also induces a better coupling with the fuel pin thermics through the  $T_{wall}(r,t)$  boundary condition.
- Present Thermohydraulical challenges in perspective of a Best Effort multiphysics calculation:
  - In the Thermohydraulics models, limitations appear from the constant porosity term of the conservation equations. Indeed, regarding the Thermohydraulical effects, the homogeneous porous equations are using a constant porosity, which implies that we neglect the fuel pin deformation (PCMI, swelling, burst and so on) and thus the sub channel diameter variation during a transient situation. In case of REA, the sub channel barely changes in diameter which legitimates the hypothesis of a constant sub channel diameter. Nevertheless, this would be a serious limitation in case of transient scenarii with large mechanical deformations of fuel pins at the scale of the sub channel.
  - In the Thermohydraulics models, limitations appear from the Thermohydraulical phase threshold effects. Indeed, they had been determined by performing steady state experiments that do not reflect the dynamic of the transient, which is a potential source of discrepancy. Moreover the numerical treatment of the threshold effect in the thermal flux rate lacks robustness in coupling situations.
  - In case of precise discretization of core (local scale), the conforming discretization used here can be very demanding in computer resources. The general nonconforming approach [27] could be a solution.

## Part V

# Multiphysics Best Effort coupling - Proof of Concept



---

In this part, we are going to define our coupling methodology and expose the results we obtained according to the previous model parts ( III),( 6), ( 9) and following our global coupling scheme.

First of all, we will work on proof of concept studies regarding the Thermohydraulics-Thermomechanics coupling approach defined in section ( 7.1) and fed by a pre-calculated neutronic power pulse. Then, in a second time, we will define the algorithms we develop regarding Neutronics -Thermohydraulics - Thermomechanics coupling with different level of accuracy and through specialized codes APOLLO3, ALCYONE and FLICA4 (and thier simplified models of other disciplines). Thus, we will compare our multiphysics coupling models and present the results we obtained regarding different coupling cases:

- Hydraulics simplification coupling (Neutronics - Thermomechanics - simplified Thermohydraulics coupling)
- Thermomechanics simplification coupling (Neutronics - simplified Thermomechanics - Thermohydraulics coupling)
- Total multiphysics Best Effort coupling (Neutronics - Thermohydraulics - Thermomechanics coupling)

Specific studies will be done on effective temperature and burn up aspects in order to analyse the enhancement on modelling, according to the improvement of physical models on their way to meet the most representative and Best Effort coupling.

This part illustrates our approach and ability to couple disciplines all together in order to improve simulations in Nuclear Reactor Physics. Our academic core case and academic scenario defined in section ( 2.4) allow us to perform realistic calculations. However, this academic core and this scenario are approximations that would not be able to reflect exactly and accuratly the behavior of a real reactor: although the phenomenology is relevant, spatial distribution, amplitude and dynamic may significantly change from a standard 1300MW PWR.

---

## Chapter 11

# Thermohydraulics-Thermomechanics coupling - proof of concept

### 11.1 Methodology

From the transient part ( 2.4.2), the neutronic calculation produces a set of data of the power core distribution function of the time ( $\Delta t = 10^{-3}$ ) that would be used as input data, which would supply the coupled Thermohydraulics-Thermomechanics modelling part. On its part, the Thermohydraulics-Thermomechanics coupled modelling uses an implicit and linearized scheme ( section ( 7.1)) in order to solve the fuel pin nonlinear Thermics and the four Fluid equations (detailed respectively in chapter ( 6) and chapter ( 9)). The Coupling scheme is defined in the following figure ( 11.1). By construction, this approach defines theoretically an unconditionally stable numerical scheme [9]. This operation will be repeated at each time step without any repercussion on the neutronic data (no feedback effect).

The Thermohydraulics equations are solved over the active part of the core and we are using a similar discretization of the neutronic modelling for the Thermohydraulics, i.e., 4 radial cells per assembly and 30 axial cells. On its part, the ALCYONE Thermomechanical resolution is realized on a single pin. This way a representative pin is calculated for each quarter of assembly with the same axial discretization as the Thermohydraulics, i.e., 30 layers of cells along the vertical direction. Because of symmetry, among the 36 pieces of assembly, we just have to consider 6 representative zones as indicated on Figure ( 11.2); 1/8 symmetry is highlighted in red in figure ( 11.2). This means that we have to run six independent instances of Alcyone in parallel .

This Thermohydraulics-Thermomechanics coupling has been studied according to the



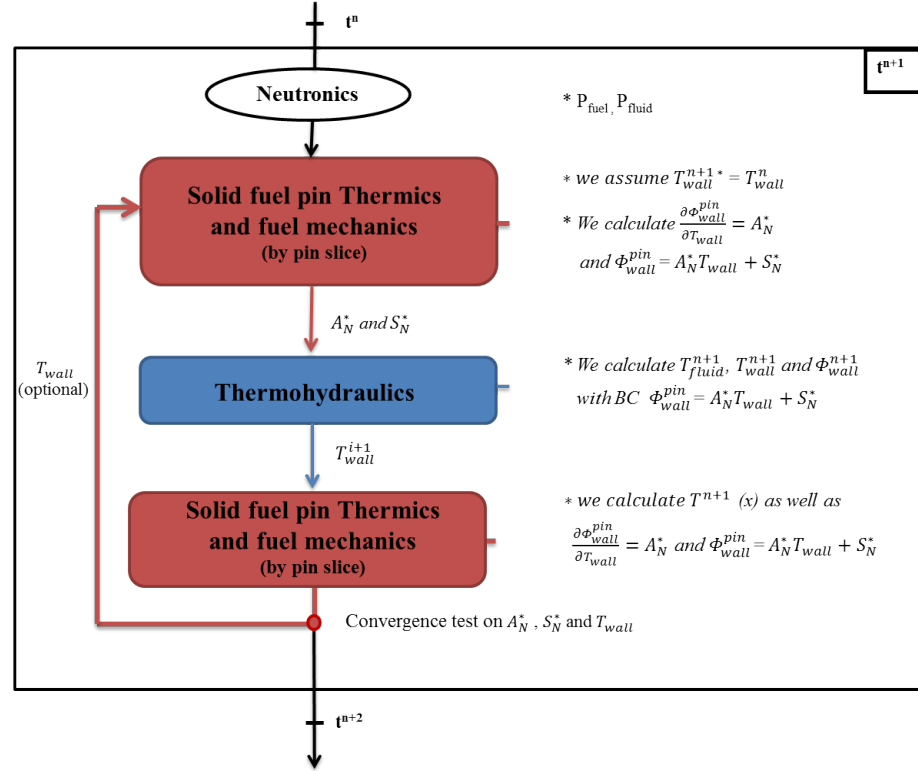


**Figure 11.1.** F4 - ALCYONE time coupling scheme with exchanged variables

scenario detailed in section ( 2.4.2). The transient REA without dryout phase that we have developed has been used in order to validate and analyze the coupling.

In conclusion, this coupling approach can be summarized as follows (figure 11.1):

Time step  $t^{n+1}$

- Fuel pin solid calculation: we obtain  $a_N^*$  and  $s_N^*$  by using the wall temperature of the previous time step  $T_{wall}^n$  at the present neutronic power  $P^{n+1}$  as precalculated in APOLLO3;
- Fluid calculation: we obtain  $T_f^{n+1}$  and thanks to the equation (7.22) we obtain the wall temperature  $T_{wall}^{n+1}$  and flux  $\Phi_{wall}^{n+1}$ ;
- Fuel pin thermal calculation: we re-calculate  $T(x)^{n+1}$  and new coefficients  $a_N^{**}$  and  $s_N^{**}$  with the right  $T_{wall}^{n+1}$  and  $P^{n+1}$ ;
- Comparison between  $a_N^{**}$  and  $a_N^*$  as well as between  $s_N^{**}$  and  $s_N^*$ . If the ratio between these two calculations of the coefficients is inferior to the convergence criterium, we

continue the time evolution of the system, otherwise we redo the calculation until the convergence is reached. In our work, due to software limitations, this fixed point correction was not implemented.

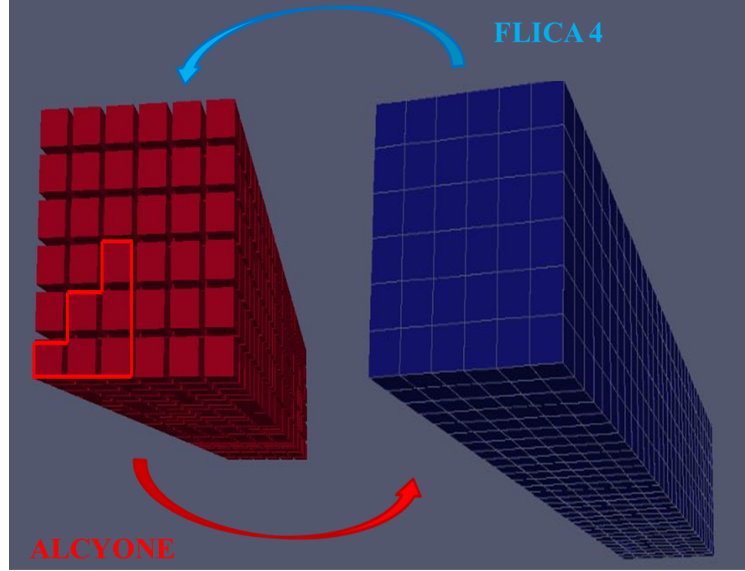


**Figure 11.2.** Multiphysics coupling scheme: spatial discretization and correspondency.

Figure ( 11.3) illustrates the fuel pin thermal axisymmetric discretization and the variables exchanges. The Fuel pin is composed by the pellet, the clad but also by the gap between the pellet and the clad. This gap is usually expressed by the Thermal exchange coefficient  $H_{gap}$  that reflects the opened or closed state of the gap. This gap is filled by gas and thus will significantly impact the thermal exchange between the pellet and the clad. This is one of the essential thermal aspects we are going to discuss in the results section of this part and is an important added value of a detailed thermal analysis as done in ALCYONE compared to a simplified analysis as done in FLICA4.

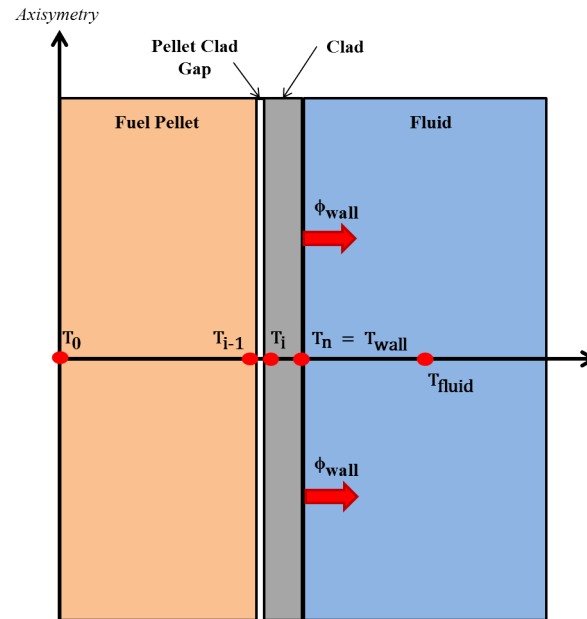


**Figure 11.3.** Radial Fuel Pin discretization and exchanged variables

During this study, regarding the thermomechanical part (input data of the fuel pins composition), we are going to work with assemblies at burn-up = 0 MWd/t (fresh fuel). The effective distribution of the burn-up inside the core is only taken into account in the neutronic part of the calculation. The burn-up heterogeneous distribution (figure ( 2.11)) should be taken into account in future simulations and studies on the physical behavior of the reactor core but ignoring it will not affect our exercise on the feasibility of a multi-physics coupling.

## 11.2 Numerical and Physical verification

The first step of this feasibility study was to validate numerically our coupling. This way we checked the exact exchange of our coupling variables. We validate the stability of the physical answer of our coupling and the preservation of the deposited energy (source term of the Thermal heat equation (6.52) by realizing a false transient which means a transient at constant power ( $P = 110 \cdot 10^{-9} \text{W}$ ) input function of time. Starting from slightly different initial temperature data in Thermohydraulics ( $T_{fluid} = 289.90 \text{ }^{\circ}\text{C}$ ) and Thermomechanics ( $T_{fuel\_pin} = 289.95 \text{ }^{\circ}\text{C}$ ), the fuel pin clad temperature finally converge to a steady state temperature equal to the fluid temperature. Figure ( 11.4) shows this convergence. Considering the center/surface fuel temperature as well as internal/external surface clad temperature, we observe a slight difference between the pellet and the clad but regarding a very long time duration we will observe the pellet temperature reaching the fluid temperature value, as it begins in the case of the surface pellet temperature.

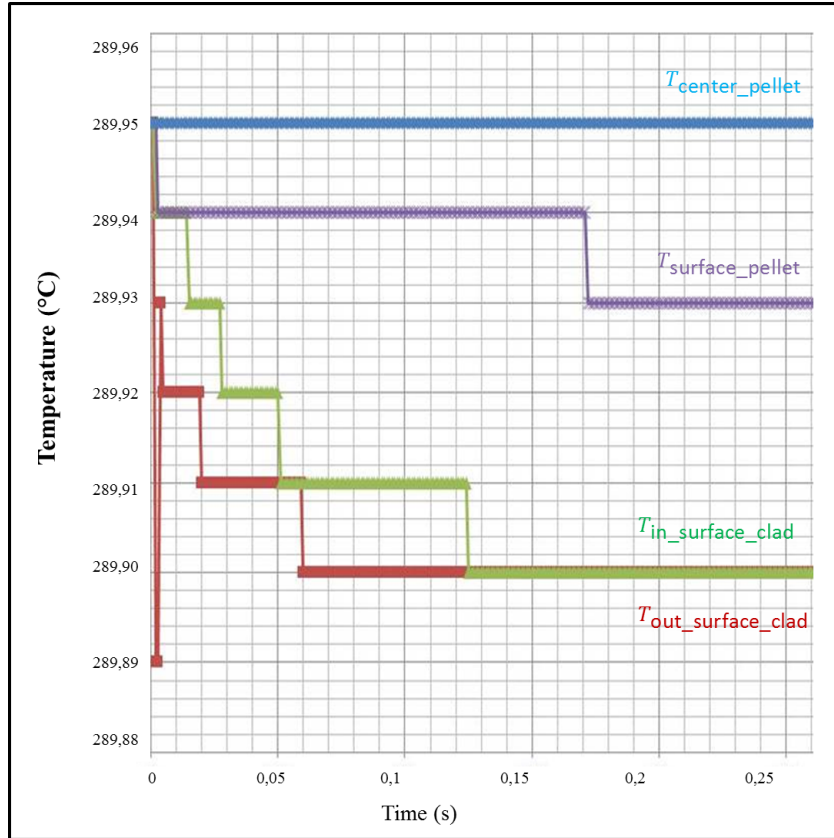
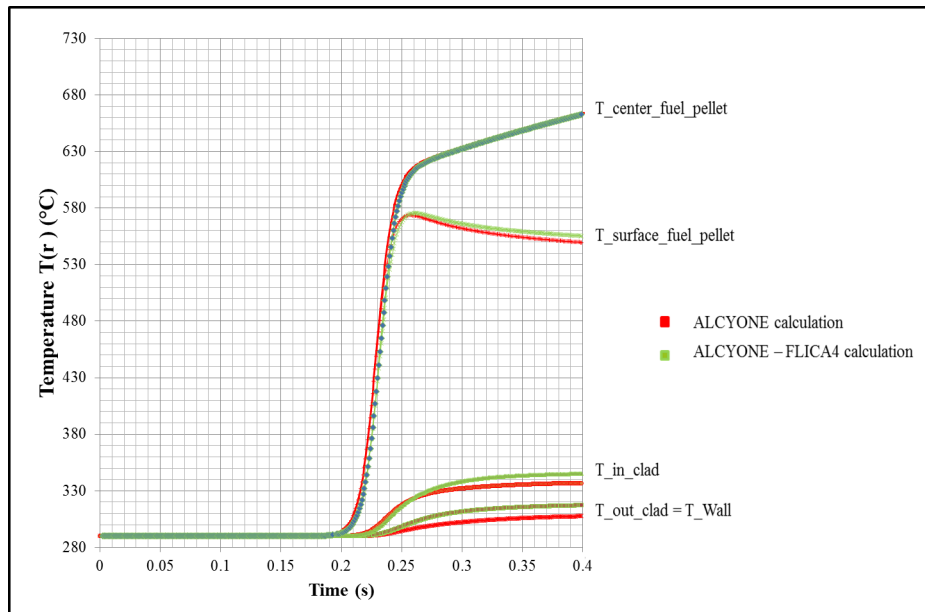


Figure 11.4. Coupling validation with Transient at constant Power

### 11.3 Results

From our numerical method laid out in the previous section ( 7.1), we implement our coupling scheme computationally. We transfer the relevant thermal coefficients from the Fuel thermics ALCYONE to Thermohydraulics FLICA4 and conversely. We obtain results and we extract values from the Hot spot cell.

More specifically, based on our calculation, and considering the fuel temperatures for example, we obtain the temperature function of time at the surface and at the center of the pellet and at the internal and external surface of the clad in figure ( 11.5).



**Figure 11.5.** Core averaged fuel pin temperature profile comparison between the fuel thermic ALCYONE standalone and F4-ALCYONE coupling using the transient scenario detailed in section ( 2.4) and Annexe( 15)

These temperatures express the conservation of the correct physical answer to the neutronic data set (same power deposition) and the physical coherency between our multiphysics coupling and the Thermomechanical ALCYONE stand alone (SA) calculation. Indeed, if we compare the fuel pin temperature distribution and time evolution, we observe that the curves are very similar, in time and distribution, between a Thermomechanical stand alone calculation (ALCYONE) and our Thermohydraulics -Thermomechanics coupling calculation (FLICA-ALCYONE). The temperature inside the pellet shows the smallest difference in terms of temperature which is logical since the two calculations are using the same fuel pellet model and the same Power source term. The real impacts on fuel pin temperatures comes from the thermal exchange model we use between the clad and the

fluid. It slightly impact the central part of the pin due to the thermal conductivity of the pellet but drastically impacts the clad surface temperature. Indeed, if we zoom in on the clad surface temperature ( $T_w$ ) and its evolution in time (figure ( 11.6)), we observe a difference of about 10 °C between the Thermomechanical stand alone calculation (ALCYONE) and our Thermohydraulics-Thermomechanics coupling calculation (FLICA4-ALCYONE).

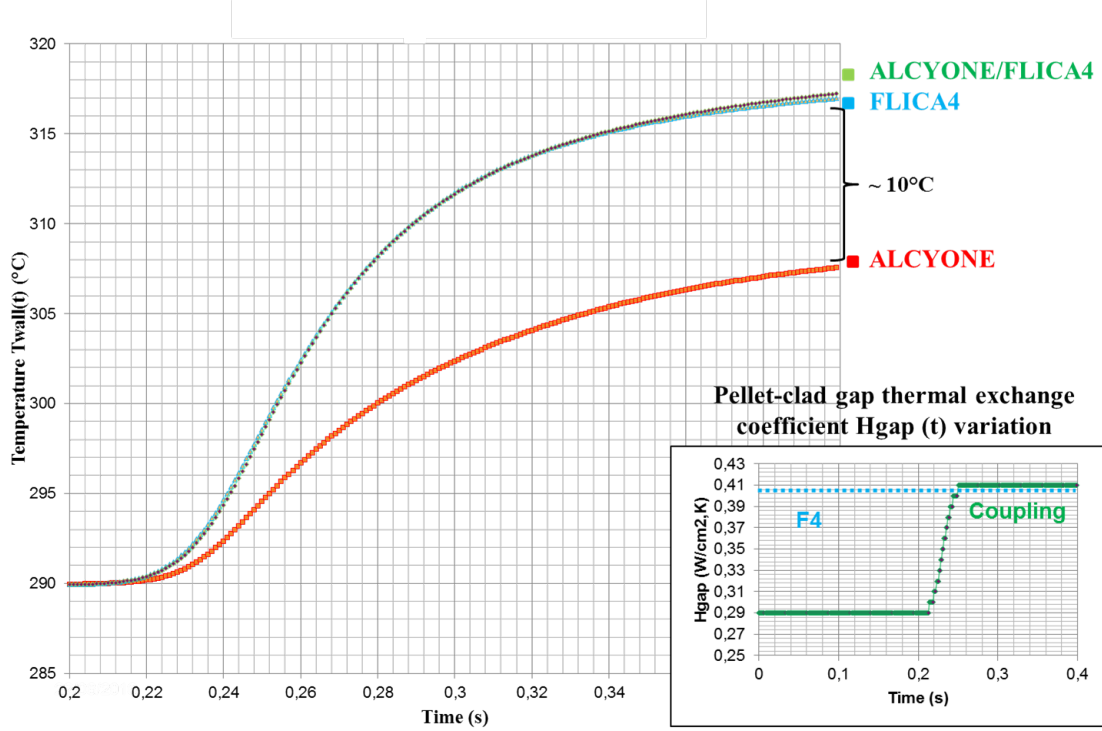


**Figure 11.6.** Observation of the thermohydraulic effet through the ALCY-ONE SA / FLICA4-ALCYONE comparison

In the same time we observe that the Thermohydraulical stand alone calculation (FLICA) and our Thermohydraulics-Thermomechanics coupling calculation yield almost identical  $T_w$  results. The Thermohydraulical stand alone calculation (FLICA) is obtained using an arbitrary  $H_{gap}$  that we choose regarding the value we obtain in the coupling calculation. Consequently, with the  $H_{gap}$  value from the coupling calculation ( $H_{gap} = 0.41$  W/(cm<sup>2</sup>.K)), the fuel thermic of FLICA4 is very similar to the fuel thermic of ALCYONE. However, the fluid part of FLICA4 is a far better description than the fluid part of the Thermohydraulics simplified solver of ALCYONE stand alone. More precisely, we have respectively a Navier Stockes 4 homogeneous equation resolution in the one hand and a simplified model that consists in an enthalpy balance without any pressure loss, turbulence and so on, on the other hand. This 10 °C difference is therefore due to the Thermohydraulical effect appearing from our coupling.

In conclusion, the coupling yields an improvement of the fuel pin temperature simulation and heat transfer to the fluid which will impact Power evolution in case of a coupling with neutronics through the Doppler and moderator feedback reactions. It also shows the need to accurately define the Hgap coefficient (according to the gap size, gap gas inventory and so on). Indeed, thermohydraulics commonly use a closed gap which leads to a Hgap coefficient of about  $50000 \text{ W.m}^{-2}.\text{K}^{-1}$ . This Hgap is chosen in order to get the most penalizing situation according to the fluid which means ebullition and dryout situation. However, this does not reflect the reality of the transient and feedback effects that occur during the transient.

The following figure ( 11.7) shows the differences between  $T_{wall}$  curves function of time and function of Hgap (from  $\text{Hgap}=25000 \text{ W.m}^{-2}.\text{K}^{-1}$  to  $\text{Hgap}=2500 \text{ W.m}^{-2}.\text{K}^{-1}$ ), without neutronics feedback effects. Indeed, we observe a maximal difference of about  $30 \text{ }^{\circ}\text{C}$  for stand alone FLICA calculations, in our academic scenario, just by changing the value of the input data Hgap.

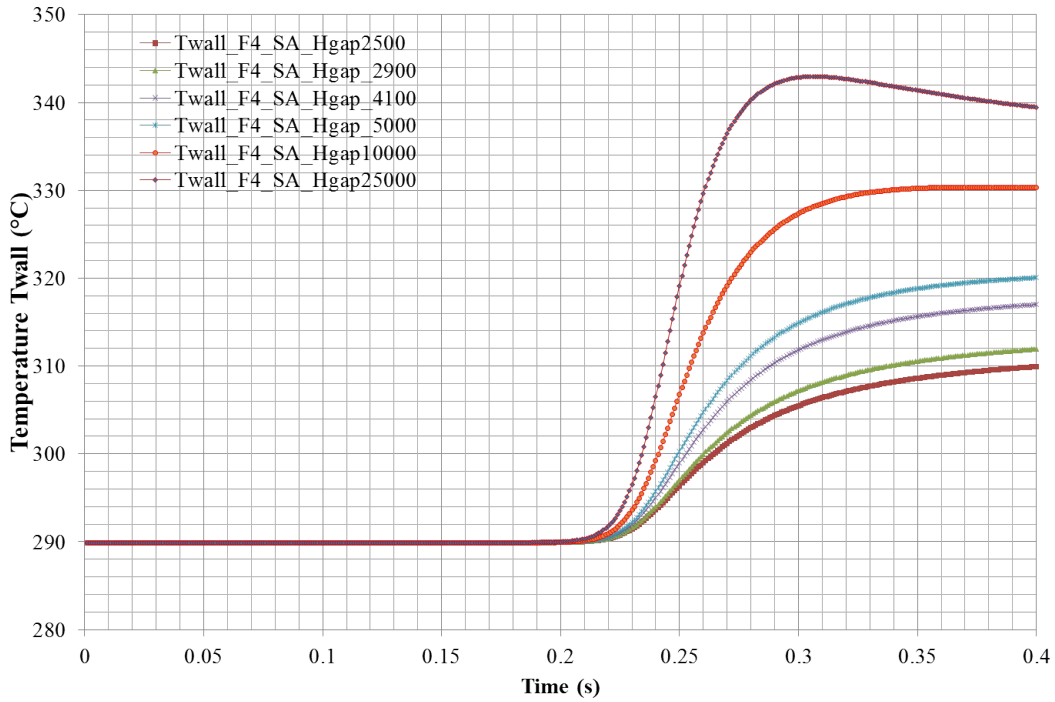


**Figure 11.7.** Tw sensivity and comparison regarding FLICA4 SA calculations with different input data of Hgap

During this study the fixed point was not necessary to realize the calculation because thermal coefficient, i.e.,  $a_N$  and  $s_N$  barely change between the two thermechanical calculations of a time step (maximal relative difference is less than 0.35 %). Figure ( 11.8) shows the thermal coefficient and Tw evolutions and differences during the transient.

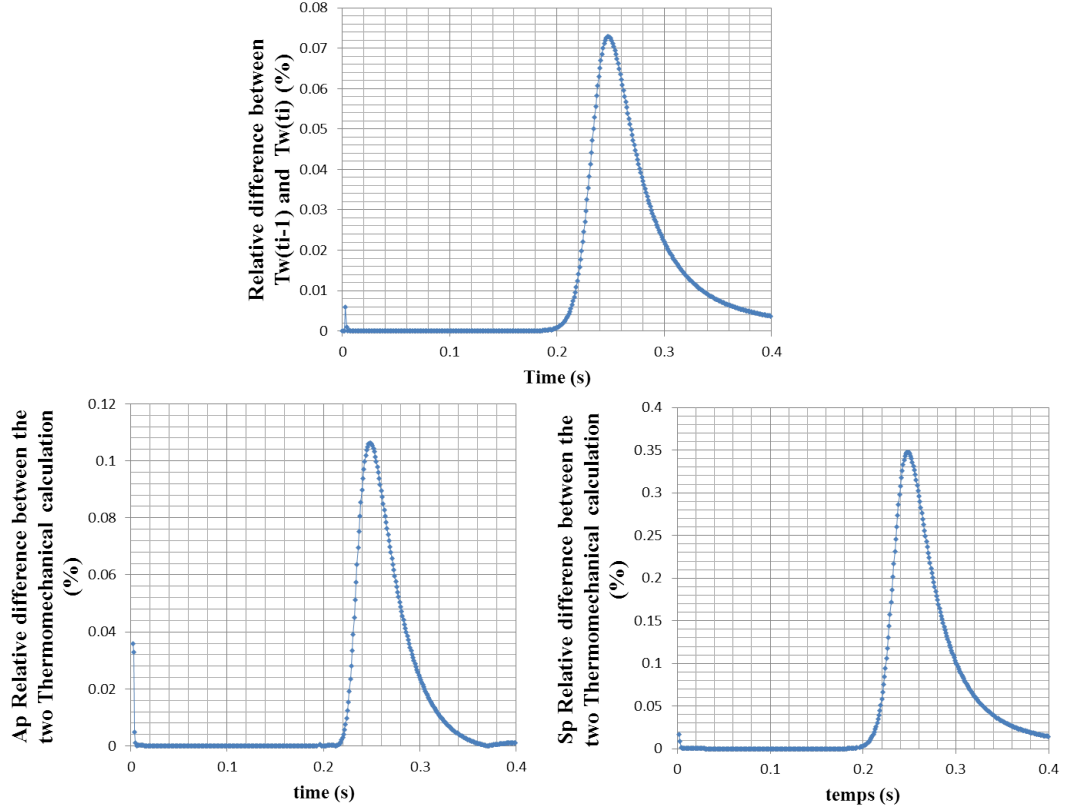


Figure 11.8. A, S and Tw relative difference (FLICA-ALCYONE coupling)

## 11.4 Conclusion

We have validated our exercise of coupling the nonlinear thermics model of the ALCY-ONE code with the Thermohydraulics model of the FLICA4 code by using a linearized coupling scheme through a realistic REA scenario. It shows the need to accurately reflect the reality of the physical disciplines during transient that would change the power transient through the neutronics feedback effects.





## Chapter 12

# Neutronics - Thermohydraulics - Thermomechanics coupling Algorithms and methodology - Proof of Concept

### 12.1 Total coupling algorithms

According to the previous block diagrams defined by discipline in the code models (parts ( 5), ( 8), ( 10)), we connect all these blocks together in order to obtain the Global block diagram which is the goal of this multiphysics coupling work, shown in figure ( 12.1). The coupling variables we already pinpointed are:

- Fuel temperature ( $T_{eff}$ ) and moderator density ( $D_{mod}$ ) as volumic distributed input variables for the neutronic part ( 5) ,
- Fuel power ( $P_{fuel} = (1 - \gamma) * P_{core}$ ) and clad surface temperature ( $T_{wall}$ ) as distributed input variables for the Thermomechanical part ( 8),
- Fluid power ( $P_{fluid} = \gamma P_{core}$ ) and thermal fuel pin coefficient ( $A_N$  and  $S_N$ ), respectively volumic distributed and surface input variables for the Thermohydraulical part ( 10).

On our way to this global coupling, we start by pairing codes while using internal simplified model in order to compute the missing third accurate model. Then we may

discriminate the contribution of each physical model on the global transient behavior. This way, we obtain result for:

- Hydraulics simplification coupling (Neutronics - Thermomechanics - simplified Thermohydraulics coupling)
- Thermomechanics simplification coupling (Neutronics - simplified Thermomechanics - Thermohydraulics coupling)
- Total multiphysics Best Effort coupling (Neutronics - Thermohydraulics - Thermomechanics coupling)

The algorithms and methodology we use are defined in the following section:

- Hydraulics simplification coupling in section ( 12.2),
- Thermomechanics simplification coupling in section ( 12.3),
- Total multiphysics Best Effort coupling in section ( 12.4).

The results will be compared and discussed in section ( 13).

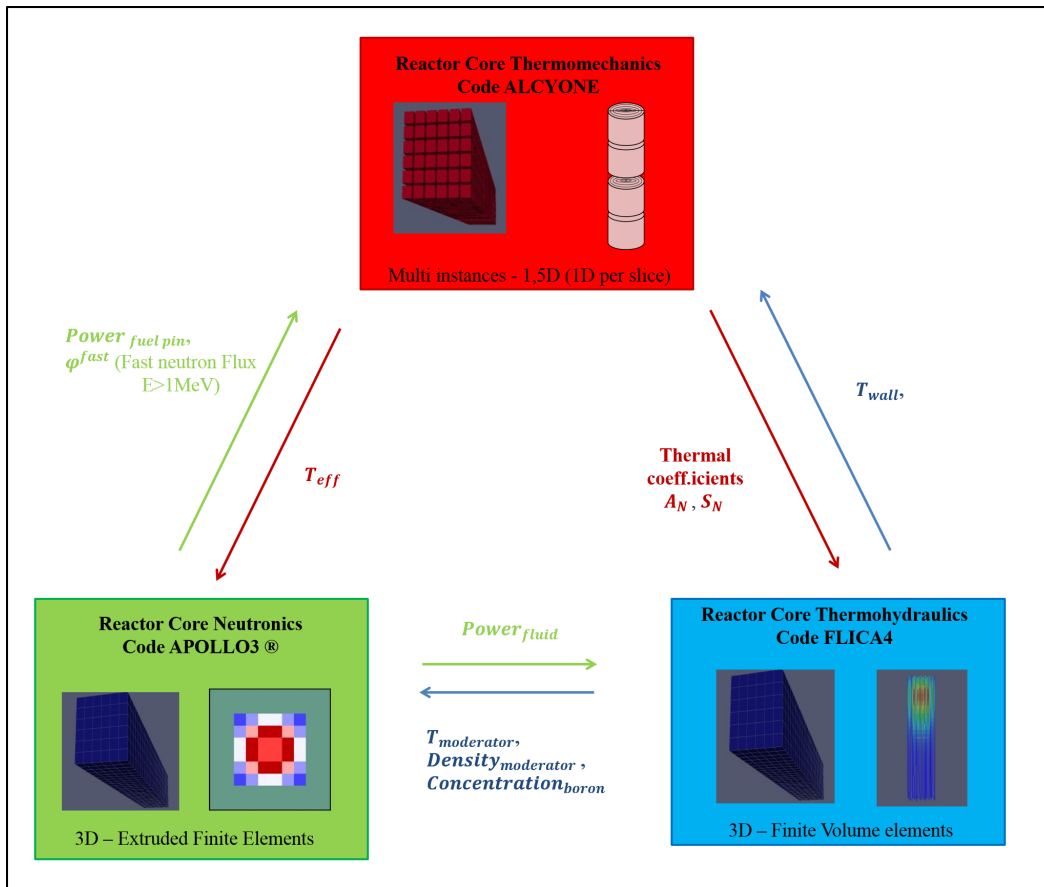


**Figure 12.1.** Global coupling scheme and exchanged variables

## 12.2 Hydraulics simplification : Neutronics - Thermomechanics coupling Methodology

To simulate the transient part ( 2.4.2), we couple an accurate Neutronics model (APOLLO3) with an accurate Thermomechanics model (ALCYONE). The Thermohydraulical part would be completed using the Thermohydraulics simplified model of the ALCYONE code which is a diphasic enthalpy balance model with a constant fluid pressure and neglecting kinetic effects, gravity, viscosity of the fluid and so on. The Neutronics-Thermomechanics coupling approach uses a semi explicit scheme [191] [145] in order to solve the Neutronics model detailed in section ( 5) and the fuel performance models detailed in section( 8). The neutronics impose a small time step of  $\Delta t = 10^{-3}$  which allows an explicit coupling. This explicit coupling scheme is defined in figure ( 12.2).

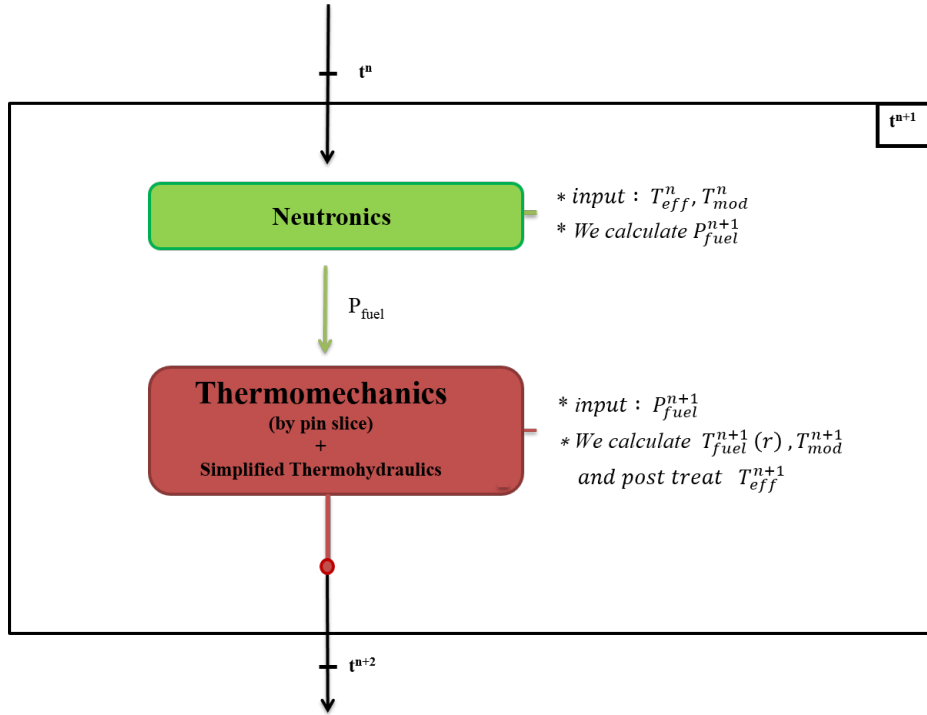


**Figure 12.2.** APOLLO3 - ALCYONE time coupling scheme with exchange variables

This coupling approach can be summarized as follows (figure 12.2):

Time step  $t^{n+1}$

- Neutronics calculation: we obtain  $P_{fuel}^{n+1}$  according to  $T_{mod}^n$  and  $T_{eff}^n$  of the previous time step;
- Thermomechanics calculation: we obtain  $T_{fuel}^{n+1}(r)$ ,  $T_{eff}^{n+1}$  and  $T_{mod}^{n+1}$ ;

The Neutronics equations are solved over the whole core and we are using a discretization of 4 radial cells per assembly and 30 layers of cells along the vertical direction. On its part, the Thermomechanical resolution is realized on a single pin. A representative pin is calculated for each quarter of assembly of the active part of the core (no reflector) with the same axial discretization as the Thermohydraulics, i.e., 30 axial layers. As in section (11), for symmetry reasons, we just have to consider here six representative Alcyone instances (figure 12.3)).

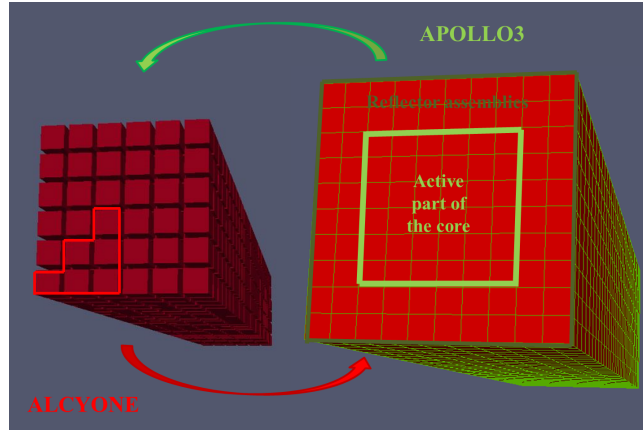


**Figure 12.3.** Multiphysics coupling scheme: spatial discretization and correspondence.

This Neutronics-Thermomechanics coupling have been studied according to the REA scenario detailed in section (2.4.2). And as in the previous section (11.1), regarding the thermomechanical part, we are going to work with assemblies at burn-up = 0 MWd/t.

### 12.3 Thermal simplification : Neutronics - Thermohydraulics coupling Methodology

To model the transient part ( 2.4.2), we couple in this section an accurate Neutronics model (APOLLO3) with an accurate Thermohydraulics model (FLICA4). The thermomechanical part would be completed by the fuel pin thermics simplified model of the FLICA4 code which works with constant geometry in time, resulting in a fixed value of the coefficient Hgap. The Neutronics-Thermohydraulics coupling approach is using an explicit scheme [247] [145], in order to solve at each time step first the Neutronics model detailed in section ( 5) and then the Thermohydraulics model detailed in section( 10). The neutronics impose a small time step of about  $\delta t = 10^{-3}$  which allows for an explicit coupling. This explicit coupling scheme is detailed in Figure ( 12.4):

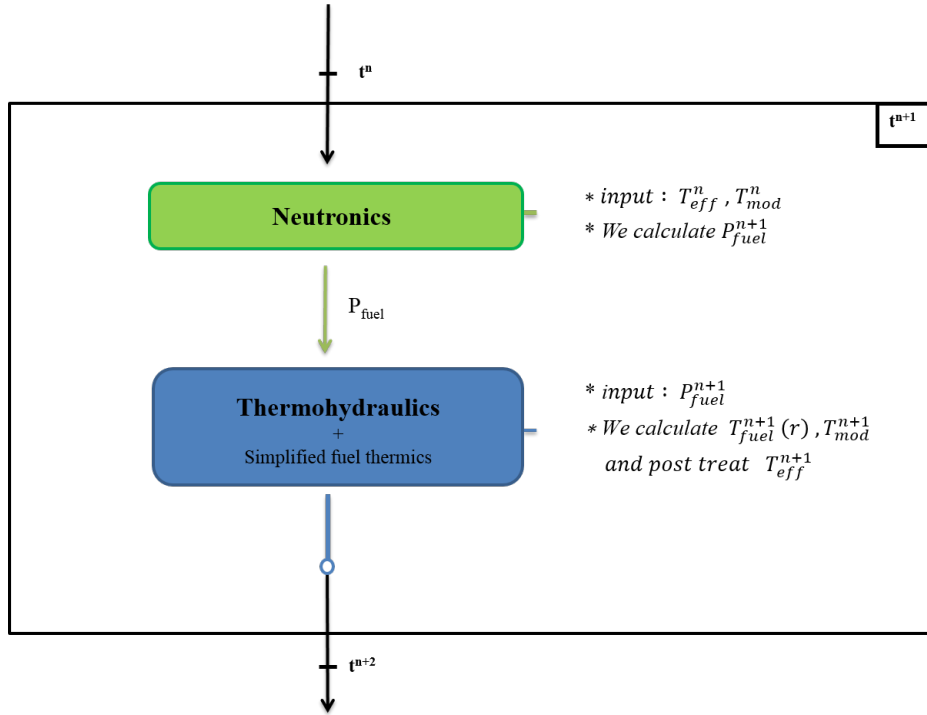


**Figure 12.4.** AP3 - FLICA4 time coupling scheme with exchange variables

This coupling approach can be summarized as follows:

Time step  $t^{n+1}$

- Neutronics calculation: we obtain  $P_{fluid}^{n+1}$  according to  $T_{mod}^n$  and  $T_{eff}^n$  of the previous time step;
- Thermohydraulics calculation: we obtain  $T_{mod}^{n+1}$  and  $T_{eff}^{n+1}$ ;

The Neutronics equations are solved over the whole core and we are using a discretization of 4 radial cells per assembly and 30 layers of cells along the vertical direction. On its part, the Thermohydraulics resolution uses the same discretization over the active part of the core (active assemblies without the reflector part) in figure ( 12.5).

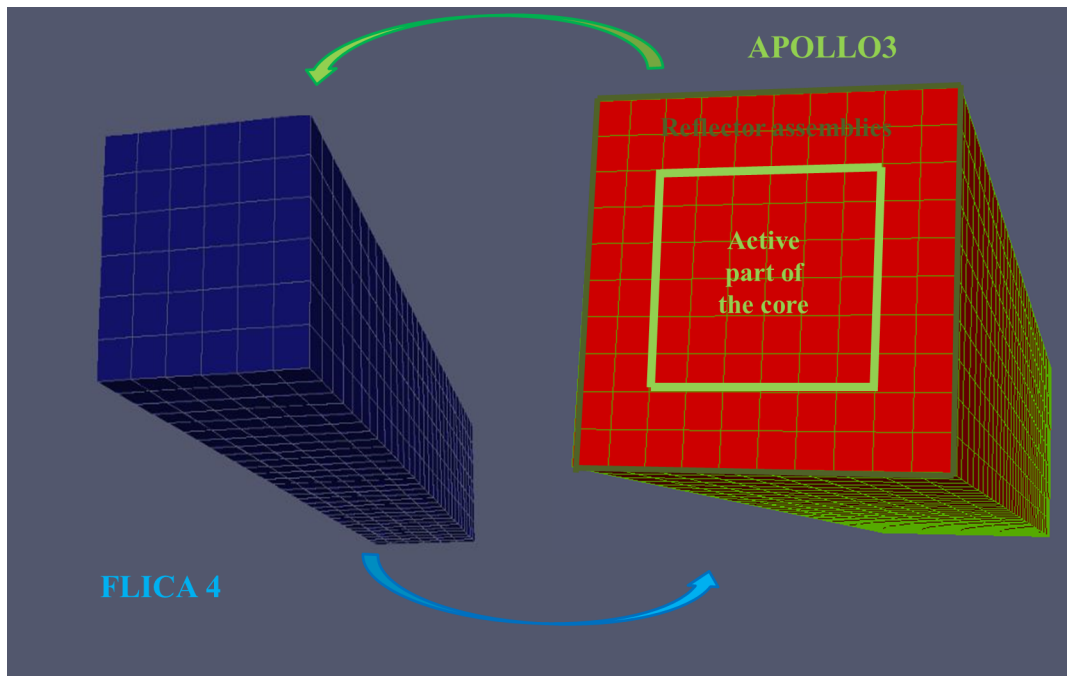


**Figure 12.5.** Multiphysics coupling scheme: spatial discretization and correspondence.

This Neutronics-Thermohydraulics coupling has been studied according to the REA standard scenario detailed in section ( 2.4.2). And as in the previous section ( 11.1), regarding the thermomechanical part, we are going to work with assemblies at burn-up = 0 MWd/t.



## 12.4 Neutronics - Thermomechanics - Thermohydraulics coupling Methodology

To describe the transient part of section ( 2.4.2), we fianlly couple an accurate Neutronics model (APOLLO3) with an accurate Thermohydraulics model (FLICA4) and an accurate Thermomechanics model (ALCYONE). No simplified model of the code would be used in this part. In orther words, we couple the Neutronics model detailed in section ( 5), the Thermohydraulics model detailed in section ( 10) and the Fuel performance model detailed in section ( 8). The Coupling scheme is detailed in Figure ( 12.6).

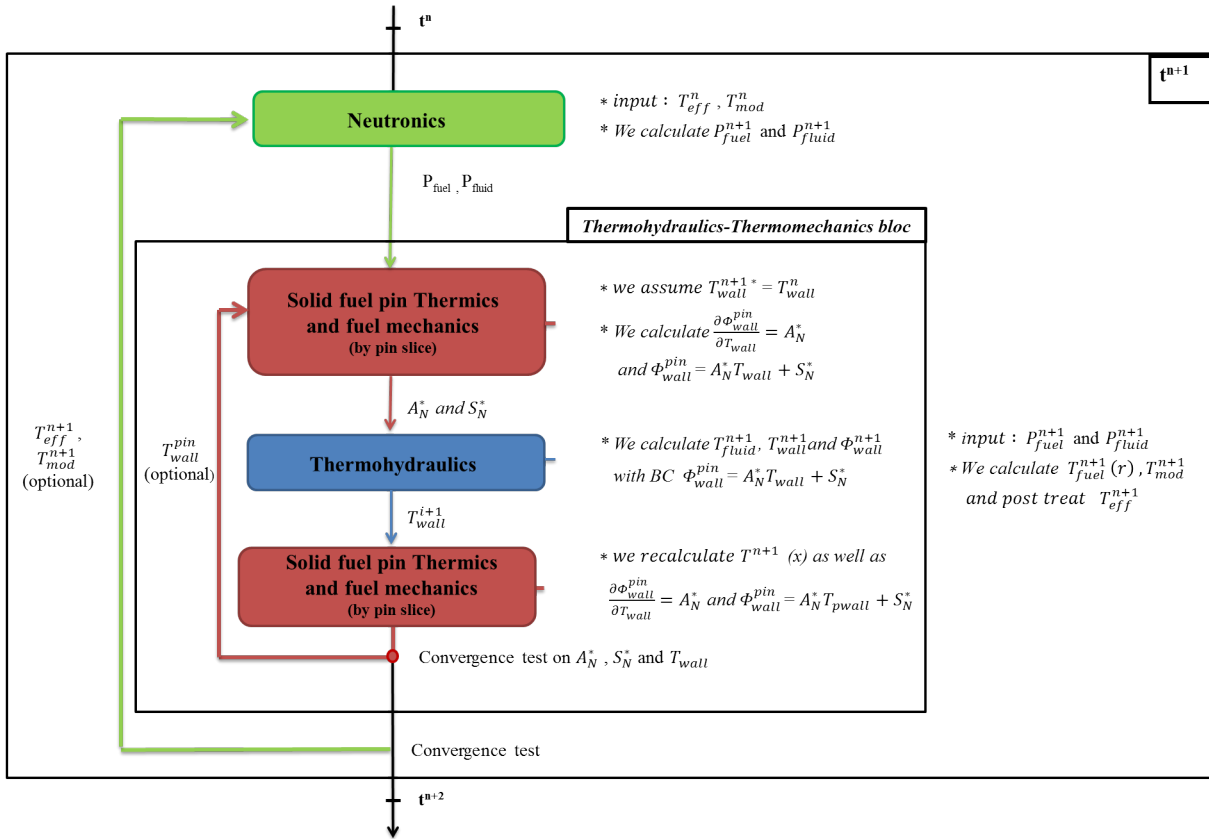


Figure 12.6. Total time coupling scheme with exchange variables

This coupling approach can be summarized as follows:

Time step  $t^{n+1}$

- Neutronics calculation: we obtain  $P_{fluid}^{n+1}$  using the temperatures  $T_{mod}^n$  and  $T_{eff}^n$  of the previous time step;
- Thermomechanics-Thermohydraulics Bloc:
  - Thermomechanics calculation: we obtain  $a_N^*$  and  $s_N^*$  by using the wall temperature of the previous time step  $T_{wall}^n$  with the updated neutronic power  $P^{n+1}$ ;
  - Fluid calculation: we obtain  $T_f^{n+1}$  and thanks to the equation (7.22) we obtain the wall temperature  $T_{wall}^{n+1}$  and  $\Phi_{wall}^{n+1}$ ;
  - Thermomechanics calculation: we re-calculate  $T(x)^{n+1}$  and new coefficients  $a_p^{**}$  and  $s_p^{**}$  with the right  $T_{wall}^{n+1}$  and  $P^{n+1}$ ;
  - Convergence test. **In our work, due to software limitations, this fixed point correction was not implemented.**
  - we obtain  $T_{mod}^{n+1}$  and  $T_{eff}^{n+1}$ ;
- If the fixed point approach is activated, we recalculate the time step and we verify that we have a converged solution according to an error  $\epsilon$ . If the ratio between these two calculations is inferior to the convergence criterium, we continue the time evolution of the system, otherwise we redo the calculation until the convergence is reached. **our work, due to software limitations, this fixed point correction was not activated.**

The Neutronics equations are solved over the whole core and we are using a discretization of 4 radial cells per assembly and 30 layers of cells along the vertical direction. On its part, the Thermohydraulics resolution uses the same discretization over the active part of the core (active assemblies without the reflector part). Finally, the ALCYONE Thermomechanical resolution is realized on single pins with a representative pin calculated for each quarter of assembly with the same axial discretization as the Thermohydraulics, i.e., 30 axial cells. As for Section ( 11.1), due to symmetry arguments we can reduce by a 1/8 symmetry to 6 ALCYONE we launch separately in parallel (figure 12.7).

This Neutronics-Thermohydraulics-Thermomechanics coupling has been studied on the REA standard scenario detailed in section ( 2.4.2), with specific studies on the impact of the  $T_{eff}$  formulations on the simulation. And as in the previous section ( 11.1), regarding the thermomechanical part, **we are going to work with assemblies at burn-up = 0 MWd/t.**

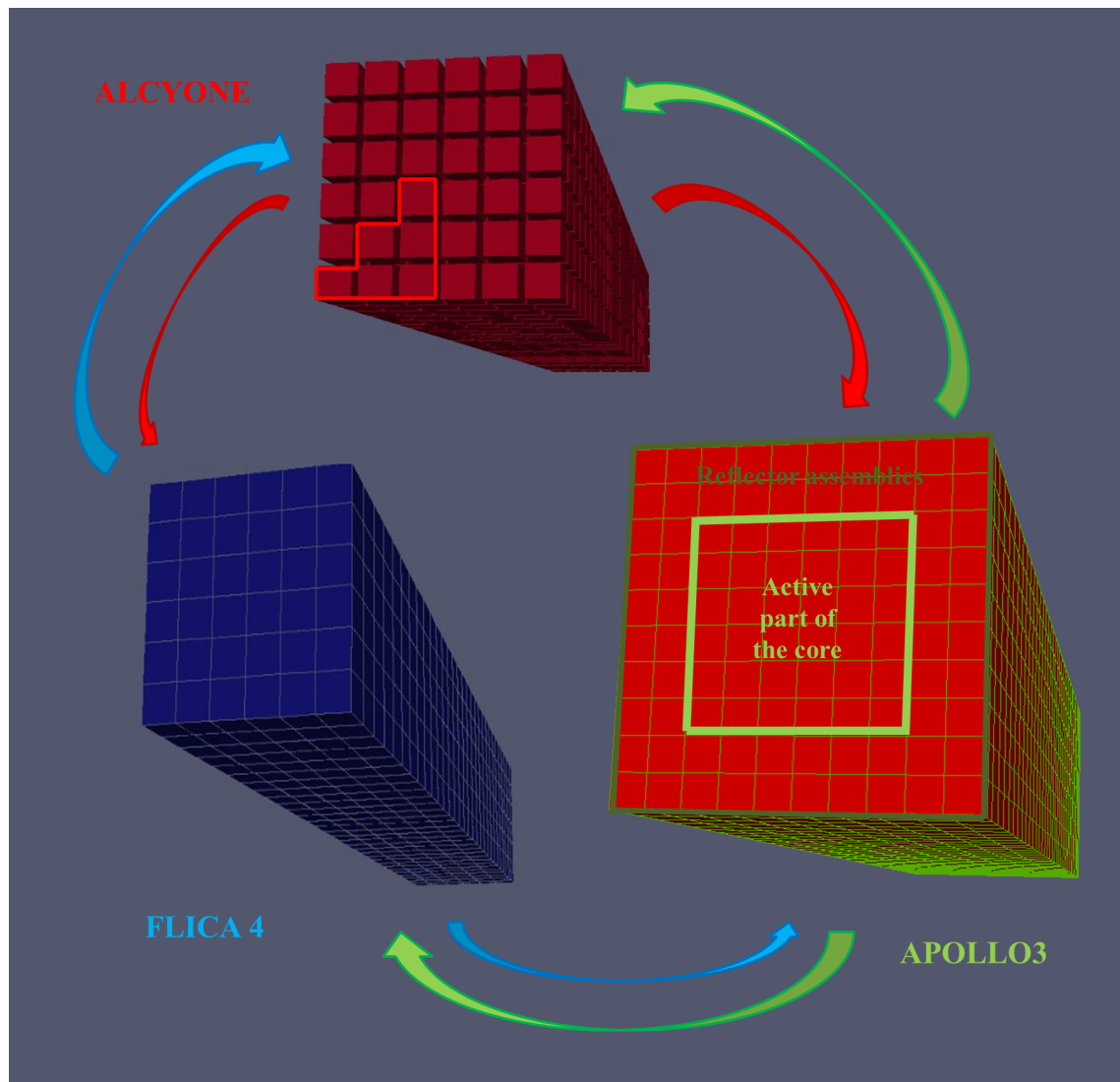


**Figure 12.7.** Multiphysics coupling scheme: spatial discretization and correspondence.

## Chapter 13

# Neutronics - Thermohydraulics - Thermomechanics coupling results and analysis - Proof of Concept

According to the algorithms and methodology part in chapter 12, we realized and compared the three coupling strategies (see figure 13.1), based respectively on a simplified Thermohydraulics description (APOLLO3-ALCYONE coupling (AP3-ALC)), a simplified fuel Thermomechanics description (APOLLO3-FLICA4 coupling (AP3-F4)) and a Best Effort description (APOLLO3-ALCYONE-FLICA4 coupling-goal of this work (AP3-ALC-F4)).

	AP3-ALC	AP3-F4	AP3-ALC-F4
Overview	<b>Simplified Thermohydraulics</b> description	<b>Simplified Fuel Thermomechanics</b> description	<b>Best Effort</b> description
Neutronics	AP3 <b>accurate</b> neutronics model MINOS SPn		
ThermoMechanics	ALC <b>accurate</b> Thermal and Mechanical model	Thermal heat equation with F4 <b>simplified</b> Mechanical model (constant core Hgap)	ALC <b>accurate</b> Thermal and Mechanical model
Thermohydraulics	ALC <b>Simplified</b> thermohydraulics model (enthalpy balance)	F4 <b>accurate</b> Thermohydraulics model	

**Figure 13.1.** Coupling models description and comparisons

## CHAPTER 13. NEUTRONICS - THERMOHYDRAULICS - THERMOMECHANICS COUPLING RESULTS AND ANALYSIS - PROOF OF CONCEPT

Regarding these three modelling, we defined a color standard in order to simplify the comparison between curves and their analysis. The color standard we are going to use during this whole chapter is defined as follows:

- A. Red color for APOLLO3-ALCYONE results,
- B. Blue color for APOLLO3-FLICA4 results,
- C. Green color for APOLLO3-ALCYONE-FLICA4 results.

In these tests, we monitor the evolution of key global and local (Hot Spot) variables, which have been indentified in parts (5, 8 and 10) and which are listed in figure ( 13.2).

Disciplines	Scales	Parameters
Neutronics	Global	$p_{core}^{integrated}(t), \rho_{Total}(t), \rho_{Doppler}(t), \rho_{moderator}(t)$
	Local HS	$F_{xyz}(t), p^{HS}(t)$
ThermoMechanics	Global	$T(t)(x), T_{eff}(t), H_{gap}(t), \Phi_{wall}(t)$
	Local HS	$T^{HS}(t)(x), T_{eff}^{HS}(t), H_{gap}^{HS}(t), \Phi_{wall}^{HS}(t)$
Thermohydraulics	Global	$T_{wall}(t), D_{moderator}(t),$
	Local HS	$T_{wall}^{HS}(t), D_{moderator}^{HS}(t)$
HS correspond to the Hot Spot location in terms of power (defined in section 2,4) and x the local space variable.		

**Figure 13.2.** Global and local variables/parameters regarding our three physical disciplines

These parameters are going to strongly help us during our comparison and analysis of our three coupling calculations. Nevertheless, not all parameter curves will be discussed during this study part. We will only focus on relevant aspects and parameters that are likely to express the difference between our coupling calculations. This way, some results will not be used in this study but will be moved to the chapter ( 20) in Annexe part.

*Remark: in these tests, we used a burn-up distribution in the Neutronics part (APOLLO3) but the Burn-up is assume at 0 MWd/t in the fuel ThermoMechanics part (ALCYONE). The introduction of Burn-up distribution in the ThermoMechanics part will be one the future improvement to be done regarding the representativeness of our coupling.*

### 13.1 Results Comparisons and Analysis

From the implementation of the AP3-ALC, AP3-F4 and AP3-ALC-F4 couplings, we obtained the following results.

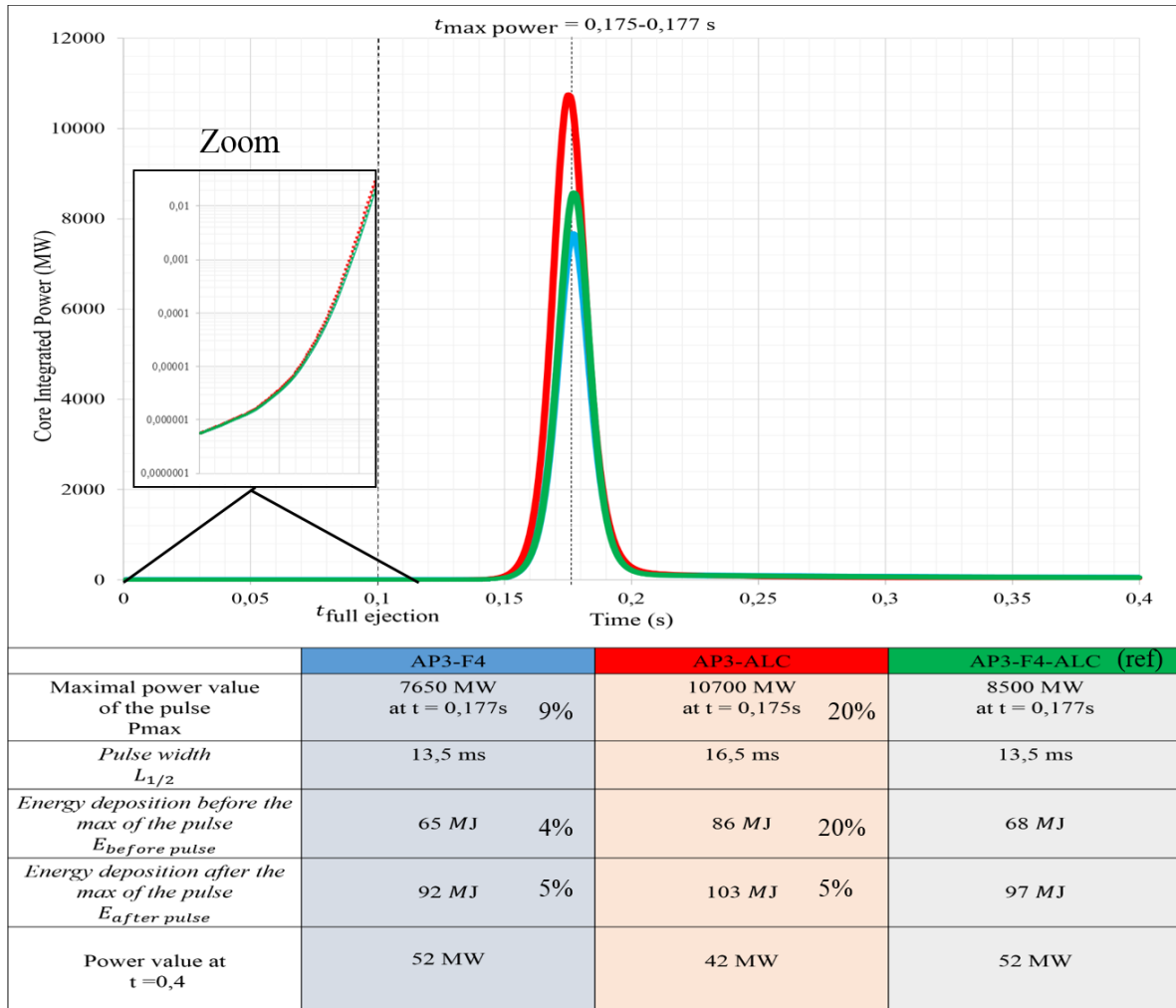


Figure 13.3. Integrated core power and energy comparison

The neutronics power in figure ( 13.3) is the main result that will help us to discriminate specific time steps or ranges to be studied in order to highlight major contributions of each coupling.

The neutronics power  $P_{core}^{integrated}(t)$  expresses the power production and reactor core behavior regarding the control rod ejection accident situation. For this purpose we first observe the maximal value of the power at the pulse peak and the pulse width. Then we calculate the total Energy deposition before the power peak and the total energy deposition after the peak. We observe a similar reactor behavior with very similar curves and more precisely (see figure 13.3):

- A pulse width of 13.5 ms for AP3-ALC-F4 and AP3-F4 couplings while we have a pulse width of 16.5 ms in the AP3-ALC coupling,
- A power peak reached at  $t=0.177$  for AP3-F4 ( $P_{max\_core}^{integrated} = 7600\text{MW}$ ) and AP3-ALC-F4 ( $P_{max\_core}^{integrated} = 8500\text{MW}$ ) calculations, and reached a little bit earlier at  $t=0.175$  ( $P_{max\_core}^{integrated} = 10700\text{MW}$ ) for the AP3-ALC calculation.

The max power and pulse width differences logically induces the observation of a difference in terms of energy deposition before and after the pulse. AP3-F4 and AP3-F4-ALC calculations have a similar energy deposition before the pulse of about  $E_{before\_peak}^{AP3-F4} = 65$  MJ and  $E_{before\_peak}^{AP3-ALC-F4} = 68$  MJ respectively (the AP3-ALC-F4 Best Effort coupling meet almost the same behavior we would expect from the standard Best-Effort AP3-F4 coupling) but smaller than the energy deposition of the AP3-ALC calculation which is about  $E_{before\_peak}^{AP3-ALC} = 86$  MJ. The AP3-ALC-F4 coupling shows an averaged behavior between the two other calculations. These values are close but reflect differences we directly observe on global and local parameters, such as total reactivity. They can also be observed on the feedback effects (Doppler or moderator reactivities) and the effective fuel temperature and moderator density they are connected with. The time range between the increase of the power and the power peak ( $t_{1-2} = [t_1 = 0.15\text{s}; t_2 = 0.18\text{s}]$ ) as well as between the power peak and the asymptotic part ( $t_{2-3} = [t_2 = 0.18\text{s}; t_3 = 0.2\text{s}]$ ) should be specifically studied in detail.

Locally, in the Hot Spot (HS detailed in section ( 2.4 )) we observe the exact same difference between Power evolutions (see figure 13.4).

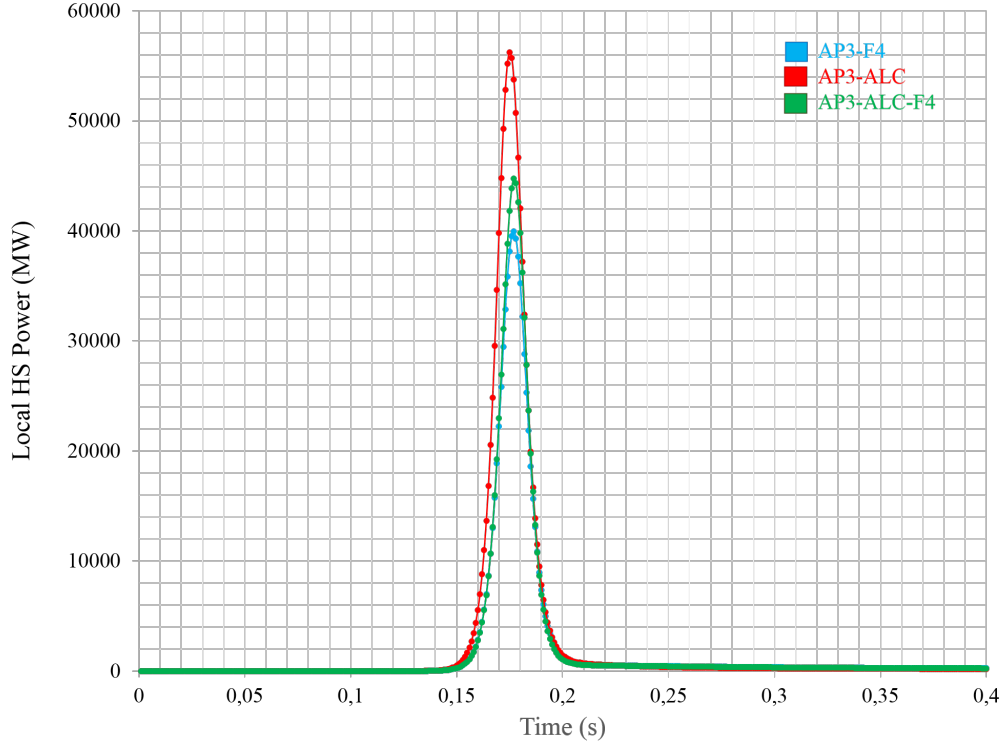


**Figure 13.4.** Hot Spot Power comparison

The power value at the Hot Spot  $P^{HS}$  corresponds to the core Power multiplied by the 3D shape factor  $P^{HS}(t) = F_{xyz}(t) \cdot P_{core}^{integrated}(t)$ . In our case, the 3D shape factor variation is mainly carried by the variation of the axial shape factor  $F_z(t)$  during the transient (see figure 13.5). Indeed, regarding the  $F_{xyz}(t)$  or the  $F_z(t)$  shape factor indifferently, we observe a similar shape of the three curve calculations until  $t = 0.2s$ . Then the AP3-F4 and AP3-F4-ALC stay close and slightly decrease to an asymptotic value ( $F_{xyz}(t_4=0.4)=4.6$ ) when the AP3-ALC curve continues to sharply decrease and finally reaches a lower asymptotic value ( $F_{xyz}(t_4=0.4)=4.4$ ). A specific attention should be given during our study to the time range  $t_{3-4} = [t_3 = 0.2s; t_4=0.4s]$ .



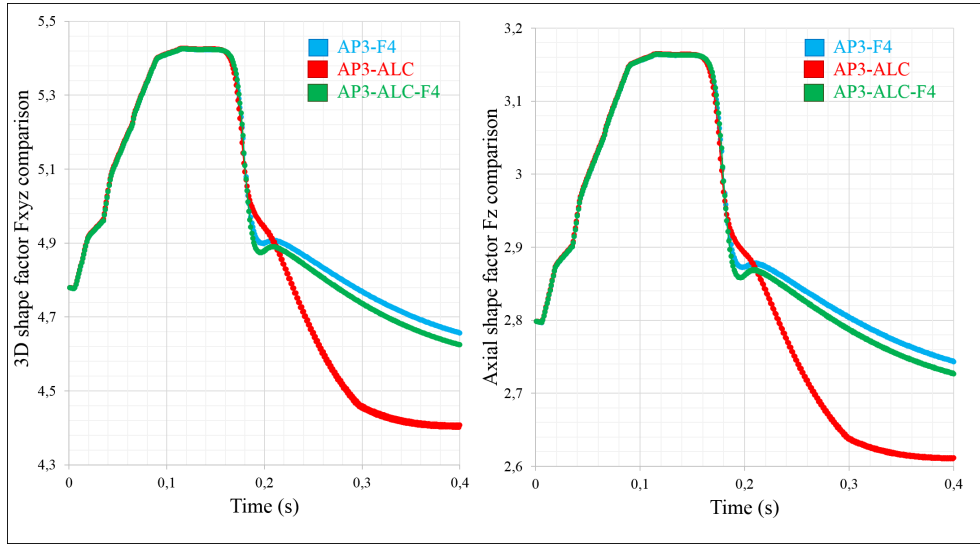


**Figure 13.5.** Shape factor  $F_{xyz}$  and  $F_z$  variation comparisons

If we compare the total reactivity  $\rho_{Total}(t)$  (see figure 13.6), we observe an evolution of the three curves up to  $t_3=0.2s$  similar to what we observed in the shape factor case. Then the AP3-F4 and AP3-F4-ALC curves stay close when the AP3-ALC curve follows a significantly separated evolution. This stresses the fact that a specific attention should be given to study the time range  $t_{3-4} = [t_3=0.2s; t_4=0.4s]$ .

remark: in this curve we start from 787 pcm which correspond to the reactivity inserted by the control rod which is totally ejected at  $t_{ejection}=0.1s$ . Then, in the following reactivity curve we will work only with respect to the Doppler and Moderator reactivity, taking apart the control rod reactivity.

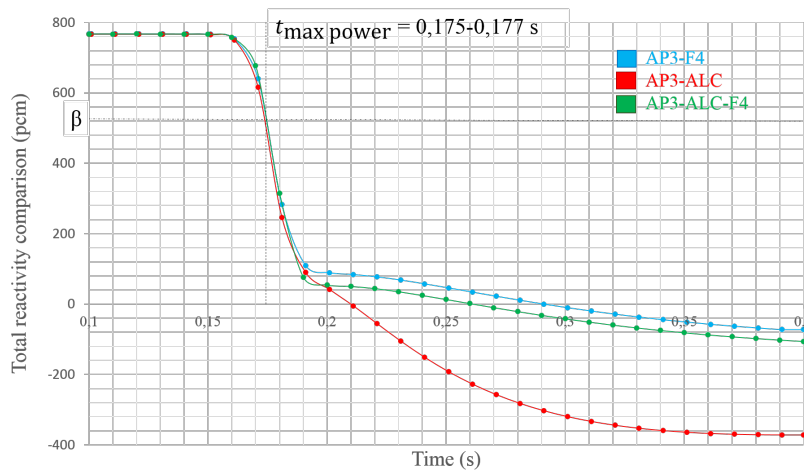


**Figure 13.6.** Total reactivity variation comparison

### 13.1. RESULTS COMPARISONS AND ANALYSIS

Figure ( 13.7) and figure ( 13.8) show the decomposition of the Total reactivity into two parts respectively the Doppler reactivity (linked to the effective fuel pin temperature evolution) and the moderator reactivity (linked to the moderator density evolution). In these two figures we again find the time ranges of interest we observed in the previous figures, i.e., time range  $t_{1-2} = [ 0.15\text{s}; 0.18\text{s} ]$  ,  $t_{2-3} = [0.18\text{s};0.2\text{s}]$  and  $t_{3-4} =[0.2\text{s};0.4\text{s}]$ .

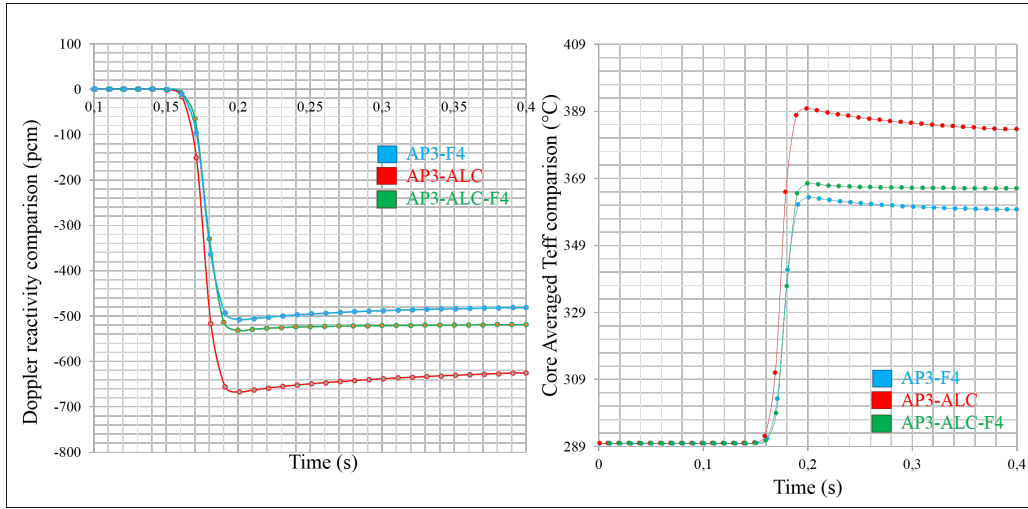


**Figure 13.7.** Doppler reactivity and Core Averaged Effective fuel temperature variation comparisons

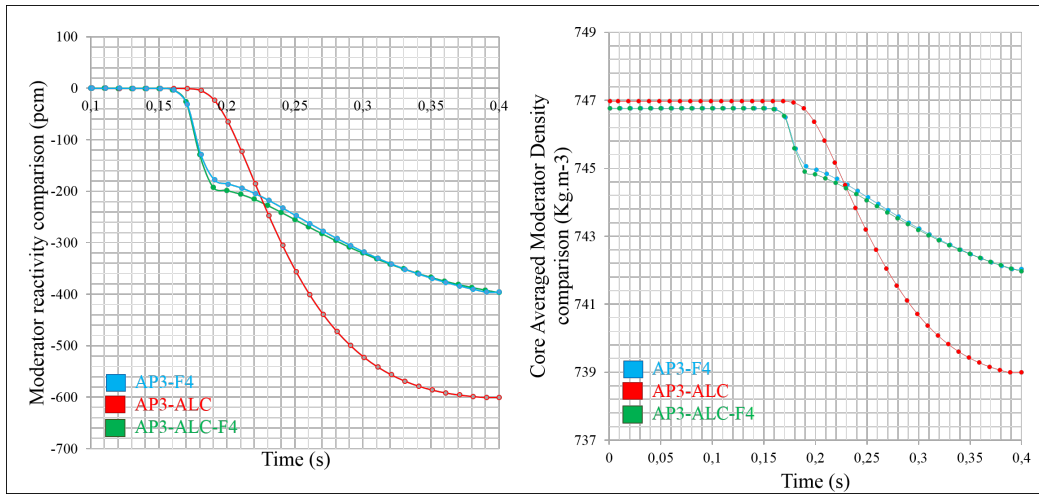


**Figure 13.8.** Moderator reactivity and Core Averaged Moderator Density variation comparison

For a more detailed analysis, we will now split the transient behavior in 4 time ranges (figure 13.9) according to time steps  $t_0=0.0s$ ,  $t_1=0.15s$ ,  $t_2=0.18s$ ,  $t_3=0.2s$  and  $t_4=0.4s$  :

- $t_{0-1} = [ 0.0s; 0.15s ]$  which corresponds to the part where the power increase without significant increase of the other parameters,
- $t_{1-2} = [ 0.15s; 0.18s ]$  ,
- $t_{2-3} = [ 0.18s; 0.2s ]$  ,
- $t_{3-4} = [ 0.2s; 0.4s ]$  .

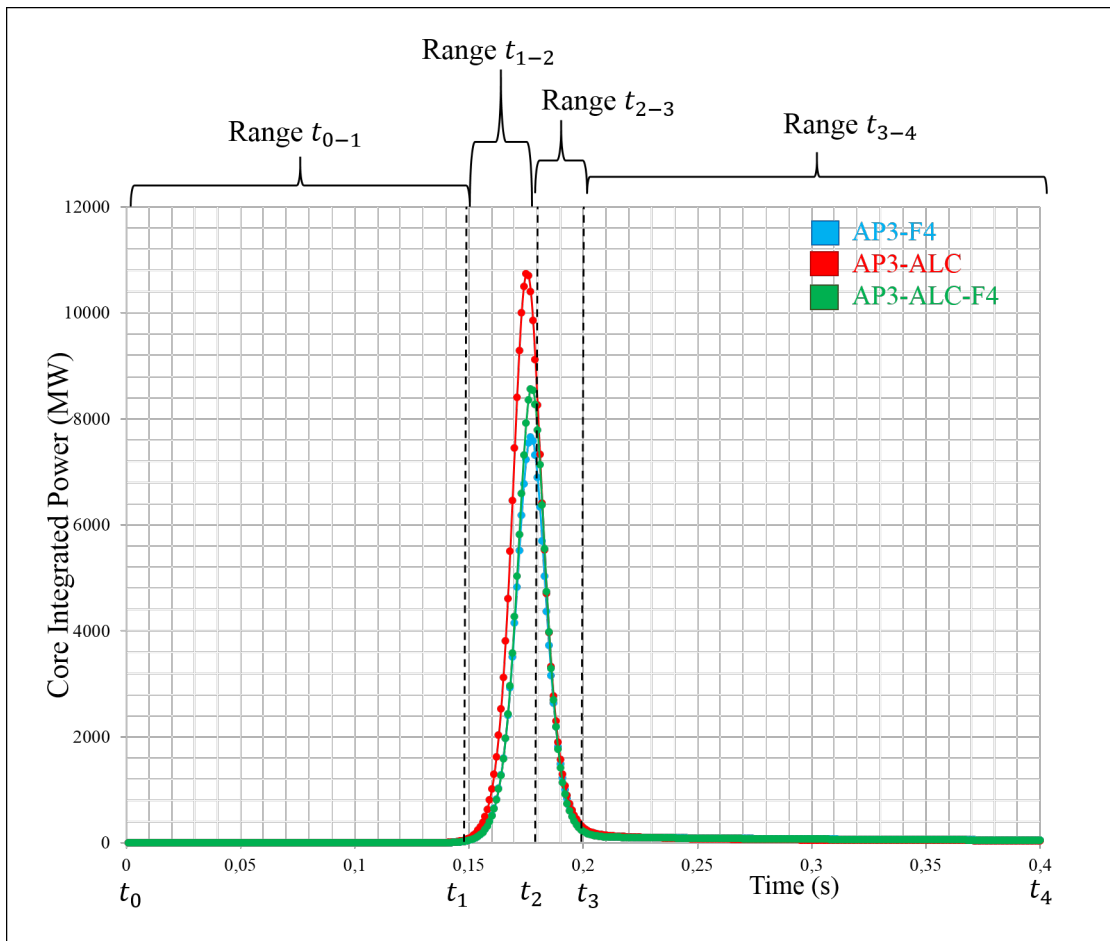


**Figure 13.9.** Integrated Power time ranges definition

The time ranges  $t_{1-2}$  ,  $t_{2-3}$  and  $t_{3-4}$  will be discussed in detail below in this study.

**Time range  $t_{1-2}$  :**

Now we are interested in the time range  $t_{1-2}$  from  $t_1=0.15$  s to  $t_2=0.18$ s. During this time range we observe the Core power evolution (see figure 13.10 ) and we observe that the power predicted from the AP3-ALC calculation starts to increase early and sharply while AP3-F4 and AP3-ALC-F4 stay together and increase later with a lower maximum.

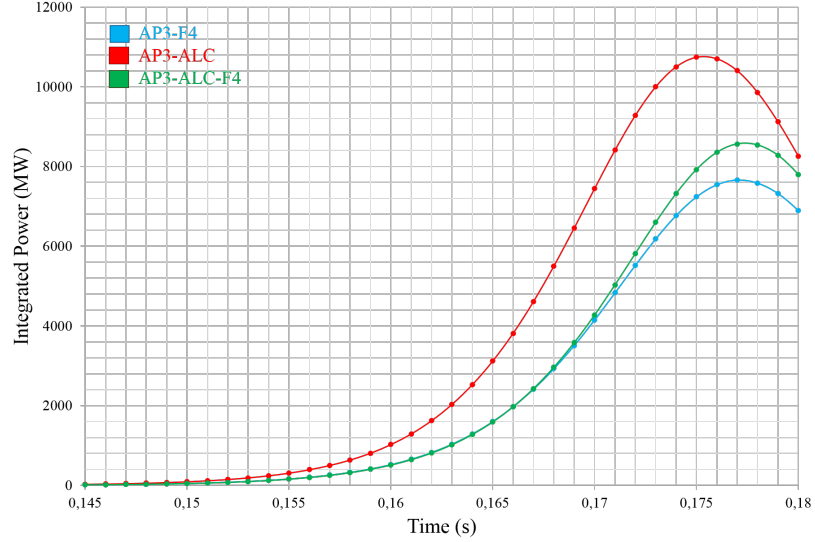


**Figure 13.10.** Integrated core Power comparison  $t_{12}$

We observe the same global behavior regarding the Total reactivity (see figure 13.11) but the small delay of reactivity decreasing between curves induces a discrepancy of about 40 pcm between the AP3-ALC calculation and the two others at  $t_2=0.18$ s

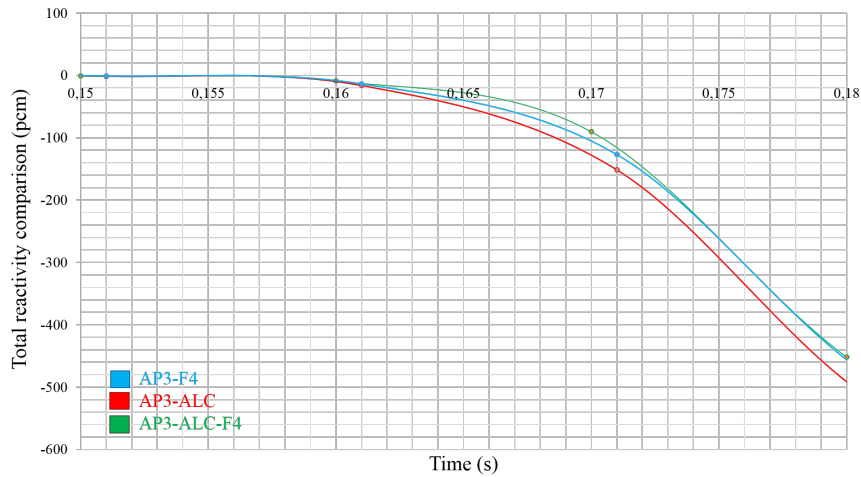


**Figure 13.11.** Total feedbacks reactivity variation comparison  $t_{12}$

If we decompose the reactivity (see figure 13.12 and 13.13), we observe a significant difference between the AP3-ALC calculation and the AP3-F4/AP3-ALC-F4 calculations. First of all, we observe that the temperature increases more in the case of the AP3-ALC calculation and induces a higher Doppler reactivity feedback effect (see figure 13.12 ). The Doppler feedback effect is the first order contribution that impacts the reactivity and shuts down the power increase.

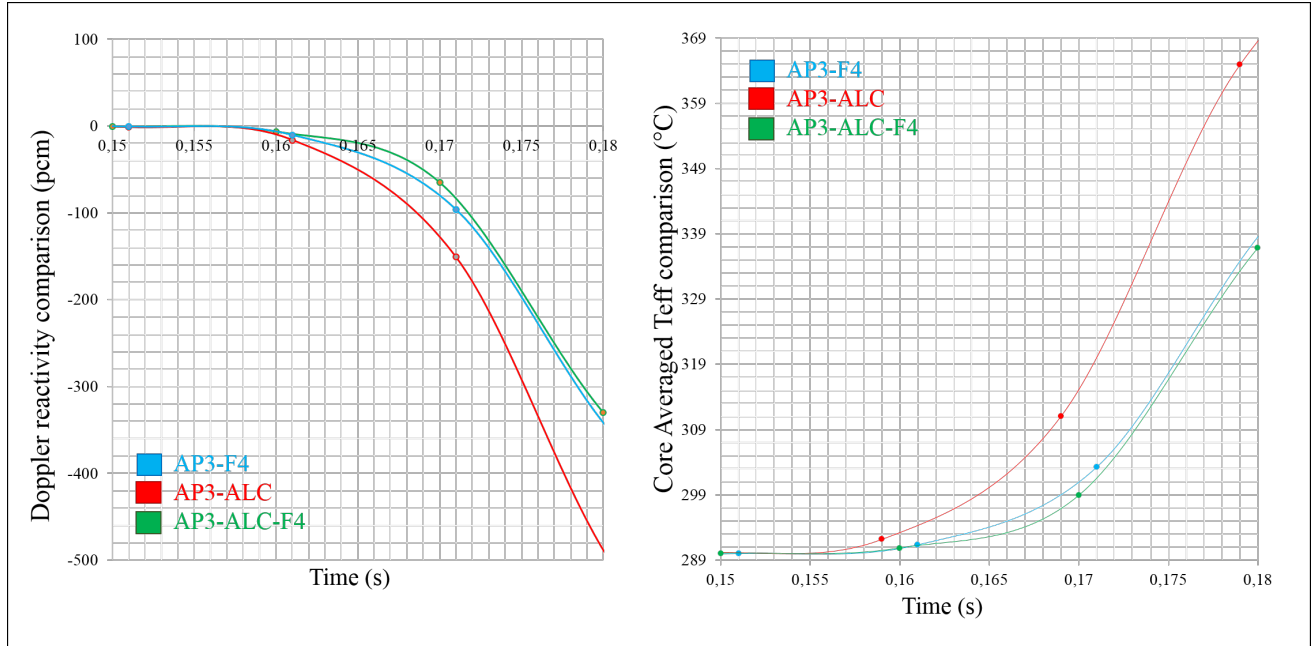


**Figure 13.12.** Doppler reactivity and Core Averaged fuel effective temperature variation comparison  $t_{12}$

The difference between the AP3-ALC calculation and the two other calculations is about 150 pcm at  $t_2=0.18s$ . At this time range the AP3-ALC calculation is more impacted by the Doppler feedback effect (fuel pin temperature increase) than the two other calculations.

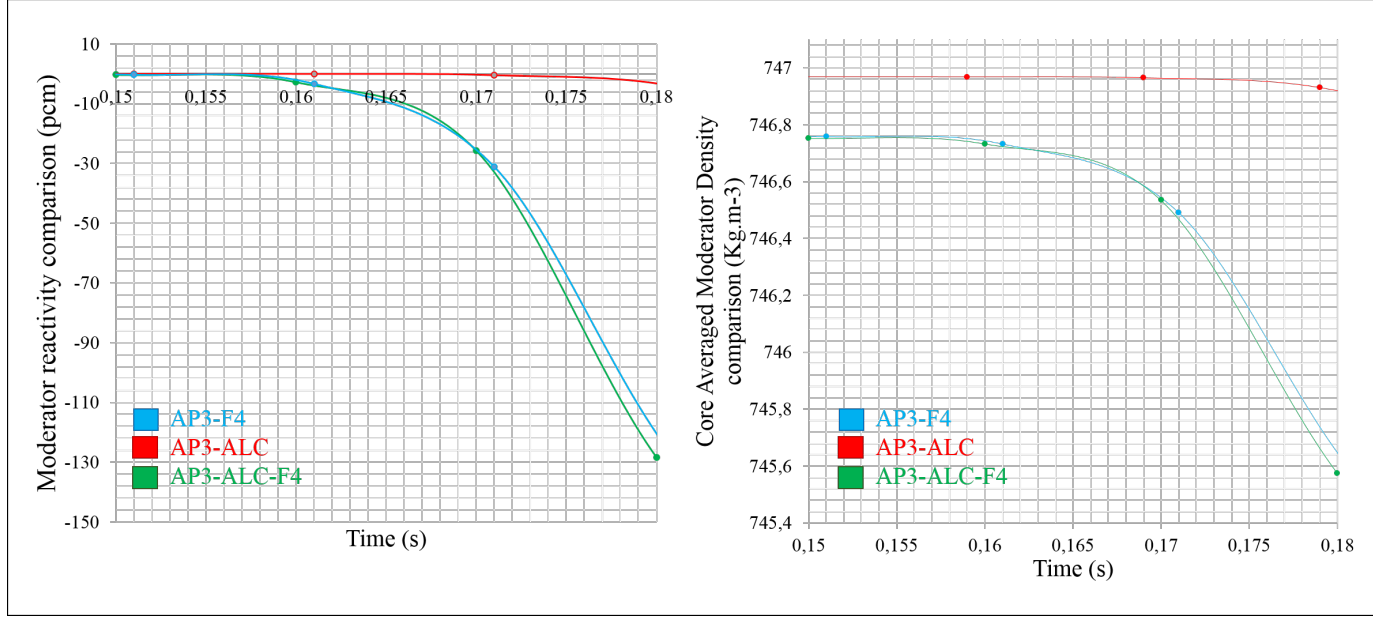


**Figure 13.13.** Moderator reactivity and Core Averaged moderator density variation comparison  $t_{12}$

Indeed, if we compare the moderator density (see figure 13.13) we notice that the AP3-ALC results barely change while the AP3-F4 and AP3-ALC-F4 densities decrease. It induces a higher moderator anti reactivity in the AP3-F4 and AP3-ALC-F4 calculations. The AP3-ALC moderator reactivity does not change and the difference at  $t_{max\_power}=0.175-0.177s$  is about 70-90 pcm.

*Remark: we observe a small difference of  $0.2 \text{ kg.m}^{-3}$  between AP3-ALC and the two other calculations. This difference comes from the initialization of the calculation but does not impact the transient.*

In this time range the Doppler contribution is the major contribution of the Total reactivity evolution but the Moderator contribution is also significant in the AP3-F4 and the AP3-ALC-F4 couplings. This shows the impact of the Thermohydraulics from the very first moment of the thermal activation. This hydraulical effect shows that this time range can not be rightfully considered as an adiabatic or quasi-adiabatic time range such as it is in the standard REA time range decomposition ( 2.2.1).

We locally observe the same Thermal behavior at the Hot Spot regarding the effective temperature and the moderator density (see figure 13.14 ).

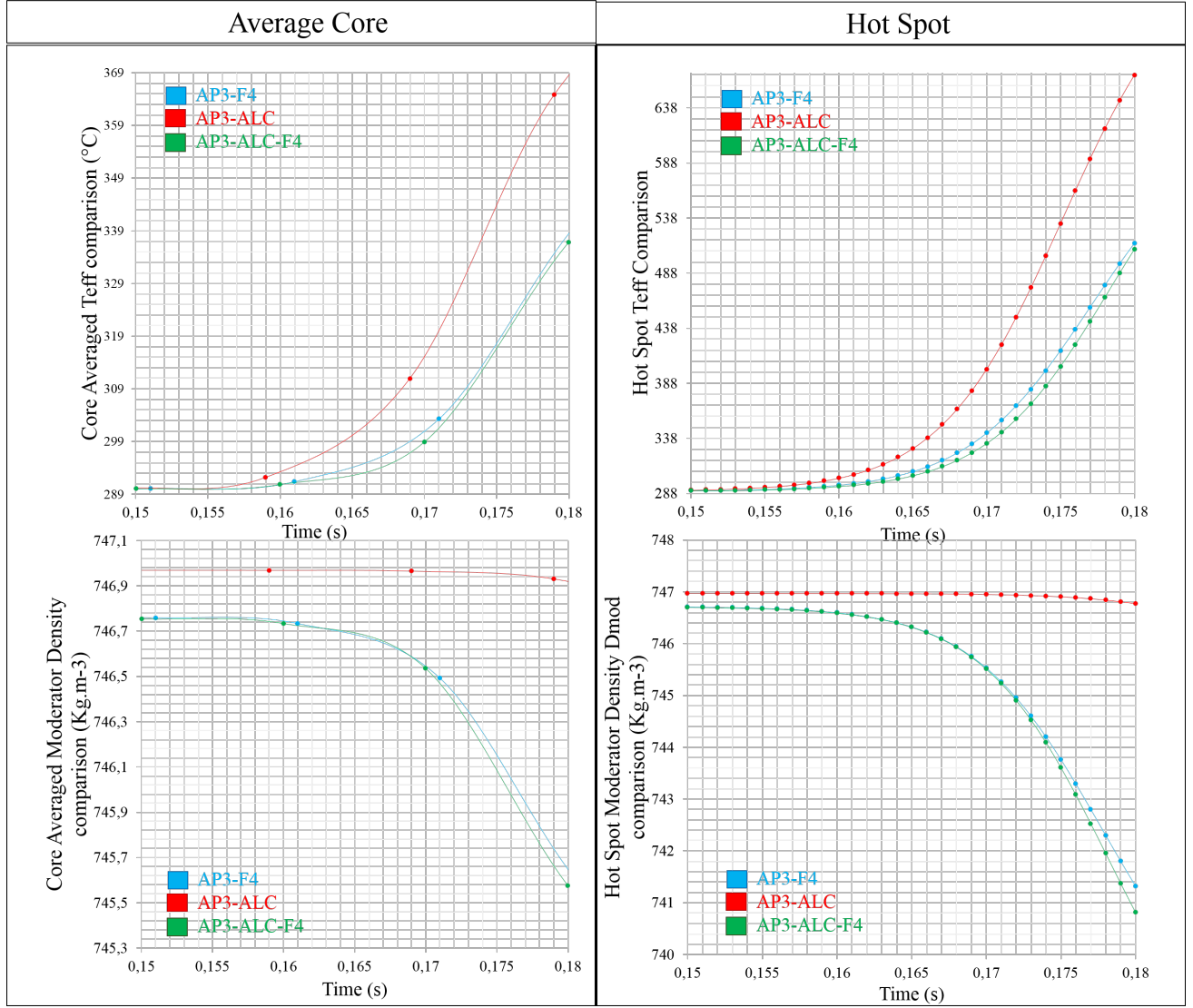


**Figure 13.14.** Global Core Averaged - Local Host Spot Effective temperature and Moderator density variation comparison  $t_{12}$

This behavior is also observed regarding the fuel pin surface temperature  $T_{wall}$  (see figure 13.15) even if the differences between curves are very small and even if we take into account initial round error at this level. Indeed, taking apart initial small difference (inferior to  $10^{-3}$  °C), we observe an earlier increase of the  $T_{wall}$  temperature in the AP3-ALC-F4, directly followed by the AP3-F4 calculation and then a slower increase of the  $T_{wall}$  in the AP3-ALC case. At  $t_2$ , we observe a difference of about 0.7 °C between AP3-ALC-F4 and AP3-ALC calculation, and a difference of about 0.5 °C between AP3-ALC-F4 and AP3-F4 calculations.

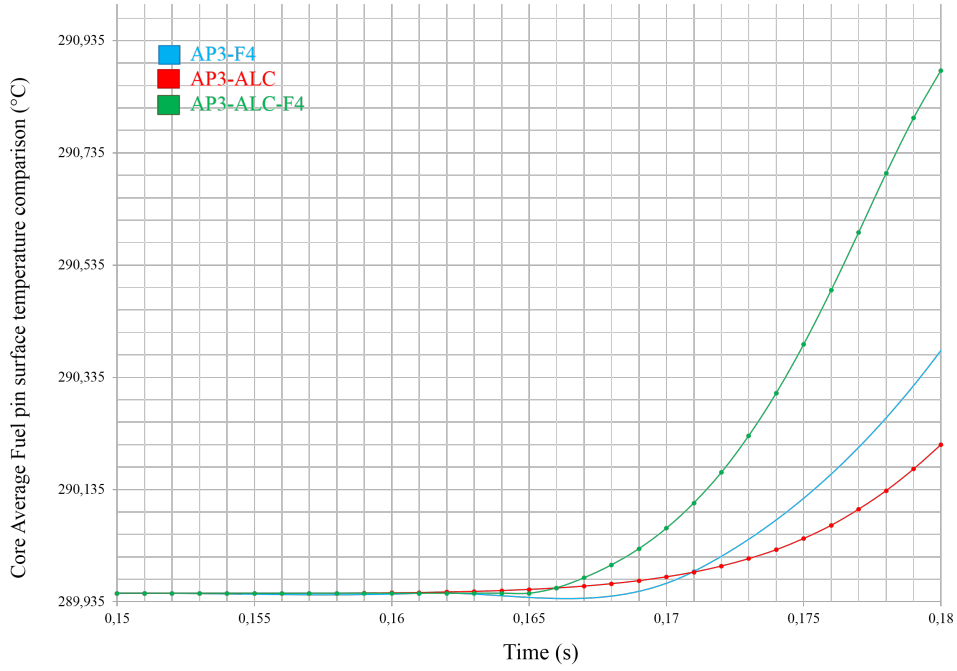


**Figure 13.15.** Core Averaged Fuel pin surface  $T_{wall}$  comparison  $t_{12}$

Between the AP3-ALC calculation and the two other calculations we have a major difference that comes from the Thermohydraulical model used. In the AP3-F4 and AP3-ALC-F4 we are using the accurate Thermohydraulical model from FLICA4 while the AP3-ALC calculation is using the rough Thermohydraulical model from ALCYONE (enthalpy balance). In the second modelling, we store the energy inside the fuel which induce a higher increase of the fuel temperature and Doppler reactivity while the moderator is slightly impacted. In the same time the fuel thermal model of AP3-F4 is improved by using the Hgap value obtained from ALC standalone calculation (cf. FLICA-ALCYONE coupling in chapter V). The FLICA4 code model induces a better thermal exchange from the beginning of the transient that strongly impacts the transient behavior and thus the shape of the power pulse.

Despite the time range  $t_{0-1}$  (power increase without any temperature increase), in time



range  $t_{1-2}$  we transfer the deposited energy very early to the fluid which impacts the moderator density and thus the moderator feedback effect. In the case of the AP3-ALC calculation the lack of thermal transfer to the fluid induces the conservation of the energy in the fuel pin waiting to slowly transfer the accumulated energy. ALCYONE Thermo-mechanical models are well validated thank to CABRI-Na experiments but the Sodium primary circuit used in the experiment may explain the differences we obtained. This can be easily observed in figure 13.16 where Hot Spot fuel pin temperatures  $T^{HS}(t)$ , i.e. the fuel pellet center and surface temperature and the fuel clad inner and outer temperature, are plotted. We observe a significant difference between the couplings regarding the fuel pellet temperature as well as the clad inner temperature during the transient. These difference can be explained by the significant difference of power between couplings. In addition, the T<sub>wall</sub> value is close in the three couplings which impacts the fuel pin temperature distribution. In case of AP3-ALC the transfer is slower, consequently, the fuel pin stores more energy later which is transferred to the fluid with a delay. This Thermohydraulics contribution will be then seen in the time range  $t_{3-4}$ .

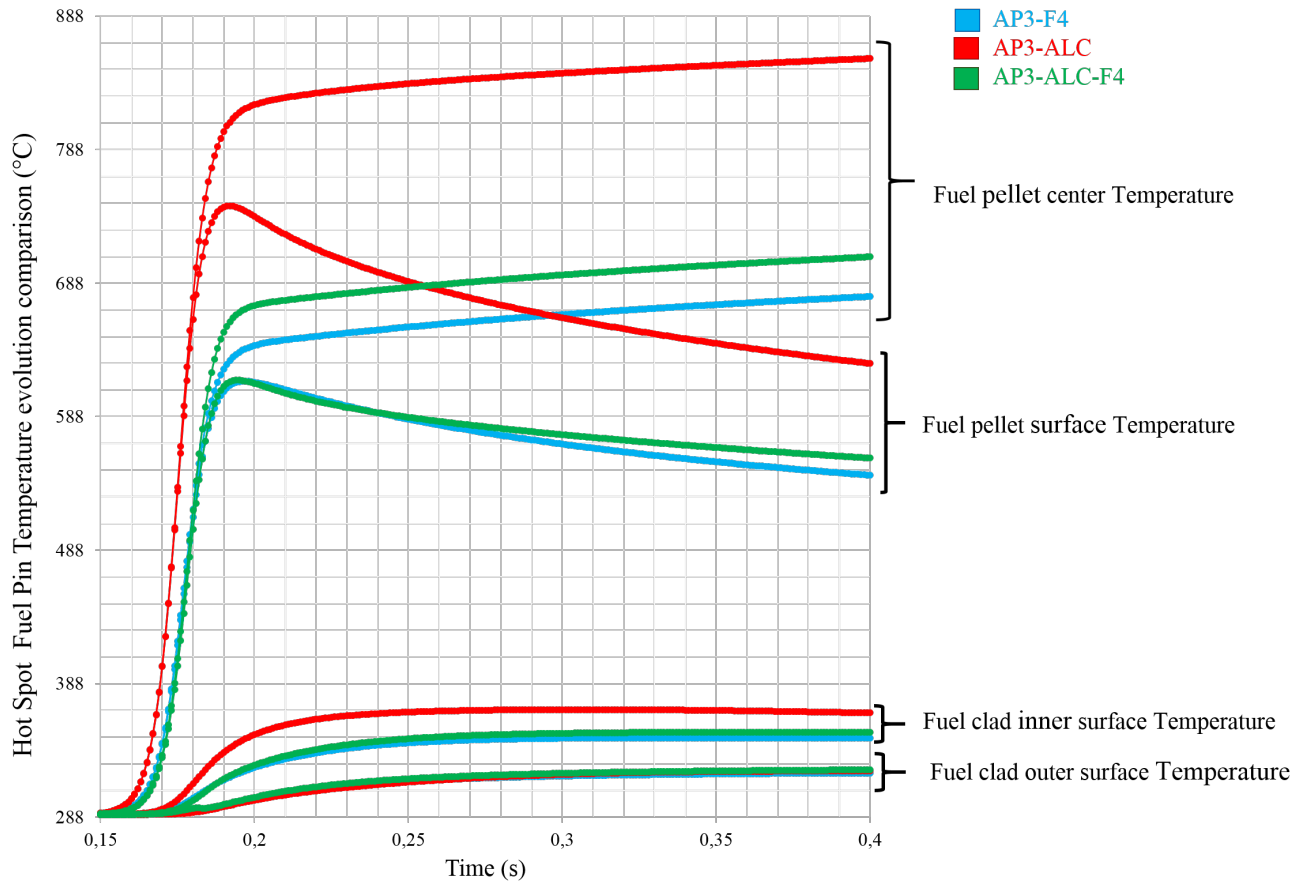


**Figure 13.16.** Hot Spot Fuel pin temperature distribution comparison

As we said above, the AP3-ALC-F4 and AP3-F4 calculations are very close due to the fact that we reach an improved thermomechanical behavior in F4 by using a realistic Hgap value (imposed constant in time and space). This Hgap value we arbitrarily imposed in the F4 model has been obtained thanks to ALCYONE standalone calculation (cf section 11.3). The Hgap value strongly changes regarding the REA transient and stage of the core we are studying. The exact Hgap value cannot be known without doing an accurate Thermomechanical pre calculation and is not constant during the whole transient. The Hgap value dramatically increases with the thermal increase and then slightly decreases when the fuel pin temperature decreases. Moreover, we observe that the Hgap value is different between the AP3-ALC and the AP3-ALC-F4 calculations, also in terms of average and local HS values (see figure 13.17).

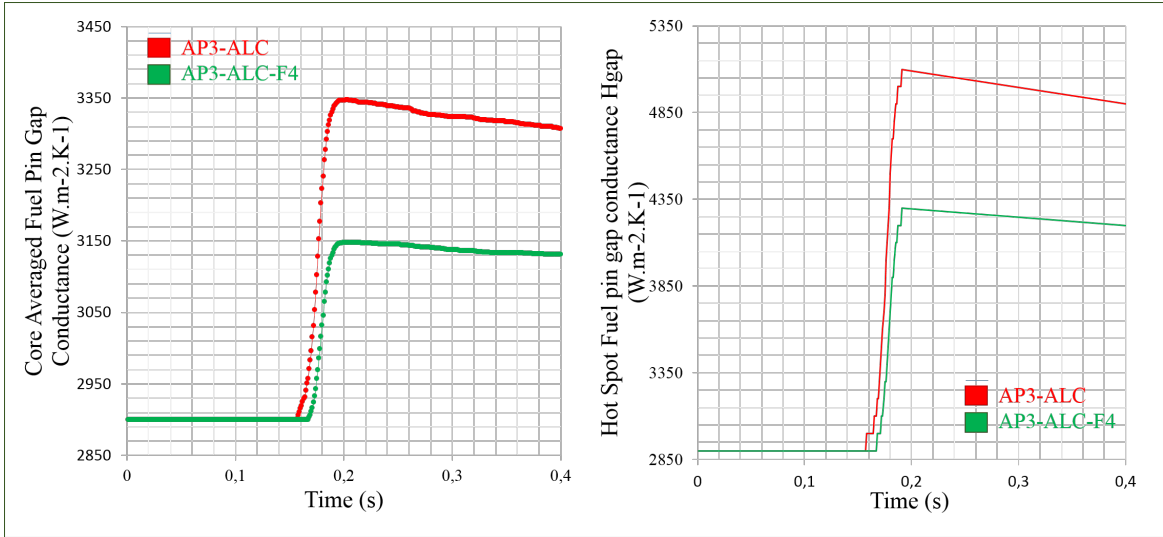


**Figure 13.17.** Hgap Global/Local Hot Spot comparison

More precisely, we get at  $t_2$ :

- AP3-ALC maximal core average value =  $3350 \text{ W.m}^{-2}.\text{K}^{-1}$ ,
- AP3-ALC-F4 maximal core average value =  $3150 \text{ W.m}^{-2}.\text{K}^{-1}$ .

And locally:

- AP3-ALC maximal Hot Spot value =  $5100 \text{ W.m}^{-2}.\text{K}^{-1}$ ,
- AP3-ALC-F4 maximal Hot Spot value =  $4300 \text{ W.m}^{-2}.\text{K}^{-1}$ .

The following histogram in figure 13.18 shows the effective Hgap distribution of Hgap value inside the core in percentage at the time step  $t_3=0.2s$  when the Hgap value is maximum. More precisely, we observe the quantity (in percentage) of cells in the reactor core that contain a Hgap at each value defined between the extremal Hgap value  $2900 \text{ W.m}^{-2}.K^{-1}$  and  $4300 \text{ W.m}^{-2}.K^{-1}$ ).

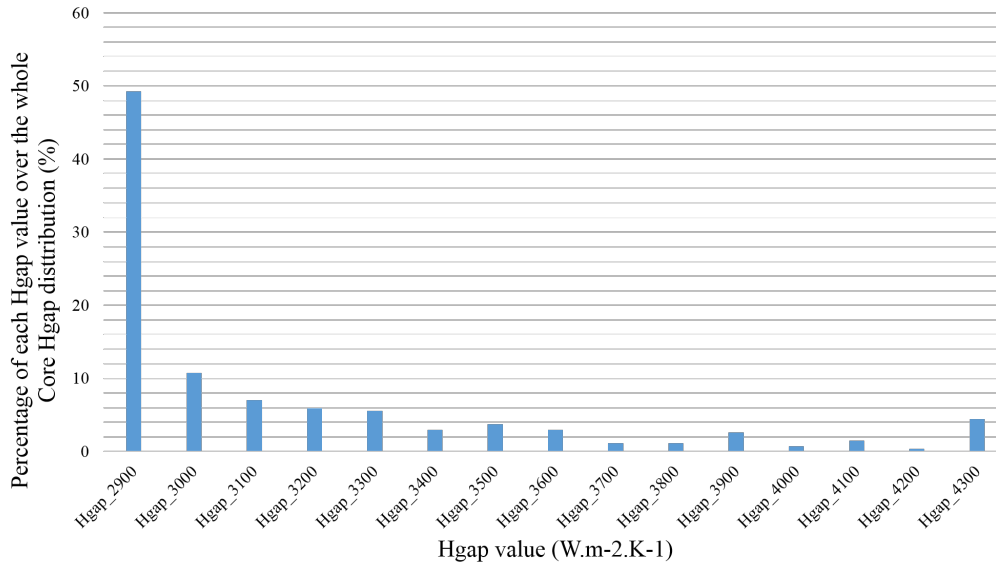


**Figure 13.18.** percentage of each Hgap value regarding the core Hgap distribution at  $t_3= 0.2s$

We observe than the Hgap in 50% of the core cells does not change from its initial value. It stem from the strong heterogeneity with lower half part at initial value and in the upper part a quite spherical distribution around the hot spot axial layer. The Hgap time evolution and spatial heterogeneous distribution induces a difference in terms of temperature distribution between AP3-F4 and AP3-ALC-F4 calculations (see figure 13.16). Indeed, in the AP3-F4 calculation the Hgap is assumed constant (about  $4100 \text{ W.m}^{-2}.K^{-1}$  in all core cells) while in the AP3-ALC-F4 the Hgap value evolves. For instance, in the one hand, in the AP3-F4 case, the Hgap value is constant (and low), thus, the temperature at the pellet surface stays close to the temperature at the center of the pellet, and increase as well as the the power increase. In the ohter hand, in the AP3-ALC-F4 case, the higher energy deposition induces a higher fuel pellet center temperature value than the AP3-F4 case. Moreover, the Hgap increase induces a higher thermal transfer between the pellet and the clad which modifies the fuel pellet thermal gradient and leads to a smaller increase of the surface pellet temperature. Consequently, it induces a significant difference in terms of fuel pin temperatures distribution and evolution between AP3-F4 and AP3-ALC-F4 calculations (see figure 13.19).

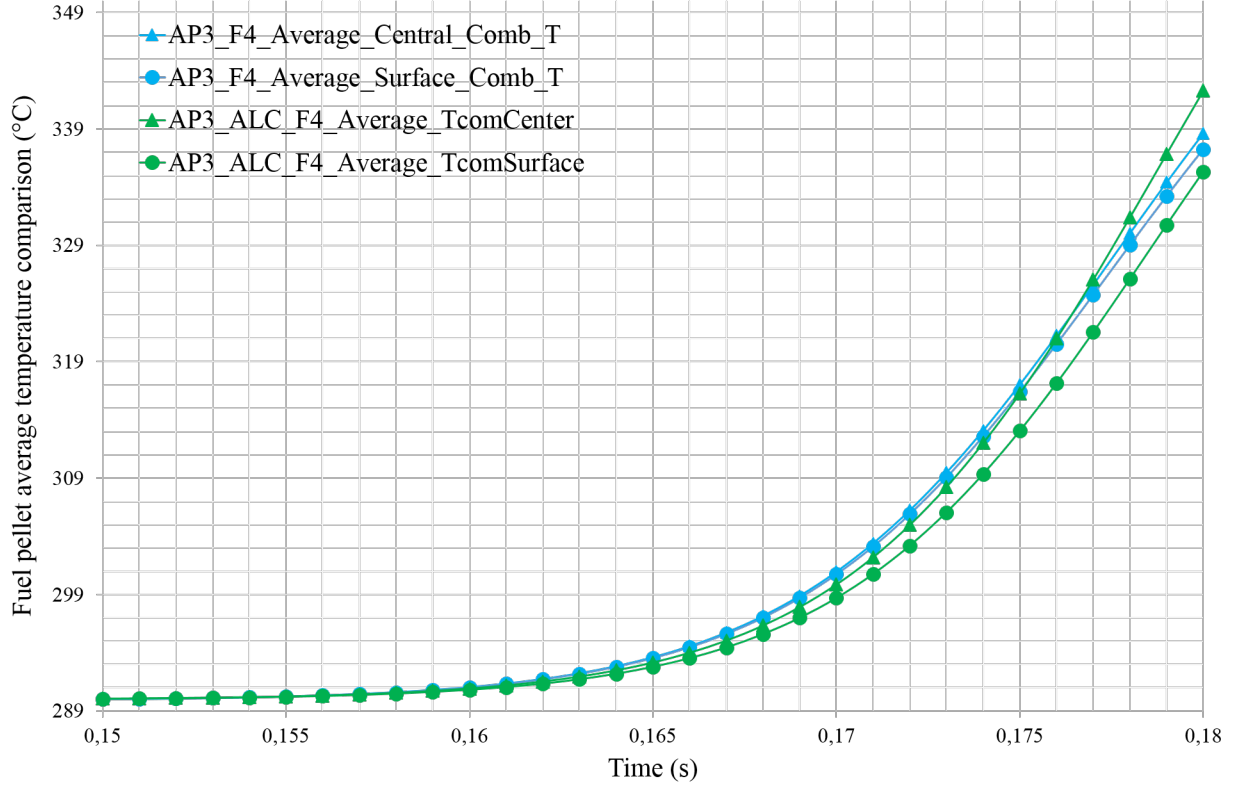


**Figure 13.19.** Core averaged Fuel pellet center/surface comparison  $t_{12}$

This aspect highlights the Thermomechanical contribution of an accurate Thermomechanics in our calculation and moreover it shows the impact of Thermomechanics on the transient. Indeed, this Global/local difference induces the pulse we observe between AP3-F4 and AP3-ALC-F4 calculations. The following figure ( 13.20) shows the integrated and local Power pulse we obtain if we set different Hgap values corresponding to the extremal value we obtained in our coupling calculation (see figure 13.20).

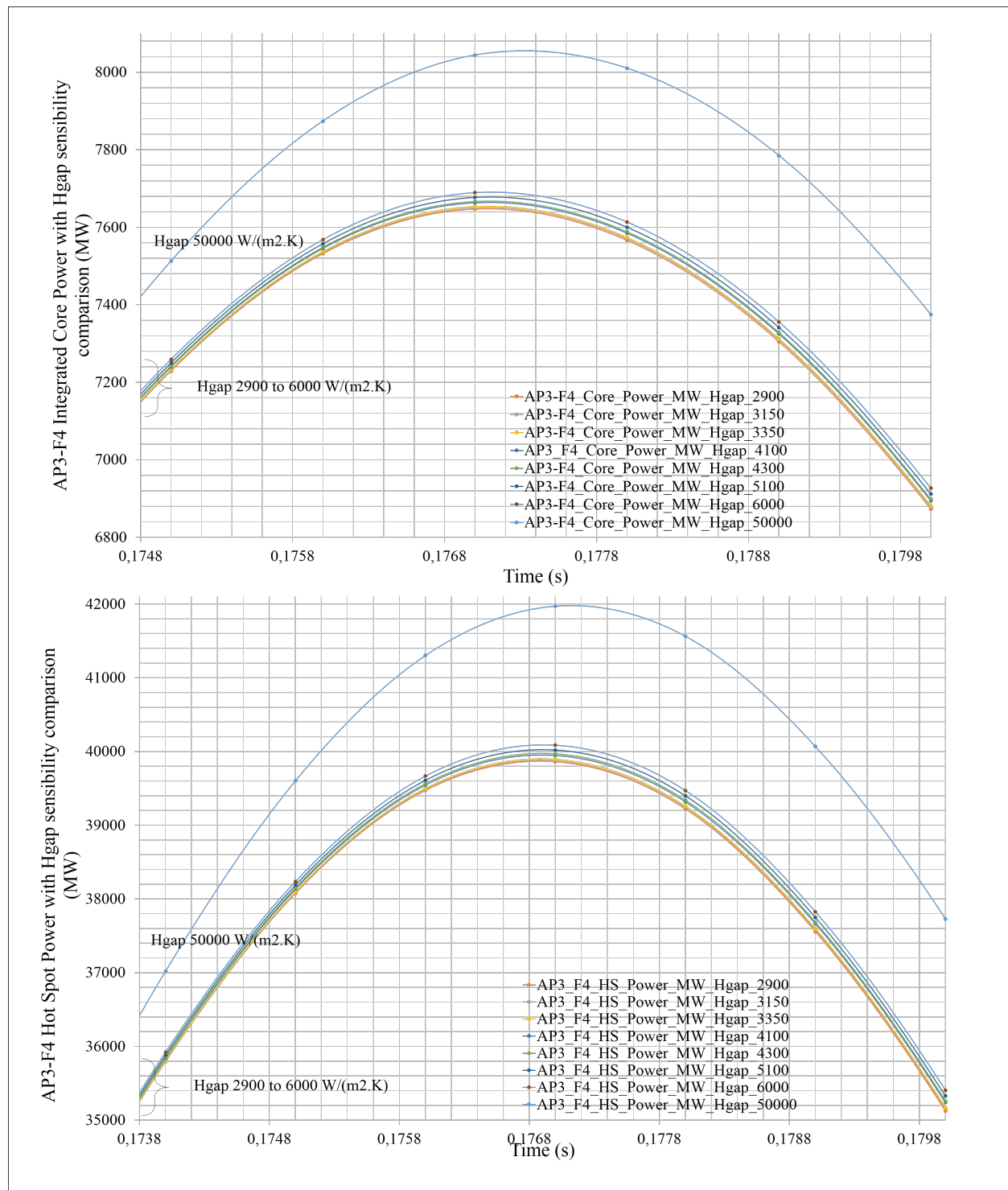


**Figure 13.20.** AP3-F4 Average Core / HS power with Hgap sensibility comparison around  $t_{max\_power}$

We observe that none of the Hgap values are correct to reach the exact behavior of the AP3-ALC-F4 transient calculation (see figure 13.3). We also observe that the change Hgap constant value in AP3-F4 is not sufficient to induce a correct physical answer of the transient. Indeed, if we assume a Hgap values close to an open gap value (for instance, between 2900 and 6000  $W.m^{-2}.K^{-1}$ ) in the AP3-F4 calculation, we observe a similar evolution up to a max core power about 7650 MW. In addition, if we assume a Hgap value at 50000  $W.m^{-2}.K^{-1}$  which simulate a closed gap, we observe a higher core power evolution (respectively local power evolution) with a maximal core power about 8000 MW which is lower than in the AP3-ALC-F4 calculation. Indeed, by assuming a constant Hgap in time and space we assume a constant closed or open gap in time and space. In either cases, we under- or overestimate the thermal transfer evolution between the pellet and the clad, and thus the thermal transfer to the fluid. This strongly highlights the need to take into account the heterogeneity and evolution, function of time, inside the core by using accurate Thermomechanics models (ALCYONE) in order to accurately compute the Thermomechanical behavior. This observation would be exacerbated in a real full core reactor where we have a stronger power distribution heterogeneity.

In conclusion, this time range strongly highlights the impact of using accurate Thermohydraulics coupled to accurate Thermomechanics on the transient evolution from the very first moment of the power increase and thermal activation. In addition to the validation of section (11.2), the fact that AP3-ALC-F4 transient behavior is similar to the AP3-F4 transient behavior validates our Thermohydraulics-Thermomechanics coupling between FLICA4 and ALCYONE as well as the energy conservation through a real transient situation.

**Time range  $t_{2-3}$  :**

Now we are interested in the time range  $t_{2-3}$  from  $t_2=0.18$  s to  $t_3=0.2$  s (see figure 13.21). During this time range we observe that the Core integrated power evolution of AP3-ALC, which has been separated from AP3-F4 and AP3-ALC-F4 calculations, is reaching a similar value than the two other calculations.

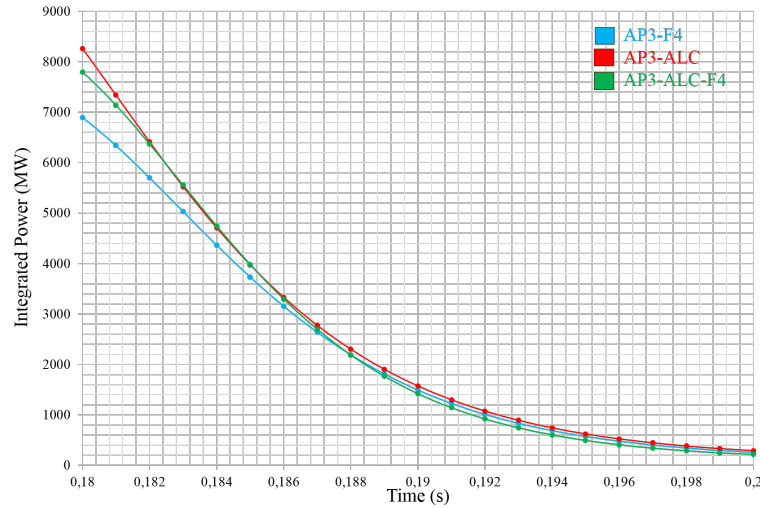


**Figure 13.21.** Integrated Power comparison  $t_{23}$

This behavior is confirmed by the total feedbacks reactivity evolution (see figure 13.22).

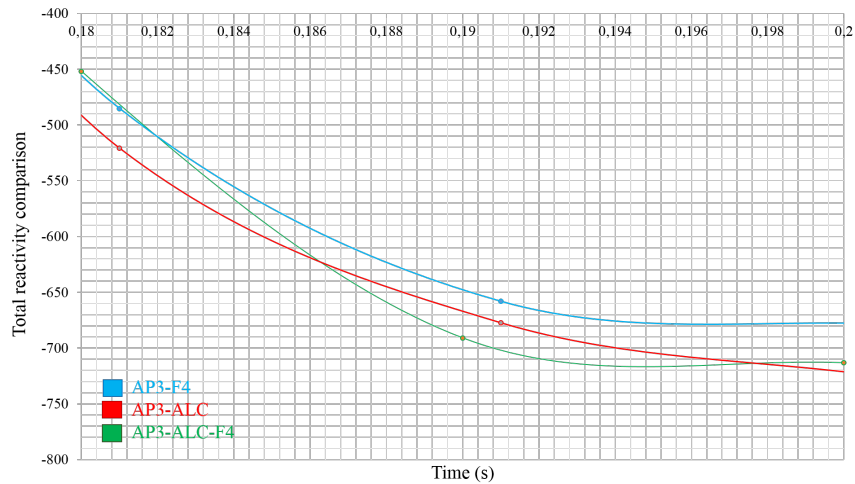


**Figure 13.22.** Total feedbacks reactivity comparison  $t_{23}$

If we focus on the Doppler reactivity and the effective temperature (see figure 13.23), we observe that the initial difference in  $t_{1-2}$  range within the Thermal transfer computation leads to a significant temperature difference of about 20 °C between AP3-ALC and the two other coupling calculations.

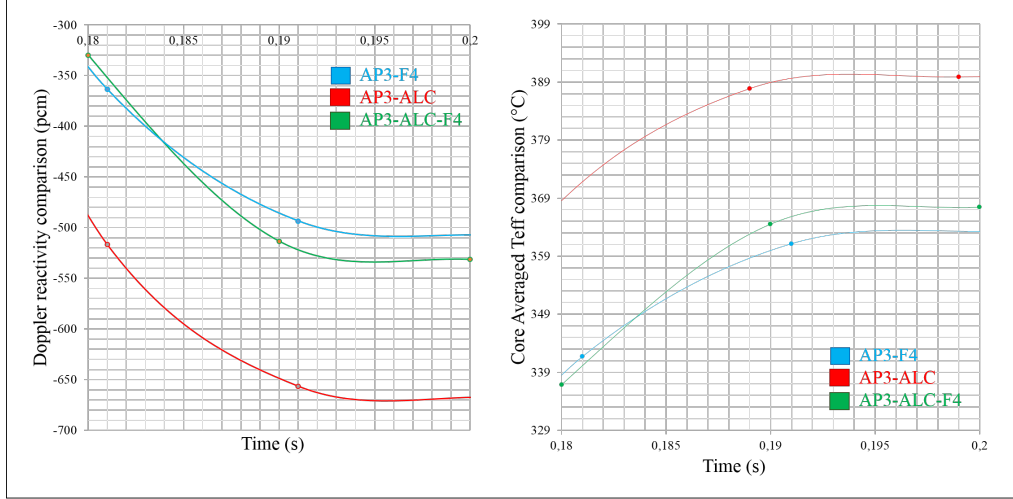


**Figure 13.23.** Doppler reactivity and Core averaged Effective temperature comparison  $t_{23}$

In the same way, regarding the moderator density and reactivity (see figure 13.24), we observe that AP3-ALC-F4 and AP3-F4 are reaching an asymptotical value of about  $745 \text{ kg.m}^{-3}$ . Meanwhile, in the AP3-ALC case, the initial lack of thermal transfer (due to the Hydraulical simplification in ALCYONE code) induces a delay in the moderator density decrease, which only starts to slightly decrease during  $t_{2-3}$ .

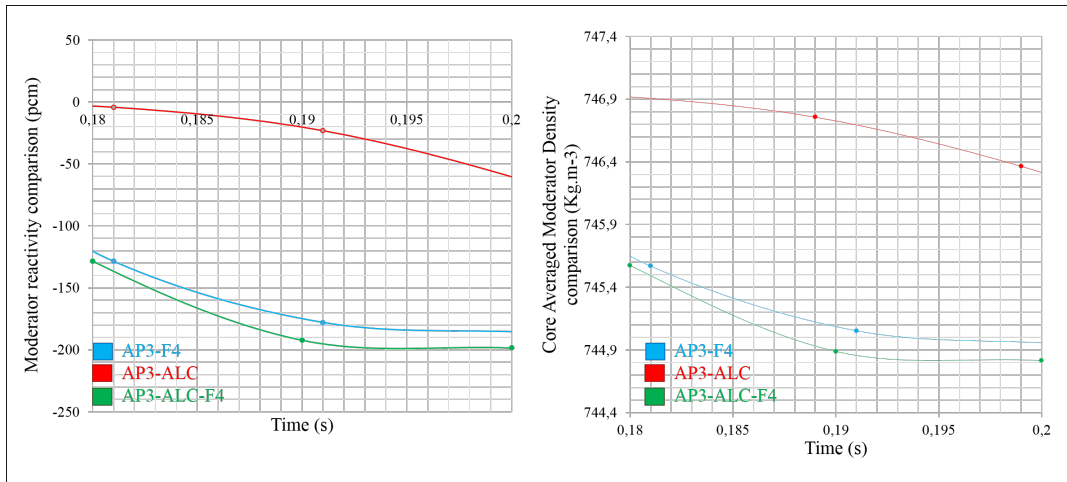


**Figure 13.24.** Moderator reactivity and moderator density comparison  $t_{23}$



## CHAPTER 13. NEUTRONICS - THERMOHYDRAULICS - THERMOMECHANICS COUPLING RESULTS AND ANALYSIS - PROOF OF CONCEPT

In this time range the moderator contribution starts to be the major contribution to the Total reactivity evolution considering that the doppler contribution has already stabilized.

We locally observe the same Thermal behavior at the Hot Spot regarding the effective temperature and the moderator density (see figure 13.25 ).

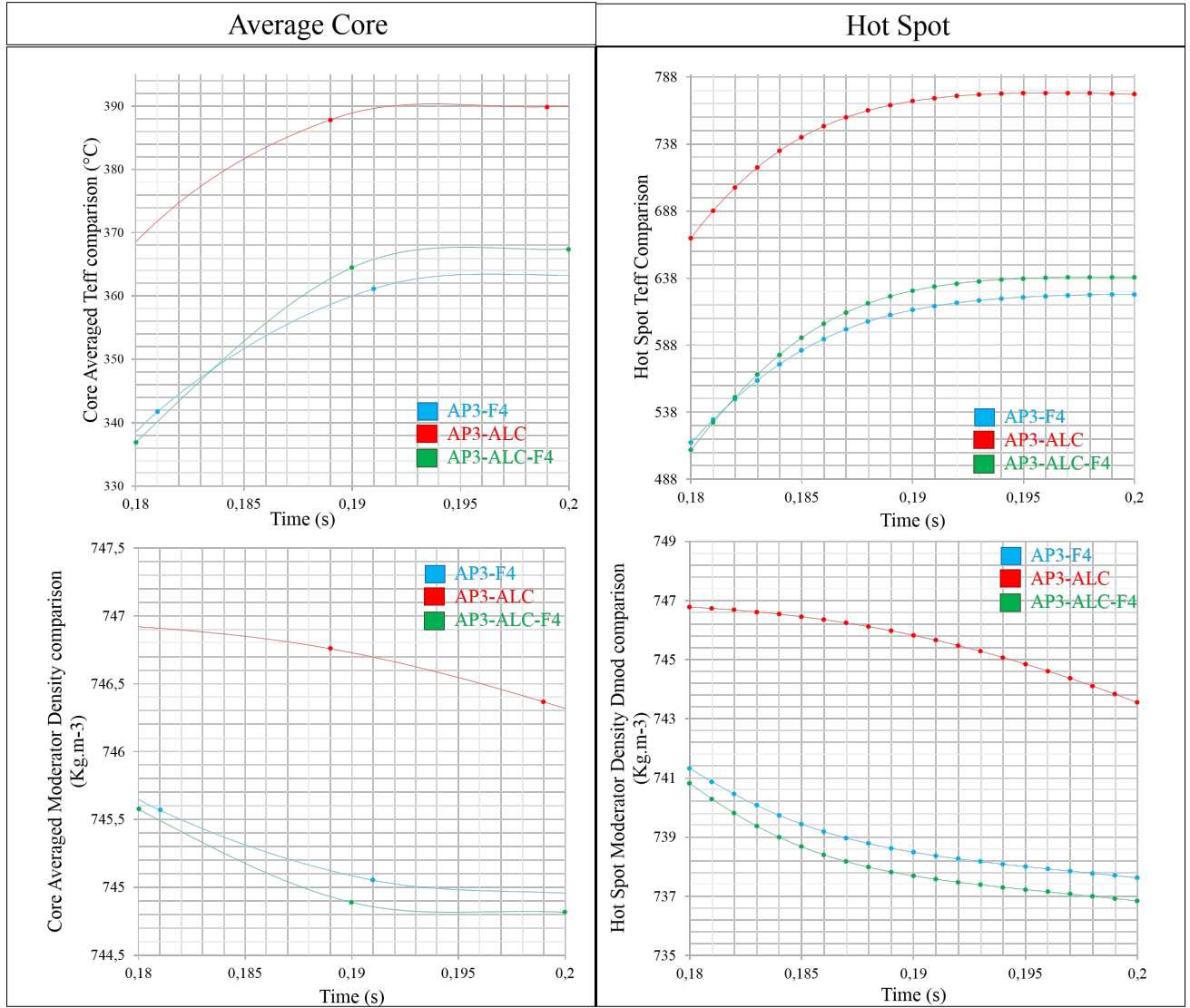


**Figure 13.25.** Global core averaged / Local Hot Spot effective temperature and moderator density comparison  $t_{23}$

**Time range  $t_{3-4}$  :**

Finally, if we focus on the time range  $t_{3-4}$  (see figure 13.26) we observe that the three couplings are reaching an asymptotical power value. These asymptotical value are close (about 10MW) but this steady state difference is a direct consequence of the differences we observe in the previous time range.

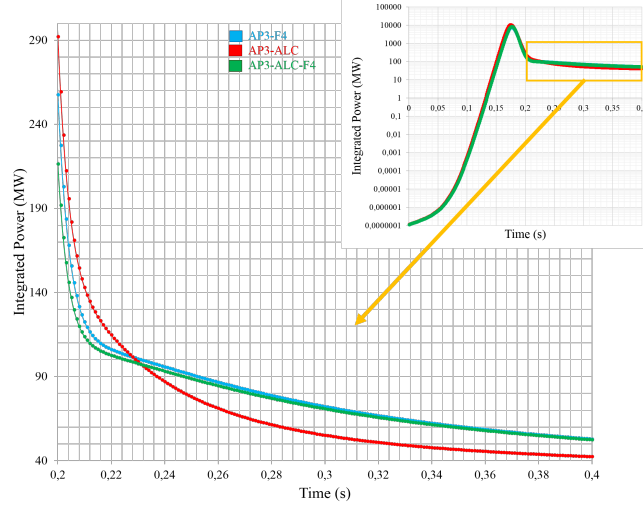


**Figure 13.26.** Integrated Power comparison  $t_{34}$

Regarding the total feedbacks reactivity in figure ( 13.27) , we observe a small difference between AP3-ALC-F4 and AP3-F4 calculation about 30 pcm while we observe a huge difference between these two calculations and the AP3-ALC case. This corresponds proportionally to the difference we observe during the range  $t_{1-2}$  within the thermal transfer computation and leads to a difference of about 240 pcm.

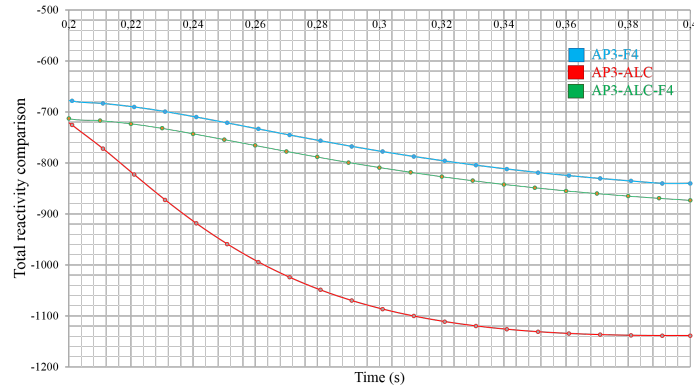


**Figure 13.27.** Total feedbacks reactivity comparison  $t_{34}$

On the one hand, the fuel temperature and more precisely the effective temperature is reaching an asymptotical value or slightly decreasing, which induces the stabilization of the Doppler reactivity or a slight injection of reactivity (see figure 13.28). So, it cannot explain the reactivity behavior seen in figure (13.27).

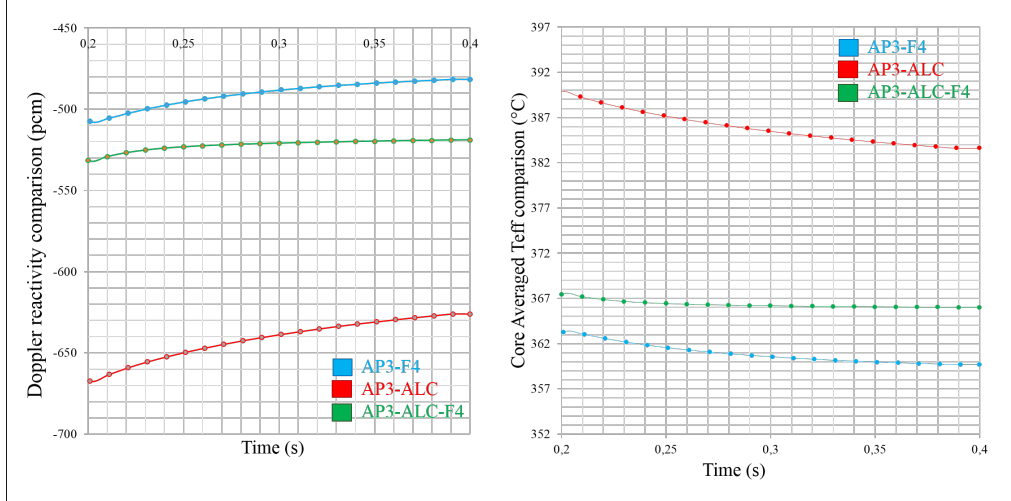


**Figure 13.28.** Doppler reactivity and effective temperature comparison  $t_{34}$

On the other hand, the difference we observe in terms of thermal transfer between the fuel pin and the fluid induces a delay of energy release to the fluid and a higher accumulation of the energy inside the fuel pin. This induces a higher moderator anti reactivity feedback effect in the case of the AP3-ALC calculation (see figure 13.29).

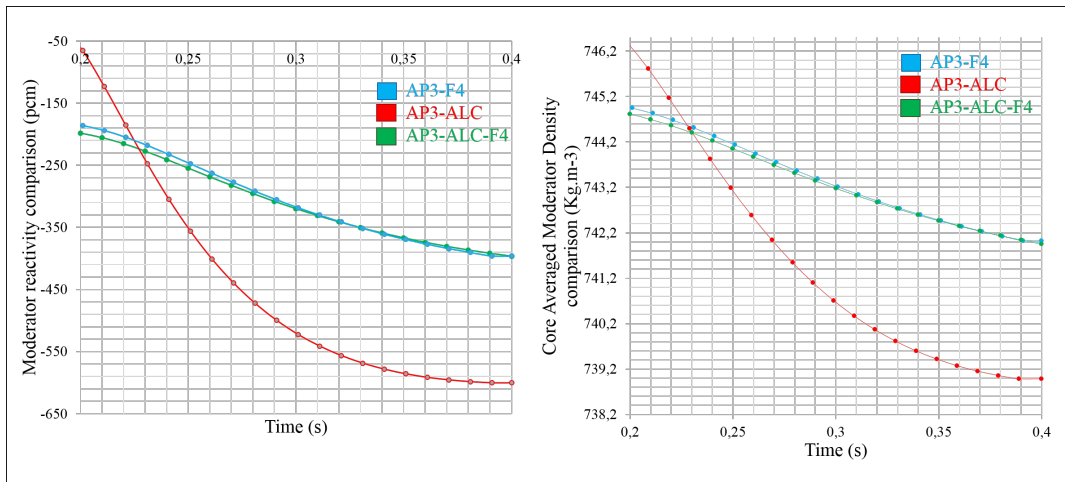


**Figure 13.29.** Moderator reactivity and Moderator density comparison  $t_{3-4}$

### 13.1. RESULTS COMPARISONS AND ANALYSIS

We locally observe the same Thermal behavior at the Hot Spot regarding the effective temperature and the moderator density (see figure 13.30).

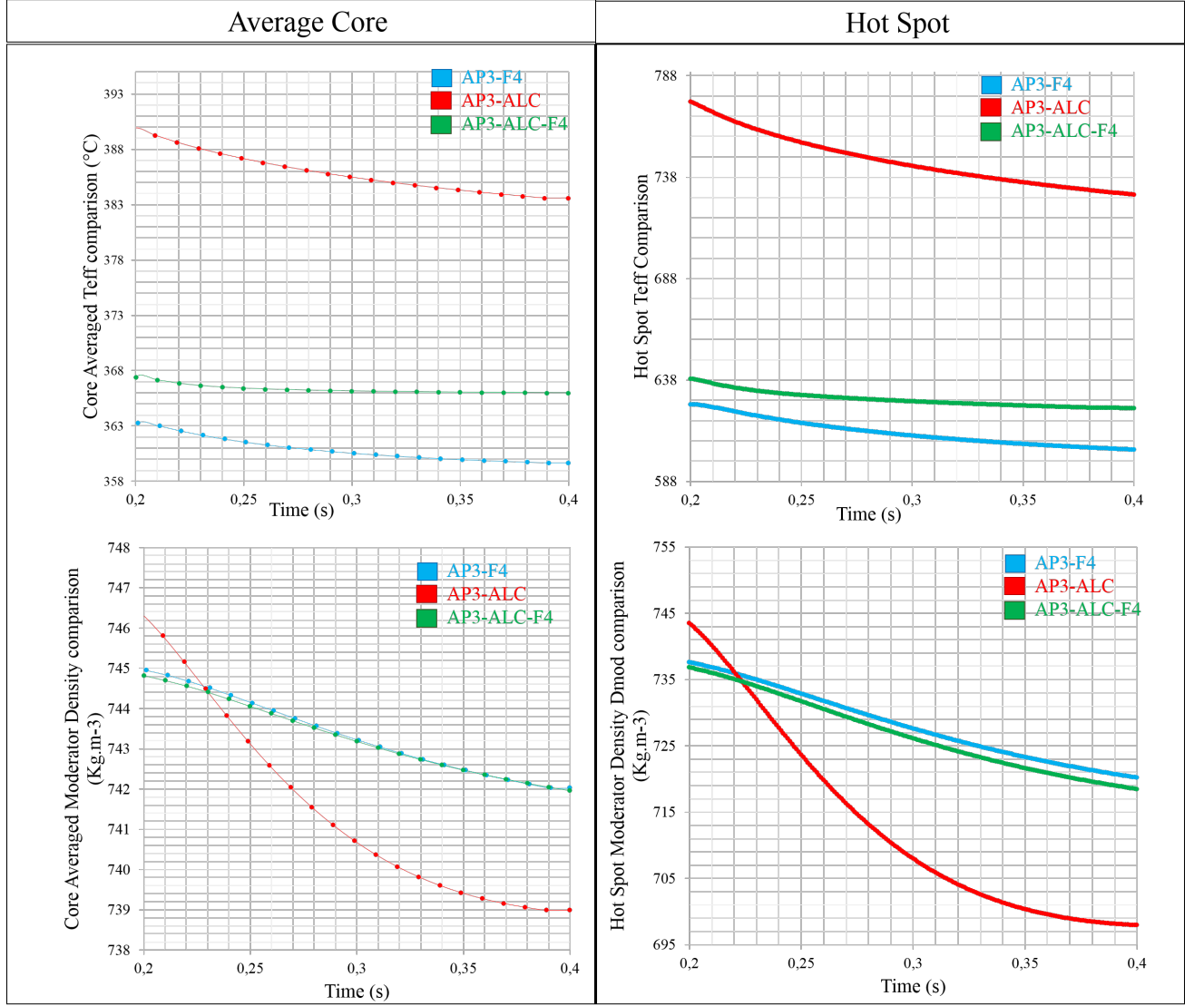


**Figure 13.30.** Global core averaged / Local Hot Spot effective temperature and moderator density comparison  $t_{3-4}$

In this time range the Moderator contribution is the major contribution to the Total reactivity. Indeed, the Doppler reactivity is stabilized (variation between 0 to 50 pcm) while the Moderator reactivity still decrease with a variation about 200 pcm in AP3-F4 and AP3-ALC-F4 calculation and about 500 pcm in AP3-ALC calculation. In the AP3-ALC calculation, the energy is slowly but finally release to the fluid moderator, which decreases the fluid density, induces a higher moderator feedback effect and continues to shut down the core power. This difference stems from the previous evolution difference we observe

in the previous time range, i.e., a lower thermal transfer between the fuel and the fluid from the beginning in AP3-ALC calculation. It also highlights the importance of accurate Thermohydraulics and Thermomechanics in order to simulate the reactor core behavior precisely during the transient, from the beginning of the thermal activation to the end of the transient (to the new equilibrium state).

### Summarized relative variations between couplings

In conclusion, we summarized our observation by showing the relative variation between coupling results in the following tabs. We consider the Total coupling as the reference calculation and we calculate  $\Delta X = (X - X^{reference})$  regarding the AP3-F4 and AP3-ALC calculations.

The first tab ( 13.1) compare the result we obtained from the AP3-FLICA4 calculation and the AP3-ALC-F4 calculation:

Difference between AP3-FLICA4 and AP3-ALCYONE-FLICA4 calculation			
Parameter	End of Time range $t_1^{end} = 0.18$	End of Time range $t_2^{end} = 0.2$	End of Time range $t_3^{end} = 0.4$
$\Delta P^{integrated}$	-900 MW	41 MW	0.4 MW
$\Delta Reactivity$	-4 pcm	36 pcm	33 pcm
$\Delta F_{xyz}$	0.001	0.02	0.03
$\Delta \Delta P^{HS}$	-4500 MW	207 MW	3.7 MW
$\Delta T_{eff}^{averaged}$	1 °C	-4 °C	-6 °C
$\Delta T_{eff}^{HS}$	5 °C	-12 °C	-20 °C
$\Delta T_{wall}^{averaged}$	-0.4 °C	0.04 °C	0.014 °C
$\Delta T_{wall}^{HS}$	-2.36 °C	-1.2 °C	-2.3 °C
$\Delta \Phi_{wall}^{averaged}$	-1.8 W.cm <sup>-2</sup>	-2.6 W.cm <sup>-2</sup>	0.02 W.cm <sup>-2</sup>
$\Delta \Phi_{wall}^{HS}$	-6 W.cm <sup>-2</sup>	-3 W.cm <sup>-2</sup>	-6 W.cm <sup>-2</sup>
$\Delta D_{mod}^{averaged}$	0.026 Kg.m <sup>-3</sup>	0.2 Kg.m <sup>-3</sup>	0.06 Kg.m <sup>-3</sup>
$\Delta D_{mod}^{HS}$	0.5 Kg.m <sup>-3</sup>	0.8 Kg.m <sup>-3</sup>	1.7 Kg.m <sup>-3</sup>

**Table 13.1.** Difference between AP3-FLICA4 and AP3-ALCYONE-FLICA4 calculation

### 13.1. RESULTS COMPARISONS AND ANALYSIS

Then the second tab ( 13.2) compare the result we obtained from the AP3-ALCYONE calculation and the AP3-ALC-F4 calculation:

Difference between AP3-ALCYONE and AP3-ALCYONE-FLICA4 calculation			
Parameter	End of Time range $t_1^{end} = 0.18$	End of Time range $t_2^{end} = 0.2$	End of Time range $t_3^{end} = 0.4$
$\Delta P^{integrated}$	464 MW	75 MW	-10 MW
$\Delta Reactivity$	-38 pcm	-8 pcm	-265 pcm
$\Delta F_{xyz}$	-0.01	0.06	0.2
$\Delta P^{HS}$	2234MW	388 MW	-55 MW
$\Delta T_{eff}^{averaged}$	28 °C	22 °C	17 °C
$\Delta T_{eff}^{HS}$	158 °C	136 °C	105 °C
$\Delta T_{wall}^{averaged}$	-0.6 °C	-0.7 °C	-0.3 °C
$\Delta T_{wall}^{HS}$	-3.47 °C	-3.45 °C	-0.16 °C
$\Delta H_{gap}^{averaged}$	190 W.m <sup>-2</sup> .K <sup>-1</sup>	200 W.m <sup>-2</sup> .K <sup>-1</sup>	175 W.m <sup>-2</sup> .K <sup>-1</sup>
$\Delta H_{gap}^{HS}$	800 W.m <sup>-2</sup> .K <sup>-1</sup>	800 W.m <sup>-2</sup> .K <sup>-1</sup>	700 W.m <sup>-2</sup> .K <sup>-1</sup>
$\Delta D_{mod}^{averaged}$	1.35 Kg.m <sup>-3</sup>	1.5 Kg.m <sup>-3</sup>	-3 Kg.m <sup>-3</sup>
$\Delta D_{mod}^{HS}$	6 Kg.m <sup>-3</sup>	6.7 Kg.m <sup>-3</sup>	-20 Kg.m <sup>-3</sup>

**Table 13.2.** Difference between AP3-ALCYONE and AP3-ALCYONE-FLICA4 calculation

## 13.2 Effective Temperature Comparisons

In this section, we are going to compare results we obtained from the calculation where we change the formulation of the effective temperature  $T_{eff}$  constructed from the fuel pin radial temperature  $T(r)$ . Three ways have been defined in section ( 7.3) and used in this study, i.e, the Rowland ( $T_{eff}^{Rowland}$ ), the SantaMarina ( $T_{eff}^{C-SM}$ ) and the ALCYONE Isotopic ( $T_{eff}^{Iso}$ ) effective temperatures.

The power pulses obtained from AP3-FLICA4-ALCYONE ( $T_{eff}^{Rowland}$ ) and AP3-FLICA4-ALCYONE ( $T_{eff}^{C-SM}$ ) are shown in figure ( 13.31).

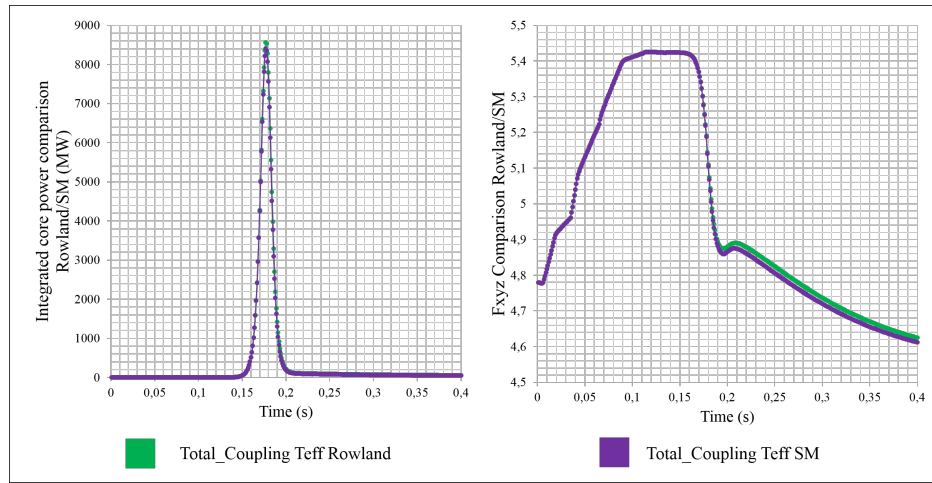


**Figure 13.31.** AP3-FLICA4-ALCYONE (Rowland) and AP3-FLICA4-ALCYONE (C and SM) power pulse comparison

The relative differences between these two calculations are catalogued in the following tab.

Maximal relative difference between AP3-ALC-F4 ( $T_{eff}^{Rowland}$ ) and AP3-ALC-F4 ( $T_{eff}^{C-SM}$ ) (where $\Delta X = (X^{SM} - X^R)/X^R$ )		
Power	-12% (26 MW)	at t = 0.2s
$T_{eff}$	1.9% (7 °C)	at t = 0.4s
$T_{wall}$	0.075% (0.13 °C)	at t = 0.4s
$D_{modW}$	0.02% (0.2 Kg.m <sup>-3</sup> )	at t = 0.4s
Hgap	0.3% (11 W.m <sup>-2</sup> .K <sup>-1</sup> )	at t = 0.4s

**Table 13.3.** Maximal relative difference between AP3-ALC-F4 ( $T_{eff}^{Rowland}$ ) and AP3-ALC-F4 ( $T_{eff}^{C-SM}$ )

The improvement of the  $T_{eff}$  formulation induces a significant impact on the core Power with a relative difference of about 12% (26MW). Nevertheless, regarding the effective tem-

### 13.2. EFFECTIVE TEMPERATURE COMPARISONS

perature we only observe a small relative difference of about 2% (7 °C) between the two calculations which leads to a Hgap relative difference of about 0.3%, to a  $D_{mod}$  maximal relative difference about 0.02% and to a  $T_{wall}$  relative difference only about 0.075%.

Then, we compare the Power pulses we obtained from AP3-ALC-F4 ( $T_{eff}^{Rowland}$ ) and AP3-ALC-F4 ( $T_{eff}^{Iso}$ ) and shown in figure ( 13.32).

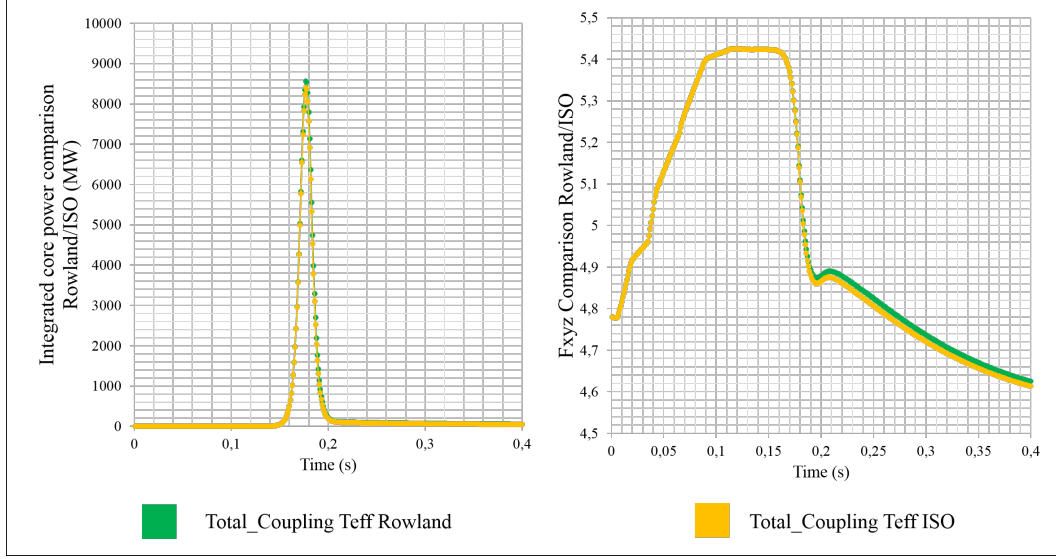


**Figure 13.32.** AP3-FLICA4-ALCYONE (Rowland) and AP3-FLICA4-ALCYONE (Isotopic) power pulse comparison

Same as in before, the relative differences between these two calculations are catalogued in the following tab.

Maximal relative difference between AP3-ALC-F4 ( $T_{eff}^{Rowland}$ ) and AP3-ALC-F4 ( $T_{eff}^{Iso}$ ) (where $\Delta X = (X^I - X^R)/X^R$ )		
Power	-12% (26 MW)	at t = 0.2s
$T_{eff}$	1.7% (7 °C)	at t = 0.4s
$T_{wall}$	0.07% (0.13 °C)	at t = 0.4s
$D_{modW}$	0.02% (0.2 Kg.m <sup>-3</sup> )	at t = 0.4s
Hgap	0.3% (11 W.m <sup>-2</sup> .K <sup>-1</sup> )	at t = 0.4s

**Table 13.4.** Maximal relative difference between AP3-ALC-F4 ( $T_{eff}^{Rowland}$ ) and AP3-ALC-F4 ( $T_{eff}^{Iso}$ )

As it was expected, the improvement of the isotopic  $T_{eff}^{Iso}$  formulation induces a significant impact on the core Power with a relative difference of about 12% (26MW). Nevertheless, regarding the effective temperature we also observe a small relative difference of about 2% (7 °C) between the two calculations which leads also to a Hgap relative difference of



about 0.3%, to a  $D_{mod}$  maximal relative difference about 0.02% and to a  $T_{wall}$  relative difference only about 0.07%.

Moreover, regarding the core Power we observe a relative difference of only 0.4% at  $t=0.2s$  and 0.6% at  $t=0.4s$  between the  $(T_{eff}^{C-SM})$  and  $(T_{eff}^{Iso})$  calculations. These results can be explained according to the fact that we are using fuel pin at zero burn-up in the thermomechanical equations and thus we have a quite planar distribution of isotopes (homogeneous medium) inside the pellet. Consequently, this isotopic distribution does not significantly impact the result of the  $T_{eff}^{Iso}$  formulation. A calculation in which we would take care of an heterogeneous burn-up map regarding the thermomechanics would certainly provide a significant difference in our results.

### 13.3 Results Conclusion

We realize couplings by pairing disciplines through explicit and implicit schemes and then we couple the three disciplines all together. This Multiphysics proof of concept first study show significant differences and improvements, regarding our academic core case and academic scenario detailed in section ( 2.4).

The difference between calculations mainly stems from the approximation we have done in our simplified model (in section 12.2 and 12.3). It makes Multiphysics coupling necessary in order to not under- or overestimate the transient behavior of the core (Neutronic, Thermal, Mechanical or Hydraulical). APOLLO3-FLICA4 calculation and APOLLO3-ALCYONE-FLICA4 give similar results (closer than APOLLO3-ALCYONE) but in APOLLO3-FLICA4 calculation FLICA4 requires the constant value of the Hgap we arbitrarily define. The Hgap needs to be calculated using at least an ALCYONE standalone calculation over the same core geometry. Obviously the APOLLO3-ALCYONE-FLICA4 will take less time, less steps and less approximations to achieve an accurate Multiphysics calculation.

We also realized studies concerning the effective temperature formulation that show small differences. Although, in our case, the Burn-up in the ALCYONE part is assumed at 0MWd/t, which smooths the difference that a real burn-up distribution, with heterogeneity at the scale of the fuel pin, should induce. This will be specifically true if we use our Isotopic effective temperature formulation in which the isotopic distribution inside the pellet will impact the effective temperature value and thus the transient evolution.

## Part VI

### Conclusion and Perspectives



---

This PhD thesis has been dedicated to the "Development of a Multiphysics and Multiscale Best Effort modelling for accurate analysis of a Pressurized Water Reactor under accidental operating situations".

The goal of the Thesis was to illustrate, through a proof of concept, our approach and ability to couple disciplines all together in order to improve in the futur simulations in Nuclear Reactor Physics. Our academic core case and academic scenario will allow us to perform realistic calculations by taking into account all the main physical aspects of a Nuclear Power Plant REA scenario in terms of representativeness (burn-up distribution), of phenomena (boiling and dry-out) and scale effects. During this thesis, we have reached our goal to couple Neutronics, Thermohydraulics and Thermomechanics disciplines and, using an academic reactor core and transient scenario, we observe a similar evolution of the core behavior that we obtain using a standard Best Estimate Neutronics-Thermohydraulics modelling. This Best Effort proof of concept coupling demanded several steps of work in order to be able to couple our disciplines. It involved understanding and detailing physical models from the CEA codes we used. It also required the improvement of models as well as structures in order to access the local physical information at the elementary scale of the fuel. Finally, all this work aims to implement Multiphysics coupling algorithms and to effectively couple our disciplines all together.

This coupling proof of concept shows improvement yielding:

- In terms of Neutronics, a better awareness of the Power evolution through precise feedback effects (Doppler, moderator), thanks to a more accurate thermal description of the Thermomechanics and Thermohydraulics aspects of the core.
- In terms of Thermohydraulics, a better awareness of the thermal exchange between the fluid and the fuel pin from the very beginning of the thermal activation.
- In terms of Thermomechanics, a better awareness of the thermomechanical evolution and thermal release through the cladding surface to the fluid, including a strong contribution at the interface between cladding and pellet (Hgap).

Our proof of concept paves the way to Best Effort calculation though some aspects are left to be developed or studied in future research works. The following figure ( 14.1) shows the optimal aspect of Best Effort coupling modelling (in blue) within which this PhD work took place (in red).

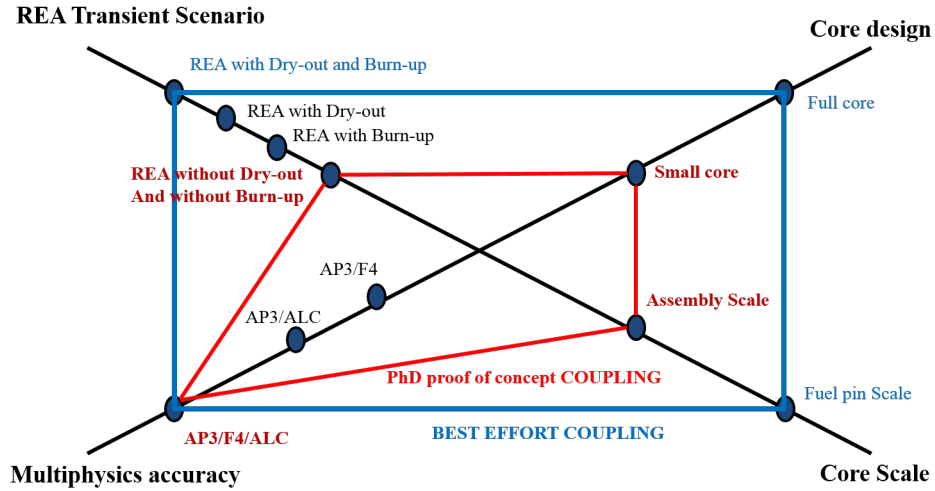


**Figure 13.33.** Best Effort Coupling perspectives diagram regarding our PhD proof of concept coupling

Looking at the above figure we observe that limitations and perspectives may be discussed regarding:

- core design aspects,
- transient scenario aspects,
- Multiphysics models accuracy and access to local parameters aspects.

Below we are going to present limitations and perspectives of these aspects.

### Core design limitations and perspectives

Limitations obviously appear from our academic core case. Indeed, the control rod area of impact is equal to the size of the small academic core we are using. This obviously will not be the case with real reactor geometry. We observe heterogeneous and symmetrical distribution of parameters but shape factors are lower than in the real core case. Indeed, core geometry approximation prevents any direct extrapolation to real PWR case and scenario. This aspect has been taken into account during the result analysis.

In terms of perspectives, studies should be performed using classical PWR core geometry, with fuel pin scale of discretization in assemblies of interest. These studies would be done in order to confront our results to a real case.

### Transient scenario limitation and perspectives

Limitations appear from the scenario we have effectively implemented. Indeed, a stronger scenario in terms of power production would lead to stronger energy deposition and thermal transfer with possible boiling phase and dry out phase. These fluid phase changes would bring strong nonlinearity (abrupt and local changes in the hydraulic state of the core) in our coupling. It would induce the necessity to use a fixed point method in order to converge our results. This would require some improvements of codes in order to be able to effectively complete a fixed point approach within our Multiphysics coupling.

Moreover, calculations have been done using a burn-up distribution equal to zero regarding the thermomechanical part. This aspect limits our analysis on the effective temperature formulations as well as the realism of the fuel pins behavior during the transient. Consequently, studies should be performed with heterogeneous burn-up distribution as well as with discretization at the scale of the fuel pin, in order to accurately interpret the impact, for instance, of the new isotopic effective temperature we developed.

### Multiphysics models accuracy, access to local parameter limitations and perspectives

As it is presented in the figure ( 13.34), individual disciplines and code descriptions still have small deficiencies and limitations to perfectly reach the same level of accuracy. Indeed, each code has limitations according to its numerical approach or through the implementation of physical phenomena occurring inside the core.

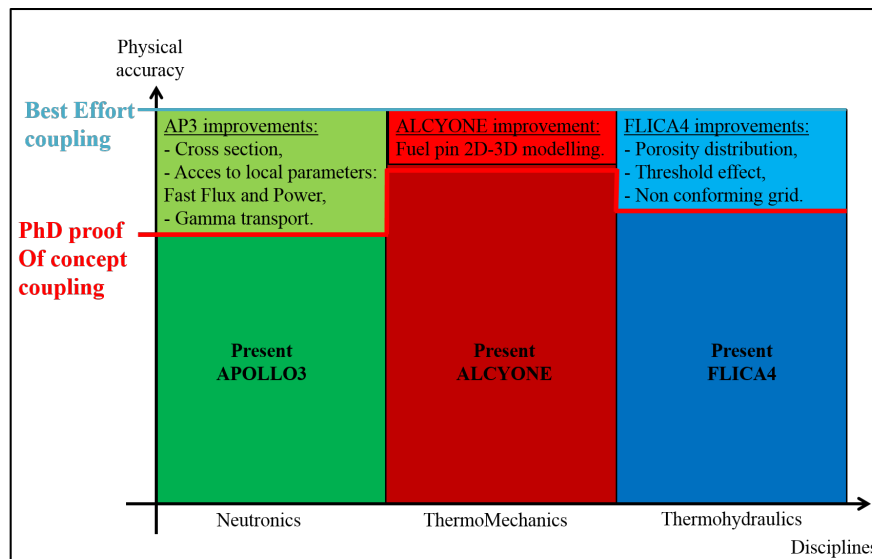


**Figure 13.34.** Best Effort disciplines models perspectives diagram regarding our PhD proof of concept coupling

Regarding the Neutronics part, limitations appear from the use of a precalculated cross

---

sections library and a static space discretization of the core. On the one hand, the pre-calculated cross sections library with reflection boundary condition could be considered as a significant source of uncertainty and discrepancy in an accurate Best Effort calculation (environmental aspects and core/reflector flux transition would be two principal requirements in cross section improvements). Moreover, cross sections with fewer number of energy groups allow calculations with shorter computing time but may induce limitations regarding the fast neutron flux computation. Currently, the fast neutron flux computation requires to define an energy group specifically or a cluster of energy groups that corresponds to an energy higher than 1 MeV. In this regard, the Fine Flux reconstruction we carried out or the coupling reconstruction we proposed (with a specific area where we refine space and energy) could be solutions in order to optimize our calculations. Moreover, without fuel pellet accurate discretization, it is compulsory to post treat the accurate temperature given by the fuel pin thermal model in order to respect the physical behavior of the core according to the Doppler feedback reaction. Consequently, limitations could appear from the effective temperature computation approach. This way, we implement the SantaMarina approach into our coupling and develop an isotopic computation of the temperature in order to take into account the rim effect and thus its effect on Doppler feedback reaction. Considering the access to the local Neutronics information at the elementary scale of the fuel, we developed a Fine Flux Reconstruction which allowed us to produce power to be deposited in the fluid and in the fuel. This method still lacks accuracy at this stage to be used in a proper multiscale coupling and could be coupled to a Gamma transport solver. Nevertheless, this first step showed a substantial asset in the perspective of a future Multiphysics and multiscale Best Effort or Best Estimate coupling. This first approach shall be shortly followed by a more accurate multisolver coupling.

Regarding the Thermomechanical part, although the single pin model is aimed to guarantee access to local parameters, limitations appear regarding the ability to realize 2D and 3D calculations over a whole axial fuel pin (of interest) instead of present single axial section computation available in the code. The axisymmetrical assumption is sufficient when we are working at the scale of a representative fuel pin per 1/4 assembly, but disymmetrical effects should appear in case of couplings directly at the scale of the fuel pin, with, for instance, differentiation between fuel pin and guide tubes.

Finally, regarding the Thermohydraulics, limitations appear from the nonconforming space discretization, from the constant porosity, and from the thermohydraulical threshold effect. Indeed, on the one hand, regarding the numerical convergence aspect of the code, the multiplicative coefficient of the refinement in the nonconforming grid should not exceed 4 [27] and thus limit the refinement opportunities. Nevertheless, it guarantees access to local parameters at the scale of the fuel pin. Then, on the second hand, regarding the thermohydraulical effects, the homogeneous porous equations are using a constant porosity, which implies that we neglect the fuel pin deformation (swelling, burst and so on) and thus the sub channel diameter variation during a transient situation. In case of REA, the sub channel barely changes in diameter which legitimates the hypothesis of a constant

---

sub channel diameter. Nevertheless, this would be a serious limitation in case of transient scenarii with large mechanical deformations of fuel pins at the scale of the sub channel.

### **Global perspectives**

In conclusion, the implementation of our global Best Effort Multiphysics coupling approach definitely paves the way for the development of more accurate Multiphysics reactor core calculations in case of REA accidents (Hot Full Power and Hot Intermediate Power), as well as in the case of other transient scenarii, such as MSLB or LOCA, or in case of a reactor operation optimization. Nonetheless, other more accurate studies would be required in order to test our coupling approach in detail, more accurately express the physical repercussions of this approach and precisely define the contribution on each discipline (regarding small time scale and small spatial scale). Moreover, studies on the uncertainties and comparisons with experimental tests such as the CABRI experiments would be paramount in order to fully validate our coupling and the assets of this approach in a safety analysis context. On this purpose, two thesis have recently started at the CEA/SERMA.

In addition, this transient scenario will be soon proposed as a specific Benchmark (NEA-UAM) to be compared with future Neutronics-ThermoMechanics-Thermohydraulics multiphysics couplings.



---

## Part VII

## ANNEXE



## Chapter 14

# ANNEXE 0 - French Abstract

L'analyse de sûreté des réacteurs nucléaires nécessite la modélisation fine des phénomènes y survenant et plus spécifiquement ceux permettant d'assurer l'intégrité des barrières de confinement. Les outils de modélisation actuels favorisent une analyse fine du système réacteur par discipline dédiée, et couplée avec des modèles simplifiés. Néanmoins, le développement depuis plusieurs années d'une approche dite "Best Effort", basée sur des calculs multiphysiques et multi-échelle, est en cours de réalisation. Cette approche permettra d'accéder au suivi et à l'analyse détaillée de problèmes complexes tels que l'étude des Réacteurs nucléaires en situation standard et accidentelle. Dans cette approche, les phénomènes physiques sont simulés aussi précisément que possible (selon la connaissance actuelle) par les modèles couplés. Par exemple, des codes disciplinaires existent et permettent la modélisation précise de la neutronique, de la thermohydraulique du coeur du réacteur, ou de la thermomécanique du combustible. Une approche "Best Effort" consiste donc à coupler des modèles disciplinaires afin de réaliser une modélisation globale et précise du système de réacteur nucléaire.

C'est dans ce contexte de travail que s'inscrit cette thèse. Elle consiste dans le développement d'un couplage multiphysique et multi-échelle "Best Effort" afin d'illustrer, par une "preuve de concept" et une première analyse physique accidentelle de type Ejection de Barre de contrôle (REA), notre capacité à coupler ensemble nos modèles disciplinaires et ainsi pouvoir proposer des simulations et analyses précises des Réacteurs à Eau Légère (REP) en situation normale ou accidentelle.

Elle a consisté principalement en l'analyse des modèles, de leurs interactions et en la mise en oeuvre d'un algorithme de couplage multiphysique entre une neutronique et une thermohydraulique exprimées à l'échelle du réacteur, ainsi qu'avec une thermomécanique fine à l'échelle élémentaire du crayon combustible. En outre, un travail spécifique a été effectué afin de préparer ou d'améliorer l'accès à l'information physique locale nécessaire à la mise en oeuvre de modélisations couplées multi-échelles, à l'échelle du combustible.

Outre des aspects méthodologiques et l'inscription de ce travail de Thèse dans un projet à long terme, notre travail a aussi porté sur l'établissement d'un scénario académique simplifié mais physiquement représentatif. Ce coeur de réacteur et ce scénario académiques seront présentés dans un futur proche en tant que BENCHMARK spécifique (NEA-UAM) et pourront ainsi être utilisés comme base de comparaison avec de futurs couplages multiphysiques "Best Effort".

Finalement, suite à ce travail de Thèse, nous avons atteint notre but de couplage multiphysique (neutronique, thermohydraulique et thermomécanique fines) et son illustration via l'utilisation de notre coeur et scénario académique. En conclusion, ce travail de "preuve de concept" d'un couplage multiphysique "Best Effort" a permis de mettre en exergue des apports liés au couplage de ces disciplines fines:

- En termes de Neutronique, le couplage avec une thermohydraulique et thermomécanique fines entraîne une meilleure estimation de l'évolution de la puissance via une meilleure prise en compte des phénomènes de contre réaction Doppler et modérateur.

- En termes de Thermohydraulique, on observe une meilleur prise en compte des échanges thermiques entre le combustible et le fluide et cela dès le début de l'activation thermique du combustible.
- En termes de Thermomécanique, on observe une meilleur prise en compte de l'évolution et du transfert thermique du combustible et tout particulièrement au niveau du gap combustible/gaine (Hgap) et gaine/fluide.

Notre preuve de concept participe à ouvrir la voie à la simulation multiphysique "Best Effort" et "Best Estimate". Il sera néanmoins encore nécessaire d'approfondir certains aspects de modélisation et de représentativité physique par des développements spécifiques et études fines dans de prochains travaux de recherche ou lors des Thèses qui suivront celle-ci. La figure suivante( 14.1) présente les aspects de base à étudier pour améliorer ce travail de "preuve de concept" ( décrit [En bleu](#)) et le couplage optimal futur dans lequel il s'inscrit ([en rouge](#)).

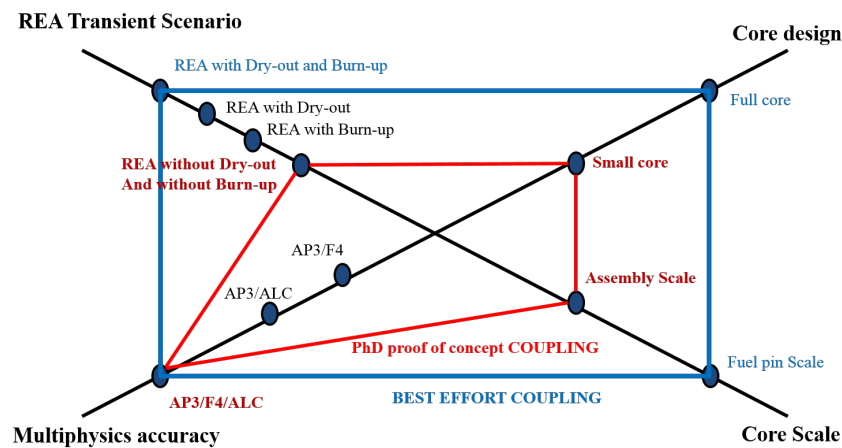


**Figure 14.1.** Perspectives et améliorations du couplage Best Effort preuve de concept pour atteindre le couplage Best Effort optimum

Finalement, en termes de perspectives, outre des travaux d'approfondissement de notre "preuve de concept" et de notre réacteur/scénario académique, ce premier couplage multiphysique trace la voie pour d'autres études de transitoire REA (pleine puissance et puissances intermédiaire) mais aussi, par adjonction/soustraction de modèles physiques, pour des études de scénarios de type Rupture Tuyauterie Vapeur ou Accident de perte de réfrigérant primaire, ou encore, dans des cas d'optimisation de la gestion d'un cœur de réacteur. En outre, un travail de thèse a débuté sur l'étude des incertitudes issues de chaque discipline et leurs répercussions et un futur travail de thèse s'intéressera à comparer ce couplage et ses versions améliorées face à des expériences CABRI. Ces travaux de thèse et ceux qui suivront permettront de valider définitivement notre approche et ses apports pour l'étude des réacteurs, et l'analyse de sûreté.



## Chapter 15

# ANNEXE I



## 15.1 Pressurized Water Reactor and academic simplification

In this part, we describe the industrial context and the type of reactor we are working with. For the purpose of this study, an academic case has been defined, through a specific effort has been made in order to stay within an industrial configuration and thus allow the perspective to apply our methodology to a PWR reactor.

### 15.1.1 Industrial context

This work has been done in the context of an PWR 1300 MWe (core thermal Power,  $P_{nominal} = 3800$  MWth) made up of 194 assemblies. These assemblies are following a steady GEMMES fuel management, characterized by:

- 18 month cycle (campaign);
- core reloading by a third of the core (64 assemblies per cycle);
- a maximal average burn-up per assembly of 52 GWj/t (the burn-up measures the fraction energy (in GW x days) which has been produced per ton of fuel. It is commonly used in nuclear industry to define the age of assemblies);
- a fuel UO<sub>2</sub> enrichment of 4 % ;
- a reloading of 24 gadolinium assemblies per cycle in order to restrain the core reactivity at the beginning of the cycle.

The fuel assembly reference is AFA-3GL.

Further informations concerning the physical parameter and desing of the core are given in annexe I section 15.2 .

The reloading map with or without gadolinium as well as the irradiated map (showing the number of cycles completed per each assembly) are respectively given in the picture ( 15.1), ( 15.2) and ( 15.3).

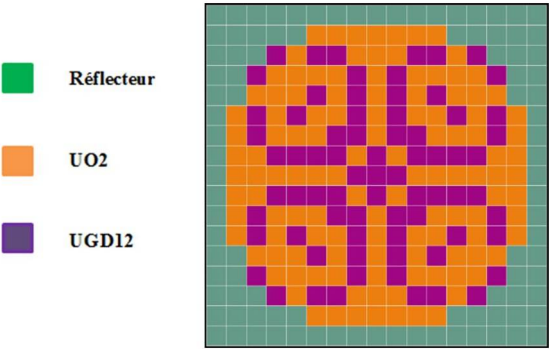


Figure 15.1. PWR 1300 MW core map

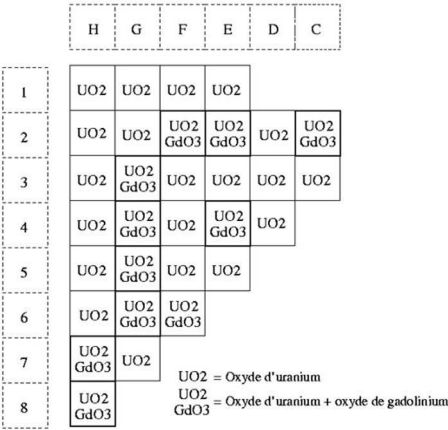
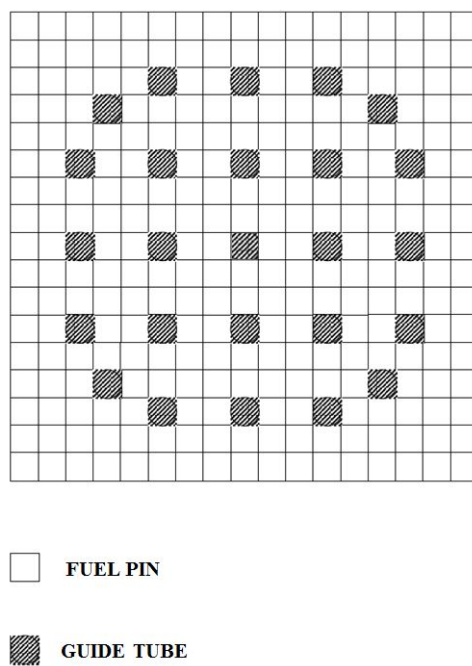


Figure 15.2. PWR 1300 MW core map and assembly location



**Figure 15.3.** Assembly within a PWR 1300MWe

### 15.1.2 Academic model

This reactor is a 5x5 geometry reactor made of 9 internal fuel assemblies and of an external ring of 16 reflectors. It has a Power of 110 MW, and is 468,72 cm in height. The central assembly has a central control rod. The small core has been designed in order to preserve the 1/8 core symmetry that exists in standard 1300MW PWR core and the side-effect induced by the presence of reflector assemblies around the fuel assemblies. In addition, a steady state planar distribution of the flux has been defined working with the burn-up and Boron distribution. The burn-up distribution also allows us to produce a hot point during the transient in lateral assembly instead of the assembly that contains the control rod. This geometry preserves the physical specificities as well as the behaviors of the PWR 1300 MWe in case of nominal and accidental situations.

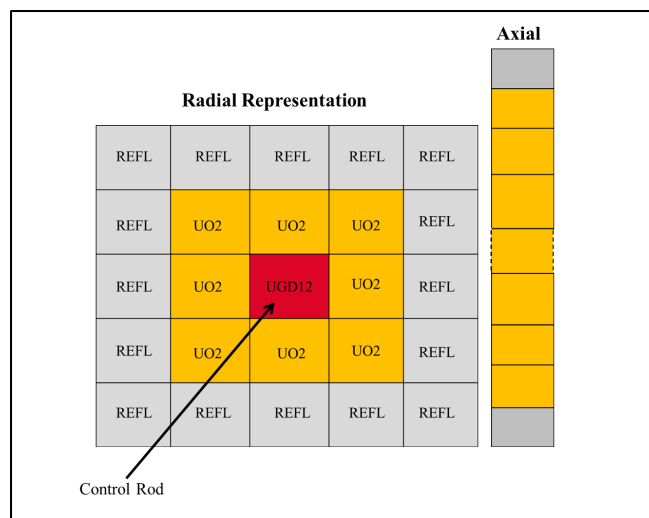


**Figure 15.4.** PWR small core (5x5) scheme

## 15.2 Nuclear reactor core material design, properties and composition

[67] [216]

### 15.2.1 Core description

#### Core description geometry

Core and Assemblies description		
number of assembly	193	
grid of rods by assembly (grid)	17x17 (289 rods)	
side lenght of an assembly	215.04	mm
fuel height of the assembly	4267.2	mm
number of fuel rods per assembly	265	
step network discretisation	12.6	mm
total transversal dimension	214x214	mm
weight of the fuel by assembly	598 UO <sub>2</sub> and 527.5 U	kg
total number of Fuel rod bundle spacer	10	
Fuel rod bundle spacer composition	Zircalloy and Inconel	
number of guide thimble (guide tube (TG)) per assembly	24	
composition of the guide tube	Zircalloy	
external diameter of the Guide Tube (upper part)	12.45 (12.24)	mm
internal diameter of the Guide Tube (upper part)	11.45 (11.43)	mm
core symetry	1/8	
equivalent diameter	3370	mm

**Table 15.1.** Core and Assembly description

Changes for the simplified small core reactor:

simplified small core		
number of assembly	25	
number of fuel assembly	9	
number of reflector assembly	16	
equivalent diameter	1213.24	mm

**Table 15.2.** Core and Assembly description (academic core)

## Power and flux property

Core Power and flux property		
nominal thermal power	3800	MWth
nominal electrical power	1300	MWe
power density during standard operation	79.8	$kW.coeur.10^{-3}.m^3$
average lineical power during standard operation	1705	$kW.m^{-1}$
max lineical power during standard operation	4520	$kW.m^{-1}$
extremal lineic power safety criterion	59000	$W.m^{-1}$
average flux	571	$kW.m^{-2}$
maximal flux (fuel pin) in standard operation	1514	$kW.m^{-2}$
average percentage of heat deposition inside the fuel pellet	97.4	%

**Table 15.3.** Power and flux properties

Changes for the simplified small core reactor:

Core Power property		
nominal thermal power	110 - 177.2	MWth
power density during operation	3.72	$kW.coeur.10^{-3}.m^3$

**Table 15.4.** Power and flux properties (academic core)

## Thermal and coolant property

Hydraulic and Cooling flow properties		
heat exchange surface	6477	$m^2$
number of loops	4	
nominal internal pressure of the primary loop in standarad operation	15.5	MPa
minimal internal pressure of the primary loop in standarad operation	15.3	MPa
hydraulic friction loss	0.29	MPa
hydraulic cross section	4.7629	$m^2$
flow of the wessel	90940	$m^3.h^{-1}$
average fluid velocity along the rods	5.21	$m.s^{-1}$
average massic velocity of the fluid	3640	$kg.m^{-2}.s^{-1}$
Thermal properties		
inlet nominal core coolant temperature	288.8	$^{\circ}C$
outlet nominal core coolant temperature	326.5	$^{\circ}C$
outlet nominal vessel coolant temperature	32425	$^{\circ}C$
average core temperature	307.7	$^{\circ}C$
average vessel temperature	312.8	$^{\circ}C$
average increase of the temperature inside the core	37.7	$^{\circ}C$
average increase of temperature inside the vessel	35.4	$^{\circ}C$

**Table 15.5.** Hydraulic propreities

Changes for the simplified small core reactor:

Hydraulic and Cooling flow properties		
heat exchange surface	254.76	$m^2$
hydraulic cross section	0.1873	$m^2$
flow of the wessel	4240.72	$m^3.h^{-1}$

**Table 15.6.** Hydraulic properties(academic core)

### 15.2.2 Fuel pins description and properties

[100]

No changes are observed between the 1300PWR and the simplified small core reactor.

Fuel pins description		
number of fuel pins per assembly	265	
external diameter	9.5	mm
gap between clad and pellet	0.17	mm
clad thickness	0.57	mm
clad material	M5	
fuel pellet diameter	8.192	mm
fuel pellet material	UO2 or MOX	
fuel pellet enrichment	5 %	% of the mass

**Table 15.7.** Fuel pin description

Thermal Fuel pins properties		
effective temperature of the fuel pellet in standard operation	620	$^{\circ}C$
temperature inside the pellet at 100% of the power	1900	$^{\circ}C$
average temperature of the clad	340.8	$^{\circ}C$

**Table 15.8.** Thermal fuel pin properties



### 15.2.3 Moderator and poison description and properties

No changes are observed between the 1300PWR and the simplified small core reactor.

#### moderator and poison description

Control rods (dimension are given at 20 °C)	
number of grapp	89
number of control rods by grapps	24

**Table 15.9.** Control rods properties

#### moderator and poison composition

poison integrated inside the fuel		
material	Gd <sub>2</sub> O <sub>3</sub>	
Gadolinium enrichment	8	% of mass
Uranium enrichment	2.2	% of mass
Control rods grapps (dimension are given at 20 °C)		
B <sub>4</sub> C part (upper part)		
Natural boron (B <sub>10</sub> percentage)	19.9	% of mass
Adensity	1.79	<i>g/cm<sup>3</sup></i>
External Diameter	7.47	mm
length	2610	mm
AIC part (lower part)		
Ag	80	% of mass
In	15	% of mass
Cd	5	% of mass
density	10.17	<i>g/cm<sup>3</sup></i>
External Diameter	7.65	mm
length	1500	mm
Cladding		
External Diameter	9.68	mm
External Diameter	7.72	mm
thickness	0.98	mm
material	stainless steel	

**Table 15.10.** Moderator and poisons properties and composition

#### 15.2.4 Reflector description and properties

No changes are observed between the 1300PWR and the simplified small core reactor.

Reflector		
thickness	between 77 and 297 (average 194)	mm
composition	95% steel and 5% water	% of the volum

**Table 15.11.** Reflector properties



## Chapter 16

# ANNEXE II

## 16.1 Multiphysics approach

A multiphysics problem involves many physical disciplines such as, in Nuclear Reactor Engineering, Neutronics, core ThermoMechanics, system ThermoMechanics, core Thermohydraulics and system Thermohydraulics. These disciplines imply mathematical models, numerical options, but also uncertainties and approximations that all together describe the whole system we are working on. The computation of the system behavior, evolution, and so on, require to solve all these equation. The solution we get will be function of the accuracy of this set of equation but also function of the system, spatial and time discretization, as well as of the model approximations and data uncertainties.

Several Multiphysics modelling approaches have appeared from latest scientific research. These methodology are organized following an increasing accuracy of the system prediction described below.

### 16.1.1 Simulator approach

The Simulator approach is characterized by:

- Small computing time,
- It uses simplified modelling for each disciplines arbitrary choosen (meta models),
- It approximates behavior prediction well knowing the uncertainties of each model,
- It allows real time simulations.

### 16.1.2 Best Estimate

The Best Estimate approach is characterized by:

- Reasonable computing time,
- It uses an PIRT approach (Phenomena Identification and Ranking Table) in order to rank the paramount phenomena to be modeled and to define the accuracy of all the discipline models we are going to use,
- It uses optimized modelling with choosen approximation and well known uncertainties,
- It allows industrial calculations.

### 16.1.3 Best Effort

The Best Effort approach is characterized by:

- Computing time is not a constraining aspect,
- It focuses on the most accurate description of the system that discipline models allow,
- It balances and compares every disciplines all together in order to get the same spatial, time, numerical, and so on, level of accuracy, which correspond to realize Best estimate approach for each discipline model.
- It allows precise industrial (with computing time optimization) or research calculations.

This approach is based on 3 requirements:

- It allows the measurement of the biais of modellings,
- It allows to give assessments or to realize studies on the uncertainties regarding each model we use,
- It allows to pronounce judgements on the conservative aspect of the modelling.

### 16.1.4 High Fidelity

The High Fidelity approach is a simulation and modelling of the system at its higher level of prediction. Physical phenomena are descibe and compute by the cutting edge existing models. This approach is characterized by several goals:

- Production of accurate Benchmarks in order to validate Best Estimate and Best Effort modelling approach calculations,
- To allow very extem and contraining simulations such as severe accidents.

This approach is based on the same requirements than the Best Effort approach.



## Chapter 17

# ANNEXE III



## 17.1 Transient scenario definition

From the first stage of the creation of a nuclear reactor the nuclear safety and security are paramount in its design. Nuclear safety and security cover the actions taken to prevent nuclear and radiation accidents or to limit their consequences. Whatever the situation, a nuclear reactor has to respect 3 safety functions [109]:

- Reactivity : it must control the reactivity at any time,
- Cooling : it must ensure reactor cooling,
- Containment : it must keep operational radioactive material containment.

For these reasons, some principles of "defense in depth" have been defined:

- 1<sup>o</sup> : design studies, manufacture quality and operational process ensure that no failure should occur in normal operating conditions,
- 2<sup>o</sup> : surveillance and protection system studies should minimize abnormal and incidental transients consequences,
- 3<sup>o</sup> : safeguard system studies should limit hypothetical accident consequences that involve radioactive material confinement.

According to these principles and safety functions, confinement barriers have been created. These barriers are decomposed in 3 parts:

- Fuel pin cladding (first barrier),
- Reactor vessel (second barrier),
- Reactor building (third barrier).

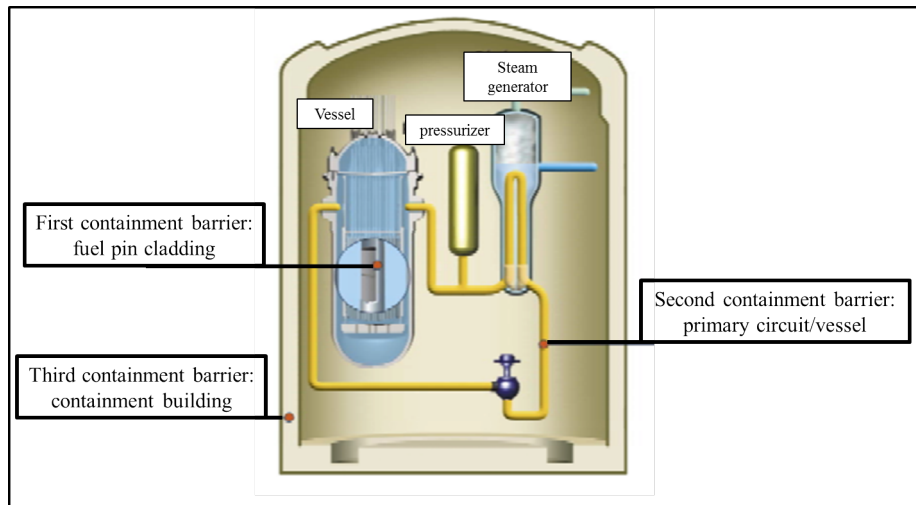


**Figure 17.1.** Nuclear Reactor containment barriers

Accidental situations will occur in case of violation of these reactor safety functions and barriers. They are classified following 7 categories according to their gravity and probability of occurrence, 4 are used in order to design the reactor and the 3 other take into consideration unforgiven accidents (Fukushima) [250]. The rod ejection accidents (REA) are classified from the category 2 to the category 4. Several parameters influence the transient answers [250]:

- The state characteristics of the core:
  - initial operating point:
    - \* Power level (fission) and Fuel pin temperature,
    - \* fluid pressure, flow and temperature,
    - \* control rod organisation;
  - the state of progress of the fuel cycle:
    - \* fuel state (Burn-up),
    - \* burn-up map of the core
    - \* neutronic properties (the fuel state influences the fraction of delayed neutrons and the value of the neutronic feedbacks):
      - $\beta$  : the delayed neutrons fraction
      - neutronic feedbacks :
        - A.  $\alpha_{moderator}$  : the moderator feedback
        - B.  $\alpha_{doppler}$  : the Doppler feedback
    - \* characterisation of the weight, in terms of reactivity, of the control rods

- The origin of the reactivity insertion, its dynamics, its celerity and its distribution in the core.

The following tab synthetises the features of the main rod ejection accidents [250]:

Accidents	Symmetrical distribution	Category category	Typical reactivity insertion	Duration of insertion	Prompt reactivity	Main feedback reactions
Ejection of a group of rods in a subcritical reactor	YES	2	2000 pcm	30 s	YES	Doppler
Group of rod ejection in critical reactor	YES	2	500 pcm	15 s	NO	Doppler and moderator
rod ejection in critical reactor	NO	3	100 pcm	100 s	NO	Doppler and moderator
Rod Ejection Accident (REA)	NO	4	600 pcm	0.1 s	YES	Doppler

**Table 17.1.** Features of the main rod ejection accidents [250]

Remarks: pcm is a neutronic unit which means per cent mille =  $10^{-6}$ .

The fourth category regroups the worst accidents and the REA is one of them. It is one of the most constraining scenario in terms of fuel pin integrity and it may induce rod failure and spread out the fuel from its cladding.

## Chapter 18

# ANNEXE IV

## 18.1 Major Hypotheses of the transport theory

We recall the major hypotheses of the transport theory [58]:

- Particles are assumed as single points: this hypothesis is applicable if the wavelength associated to the particle is smaller than the atomic scale. Indeed, inside a reactor core, particles have a mean free path equal to several interatomic distances. This way, this hypothesis is relevant in order to model the position and velocity of a neutron.
- Neutron-Neutron interactions are neglected: the neutron density inside the reactor core is very small compared to the density of the medium, even if it's a gas. For instance, inside a PWR, the neutron density is about  $10^{16}$  neutrons per  $cm^3$  and per second which is less by a factor  $10^{11}$  than the average density of the solid part of the core that is about  $10^{22}$  nucleus per  $cm^3$ .
- Particles travel in a straight line between two collisions: neutrons and gamma rays are not electrically charged and thus they are not affected by the electromagnetic forces. Nuclear forces can be considered like collisions according to their small radius of action. Concerning the neutrons, we need to consider collision with nucleus as well as for the gamma rays (photoreaction). In our case, we only focus on the neutron transport inside the core and we neglect the gamma transport.
- Neutronic collisions are assumed to be punctual: the radius of action of the nuclear forces is about  $10^{-12}$  while the distance travelled by a neutron between two collisions may achieve several centimeters.
- The properties of the medium are assumed isotropic: at our finest scale of modelling (usually the fuel pin) this hypothesis is correct and cross sections are treated this way.
- Cross sections and the composition of the medium are known at the time of interest.

## Chapter 19

# ANNEXE V

## 19.1 Physical details concerning thermal parameters of the heat transfer equation

Two important quantities in equation (6.62) have to be discussed in more detailed: the thermal conductivity  $\lambda_g$  and the gas extrapolation length  $l$ . For the sake of simplicity the indices f or cl are dropped.

The thermal conductivity of a multicomponent gas mixture is usually calculated by

$$\lambda_g = \sum_{f=1}^n \left\{ \frac{\lambda_j}{\left(1 + \sum_{k=1, j \neq k}^n \phi_{jk} \frac{C_k}{C_j}\right)} \right\} \quad (19.1)$$

where

$c$  = molar concentration,

$\phi_{jk}$  = weighting factor.

The weighting factor  $\phi_{jk}$  has been investigated by several authors. Well known are the correlation of Lindsay-Bromley [148] and Tondon-Saxena [252]. Tondon and Saxena's correlation requires somewhat less experimental information than the correlation of Lindsay and Bromley, which may be an advantage for certain applications. Nevertheless, Lindsay and Bromley's correlation in the present investigation was found to be slightly more accurate and was therefore chosen as the standard option of the revised URGAP model. Tondon and Saxena's correlation is optional. The importance of the gas extrapolation length  $l$  (sometimes called the temperature jump distance) can directly be concluded from equation (6.63). All detailed models are based on the work of Kennards [124] who obtained

$$l = \frac{2-a}{a} \frac{2}{\gamma+1} \frac{\lambda}{\mu C_v} L, \quad (19.2)$$

where

$a$  = accommodation coefficient,

$\gamma = C_p/C_v$ ,

$C_p$  = specific heat at constant pressure,

$C_v$  = specific heat at constant volume,

$\mu$  = viscosity,

$L$  = mean free path.

Difference between existing models have been discussed by Lanning and Hann [130]. The striking fact is that none of these detailed correlations include a model parameter which may be adapted to experimental data. Consequently, large differences result for gas extrapolation length  $l$  mainly due to uncertain accommodation coefficients (see Appendix

### 19.1. PHYSICAL DETAILS CONCERNING THERMAL PARAMETERS OF THE HEAT TRANSFER EQUATION

---

A of [133]. Only [99] proposed a simplistic empirical correlation which includes a model parameter by assuming that,

$$l \sim L. \quad (19.3)$$

In accordance with the correlation used in the URGAP model, the empirical correlation with a newly introduced model parameter  $\beta_3$  has been chosen:

$$l = \beta_3 \frac{2 - 0.827\bar{a}}{\bar{a}} L_g, \quad (19.4)$$

where

$\beta_3$  = model parameter,

$$\bar{a} = \frac{\sum_{j=1}^n \frac{c_j a_j}{\sqrt{M_j}}}{\sum_{j=1}^n \frac{c_j a_j}{\sqrt{M_j}}},$$

M = gas atomic weight,

$$L_g = \sum_{j=1}^n c_j L_j,$$

$$L_j \sim \frac{\mu_j}{P_{gas}} \sqrt{\frac{T}{M_j}},$$

$P_{gas}$  = gas pressure.

A detailed discussion is given in [132]. In addition, the correlation (19.3) is also investigated. Moreover, gas data used in the URGAP model are given in the appendix B of [133].





## Chapter 20

# ANNEXE VI

In this part we expose the results we obtains through our couplings (AP3-F4, AP3-ALC and AP3-ALC-F4) regarding core average parameter results and local Hot Spot parameter results.

### 20.1 Global average parameters coupling comparisons

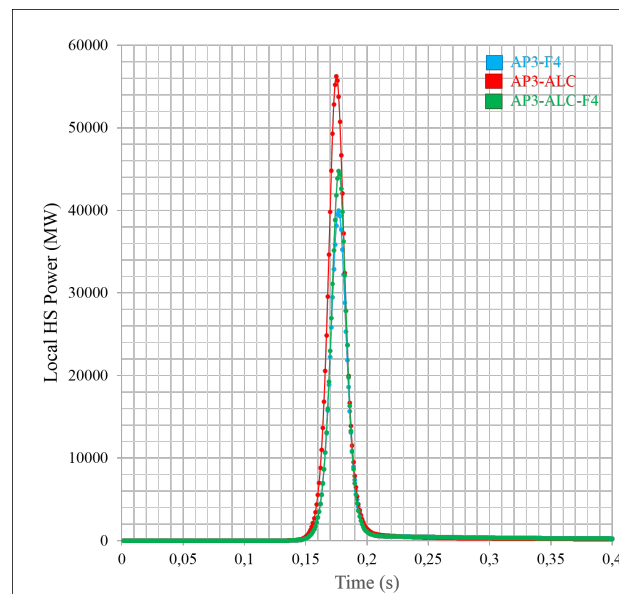


**Figure 20.1.** Global core Power evolution couplings comparison

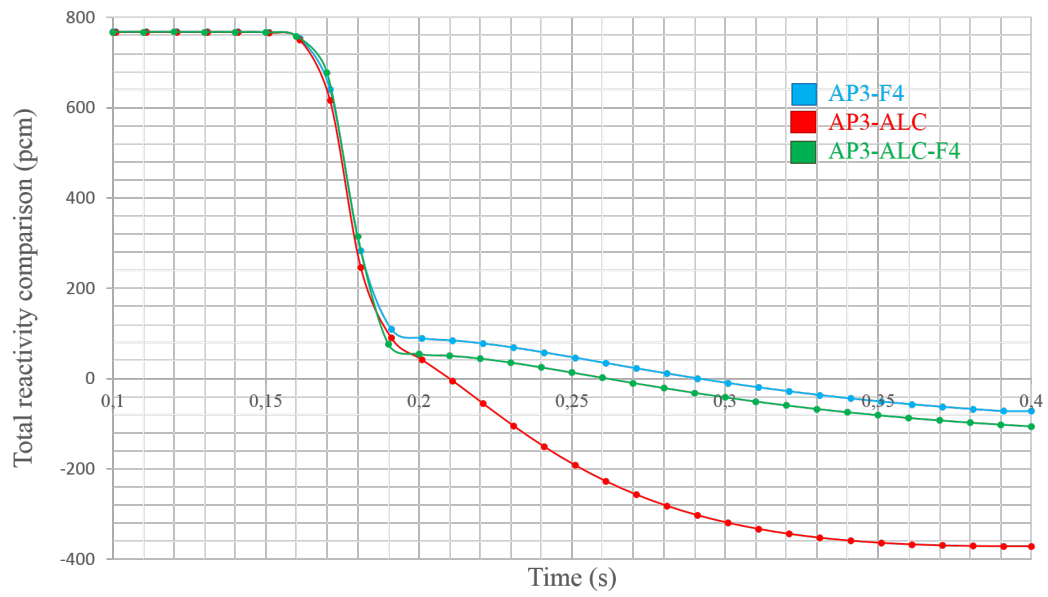


**Figure 20.2.** Total reactivity evolution couplings comparison

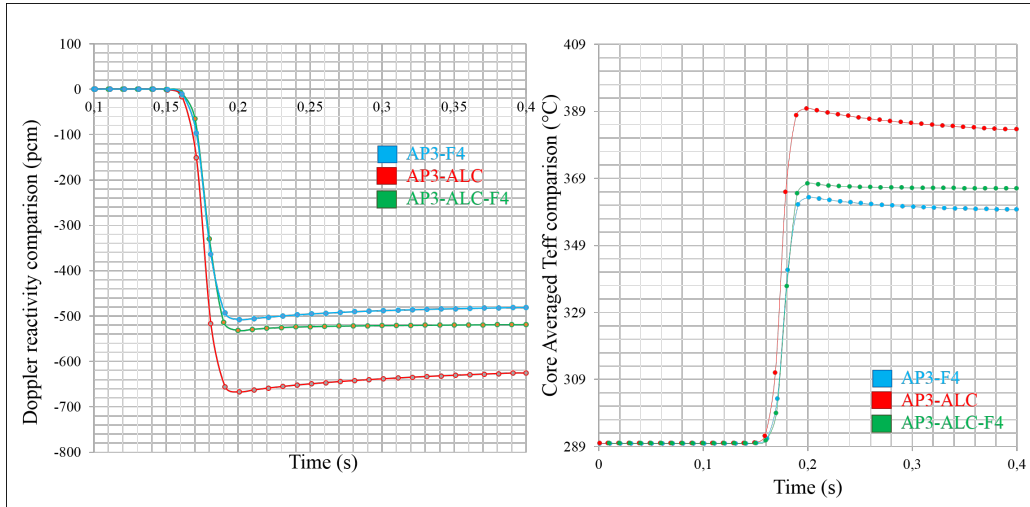


**Figure 20.3.** Doppler reactivity and core average Effective temperature evolution couplings comparison

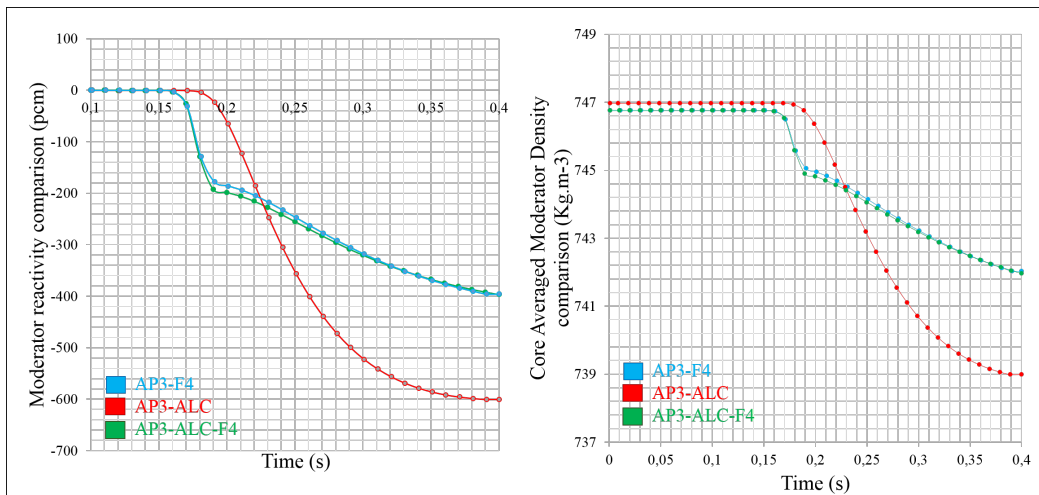


**Figure 20.4.** Moderator reactivity and core average Moderator Density evolution couplings comparison

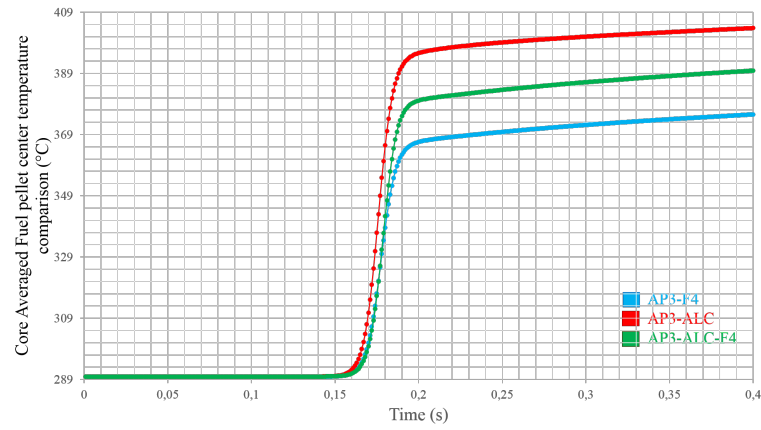


**Figure 20.5.** Core average fuel pellet center temperature evolution couplings comparison

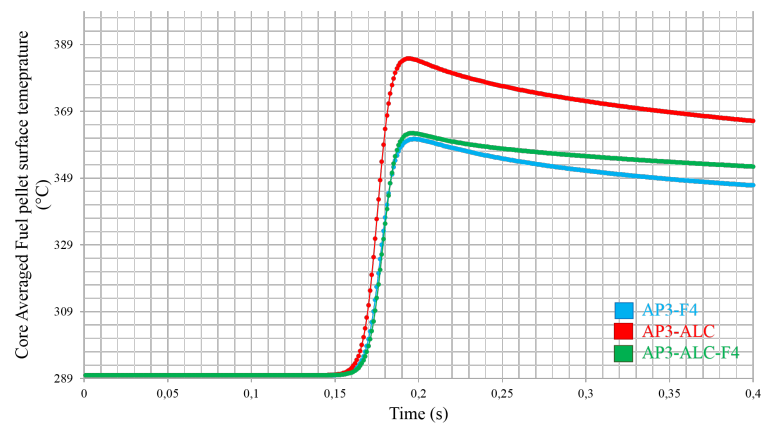


**Figure 20.6.** Core average fuel pellet surface temperature evolution couplings comparison

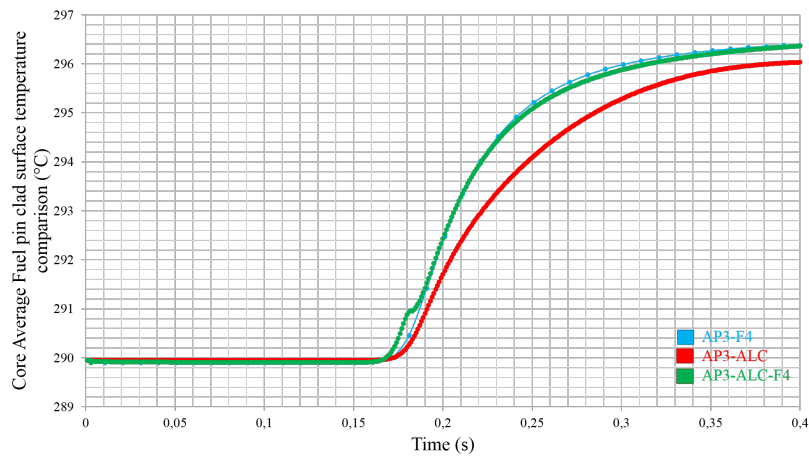


**Figure 20.7.** Core average clad surface temperature evolution couplings comparison

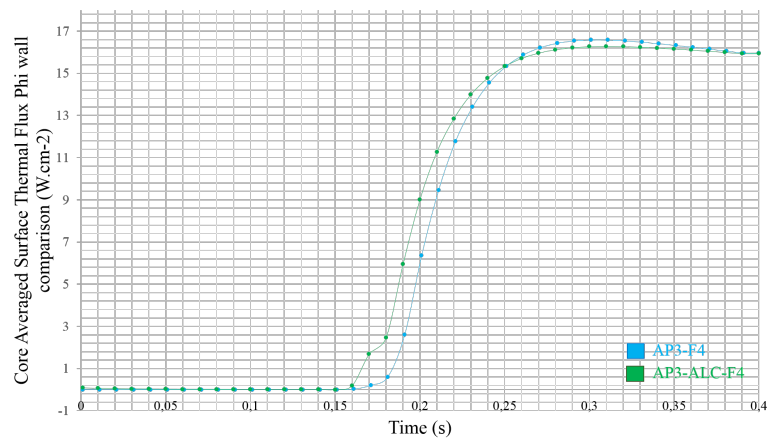


**Figure 20.8.** Core average clad surface thermal flux evolution couplings comparison

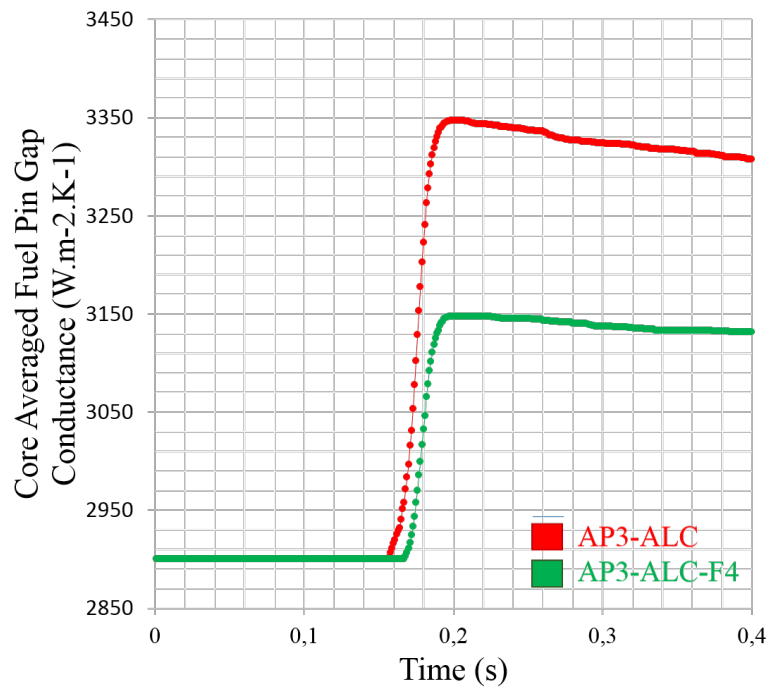


**Figure 20.9.** Core average Hgap evolution couplings comparison

## 20.2 Local Hot Spot parameters coupling comparisons

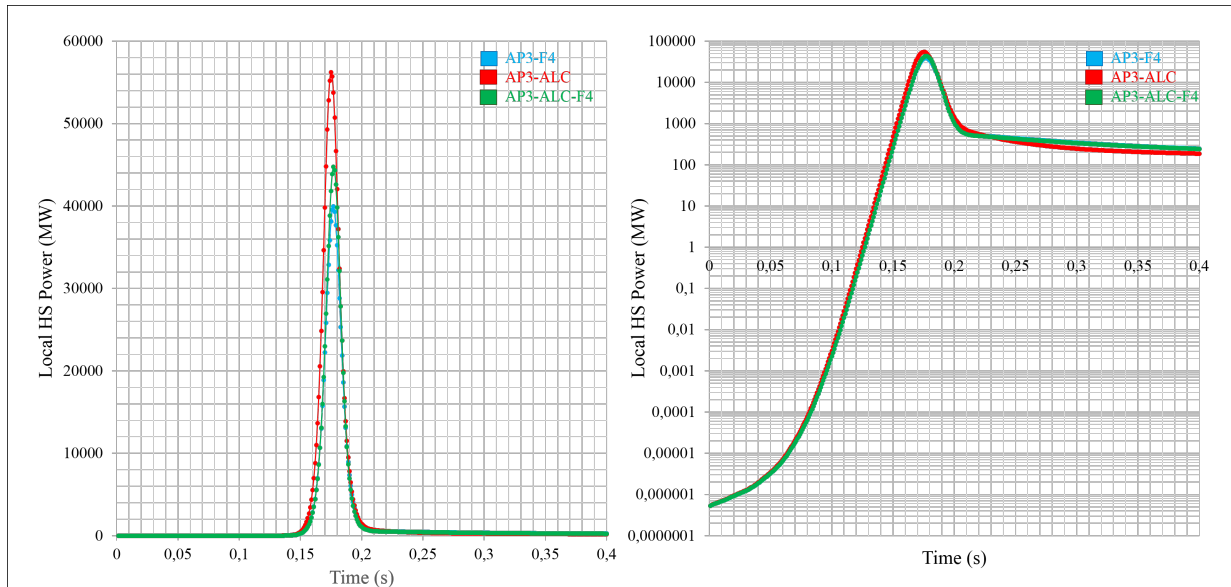


**Figure 20.10.** Local Hot Spot Power evolution couplings comparison



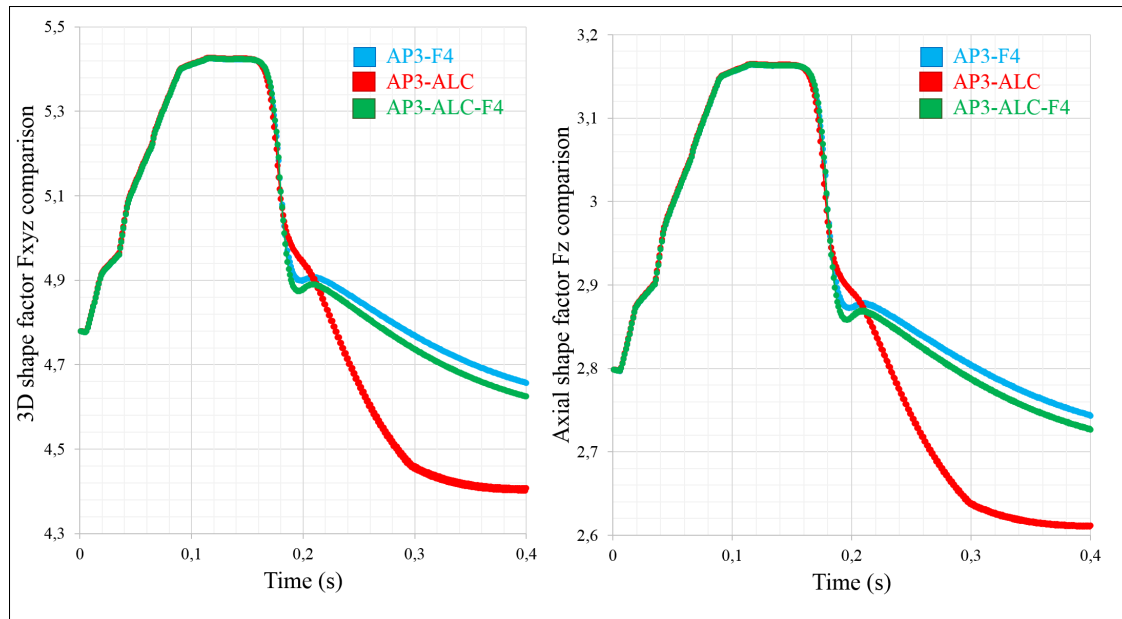


**Figure 20.11.** Fxyz and Fz shape factor evolution couplings comparison

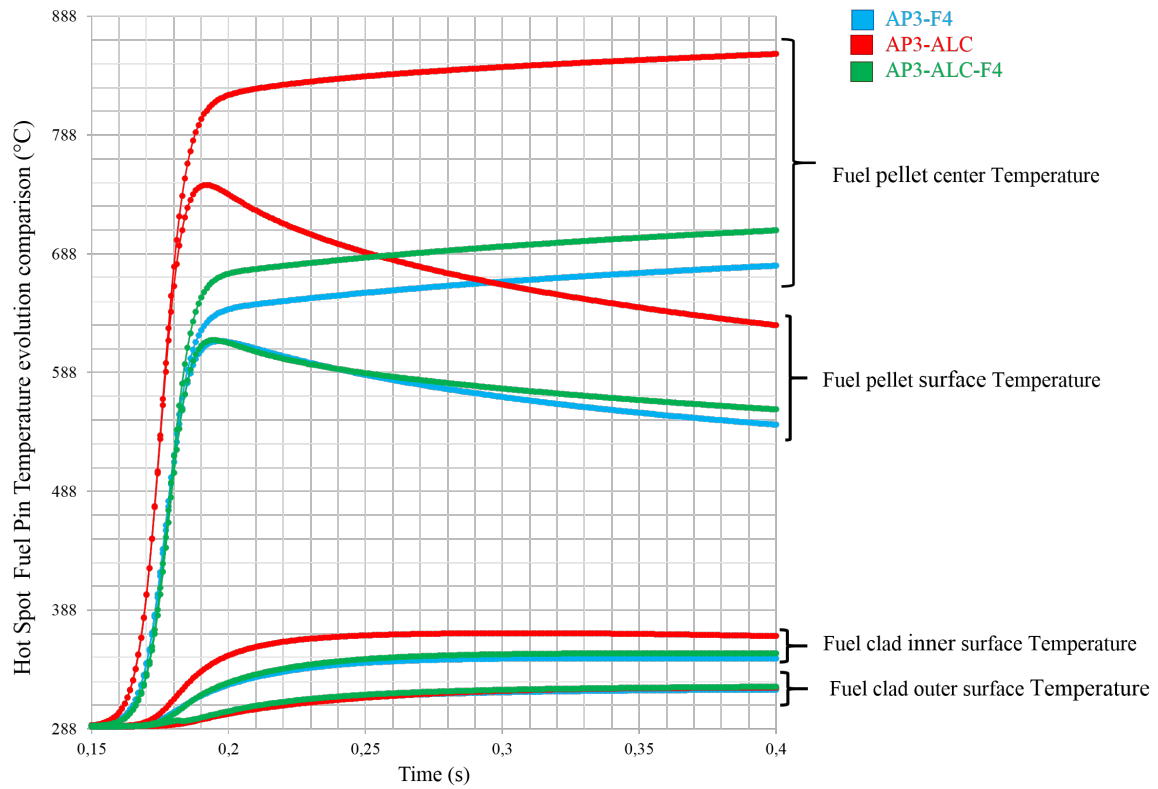


**Figure 20.12.** Local Hot Spot fuel pellet and cladding evolution couplings comparison

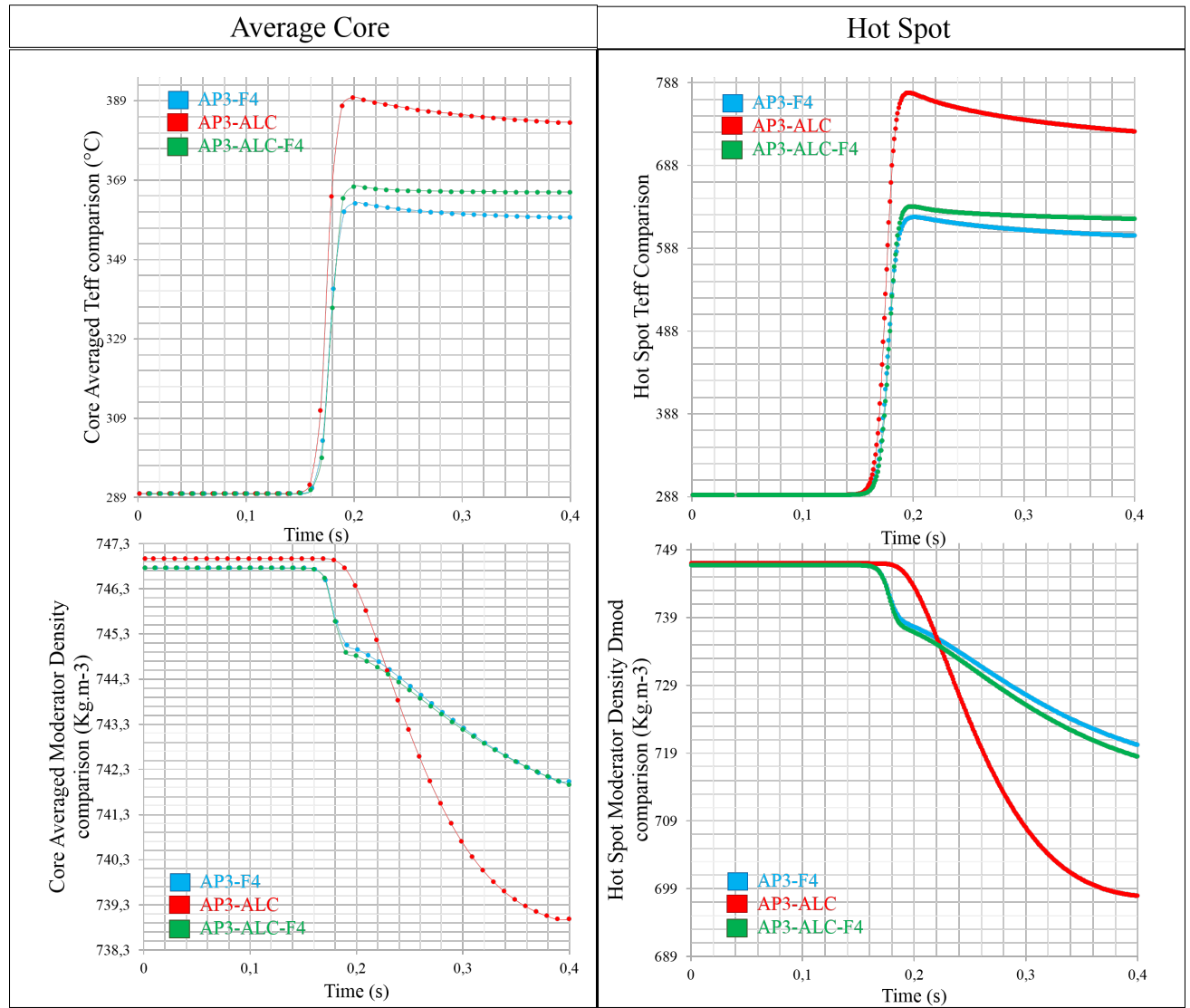


**Figure 20.13.** Global averaged/Local Hot Spot Effective temperature and Moderator density evolution couplings comparison

## 20.2. LOCAL HOT SPOT PARAMETERS COUPLING COMPARISONS

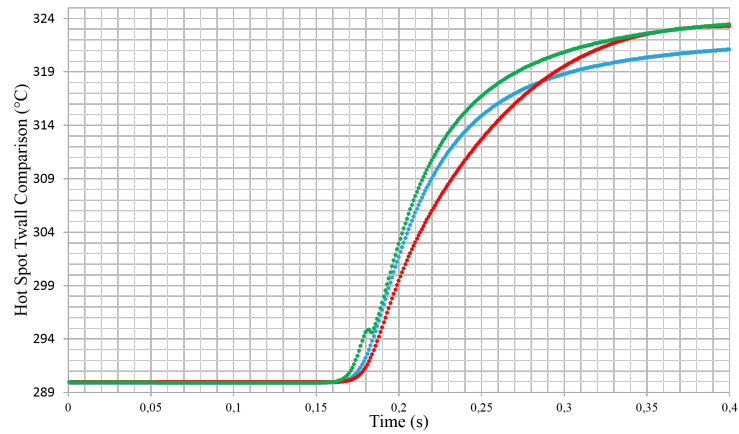


**Figure 20.14.** Local Hot Spot clad surface temperature evolution couplings comparison

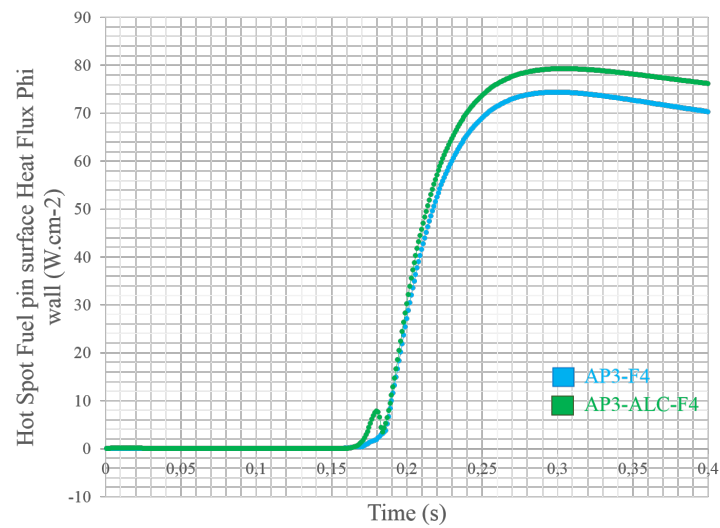


**Figure 20.15.** Local Hot Spot clad surface heat flux evolution couplings comparison

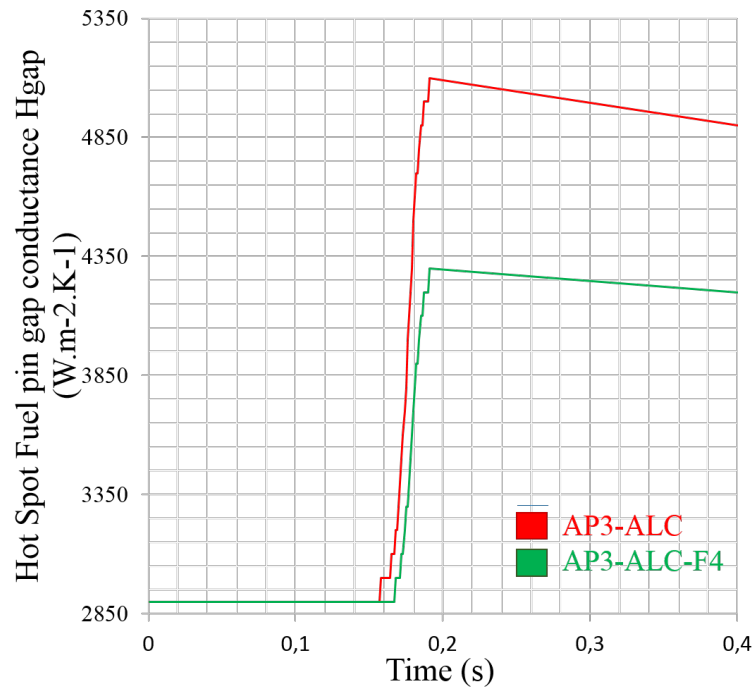


**Figure 20.16.** Local Hot Spot Hgap evolution couplings comparison

## 20.3 Effective temperature formulation comparisons

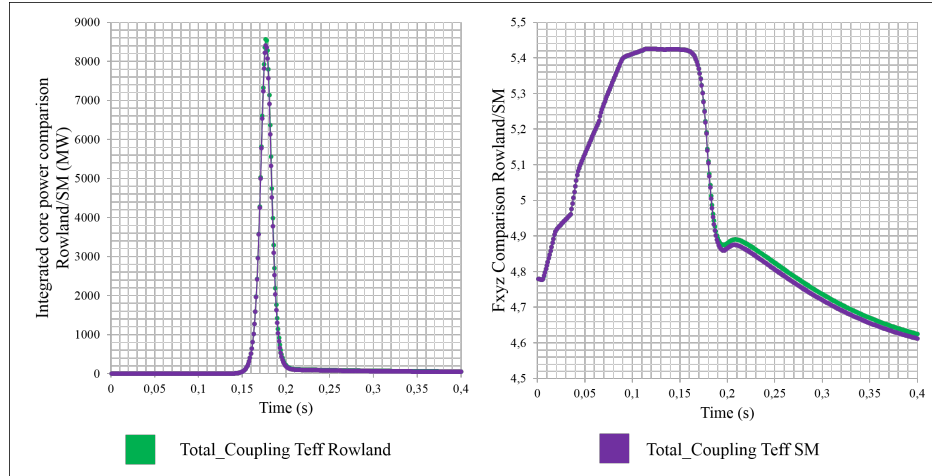


**Figure 20.17.** AP3-FLICA4-ALCYONE (Rowland) and AP3-FLICA4-ALCYONE (C and SM) power pulse comparison

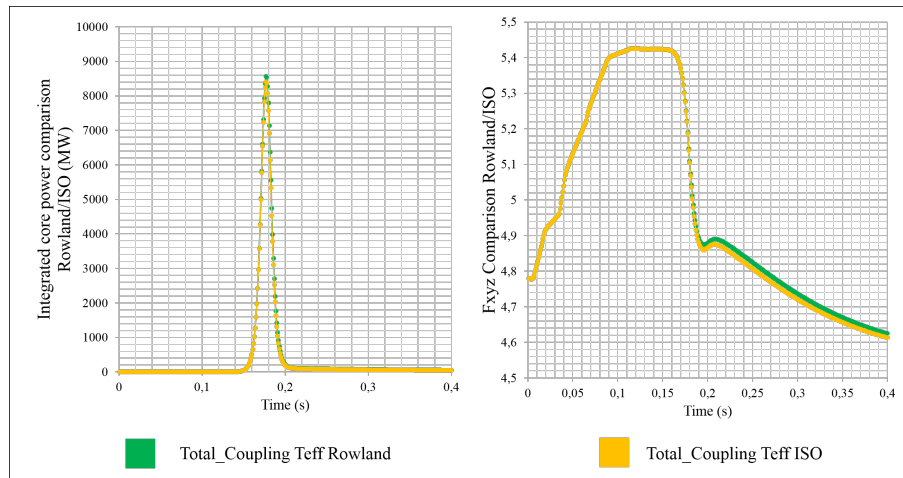


**Figure 20.18.** AP3-FLICA4-ALCYONE (Rowland) and AP3-FLICA4-ALCYONE (Isotopic) power pulse comparison



# Bibliography

- [1] CASL Project :  
<http://www.casl.gov/>,
- [2] CASTEM Project:  
<http://www-cast3m.cea.fr/cast3m/index.jsp> ,
- [3] MOOSE project:  
<http://www4vip.inl.gov/research/moose-applications/>,
- [4] NURES SAFE project:  
<http://www.nuresafe.eu/index.php?art=25>,
- [5] NEAMS project:  
<http://energy.gov/ne/downloads/nuclear-energy-advanced-modelling-and-simulation-neams-program-plan>,
- [6] STRARS project:  
<https://www.psi.ch/stars/research>,
- [7] SALOME project:  
*SALOME*: <http://www.salome-platform.org/>,
- [8] S. ABIDE and F. CARO,  
*Maquette solveur volumes finis multi-physique*,  
CEA Report DEN/DM2S/SFME/MTMS/RT/07-005/B, June 2007.
- [9] G. ALLAIRE,  
*Optimization*,  
Ecole Polytechnique, Cours, 2016.
- [10] S. ANIEL, E. ROYER, P. FERRARESI,  
*Calculation of a Reactivity Initiated Accident with a 3D Cell-by-Cell Method: Application of the SAPHYR System to a Rod Ejection Accident in TMI1*,  
IRSN, CSNI, Barcelone, 2001.



## BIBLIOGRAPHY

---

- [11] S. ANIEL, A. BERGERON, P. FILLION, D. GALLO, F. GAUDRIER, O. GREGOIRE, M. MARTIN, E. RICHEBOIS, E. ROYER, P. SALVATORE and S. ZIMMER,  
*FLICA4: Status of numerical and Physical models and overview of applications*,  
The 11th International Topical Meeting on Nuclear Thermal-Hydraulics (NURETH-11) Popes Palace Conference Center, Avignon, France, October 2-6, 2005,
- [12] K. ATT and R.F. NEUHOLD,  
*Nuclear reactor dynamics*,  
American nuclear society, 1985.
- [13] F. AURIA, A. BOUSBIA-SALAH, A. PETRUZZI and A. DEL NEVO,  
*State of the art in using Best Estimate calculation tool in Nuclear technology*,  
Dipartimento di Ingegneria Meccanica, Nucleare e della Produzione, Università di Pisa, 2006, Pisa, Italy
- [14] M. AVRAMOVA, K. IVANOV, T. KOZLOWSKI, I. PASICHNYK, W. ZWERMANN, K. VELKOV, E. ROYER, A. YAMAJI and J. GULLIFORD,  
*Multi-Physics and multiscale Benchmarking and uncertainty quantification within OECD/NEA framework*,  
Annals of Nuclear Energy 84, 178-196, 2015.
- [15] A. AVVAKUMOV, V. MALOFEEV, and V. SIDOROV,  
*Analysis of Pin-by-Pin Effects for LWR Rod Ejection Accident*,  
Russian Research Centre - Kurchatov Institute, NUREG/IA-0175, U.S. Nuclear Regulatory Commission, March 2000.
- [16] BADCOCK and WILCOX,  
*David Besse 900MW*,  
1970.
- [17] H. BAILLY, D. MENESSIER and C. PRUNIER,  
*Le combustible nucléaire des réacteur à eau sous pression et des réacteur à neutrons rapides, conception et comportement*,  
Commissariat à l'Energie Atomique, 688 pages ,1997.
- [18] BATEMAN,  
*Solution of a system of differential equations occuring in the theory of radioactive transformations*,  
Proceedings, Cambridge Philosophical Society, 15, p. 423-427, 1910.
- [19] F. BARRE, O. MARCHAND, Y. MONERIE and F. PERALES,  
*Advanced modelling of complex material properties - a significant step towards predictive computation of cladding rupture* ,  
EUROSAFE forum, 2010.

- [20] A.M. BAUDRON and J.J. LAUTARD,  
*MINOS: A Simplified Pn Solver for Core Calculation*,  
Nuclear Science and Engineering, 155, pp.250-263, February 2007.
- [21] A.M. BAUDRON and J.J. LAUTARD,  
*Simplified PN Transport core calculation in the APOLLO3 system*,  
International Conference on Mathematics and Computational Methods Applied to  
Nuclear Science and Engineering (M&C 2011), Rio de Janeiro, RJ, Brazil, May 8-  
12, 2011, on CD-ROM, Latin American Section (LAS) / American Nuclear Society  
(ANS), ISBN 978-85-63688-00-2.
- [22] R. BEAUWENS,  
*Théorie des réacteurs nucléaires I*,  
Université libre de Bruxelles, septembre 2004.
- [23] G. BELL and S. GLASSTONE ,  
*Nuclear Reactor Theory*,  
Van Nostrand, NY, 1970.
- [24] R. BENJAMEN and Jr. STRONG,  
*Properties of steam and water interactive desk*,  
Reference NBS/NRC IAPS'84, IMPULES engineering San Francisco, 1984.  
<ftp://ftp.cdrom.com/pub/asme/THERMO>
- [25] A. BERGERON, Ph. FILLION, D. GALLO and E. ROYER,  
*FLICA4 v1.8. Modèles Physiques*, Report, CEA/DEN/DM2S/SFME/LETR/RT/02-  
005/A, 2005.
- [26] A.A. BISHOP, R.O. SANDBERG and L.S. TONG,  
*Forced convection heat transfer at high pressure after the critical heat flux*,  
New York, ASME, 1965.
- [27] G. BOIS,  
*Analyse de schémas de diffusion pour les maillages non-conforme dans FLICA4: im-  
plementation et éléments de validation*,  
Report, DEN/DANS/DM2S/STMF/LATF/NT/13-007/A, 2007.
- [28] I.I. BONDARENKO,  
*Group constants for Nuclear Reactor calculation*,  
Constant Bureau, New York, 1964.
- [29] G. BOUDSOCQ,  
*Fonctions d'état de l'eau pour le code FLICA4*,  
Report DMT, SERMA/LETR/RT/99-2594, 2000

## BIBLIOGRAPHY

---

- [30] J. BRACHET, L. PORTIER, T. FORGERON, J. HIVROZ, D. HAMON, T. GUILBERT, T. BREDEL, P. YVON, J. MARDON, P. JACQUES,  
*Influence of hydrogen content on the  $\alpha/\beta$  phase transformation temperatures and on the thermal-mechanical behavior of Zy4, M4 (ZrSnFeV), and M5TM (ZrNbO) alloys during the first phase of LOCA transient,*  
13th International Symposium on Zirconium in the Nuclear Industry, ASTM STP 1423, pp. 673-701, Annecy, France, 2002.
- [31] J. BROCHARD and al.,  
*Modelling of Pellet Cladding Interaction in PWR Fuel,*  
SMIRT 16, 2001.
- [32] G.B. BRUNA, F. FOUQUET, F. DUBOIS, JC. LE PALLEC, E. RICHEBOIS, E. HOURCADE, C. POINOT SALANON and E. ROYER,  
*HEMERA: a 3D coupled core-plant system for accidental reactor transient simulation,*  
ICAPP 2007 Proceedings, Paper 7205, May 13-18, 2007 NICE, France.
- [33] A. BUCALOSSI,  
*Current use of Best Estimate plus Uncertainty methods on operational procedures addressing normal and emergency conditions,*  
European Commission Joint Research Centre Institute for Energy, 2008.
- [34] R. CAPANNA,  
*Contribution to the development of a calculation scheme into the code APOLLO3 @dedicated to the modelling of an accident scenario of type RIA in a nuclear power plant,*  
Master Thesis, Politecnico Milano, December 2014.
- [35] A. CASENAVE,  
*Etude d'un Schéma de calcul pour la détermination des sections efficaces d'un coeur de REP,*  
PhD Thesis, Ecole Polytechnique de Montréal, 2012.
- [36] D. CARPENTER,  
*Comparison of Pellet-cladding mechanical interaction for Zircaloy and Silicon carbide clad fuel rods in PWR,*  
MIT, Dept. Nuclear Engineering, Lecture, december 2006.
- [37] B. CAZALIS, J. DESQUINES, C. POUSSARD, M. PETIT, Y. MONERIE, C. BERNAUDAT, P. YVON and X. AVERTY,  
*The PROMETRA program : Fuel cladding mechanical behavior under high strain rate.*  
Nuclear Technology 157, 215-229, 2007
- [38] B. CAZALIS and V. GEORGENTHUM,  
*MOX fuel behavior under reactivity initiated accident,*  
Top Fuel - reactor fuel performance, Manchester, United Kingdom, 2-6 sept. 2012

- [39] CEA,  
*La neutronique - Les méthodes de la neutronique*,  
Commissariat à l'Energie Atomique et aux Energies Alternatives (CEA),  
eDEN/DM2S/CEA,2013.  
<http://www.cea.fr/energie/la-neutronique>.
- [40] C. CHABERT and A. SANTAMARINA,  
*Calcul du coefficient Doppler pour les réacteur à eau*,  
Report, CEA/DEN/CAD/DER/SPRC.LEPH/99-205, 1999.
- [41] S. CHAUVET,  
*Méthode multi-échelle pour la résolution des équations de la cinétique neutronique* ,  
Thèse de Doctorat, Université de Nantes, tel-00348435, 2008.
- [42] B. CHANARON and Al.,  
*Advanced multi-physics simulation for reactor safety in the framework of the NURE-SAFE project*,  
Annals of Nuclear Energy 84, 166-177, 2015.
- [43] P. CHEMIN,  
*Approximation des tables de l'eau*,  
Report, LMC-IMAG, DRT, 2003.
- [44] S. CHEMIN,  
*D11.13 : New FLICA version for N/T-M/T-H coupling*  
*D11.17 : New Salome interface for FLICACRONOS coupling and data exchange with SCANAIR*,  
NURESAFE, D11.13, version 1, Issued on 10/09/2014.
- [45] S. CHEMIN,  
*D11.11 : Specifications for SCANAIR Integration*  
*D11.12 : Specifications CEA coupling in-core N/T-M/T-H*,  
NURESAFE Collaborative Project, D11.11 and D11.12, version 2, Issued on 28/07/2014.
- [46] D. CHISHOLM,  
*Friction during the two flow of Two-Phase Mixtures in Smooth tubes and channels*,  
NEL Report 529, National Engineering Laboratory, Department of trade and Industry, 1972.
- [47] H. CHU, S. WU, K. CHIEN, R. KUO,  
*Effect of radial hydrides on the axial and hoop mechanical properties of Zircaloy-4 cladding*.  
Journal of Nuclear Materials 362, 93-103. 2007

## BIBLIOGRAPHY

---

- [48] S. CLERC and Ph. FILLION,  
*FLICA4 v1.8. Méthode numérique*,  
Report, CEA/SFME/LETR/RT/01-020/A, 2002.
- [49] CNSC (Canadian Nuclear Safety Commission),  
*Guidance on Safety Analysis for Nuclear Power Plants*,  
GD-310, Minister of Public Works and Government Services Canada 2012, Catalogue  
number: CC172-85/2012E-PDF, ISBN 978-1-100-20451-2.
- [50] J.G. COLLIER, J.A. WARD, K.T. CLAXTON and D. CHISLON,  
*Heat transfer and fluid flow service*,  
Technical report AERE-R6454, AERE 1972.
- [51] J.G. COLLIER and J.R. THOME,  
*Convective boiling and condensation*,  
Third edn. Oxford: Clarendon Press, 1994.
- [52] E. CONTESTIU,  
*Description of creep-plasticity interaction with non-unified constitutive equation*,  
Nuclear engineering design, 116(3), 265-80, sept 1989.
- [53] D.E. CULLEN ,  
*Application of the probability table method to multigroup calculations of neutron trans-  
port*,  
Nuclear Science and Engineering, 55, 387-400, 1974.
- [54] D.E. CULLEN and G.C. POMRANING,  
*The multiband method in radiative transfer calculations*,  
Journal of Quantum Spectroscopie Radiative Transfer, 24, 97-117, 1980.
- [55] A. DALL OSSO and D. TOMATIS,  
*Section Efficaces à AREVA: Présent et passé* ,  
Séminaire APOLLO3, EDF Clamart, 11 septembre 2012.
- [56] R. DAUM, S. MAJUMBDAR, W. LIU, M. BILLONE,  
*Radial hydride embrittlement of high burnup Zircaloy-4 fuel cladding*,  
Journal of Nuclear Science and Technology 43(9), 1054-1067, (2006).
- [57] R. DAUTRAY and J.L. LIONS,  
*Analyse mathématique et calcul numérique pour les sciences et les techniques*,  
Tome 1: Modèles Physique, INSTN-CEA, MASSON, 1987.
- [58] C. DECURNEX,  
*Evaluation des paramètres cinétiques des réacteurs nucléaires, application aux com-  
bustibles mixtes*,  
Thèse de doctorat de l'Ecole Polytechnique Fédérale de Lausanne, 1994.

- [59] J. DESQUINES and J. FLEUROT,  
*The fracture and spallation of zirconia layers in high burnup PWR fuel claddings submitted to RIA transients.*  
18th International Conference on Structural Mechanics in Reactor Technology, C03/1,  
p. 444-453, Beijing, China.
- [60] D.J. DIAMOND, C.Y. YANG, and A.L. ARONSON,  
*Estimating the Uncertainty in Reactivity Accident Neutronic Calculations,*  
Proceedings of the Twenty-Sixth Water Reactor Safety Information Meeting, October  
1998, NUREG/CP-0166, U.S. Nuclear Regulatory Commission, March 1999.
- [61] D.J. DIAMOND and al.,  
*Intercomparison of Results for a PWR Rod Ejection Accident,*  
Proceedings of the Twenty-Seventh Water Reactor Safety Information Meeting, Octo-  
ber 1999, NUREG/CP-0169, U.S. Nuclear Regulatory Commission, March 2000, and  
Nuclear Engineering and Design, 208, 2001
- [62] D.J. DIAMOND, B.P. BROMLEY and A.L. ARONSON,  
*Studies of the Rod Ejection Accident in PWR,*  
Technical Report W-6382 1/22/02 Brookhaven National Laboratory, January 22, 2002.
- [63] T.J. DOWNAR,  
*Coupled Codes for Multi-Physics Nuclear Reactor Simulation,*  
Thesis, Purdue University, 2006.
- [64] DOWNAR,  
*PWR MOX/UO<sub>2</sub> core transient,*  
NEA/NSC/DOC(2006)20, December 2006.
- [65] J.J. DUDERSTADT and L.J. HAMILTON,  
*Nuclear Reactor Analysis,*  
Department of Nuclear Engineering, The University of Michigan, JOHN WILEY and  
SONS, inc. New York/London/sydney/Toronto.
- [66] K. DUGAN,  
*Cross Section Homogenization for Nuclear Reactor Transient Calculations using the  
APOLLO3 Multiphysics Framework,*  
PhD Thesis, Paris Saclay University, October 2016.
- [67] EDF,  
*Réacteur - Physique du coeur,*  
EDF, Documentation technique, chapitre 4, 2006.
- [68] EDF,  
*Centrale Nucléaire de Paluel - Rapport préliminaire de sureté,*  
Report EDF, 2005.

## BIBLIOGRAPHY

---

- [69] EDF and AREVA NP ,  
*FUNDAMENTAL SAFETY OVERVIEW*,  
Technical Report, Volume 2: Design and Safety, Chapter P: Reference operating condition studies (PCC), 2007.
- [70] M.S. ELLIS, J. WATSON and K. IVANOV,  
*Progress in the development of an implicit steady state solution in the coupled code TRACE/PARCS*,  
Annals of Nuclear Energy 66, 1-12, 2013.
- [71] R. EYMARD, T. GALLOUET and R. HERBIN,  
*The finite volume method*,  
Handbook for Numerical Analysis, Ph. Ciarlet, J.L. Loins eds, North Holland, 715-1022, 2000.
- [72] I. FAILLE,  
*A control volume method to solve an elliptic equation on a two-dimensional irregular meshing*,  
Computational Methods Applied Mechanical Engineering, 100, 275-290, 1992.
- [73] R.M. FERENCZ,  
*Nuclear Energy Advanced modelling and Simulation (NEAMS) Structural Mechanics Module Development Plan*,  
Methods Development Group, October 14, 2013.
- [74] Ph. FILLION, D. CARUGE and S. CLERC,  
*FLICA4: an advanced code for two-phase flow parallel computing*,  
NURETH 9, San Francisco, 3-8 October 1999.
- [75] P. FILLION, A. CHANOINE, S. DELLACHERIE and A. KUMBARO,  
*FLICA-OVAP: A new platform for core thermal-hydraulic studies*,  
Nuclear Engineering and Design, volume 241, p. 4348-4358, 2011.
- [76] Ph. FILLION, A. BERGERON, D. GALLO, O. GREGOIRE, E. RICHEBOIS, E. ROYER and S. ZIMMER,  
*FLICA4: Version 1.11.2 PUB, User guide, Reference manual of modules and procedures*,  
CEA Report, 2013.
- [77] M.C. FIORINA, M. AU FIERO, S. PELLONI, K. MIKITYUK,  
*A time dependent solver for coupled neutron transport thermal-mechanics calculation and simulation of a GODIVA prompt-critical Burst*,  
Proc. Int. Conf. ICONE22, Prague, Czech, Jul 07-11 2014.

- [78] K. FORSTER and R. GREIF,  
*Heat transfer to a boiling liquid ; mechanism and correlations*,  
Progress Report, US, 1958.
- [79] FRANKLIN  
*LWR core transient*,  
NEA/BEN Benchmark, 2001.
- [80] J. FRIEDEL,  
*Les dislocations*,  
Paris, Gauthier-Villars, 1956
- [81] L. FREIDEL,  
*Improved friction pressure drop correlation for horizontal and vertical two phase pipe flow*,  
Proceedings, European Two Phase Flow Group Meeting, Ispra, June 5-8th, 1979.
- [82] T. FUKETA, F. NAGASE, K. ISHIJIMA and T. FUJISHIRO,  
*NSRR/RIA experiments with high burnup PWR fuels*.  
Nuclear Safety 37(4), 328-342, 1996.
- [83] T. FUKETA, H. SASAJIMA, Y. MORI and K. ISHIJIMA,  
*Fuel failure and fission gas release in high burnup PWR fuels under RIA conditions*.  
Journal of Nuclear Materials 248, 249-256, 1996.
- [84] T. FUKETA,  
*High burn-up BWR fuel responds to reactivity transients and a comparison with PWR fuel response* ,  
Proc. of the 24<sup>th</sup> NSRR technical review meeting, November 13-14, 2000, Tokyo JAPAN.
- [85] FUKETA, NAKAMURA, SASAJIMA, NAGASE, UETSUKA, KIKUCHI and ABE,  
*Behavior of PWR and BWR fuel during Reactivity-initiated accident conditions* ,  
Proc. ANS topical meeting on light water reactor fuel performance, Park City, Utah, April 10-13, 2000 .
- [86] T. FUKETA, H. SASAJIMA and T. SUGIYAMA,  
*Behavior of high burnup PWR fuels with low tin Zircaloy4 cladding under reactivity initiated accident conditions*.  
Nuclear Technology 133(1), 50-62, 2001.
- [87] T. FUKETA, H. SASAJIMA, T. SUGIYAMA,  
NAKAMURA and NAGASE,  
*Effect of pellet expansion and cladding hydrides on PCMI failure of high burn-up LWR fuel during reactivity transients*,  
Nuclear safety research conference, october 21, 2003, Washington DC, USA.



## BIBLIOGRAPHY

---

- [88] Ph. GARCIA, C. STRUZIŁ, and M. AGARD,  
*The Effect of Fission Gas Swelling on Cladding Strains During Power Ramp Tests*,  
Proc. Conf. Fuel Chemistry and Pellet Cladding Interaction Related to High Burn-Up  
Fuel, Nykoping, Sweden, September 7-10, IAEA TECDOC 1179, International Atomic  
Energy Agency, 1998.
- [89] A.M. GARDE,  
*Effects of Irradiation and Hydriding on the Mechanical Properties of Zircaloy-4 at  
High Fluences*  
Zirconium in the Nuclear Industry: Eighth International Symposium, ASTM STP  
1023, L. F. P. Van Swam and C. M. Eucken Eds., American Society for Testing and  
Materials, Philadelphia, p. 548-569, 1989.
- [90] A.M. GARDE, G. P. SMITH and R.C. PIREK,  
*Effects of Hydride Precipitate Localization and Neutron Fluence on the Ductility of  
Irradiated Zircaloy4*,  
Zirconium in the Nuclear Industry: Eleventh International Symposium, ASTM STP  
1295, E. R. Bradley and G. P. Sabol Eds., American Society for Testing and Materials,  
p. 407-430, 1996.
- [91] J.M. GATT, J.C. MENARD,  
*Overall viscoplastic behaviour of uranium dioxide*,  
Transactions, SMiRT 19, Toronto, Paper C04-3 August 2007.
- [92] V. GEORGENTHUM, J. DESQUINE and V. BESSIRON,  
*Influence of outer zirconia transient cracking and spalling on thermomechanical be-  
haviour of high burnup fuel rod submitted to RIA*.  
Journal of Nuclear Science and Technology 43(9), p. 1089-1096, 2006.
- [93] S. GLASSTONE and A. SESONSKE,  
*Nuclear Reactor Engineering*,  
Chapman and Hall Inc, 1981.
- [94] F.N. GLEICHER, B. SPENCER, S. NOVASCONE, R. WILLIAMSON, R.C. MAR-  
TINEAU, M. ROSE and T.J. DOWNAR,  
*Coupling the Core Analysis Program DeCART to the Fuel Performance Application  
BISON*,  
M and C, May 2013.
- [95] H. GOLFIER, R. LENAIN, C. CALVIN, J-J. LAUTARD, A-M. BAUDRON, Ph.  
FOUGERAS, Ph. MAGAT, E. MARTINOLLI and Y. DUTHEILLET,  
*APOLLO3: a common project of CEA, AREVA and EDF for the development of a  
new deterministic multi-purpose code for core physics analysis*,  
International Conference on Mathematics, Computational Methods and Reactor  
Physics, Saratoga Springs, New York, May 3-7, (2009).

- [96] R. GODESAR,  
*Untersuchung des Einflusses des Warme Hulle auf die sicherheitstechnische Auslegung van stabformigen Brennstaben fur schnelle Brutreaktoren*,  
Dissetation TH Aachen, 1972.
- [97] S.K. GODUNOV,  
*Finite difference method for numerical computation of discontinous solution of the equations of fluid dynamics (translated from Russian)*,  
Matematicheskii Sbornik, p. 47-271, 1959.
- [98] D.C. GROENEVELD and al. ,  
*The 1995 look-up table for critical heat flux in tubes*,  
Nuclear Engineering and Design, p. 163, 1996.
- [99] C.R. HANN and al.,  
*Grapcom Thermal 1: A computer program for calculating the Gap conductance in oxide of fuel pins*,  
BNWL-1778, 1973.
- [100] J-M. HAUSONNE, J.L. BARTON, P. BOWEN and C.P. CARRY,  
*Traité des matériaux numéro 16: Céramiques et Verres*,  
Presses Polytechniques et Universitaires Romande, 1995.
- [101] A. HEBERT,  
*Applied Reactor Physics*,  
Presse internationales Polytechnique, ISBN: 9782553014369, 424 pages, 2009.
- [102] A. HEBERT,  
*Physique statistique des Réacteurs*,  
Ecole Polytechnique de Montréal, cours - ENE6101, 2014.
- [103] A. HEBERT,  
*Neutronique*,  
Ecole Polytechnique de Montréal, 1983.
- [104] M. HERMAN,  
*ENDF-6 Data formats and procedures for the evaluated nuclear data file*,  
Cross Section Evaluation Working Group, 2005.
- [105] D.L. HETRICK,  
*Dynamics of Nuclear Reactors*,  
University of Chicago Press, Chicago/London, 1971.
- [106] D.L. HETRICK,  
*Dynamic of nuclear reactor*,  
Amercian Nuclear society, La Grange Park, Illinois, USA, chap 5, p. 164-170, 1993.

## BIBLIOGRAPHY

---

- [107] M. HURSIN, T.J. DOWNAR and B. KOCHUNAS,  
*Analysis of the Core Power Response During a PWR rod ejection transient using the Parcs Nodal Code and the DeCart MOC Code*,  
Nuclear Science and Engineering, 170, p. 151-167, 2012.
- [108] M. HURSIN, T.J. DOWNAR, R. MONTGOMERY,  
*Impact of improved neutronic methodology on the cladding response during a PWR reactivity initiated accident*,  
Nuclear Engineering and Design 262, p. 180-188, 2013.
- [109] IAEA Safety Standards Series,  
*Safety of Nuclear Power Plants: Design*,  
No. NS-R-1, VIENNA, 2000.
- [110] IAEA Safety Reports Series,  
*Accident analysis for nuclear power plants with pressurized water reactors*,  
Safety reports series No.30, IAEA, 2003.
- [111] IAEA Safety Reports Series,  
*Best Estimate Safety Analysis for Nuclear Power Plants : Uncertainty Evaluation*,  
Safety Reports Series No. 52.
- [112] IAEA Safety Standards Series,  
*Deterministic Safety Analysis for Nuclear Power Plants for protecting people and the environment*,  
Safety Standards, No.SSG 2.
- [113] M. ISHII,  
*One-dimensional drift-flux model and constitutive equations for relative motion between phases in various two-phase flow*,  
Technical Report ANL-77-47. Argonne National Laboratory, 1977.
- [114] K. IVANOV and M. AVRAMOVA,  
*Verification and Validation analysis in multiphysics modelling for nuclear reactor design and safety*,  
International Conference on Mathematics, Computational Methods and Reactor Physics (M and C 2009) Saratoga Springs, New York, May 3-7, 2009, on CD-ROM, American Nuclear Society, LaGrange Park, IL, 2009.
- [115] A. IVANOV, V. SANCHEZ, R. STIEGLITZ and K. IVANOV,  
*Internal multi-scale multi-physics coupled system for high fidelity simulation of light water reactors*,  
Annals of Nuclear Energy 66, p. 104-112, 2014.
- [116] D. JAMET,  
*Analyse du couplage entre la thermique du solide et la thermohydraulique*,

- Report technique CEA - DEN, DEN/DANS/DM2S/STMF/LMEC/RT/12-013/A, 2012 .
- [117] W.H. JENS and P.A. LOTTES,  
*Analysis of heat transfer burnout, pressure drop and density data for high pressure water,*  
Tech. rept. ANL-4627. Argonne National Laboratory, 1951.
- [118] L.O. JERNKVIST, R. Ali and P.R. MASSIH,  
*A strain-based clad failure criterion for the RIA in light water reactors*  
SKI Report 32, August 2004.
- [119] L.O. JERNKVIST, R. Ali and P.R. MASSIH,  
*Assessment of fuel rod failure Thresholds for reactivity initiated accidents,*  
SKI Report 32, November 2004.
- [120] J. JIMENEZ, M. AVRAMOVA, D. CUERVO, K. IVANOV,  
*Comparative analysis of neutronics/thermal-hydraulics multi-scale coupling for LWR analysis,*  
International Conference on the Physics of Reactors "Nuclear Power: A Sustainable Resource", Casino-Kursaal Conference Center, Interlaken, Switzerland, September 14 - 19, 2008.
- [121] B.F. KAMMENZIND, D. G. FRANKLIN, H. R. PETERS and W.J. DUFFIN,  
*Hydrogen Pickup and redistribution in Alpha-annealed Zircaloy-4,*  
11th International Symposium on Zirconium in the Nuclear Industry, ASTM STP 1295. Garmisch-Partenkirchen, Germany, 1996.
- [122] J. KEARNS,  
*Terminal solubility and partitioning of hydrogen in the alpha phase of zirconium, Zircaloy 2 and Zircaloy 4,*  
Journal of Nuclear Materials 22, p. 292-303, 1967.
- [123] G.R. KEEPING,  
*Physics of nuclear kinetics,*  
Addison-Wesley Pub. Co., 1965 - 435 pages 2013.
- [124] E.H. KENNARD,  
*Kinetic theory of Gases,*  
McCraw-Hill, New York, 314, 1938.
- [125] N. KERKAR and P. PAULIN,  
*Exploitation des coeurs REP,*  
Collection du Génie Atomique, INSTN, 2008.

## BIBLIOGRAPHY

---

- [126] KLIEM S., MITTAG S., GOMMLICH A. and APANASEVICH P.,  
*D3.1.2.2: Definition of a PWR boron dilution benchmark*,  
NUclear Reactor Integrated Simulation Project of the 7th FP EURATOM, 2011.
- [127] . J. KOCLAS, M.T. SISSAOUI and A. HEBERT,  
*Solution of improved and generalized quasistatic methods using an analytic calculation or a semi-implicit scheme to compute the precursor equations*,  
Ann. Nucl. Energy 23, Number 11, 1995
- [128] A.J. KONING and al.,  
*Status of the JEFF Nuclear Data Library*,  
Proceeding of the international conference on Nuclear Data for science and technology,  
Nice, France, 2007.
- [129] KOZOLWOSKI T. and DOWNAR T.,  
*PWR MOX/UO<sub>2</sub> core transient benchmark: final report*,  
NEA/NSC/DOC (2006) 20, Purdue University, January 2007.
- [130] D.D LANNING and C.R. HANN,  
*Review of methods Applicable to the calculation of gap conductance in Zircaloy-clad UO<sub>2</sub> fuel Rods*,  
BNWL-1894, 1975.
- [131] K. LASSMAN,  
*Zum Warmedurchgang im Bereich zwischen Hulle und Brennstoff eines Brennstab*,  
Warme und Stoffubertragung 12, 185-202, 1979.
- [132] K. LASSMAN and F. HOHLEFELD,  
*Uberarbeitung des zwischen Brennstoff und Hulle*,  
EUR 10756 DE, 1986.
- [133] K. LASSMAN and F. HOHLEFELD,  
*The revised URGAP model to describe the gap conductance between fuel and cladding*  
Nuclear Engineering and Design 103, 215-221, North-Land, Amsterdam, 1987.
- [134] J.J. LAUTARD, D. SCHNEIDER and A.M. BAUDRON,  
*Mixed Dual Methods for Neutronic Reactor Core Calculation in the CRONOS System*,  
Proc. ANS Topical Mtg., Mathematics and Computation, Reactor Physics and Environmental Analysis in Nuclear Applications, 1, Madrid, Spain, 1999.
- [135] J.J. LAUTARD and al.,  
*A 3D nodal mixed dual method for nuclear reactor kinetics with improved quasistatic model and a semi-implicit scheme to solve the precursor equations*,  
Annals of Nuclear Energy 28(8), 805-824, May 2001.

- [136] F. LEMOINE,  
*High burnup fuel behavior related to fission gas effects under reactivity initiated accidents (RIA) conditions,*  
Journal of Nuclear Materials 248, p. 238-248, 1997.
- [137] F. LEMOINE and M. BALOURDET,  
*.RIA related analytical studies and separate effect tests,*  
International Topical Meeting on Light Water Reactor Fuel Performance, Portland, Oregon, 1997.
- [138] F. LEMOINE, D. BERNARD and E. FEDERICI,  
*Validation assessment of neutron calculations for radial and azimuthal distributions of actinides and fission products in PWR rods,*  
Water Reactor Fuel Performance Meeting Chengdu, China, Sept. 11-14, 2011.
- [139] R. LENAIN,  
*Modélisation axiale d'un coeur de réacteur à eau pressurisée pour l'étude d'un accident de réactivité : éjection d'une barre de contrôle,*  
Report /DEMT 84/169, SERMA/LENR/84/613.
- [140] R. LENAIN,  
*Amélioration des méthodes de calcul de  $c\lambda$  de réacteurs nucléaires dans APOLLO3 : décomposition de domaine en théorie du transport pour des géométries 2D et 3D avec une accélération non linéaire par la diffusion,*  
Université Paris 11, 2015.
- [141] J.C. LE PALLEC,  
*Modélisation réaliste d'un accident de réactivité dans les REP et analyse d'incertitudes,*  
Mémoire de thèse, Institut National Polytechnique de Grenoble, 2002.
- [142] J.C. LE PALLEC,  
*Analyse d'un accident de réactivité induit par éjection d'une grappe sur un coeur REP1300 MWe chargé en combustible CORAIL,*  
Report, CEA/DEN/DM2S/SERMA/LCA/RT/03-3349/A, 2004.
- [143] J.C. LE PALLEC, C. POINOT SALANON, N. CROUZET and S. ZIMMER,  
*HEMERA V2: An evolutionary tool for PWR multithysics analysis in SALOME platform,*  
Proceedings of ICAPP 2011 Nice, France, May 2-5, 2011, Paper 11092.
- [144] J.C. LE PALLEC and B. MICHEL,  
*Spécification du couplage entre APOLLO3 et ALCYONE pour le traitement d'un scénario de type RIA,*  
Report, CEA/DEN/DM2S/SERMA/LLPR/RT/12-5453/A, 2012.

## BIBLIOGRAPHY

---

- [145] J.C. LE PALLEC, K. MER NKONGA and N. CROUZET,  
*Neutronics/Fuel Thermomechanics Coupling in the Framework of a REA (Rod Ejection Accident) Transient Scenario Calculation*,  
PHYSOR 2016, Sun Valley, Idaho, USA, May 1-5, 2016
- [146] P. LESAINT and P.A. RAVIART,  
*On a Finite Element Method for Solving the Neutron Transport Equation*,  
Mathematical Aspects of Finite Elements in Partial Differential Equations, p. 89, C. A. DE BOOR, Ed., Academic Press, New York, 1974.
- [147] M. LE SAUX,  
*Comportement et rupture de gaines en Zircaloy-4 détendu vierges hydrurées ou irradiées en situation accidentelle de type RIA*,  
Report, CEA-R-6248, PhD Thesis, Ecole des Mines de Paris, 2008.
- [148] A.L. LINDSAY and L.A. BROMLEY,  
*Thermal conductivity of gas mixtures*,  
Ind. and Eng. chem. 42, 1508-1511, 1950.
- [149] O. LITAIZE and O. SEROT,  
*Investigation of phenomenological models for the monte carlo simulation of the prompt fission neutron and gamma emission*,  
Physical review, C82, 054616, 2010.
- [150] S. LOUBIERE, R. SANCHEZ, M. COSTE, A. HEBERT, Z. STANKOVSKI, C. VAN DER GUCHT and I. ZMIJAREVIC,  
*APOLLO2 Twelve Years Later*,  
Proc. Int. Conf. on Math. and Computations, Reactor Physics and Environmental Analysis in Nucl. Applications, Madrid, Spain, p. 1298, Sept. 1999.
- [151] P. MAGAT,  
*Analyse des techniques d'homogénéisation spatiale et énergétique dans la résolution de l'équation du transport des neutrons dans les réacteurs nucléaires*,  
Université d' Aix-Marseille I, 30 avril 1997.
- [152] J. W. MAGEDANZ and M. N. AVRAMOVA,  
*High-Fidelity Multi-Physics calculation for light water reactors using coupled CFT/TORT-TD:FRAPTRAN*,  
Physor 2014, Kyoto, Japan, sept. 28 - oct. 3, 2014.
- [153] J. W. MAGEDANZ and M. N. AVRAMOVA and Al.,  
*High-fidelity multi-physics system TORT-TD/CTF/FRAPTRAN for light water reactor analysis*,  
Annals of Nuclear Energy 84, 234 - 243, 2015.

- [154] V.S. MAHADEVAN, J.C. RAGUSA and C. MOUSSEAU,  
*A verification exercise in multiphysics simulations for coupled reactor physics calculations,*  
Progress in Nuclear Energy 55, 2012.
- [155] V. MARELLE, V. BOUINEAU, A. BOULORE, C. FILLAUX, P. GOLDBRONN,  
T. HELFER, G. JOMARD, J. JULIEN, R. MASSON, B. MICHEL, L. NOIROT and  
I. RAMIERE,  
*ALCYONE V1.4: Notice de Présentation,*  
Report, CEA/DEN/DEC/SESC/LSC NT 13-034 , décembre 2013.
- [156] MATPRO (NUREC),  
*MATPRO - VERSION 11, A HANDBOOK OF MATERIALS PROPERTIES FOR  
USE IN THE ANALYSIS OF LIGHT WATER REACTOR FUEL ROD BEHAVIOR*  
,  
NUREC/CR-0497, TREE-1280, US. Nuclear Regulatory Commission, 1979.
- [157] Z.R. MARTINSON and R. L. JOHNSON,  
*Transient Irradiation of 1/4-Inch OD Zircaloy-2 Clad Oxide Fuel Rods to 590 cal/g  
UO<sub>2</sub>,*  
IDO-ITR-102, Phillips Petroleum Company, Atomic Energy Division, November 1968.
- [158] A. McMINN, E.C. DARBY and J.S. SCHOFIELD,  
*The Terminal Solid Solubility of Hydrogen in Zirconium Al-loys,*  
Proceedings of the 12th International Symposium of the Zirconium in the Nuclear  
Industry, ASTM STP 1354, pp. 173-195, 2000.
- [159] R. MEYER, R. McCARDELL, H. CHUNG, D. DIAMOND and H. SCOTT,  
*A regulatory assessment of test data for reactivity initiated accidents,*  
Nuclear Safety 37, October-December 1996.
- [160] B. MICHEL,  
*PCMI Assessment Using 3D Modelling,*  
Trans. SMIRT 18, 2005.
- [161] B. MICHEL,  
*Modelisation 3D de l'interface Pastille-Gaine (IPG): Location de la rupture et dif-  
férenciation des combustibles UO<sub>2</sub> et UO<sub>2</sub> dopé chrome,*  
CEA/DEN/CAD/DEC/SESC/LSC NT 06-005, 2006.
- [162] B. MICHEL,  
*Introduction dans ALCYONE du modèle couplé fissuration-fluage Gatt Monerie,*  
Report, CEA/DEN/CAD/DEC/SESC/LSC NT 06-052, 2007.



## BIBLIOGRAPHY

---

- [163] B. MICHEL and J. SERCOMBE, G. THOUVENIN and R. CHATELET,  
*3D fuel cracking modelling in pellet cladding mechanical interaction*,  
Engineering Fracture Mechanics, 75, 3581 - 3598, 2008.
- [164] B. MICHEL, I. RAMIERE, J. SERCOMBE, M. AGARD and Ch. BONHOMME,  
*PLEIADE: Multi concept nuclear fuel modelling*,  
Présentation ECCM 2010, CEA Cadarache, 2010.
- [165] B. MICHEL, C. NONON, J. SERCOMBE, F. MICHEL and V. MAREL,  
*Simulation of pellet-Cladding interaction with the PLEIADE fuel performance software environment*,  
Nuclear Technology, volume 182, pages 124, number 2, 2013.
- [166] R.W. MILLER and W. G. LUSSIE,  
*The Response of UO<sub>2</sub> Fuel Rods to Power Bursts, 5/16-Inch OD, Pellet and Powder Fuel, Zircaloy Clad*,  
IDO-ITR-103, Phillips Petroleum Company, Atomic Energy Division, January 1969.
- [167] A. MOAL,  
*D11.114 : Report on SCANAIR-FLICA (CRONOS)*,  
NURESAFE, D11.114 : version 0, Issued on 18/11/2014.
- [168] J.Y. MOLLER and J.J. LAUTARD,  
*MINARET, a deterministic neutron transport solver for nuclear core calculations*,  
International Conference on Mathematics and Computational Methods Applied to Nuclear Science and Engineering (M&C 2011) Rio de Janeiro, RJ, Brazil, May 8-12, 2011, on CD-ROM, Latin American Section (LAS) / American Nuclear Society (ANS).
- [169] J.Y. MOLLER,  
*Éléments finis courbes et accélération pour le transport de neutrons*,  
PhD Thesis, tel-00659200, Université Henri Poincaré de Nancy, 2012.
- [170] L. MONDELAIN and D. SCHNEIDER,  
*APOLLO3 : Premiers calculs 3D d'un coeur en évolution avec contre-réactions*,  
Report, CEA/DEN/DM2S/SERMA/LTSD/RT/08-4613/A, 2008.
- [171] Y. MONERIE and J.M. GATT,  
*Overall Viscoplastic Behaviour of non irradiated Porous Nuclear Ceramics*,  
Mech. Mater, 38, 608, 2006.
- [172] R.O. MONTGOMERY and Y.R. RASHID,  
*Evaluation of Irradiated Fuel During RIA-Simulation Tests*,  
EPRI TR-106387, May 1996.

- [173] R. MONTGOMERY, J. RASHID, R. DUNHAM, O. OZER, and S. YAGNIK,  
*The mechanical response of cladding with a hydride lens under PCMI loading conditions I*,  
International Seminar on Pellet-Clad Interaction in Water Reactor Fuels. Aix-en-Provence, France, 2004.
- [174] P. MOSCA,  
*Conception et développement d'un mailleur énergétique adaptatif pour la génération des bibliothèques multigroupes des codes de transport*,  
Université Paris Sud 11, tel-00678561, 2012.
- [175] V.A. MOUSSEAU,  
*Implicitly balanced solution of the two-phase flow equations coupled to nonlinear heat conduction*,  
Journal of Computational Physics 200, 104–132, 2004.
- [176] O. MULA HERNANDEZ,  
*Quelques contributions vers la simulation parallèle de la cinétique neutronique et la prise en compte de données observées en temps réel*,  
Mémoire de thèse, Université Pierre et Marie Curie, tel-01068691, septembre 2014.
- [177] T. NAKAMURA, M. YOSHINAGA, M. TAKAHASHI, K. OKONOGI and K. ISHII,  
*Boiling water reactor fuel behavior under reactivity initiated accident conditions at burnup of 41 to 45 GWd/tonneU*,  
Nuclear Technology 129, 2000.
- [178] NEA website,  
<http://www.oecd-neo.org/>,
- [179] NEA,  
*Neutronic/Thermohydraulics coupling in LWR technology: vol. 1* ,  
CRISSUES-S 1 WP1, NEA No. 4452, ISBN 92-64-02083-7, 2004.
- [180] NEA,  
*Neutronic/Thermohydraulics coupling in LWR technology: state-of-the art report (REAC-SOAR), vol.2*,  
CRISSUES-S 1 WP2, NEA No. 5436, ISBN 92-64-02084-5, 2004.
- [181] NEA,  
*State-of-the-Art Report on Multi-scale Modelling of Nuclear Fuels*,  
NEA/NSC/R/2015

## BIBLIOGRAPHY

---

- [182] NEA/CRP  
*Transient Benchmark*,  
SIEMENS, OCDE, NEA/CRP/3D LWR Core, octobre 1991-janvier 1992.
- [183] NEA/CRP  
*Results of LWR Core Transient*,  
NEA/CRP/3D LWR Core, october 1993.
- [184] NEA/CSNI,  
*Reactivity Initiated Accident (RIA) Fuel Code Benchmark Phase II*,  
Volume 1: Simplified Cases Results, Summary and Analysis, March 2016.
- [185] NEA/CSNI  
*Reactivity Initiated Accident (RIA) Benchmark*,  
NEA/CSNI/R(2016), vol II, 2016 .
- [186] NEA/NSC,  
*Pressurized Water Reactor MOX/UO<sub>2</sub> Core Transient Benchmark*,  
Final Report, NEA n6048, December 2006.
- [187] NEA/NSC,  
*Benchmark for Uncertainty analysis in modelling (UAM) for design, operation and safety analysis of LWRs*,  
Volume II: Specification and support data for the core case (Phase II), April 2016.
- [188] A. NICOLAS,  
*Cours: modélisation des réacteurs*,  
CEA/DEN/DM2S/SERMA.
- [189] M. N. NICOLAEV and V. F. KHOKHLOV,  
*Systèmes des constantes en sous-groupes*,  
INDC (CCP), 4/G, 1969.
- [190] M. N. NICOLAEV,  
*Méthode des sous-groupes pour la prise en compte de la structure résonnante des sections efficaces dans les calculs neutroniques (1ère partie)*,  
Atomnaia Energia, 1970.
- [191] K. NKONGA, N. CROUZET, J-C. LE PALLEC, B. MICHEL, D. SCHNEIDER and A. TARGA,  
*Coupling of fuel performance and neutronic codes for PWR*,  
11th World Congress on Computational Mechanics (WCCM XI), 5th European Conference on Computational Mechanics (ECCM V), 6th European Conference on Computational Fluid Dynamics (ECFD VI), Barcelona, Spain, July 20-25, 2014.

- [192] L. NOIROT,  
*MARGARET - Description physique et numérique du modele de gaz applicable à chaque milieu homogène d'un combustible UO<sub>2</sub> ou MOX*,  
Technical report SESC/LSC 04-040, 2005.
- [193] L. NOIROT,  
*MARGARET: A comprehensive code for the description of fission gas behavior*  
Nucl. Eng. and Des., 241, 2099-2118, (2011).
- [194] O. ZERKAK and al.,  
*Review of Multi-physics coupling techniques and suggestions of improvements in the context of NURISP*,  
Collaborative Project (Large scale Integrating Project) Seventh Framework Programme EURATOM, 2009.
- [195] C. OTT and H.K. KOHL,  
*Evaluation of a critical fuel rod enthalpy versus Burnup under reactivity insertion accident conditions*,  
Annexe IV, Nuclear Energy safety, PSI annual report, 1995.
- [196] L.P. PAGANI,  
*On the quantification of safety margins*,  
Phd MIT, septembre 2004.
- [197] I.M. PALMER, K.W. HESKETH and P.A. JACKSON,  
*A model for predicting the radial power profile in a fuel pin*,  
IAEA specialists meeting on water reactor fuel element performance computer modelling - Preston, mars 1992.
- [198] J. PAPIN, J-C. MELIS, and C. LECOMTE,  
*Definition and Status of the CABRI International Program for High Burn-Up Fuel Studies*,  
Proceedings of the Twenty-Eighth Water Reactor Safety Information Meeting, NUREG/CP-0172, U.S. Nuclear Regulatory Commission, Bethesda, Maryland, October 23-25, pp. 185 - 190, 2000.
- [199] J. PAPIN and al.,  
*Summary and interpretation of the CABRI REP - Na program*,  
Nuclear Technology 157(3), 2007.
- [200] C. PATRICOT,  
*Couplages multi-physiques : évaluation des impacts méthodologiques lors de simulations de couplages neutronique/ thermique/mécanique*,  
Tel-01355622, PhD Thesis, Paris-Saclay University, 2016.

## BIBLIOGRAPHY

---

- [201] R. PERICAS,  
*Contribution to the validation of best estimate plus uncertainties coupled codes for the analysis of NK-TH nuclear transient*,  
PhD Thesis, Universitat Politècnica de Catalunya, 2015.
- [202] R. PERICAS, K. IVANOV, F. REVENTOS and L. BATET,  
*Code improvement and model validation for ASCO-II Nuclear Power Plant model using a coupled 3D neutron Kinetics/ThermalHydraulic code*,  
Annals of Nuclear Energy 87, 366-374, 2016.
- [203] J.P. PIRON, and al.,  
*Météor Version 1.5.0, Notice de présentation*,  
Note technique SDC/LEMC 96-2040 (DR), 1996.
- [204] G. C. POMRANING,  
*Asymptotic and variational derivations of the simplified PN Equations*,  
Ann. Nucl. Energy, 20 (9), pp.623-637, 1993.
- [205] C. POINOT SLANON, A. NICOLAS and M. SOLDEVILA,  
*Méthode de calcul neutronique des coeurs*,  
Technique de l'ingénieur bn3070, 2013.
- [206] P. PREVOT, A. NUTTIN , N. CAPELLAN and O. MEPLAN  
*Enhancements to the Nodal Drift Method for a Rod Ejection Accident in a PWR-like mini-core with lumped thermal model*,  
Annals of Nuclear Energy 101, 128-138, 2017.
- [207] A. RACINE,  
*Influence de l'orientation des hydrures sur les modes de déformation, d'endommagement et de rupture du Zircaloy4 hydruré*,  
Ph.D. thesis, Ecole Polytechnique, France, (2005).
- [208] V.H. RANSOM and V. MOUSSEAU,  
*Convergence and accuracy of the RELAP5 two-phase flow model*,  
ANS Topical Meeting on Advances in Mathematics, Computations and Reactor Physics, Pittsburg, PA, 1991.
- [209] Y.R. RASHID,  
*Mathematical modelling and analysis of fuel rods*,  
Nuclear Engineering and Design, 29, 22-32, 1974
- [210] P.A. RAVIART and J.P. THOMAS,  
*A Mixed Finite Element Method for the 2nd elliptic problems*,  
Mathematical Aspects of the Finite Element Method, Lecture Notes in Mathematics 606, Springer Verlag (1977).

- [211] P. RAYMOND,  
*FLICA3 v3.2. Equations Modèles* ,  
Technical report DMT/92-139, CEA 1992.
- [212] P. RAYMOND and I. TOUMO,  
*Numerical method for three-dimensional steady-state two-phase flow calculation*,  
NURETH-5, Salt-Lake City., 1992.
- [213] W. H. REED and T. R. HILL,  
*Triangular Mesh Methods for Neutron Transport Equation*,  
LA-UR-73-479, Los Alamos Scientific Laboratory, 1973.
- [214] P. REUSS,  
*Précis de neutronique*,  
Collection Génie Atomique, EDP science
- [215] P. RIBON and J.M. MAILLARD,  
*Les tables de probabilité : Application au traitement des sections efficaces pour la neutronique*,  
Note CEA-N-2485, 1986.
- [216] RICHEBOIS,  
*Données d'entrée des codes de calcul de coeur pour la modélisation d'une RTV d'un REP 1300MW*,  
Report DM2S, SFME/LETR/RT/02-003/A, 2004.
- [217] G. RIMPAULT,  
*Algorithmic Features of the ECCO Cell Code for Treating Heterogeneous Fast Reactor Subassemblies*,  
International Topical Meeting on Reactor Physics and Computations, Portland, Oregon, 1995.
- [218] G. RIMPAULT and al.,  
*The ERANOS data and code system for fast reactor neutronic analyses. In: Proceedings of the International Conference on the New Frontier of Nuclear Technology: Reactor Physics*,  
Safety and High-Performance Computing, PHYSOR, Seoul, South Korea, 7 à 10 October 2002.
- [219] G. ROBERTS,  
*The Concentration of Stress in Cladding Produced by the Expansion of Cracked Fuel Pellets*,  
Nucl. Eng. Des., 47, 257(1978).
- [220] ROSATOM,  
*Fuel Company*, November 2014.

## BIBLIOGRAPHY

---

- [221] A.M. ROSS and R.L. STOUTE,  
*Heat transfer coefficient between UO<sub>2</sub> and Zircaloy-2*,  
Report, CRFD-1075, 1962.
- [222] E. ROYER and I. TOUMI ,  
*CATHARE-CRONOS-FLICA coupling with ISAS: A powerful tool for nuclear studies*,  
ICONE-6 Meeting, San Diego, California, USA, 1998.
- [223] G. ROWLAND,  
*Resonance absorption and non-uniform temperature distribution*,  
1961, AERE M17
- [224] P. RUDLING and al.,  
*Annual review of information on Zircaloy technology : Loss of coolant accidents, LOCA, and reactivity initiated accidents, RIA, in BWRs and PWRs*,  
Technical Report IZNA-4 Special Topics Report, Advanced Nuclear Technology International, Sweden, 2005.
- [225] P. RUBIOLO,  
*Modélisation du transfert thermique dans un milieu poreux : application aux réacteurs nucléaires en situation accidentelle*  
Université Aix - Marseille, PhD Thesis, 2000.
- [226] J.M. RUGGIERI and al.,  
*ERANOS 2.1 : International Code System for GEN IV Fast Reactor Analysis*  
ICAPP 2006, Reno, USA, 2006.
- [227] C. SARTORIS and al., *A consistent approach to assess safety criteria for reactivity initiated accidents*,  
Nuclear Engineering and Design 240, p. 57-70, 2010.
- [228] F. SAUTER,  
*Modélisation du comportement viscoplastique du dioxyde d'uranium*,  
Ph.D. thesis, Institut National Polytechnique de Lorraine, France 2000.
- [229] H. SASAJIMA and al.,  
*Fission gas release behavior of high burnup UO<sub>2</sub> fuel under reactivity initiated accident conditions*,  
Journal of Nuclear Science and Technology 36(11), 1101-1104, 1999.
- [230] R. SANCHEZ and al.,  
*APOLLO II: A user-oriented, portable, modular code for multigroup transport assembly calculations*,  
Nucl. Sci. and Eng. 100, p. 352-362, 1988.

- [231] R. SANCHEZ and al.,  
*SAPHYR : A Code System from Reactor Design to Reference Calculations*,  
International Conference on Supercomputing in Nuclear Applications, Paris, France,  
September, 2003.
- [232] D. SCHNEIDER and al.,  
*Mixed Dual Finite Element Method for the solution of the 3D kinetic Simplified PN  
transport equation*,  
Nuclear Mathematical and Computational Sciences: A Century in Review, A Century  
Anew Gatlinburg, Tennessee, April 6-11, 2003.
- [233] D. SCHNEIDER, J.C. LE PALLEC and A. TARGA,  
*Mise en oeuvre d'un exercice de couplage APOLLO3-FLICA4 dans l'outil Multi  
Physique CORPUS dédié à l'analyse des réacteurs REP en situations de fonc-  
tionnement normal et accidentel*,  
Journée Utilisateurs SALOME, CEA-Saclay, 21 novembre 2013.
- [234] D. SCHNEIDER and al.,  
*APOLLO3®: CEA/DEN deterministic multi-purpose code for reactor physics analy-  
sis*,  
PHYSOR 2016, Sun Valley, Idaho, USA, May 1-5, 2016.
- [235] F. SCHMITZ and J. PAPIN,  
*High burnup effects on fuel behaviour under accident conditions : the tests CABRI  
REP-Na*,  
Journal of Nuclear Materials 270, 1999.
- [236] SJENITZER and al. , *Coupling of Dynamic Monte Carlo with thermohydraulic feed-  
back*,  
Ann. Nuc. Energy 76, p 27-39, 2015.
- [237] G. SERRE and M. KAMINAGA,  
*Physical laws of cathare revision 6. Pipe module*, Technical report  
SMTH/LMD/EM/98-038, CEA, 1999.
- [238] SERMA (CEA/DEN/DM2S),  
*Séminaire Etudes multi-physiques Coeur et Piscines*,  
Seminaire, CEA DIGITEO - Maison de la simulation, May 2016.
- [239] SERMA (CEA/DEN/DM2S),  
*Cronos2.10: Manuel de référence*,  
Report, CEA/DEN/DM2S/SERMA/LLPR/RT/11-5080/A, 2011.
- [240] J.R. SHEWCHUK,  
*Lecture Note on Delaunay Mesh Generation*,



## BIBLIOGRAPHY

---

- Department of electrical Engineering and computer sciences, University of California at Berkeley, CA 94720, 2012.
- [241] M. SLADKOFF , F. HUET and A. MOCELLIN,  
*Recommandation pour la loi de fluage stationnaire de l'UO<sub>2</sub> non dopé: mise à jour de fin 1998 intégrant les études de fluage sur les lots L209609 et L209619*,  
SPUA/LACA 99-007, octobre 1999.
- [242] E. SMITH,  
*The Fuel-Cladding Interfacial Friction Coefficient in Water-Cooled Reactor Fuel Rods*,  
Trans. SMIRT 5, 1979.
- [243] A. SONIAK et al.,  
*Irradiation Creep Behavior of Zr-Base Alloys*,  
Zirconium in the Nuclear Industry: 13th International Symposium, ASTM STP 1423,  
p. 837, G. D. MOAN and P. RUDLING, Eds., ASTM International, West Conshohocken, Pennsylvania, 2002.
- [244] B. SPINDLER,  
*Qualification du code FLICA-III M pour les calculs de thermohydrauliques de grappes et de coeurs de réacteurs à eau sous pression*,  
Technical report SETH/GEML/86-24, CEA, 1986.
- [245] Y. SUDO and M. KAMINAGA,  
*A New CHF Correlation Scheme Proposed for Vertical Rectangular Channels Heated From Both Sides in Nuclear Research Reactors*,  
Journal of Heat Transfer, 115(May), 1993.
- [246] T. SUGIYAMA and T. FUKETA,  
*Effect of cladding pre-oxidation on rod coolability during reactivity accident conditions*,  
In : Technical Committee Meeting on Fuel Behaviour Under Transient and LOCA Conditions, IAEA-TECDOC-1320, p. 102-110. Halden, Norway, 2001.
- [247] A. TARGA,  
*Contribution au developpement des schemas de couplage coeur neutronique-combustible dedies à la realisation d'un scénario RIA (accident d'ejection de grappe de controle)*,  
Travail de fin d'Etude, Ecole Centrale Marseille, 2013.
- [248] A. TARGA, J.C. LE PALLEC and P. LE TALLEC,  
*Multiscale and multisolver pin power reconstruction approach in a reactor core calculation*,  
ICAPP 2015, paper 15124, Nice, France, 2015.
- [249] A. TARGA, J.C. LE PALLEC, P. LE TALLEC, K. NKONGA, N. CROUZET and S. CHEMIN,

- Thermohydraulics-Thermomechanics Best Estimate coupled approach in a Rod Ejection Accident core calculation*,  
ICAPP 2016, Paper 16405, San Francisco, CA, USA, April 17-20, 2016.
- [250] B. TARRIDE,  
*Physique, fonctionnement et sûreté des REP: Maitrise des situations accidentelles du système réacteur*,  
Collection Génie Atomique, EDP science, 318 pages, 2013.
- [251] G. THOUVENIN and V. MARELLE,  
*ALCYONE V1.2.3: Notice de Présentation*,  
Report, CEA/DEN/CAD/DEC/SESC/LSC NT 12-002, 2012.
- [252] P.K. TONDON and S.C. SAXENA,  
*Calculation of thermal conductivity of polar-nonpolar gas mixtures*,  
Appl. Sci. Res. 19, 163-170, 1968.
- [253] K. TOMIYASU , T. SUGIYAMA and T. FUKETA,  
*Influence of Cladding-Peripheral Hydride on Mechanical Fuel Failure under Reactivity-Initiated Accident Conditions*,  
Journal of NUCLEAR SCIENCE and TECHNOLOGY, Vol. 44, No. 5, p. 733 - 742, 2007.
- [254] L.S. TONG and J. WEISMAN,  
*Thermal analysis of pressurized water reactors*,  
American Nuclear Society, 1996.
- [255] I. TOUMI,  
*A weak formulation of Roe's approximate Riemann solver*,  
Journal of Computational Physics, 102, 360 - 373, 1992.
- [256] I. TOUMI,  
*FLICA IV: Manuel de référence, méthode numérique*,  
CEA report (unpublished), DMT93/439, 1995.
- [257] I. TOUMI and al. ,  
*Advanced numerical methods for two-phase flow simulation*,  
OECD/NEA/CSNI workshop, Barcelona, 10 - 13 April 2000.
- [258] I. TOUMI and al. ,  
*FLICA4: a three-dimensional two-phase flow computer code with advanced numerical methods for nuclear applications*,  
Nuclear Engineering and Design, 139-155, 2000.
- [259] A.M. TORRES,  
*Further Developments of Multiphysics and Multiscale Methodologies for Coupled*

## BIBLIOGRAPHY

---

- Nuclear Reactor Simulations*, PhD Thesis, Technische Universitat Munchen, 2010.
- [260] A.M. TORRES, V.H. SANCHEZ-ESPINOZA, K. IVANOV and R. MACIAN-JUAN, *DYNSUB: A high fidelity coupled code system for the evaluation of local safety parameters - Part I: Development, implementation and verification*, Annals of Nuclear Energy 48, 108-122, 2012.
- [261] A.M. TORRES, V.H. SANCHEZ-ESPINOZA, K. IVANOV and R. MACIAN-JUAN, *DYNSUB: A high fidelity coupled code system for the evaluation of local safety parameters - Part II: Comparison of different temporal schemes*, Annals of Nuclear Energy 48, 123-129, 2012.
- [262] A. TSILANIZARA, T.H. HUYNH and C.M. DIOP, *Formulaire DARWIN: Notice de principe*, Report DEN/DANS/DM2S/SERMA/LLPR/RT/05-3772/B, 2012.
- [263] P.J. TURINSKY, *A Random Walk Toward Advanced modelling and Simulation Capabilities in Nuclear Engineering*, NEAMS presentation, North Carolina State University, 2008.
- [264] P.J. TURINSKY, *Advances in Multi-physics and High performance computing in support of nuclear reactor power systems modelling and simulation*, <http://dx.doi.org/10.5516/NET.01.2012.500>, 2011.
- [265] A.C. UGGENTI, *Amélioration de la modélisation du combustible dans le cadre d'une description neutronique de type cinétique ponctuelle - analyses physiques en situation RIA*, Master Thesis, Ecole nationale supérieure de physique, électronique et matériaux (Phelma), 2014.
- [266] P. VIZCAINO, A. BANCHIK and J. P. AABRIATA, *Solubility of Hydrogen in Zir-caloy-4: Irradiation Induced Increase and Thermal Recovery*, Journal of Nuclear Materials, Vol. 304, No. 2-3, p. 96-106, 2002.
- [267] P. VIZCAINO, A. BANCHIK and J. P. AABRIATA, *Hydrogen in Zircaloy-4 : effects of the neutron irradiation on the hydride formation*, Journal of Nuclear Materials 42, p. 6633-6637, 2007.
- [268] N. WAECKEL, S. STELLETTA, C. BERNAUDAT, G. CHAIGNE and O. PAVAGEAU,

- Domaine de surete propose par EDF pour les accidents d'ejection de grappe en REP*, presentation EDF, conference SFEN, 20 septembre 2000.
- [269] A.M. Ward,  
*A Newton-Krylov Solution to the Coupled Neutronics-Porous Medium Equations*,  
PhD Thesis, The University of Michigan, 2012.
- [270] J.K. WATSON,  
*Implicit Time-Integration Method for Simultaneous Solution of a Coupled Non-Linear System*,  
PhD Thesis, Penn State University, January 27, 2010.
- [271] J.C. WOOD, B.A. SURETTE and I.AITCHISON,  
*Pellet Cladding Interaction/Evaluation of Lubrification by Graphite*,  
J. Nucl. Mater., 88, 1980.
- [272] S. YAGNIK and al.,  
*Effect of hydrides on the mechanical properties of Zircaloy4*,  
International Topical Meeting on Light Water Reactor Fuel Performance, pp. 191 - 199. Orlando, Florida, 2004.
- [273] R. YANG and al.,  
*Revised reactivity initiated accident acceptance criteria for high burn-up fuel*,  
Topical Report on Reactivity Initiated Accident: Bases for RIA Fuel and Core Coolability Criteria, EPRI, 2003.
- [274] C.L. ZIMMERMANN, C. E. WHITE, and R. P. EVANS,  
*Experiment Data Report for Test RIA 1-2 (Reactivity Initiated Accident Test Series)*,  
NUREG/CR-0765, EG &G Idaho Inc., June 1979.
- [275] I. ZMIJAREVIC ,  
*Structure and contents of the Apollo2 output file SAPHYB*,  
Reference SERMA/LLPR/RT/09-4818/A, 2009.
- [276] I. ZMIJAREVIC and al.,  
*Generation of multi-parameter cross sections libraries by APOLLO3*,  
Report, DEN/DANS/DM2S/SERMA/LTSD/RT/10-5059/A, 2010.





**Titre:** Développement de modélisations multi-physiques Best Effort pour une analyse fine des réacteurs à eau pressurisée en conditions accidentelles.

**Mots clés:** Modélisation Multiphysique, Thermohydraulique, Thermo mécanique des Combustibles Nucléaire, Neutronique

**Résumé:** Ce travail de Thèse prend place dans un contexte de recherche en modélisation multi physique et multi échelle dans le but d'obtenir une compréhension global et fine du comportement d'un réacteur à eau pressurisée en cadre de fonctionnement standard et accidentel. Ce travail de recherche a consisté principalement en l'analyse des modèles et de leurs interactions et à la mise en oeuvre d'un algorithme de couplage multiphysique entre une neutronique (APOLLO3) et une thermohydraulique (FLICA4) exprimées à l'échelle du réacteur, ainsi qu'avec une thermomécanique fine (ALCYONE) à l'échelle élémentaire du crayon combustible. En outre, un travail spécifique a été effectué afin de préparer ou d'améliorer l'accès à l'information physique locale nécessaire à la mise en oeuvre de modélisations couplées multi-échelles, à l'échelle du combustible.

**Title:** Development of multi-physics and multi-scale Best Effort modelling for accurate analysis of Pressurized Water Reactor under accidental situation.

**Keywords:** Multiphysics modelling, Thermohydraulics, Fuel pin Thermomechanics, Neutronics

**Abstract:** This PhD Thesis takes place in the framework of multiphysics multi-scale Best Effort modelling research in order to get a full and an accurate (High Fidelity) comprehension of the reactor core behavior under standard and accidental situations. This work mainly involved the understanding of each model and their interactions, followed by the implementation of multiphysics algorithms coupling Neutronics (APOLLO3) and Thermohydraulics (FLICA4) at reactor scale to an accurate Thermomechanics (ALCYONE) at the elementary scale of the fuel pin. In addition, a work project has been carried out in order to prepare or improve the access to the local physical informations that are needed for the implementation of multiscale coupling scheme, at the elementary scale of the fuel pin.